DEVELOPMENT OF MEMS TECHNOLOGY BASED MICROWAVE AND
MILLIMETER-WAVE COMPONENTS

A THESIS SUBMITTED TO
THE GRADUATE SCHOOL OF NATURAL AND APPLIED SCIENCES
OF
MIDDLE EAST TECHNICAL UNIVERSITY

BY

ÇAĞRI ÇETİNTEPE

IN PARTIAL FULFILLMENT OF THE REQUIREMENTS
FOR
THE DEGREE OF MASTER OF SCIENCE
IN
ELECTRICAL AND ELECTRONICS ENGINEERING

FEBRUARY 2010

Approval of the thesis:

DEVELOPMENT OF MEMS TECHNOLOGY BASED MICROWAVE AND MILLIMETER-WAVE COMPONENTS

submitted by **ÇAĞRI ÇETİNTEPE** in partial fulfillment of the requirements for the degree of **Master of Science in Electrical and Electronics Engineering Department, Middle East Technical University** by,

Prof. Dr. Canan Özgen
Dean, Graduate School of **Natural and Applied Sciences** _____

Prof. Dr. İsmet Erkmen
Head of Department, **Electrical and Electronics Engineering** _____

Assoc. Prof. Dr. Şimşek Demir
Supervisor, **Electrical and Electronics Engineering Department** _____

Prof. Dr. Tayfun Akın
Co-supervisor, **Electrical and Electronics Engineering Department** _____

Examining Committee Members:

Prof. Dr. Canan Toker
Electrical and Electronics Engineering Dept., METU _____

Assoc. Prof. Dr. Şimşek Demir
Electrical and Electronics Engineering Dept., METU _____

Prof. Dr. Tayfun Akın
Electrical and Electronics Engineering Dept., METU _____

Assoc. Prof. Dr. Sencer Koç
Electrical and Electronics Engineering Dept., METU _____

Dr. Mustafa Akkul
ASELSAN REHİS _____

Date: <u>05.02.2010</u>

I hereby declare that all information in this document has been obtained and presented in accordance with academic rules and ethical conduct. I also declare that, as required by these rules and conduct, I have fully cited and referenced all material and results that are not original to this work.

Name, Last Name: ÇAĞRI ÇETİNTEPE

Signature   :

ABSTRACT

DEVELOPMENT OF MEMS TECHNOLOGY BASED MICROWAVE AND
MILLIMETER-WAVE COMPONENTS

Çetintepe, Çağrı

M.S., Department of Electrical and Electronics Engineering

Supervisor   : Assoc. Prof. Dr. Şimşek Demir

Co-Supervisor   : Prof. Dr. Tayfun Akın

February 2010, 211 pages

This thesis presents development of microwave lumped elements for a specific surface micromachining based technology, a self-contained mechanical characterization of fixed-fixed type beams and realization of a shunt, capacitive-contact RF MEMS switch for millimeter-wave applications.

Interdigital capacitor, planar spiral inductor and microstrip patch lumped elements developed in this thesis are tailored for a surface micromachining technology incorporating a single metallization layer, which allows an easy and low-cost fabrication process while permitting mass production. Utilizing these elements, a bandpass filter is fabricated monolithically with success, which exhibits a measured in-band return loss better than -20 dB and insertion loss of 1.2 dB, a pass-band located in S-band and a stop-band extending up to 20 GHz.

Analytical derivations for deflection profile and spring constant of fixed-fixed beams are

derived for constant distributed loads while taking axial effects into account. Having built experience with the mechanical domain, next, Finite Difference solution schemes are established for pre-pull-in and post-pull-in electrostatic actuation problems. Using the developed numerical tools; pull-in, release and zipping phenomena are investigated. In particular, semi-empirical expressions are developed for the pull-in voltage with associated errors not exceeding 3.7 % of FEA (Finite Element Analysis) results for typical configurations.

The shunt, capacitive-contact RF MEMS switch is designed in electromagnetic and mechanical domains for Ka-band operation. Switches fabricated in the first process run could not meet the design specifications. After identifying sources of relevant discrepancies, a design modification is attempted and re-fabricated devices are operated successfully. In particular, measured OFF-state return and insertion losses better than -16.4 dB and 0.27 dB are attained in 1-40 GHz. By applying a 20-25V actuation, ON-state resonances are tuned precisely to 35 GHz with an optimum isolation level of 39 dB.

Keywords: Lumped elements, surface micromachining, millimeter-wave, RF MEMS, switch, fixed-fixed beam, electrostatic actuation.

ÖZ

MEMS TEKNOLOJİSİ TABANLI MİKRODALGA VE MİLİMETRİK DALGA BİLEŞENLERİN GELİŞTİRİLMESİ

Çetintepe, Çağrı

Yüksek Lisans, Elektrik ve Elektronik Mühendisliği Bölümü

Tez Yöneticisi   : Doç. Dr. Şimşek Demir

Ortak Tez Yöneticisi : Prof. Dr. Tayfun Akın

Bu tezde, yüzey mikroişleme tabanlı özel bir teknoloji için toplu mikrodalga bileşenlerin geliştirilmesi, bağlı-bağlı tip kirişlerin bağımsız bir mekanik incelemesi ve milimetrik dalga uygulamaları için paralel, sığal-değeçli bir RF MEMS anahtarın gerçeklenmesi anlatılmaktadır.

Bu çalışmada geliştirilen parmaklı sığaç, düzlemsel sarmal irgiteç ve mikroşerit yama toplu bileşenleri; tek metal katman kullanan ve dolayısı ile kolay, ucuz ve seri bir üretime imkan veren yüzey mikroişleme tabanlı bir teknoloji için uyarlanmıştır. Bu bileşenler kullanılarak, bant-geçiren bir süzgeç yapısı tektaş olarak başarıyla üretilmiş ve ölçümlerde -20 dB'den iyi bant-içi geri dönüş kaybı, 1.2 dB bant-içi araya girme kaybı, S frekans bandında yer alan bir geçiş bandı ve 20 GHz'e varan bir durdurma bandı elde edilmiştir.

Bağlı-bağlı tip kirişlerin eğilme kesiti ve yay sabiti ifadeleri, eksenel etkiler göz önünde bulundurularak, düzgün dağıtılmış yükler için çözümsel bir şekilde çıkarılmıştır. Mekanik

alanında yeterli tecrübeye eriştikten sonra, hareketlendirme öncesi ve sonrası elektrostatik uyarım problemleri için Sonlu Farklar yöntemiyle sayısal çözüm biçimleri oluşturulmuştur. Geliştirilen sayısal araçlarla; hareketlendirme, bırakma ve değeç-iyileşmesi davranışları incelenmiştir. Hareketlendirme gerilimi için özel olarak yarı-deneysel ifadeler çıkarılmış ve tipik yapılanmalar için elde edilen hatanın Sonlu Eleman Yöntemi ile kıyaslandığında %3.7'yi geçmediği gözlemlenmiştir.

Paralel, sığal-değeçli RF MEMS anahtar elektromanyetik ve mekanik alanlarında Ka frekans bandı için tasarlanmıştır. İlk aşamada üretilen anahtarların tasarım belirtimlerine uymadığı görülmüştür. İlgili farklılıkların sebeplerinin anlaşılmasını takiben bir tasarım değişikliğine gidilmiş ve yeniden üretilen anahtarların başarıyla çalıştıkları gözlemlenmiştir. Ölçümlerde AÇIK-durumda geri dönüş ve araya girme kayıpları 1-40 GHz bandında sırasıyla -16.4 dB ve 0.27 dB'den iyi bulunmuş; KAPALI-durum çınlama frekansı 20-25 V uyarım gerilimiyle hassas olarak 35 GHz'e oturtulmuş ve ilgili yalıtım 39 dB olarak elde edilmiştir.

Anahtar Kelimeler: Toplu bileşenler, yüzey mikroişleme, milimetrik dalga, RF MEMS, anahtar, bağlı-bağlı kiriş, elektrostatik uyarım.

Dedicated to my family...

ACKNOWLEDGMENTS

I would like to express my gratitude to my advisors Assoc. Prof. Dr. Şimşek Demir and Prof. Dr. Tayfun Akın in the first place not only for their guidance, support and encouragement during the course of this thesis; but also for granting me the opportunity to pursue my research in the RF MEMS Group.

My dearest appreciation goes to Dr. Mehmet Ünlü and Dr. Kağan Topallı, who supervised me patiently and persistently through most of my studies. I am indebted to them for furnishing me with a background of a real engineer. Leaving the academic perspective aside; I am also obliged to express my sincere thanks to them for they furthermore have offered their friendship, shared real-life experiences and treated me as one of them during this period.

I would moreover thank RF MEMS Group members Ömer Bayraktar, Ozan Doğan Gürbüz, Caner Güçlü and Korkut Kaan Tokgöz for their cooperation and friendship which in turn rendered our office a warm workplace. I am, however, compelled to distinguish my dear colleague İlker Comart who has never denied me his help, joy and friendship during our company.

I also wish to acknowledge METU-MEMS personnel, especially Orhan Akar, for their kind support and interest during fabrication of the components described in this thesis.

I could not end this section without conveying my deepest gratitude to my family. It would be impossible to imagine myself in my current position without their everlasting love and encouragement.

TABLE OF CONTENTS

LIST OF TABLES

LIST OF FIGURES

FIGURES

CHAPTER 1

INTRODUCTION

Attention received by mobile and wireless systems nowadays is tremendous world-wide: Portable GPS systems aid navigation during transport, cell phones featuring new protocols elevate communication to a new level while furnishing the users with a plethora of other integrated multimedia functions, consumer electronics equipped with built-in wireless communication options like WiFi® or Bluetooth® render life easier etc. Faced with this ever-growing trend, manufacturers direct their attention to miniaturization of these systems, integration of more and more functions, enhancing battery lives and lowering overall costs to maintain and widen their audience. These goals eventually lend themselves to optimization of the underlying RF sections: In particular; compact-sized, low-cost, high performance RF components are required in order to satisfy even tighter specifications with optimized battery life [1–3]. The latter requirements are pushing the manufacturers to state-of-the-art RF solutions.

RF MEMS (Radio Frequency Micro-Electro-Mechanical Systems) technology is a viable solution that bears the potential to successfully address previously mentioned aspects [4–7]. In fact, RF MEMS is not limited in scope to only wireless communication systems: It is a rather recent technology capable of producing components whose performance can be hardly surpassed for a variety of applications including microwave and millimeter-wave radar, modern civil/military telecommunication, satellite and instrumentation systems [8]. Its "enabling" nature in addition, provides the ability to construct tunable or reconfigurable circuits whose realization might not be otherwise feasible, if not possible, with the existing technologies. Possessing those attributes, it is not improbable for the RF MEMS technology to revolutionize many application areas, including the thriving wire-

less communication arena exemplified at the beginning, in the near future [9, 10].

This thesis focuses on development of microwave and millimeter-wave components that aim to exploit aforementioned, yet not explicitly stated, favorable properties of RF MEMS technology. In what follows, those properties are revealed with an overview section. The bridge between the studies attempted in this thesis and RF MEMS technology is then formed in the subsequent section.

1.1 An Overview of RF MEMS

RF MEMS technology employs properly configured micro-mechanical structures fabricated using bulk or surface micromachining techniques to yield high-performance components in electrical domain at RF to millimeter-wave frequencies [11–14]. These micromechanical structures are either immovable resulting in fixed components (such as high-Q inductors [15–17], micro-cavity resonators [18, 19] and bulk micromachined or membrane-based transmission lines [20, 21], filters [22], antennas [23]) or can be actuated by several means to exhibit mechanical movement during operation. The latter category, also termed as "active RF MEMS" [24], can be further divided into two: One research area focuses on film bulk acoustic resonators (FBARs) and micromechanical resonators which serve as electromechanical filters that can achieve impressive Q-factors (1000-10000) up to (sub) GHz frequencies [25–28]. Primary research, however, pertains to the most crucial active building blocks that get RF MEMS to shine both in academia and in the market: RF MEMS *switches* and *varactors*.

Switches [29–40] and varactors [41–45] are the key elements of RF MEMS technology which bring tunability and reconfigurability into play. The basic operation principle of those devices relies on altering their electrical properties through some actuation means: Mechanical movement changes the electrical state to toggle between what are essentially open and short-circuits for the case of switches; whereas a similar movement alters either the effective gap or overlap area between the electrodes of varactors in order to vary associated capacitance. Relevant movement is generally established by electrostatic actuation

2

due to relatively faster transition times, smaller device layouts and essentially zero biasing power requirements; although other actuator forms such as piezoelectric, magnetostatic and thermal also exist [8]. In particular, Chapter 4 introduces basic implementations for RF MEMS switches, which would shed more light into mentioned operation principles.

Following properties of RF MEMS switches and varactors constitute their highlights:

- **Low Insertion Loss:** RF MEMS devices exhibit very low insertion losses ($< 0.1-0.2$ dB) up to 100 GHz [46] owing to utilized metal layers with high-conductivities and low substrate losses.

- **High Isolation:** Isolation between the ports of an RF MEMS switch is high due to low OFF-state capacitances for ohmic-contact switches and high ON-state capacitances for capacitive-contact switches[1].

- **High linearity:** As RF MEMS devices do not contain any nonlinear materials such as semiconductor junctions, they yield highly linear operation. In fact, third order intercept point (IP3) of RF MEMS devices are 20-50 dB better than their solid-state rivals [47].

- **Nearly Zero Biasing Power:** Electrostatic and piezoelectric actuation schemes demand virtually no bias power due to lack of drawn current, except for transients during which power consumption remains less than 0.1 mW [8].

- **Potentially Low Cost:** Standard surface micromachining techniques can be effectively utilized to fabricate miniature RF MEMS devices using denser wafers with a low associated cost. Moreover, recent fabrication trends help reduce additional packaging costs [48, 49].

- **Reconfigurability:** RF MEMS switches and varactors can be implemented in various combinations to yield high-performance reconfigurable/tunable circuits such as phase shifters [50–52], impedance tuners [53–55], tunable filters [56, 57], reconfigurable antennas [58–60] to name a few.

---

[1] See §4.1 for details.

Along with their strengths, RF MEMS devices also possess some drawbacks, which can be listed as follows:

- **High Actuation Voltage:** For proper operation of electrostatically actuated RF MEMS devices, voltage levels in 25-90 V range are required, which are apparently higher than digital control signal levels. In order to maintain compatibility of those voltages, high-voltage drive circuits are needed as interface elements.

- **Low Switching Speeds:** Switching times of RF MEMS devices are in 2-40 μs range for electrostatic actuation [46]. Hence, RF MEMS devices cannot be utilized in applications where transient specifications are stringent. Still, research is carried on miniature RF MEMS devices which aim to lower transient times down to 200 ns [61].

- **Power Handling:** Due to their construction, RF MEMS devices cannot attain too high power levels without sacrificing from their lifetime considerably. The power limit for reliable operation, nevertheless, shifted from 500 mW up to 10 W with the emergence of proper design and fabrication techniques.

- **Packaging:** Being miniature and fragile devices, RF MEMS components need to be packaged and must be isolated from environmental effects like dielectric contamination, water and gas vapors in order to operate reliably in a desired lifetime. This in turn requires hermetic packaging of those devices which establishes a controlled environment. Integration of a package with RF MEMS devices, however, is difficult in general as RF performance must not degrade appreciably, hermeticity of the package must be sufficient and associated packaging costs should be low. As mentioned previously, recent attempts are directed to reduce packaging costs with novel package implementations [48, 49].

- **Reliability:** Reliability and lifetime of RF MEMS devices are major concerns as this factor primarily determines whether a given device would stay as a lab prototype or may develop to a mature component. Depending on the intended application, a given lifetime of those devices should be ensured by a careful study of the failure mechanisms (like contact degradation or dielectric charging) and solving associated problems. Although state-of-the-art switches offer lifetimes reaching up to 200 bil-

lion cycles [47,62], long-term lifetime is not addressed. Moreover, reported number of cycles may decrease significantly when hot-switching conditions are considered.

1.2 Accomplished Works in This Thesis

Within the framework of this thesis, microwave and millimeter-wave components are developed which utilize RF MEMS as the underlying technology. In particular, the first study pertains to development of microwave lumped elements for a specific surface micromachining based technology, which is essentially a simple subset of RF MEMS. The second and third studies are interrelated, with the common goal to realize and characterize a millimeter-wave RF MEMS switch component. Following subsections overview these studies next.

1.2.1 Development of Microwave Lumped Elements

A microwave component is considered lumped when its largest dimension is a small fraction ($< 1/10$) of the guided wavelength (λ_g) in a transmission medium at a particular frequency. Lumped elements appeared around 1965 during the microwave integrated circuit (MIC) era in order to address chip-size related problems: Distributed-type approaches utilized at that time posed significant size issues especially at lower frequencies. Having replaced the distributed microstrip-based topologies with the lumped elements, relevant goal was attained and this progress was later followed by spread of the information related to design, measurement and application of those elements up to 12 GHz [63–65]. With its emergence in 1976, monolithic microwave integrated circuits (MMICs) then made excessive use of lumped elements and utilized them to construct impedance matching blocks, bias chokes, filters, phase shifters and other circuits [66]. The arrival of wireless and mobile applications further rendered lumped elements indispensable for low-cost and low-footprint solutions.

Lumped elements offer several advantages over the distributed counter-parts, a few of which can be summarized as follows [67]:

- Lumped elements have compact sizes compared to distributed solutions, the difference becoming prominent towards lower frequencies for which λ_g grows significantly.

- Small size property depicted above yields low-cost solutions as area of a chip can be reduced significantly, leading to denser wafers and lower fabrication costs.

- Lumped elements display wider bandwidth characteristics compared to distributed approaches. This is due to their lower complementary parasitics. For instance, a given inductance value can be generally realized with a much lower complementary reactance using a lumped inductor element than a high-impedance transmission line.

- Due to confinement of electromagnetic field in a fairly compact area (as a consequence of the lumped property), couplings between two elements are lower for lumped elements than distributed elements. This attribute further promotes chip size reduction.

Figure 1.1 presents the microwave lumped elements studied in this thesis. Depicted microstrip-based interdigital capacitor, planar spiral inductor and microstrip patch (or parallel-plate capacitor) components have been well-characterized and widely adopted in the literature [68]. Selection of these particular components is guided primarily by the fabrication-related goals of this study, which are discussed in Chapter 2. According to those goals, a surface micromachining based technology that employs only a *single metallization layer* is utilized to implement the lumped elements.

RF MEMS relation of this work is partly historical: Within the scope of METU RF MEMS Group's technology development efforts, planar spiral inductors and metal-insulator-metal (MIM) capacitors were successfully realized in [69] previously. This work forms an extension of that study with the main concerns focusing on development of different type lumped elements using a simpler implementation scheme, yet still utilizing the capabilities of RF MEMS technology. In fact, surface micromachining technology employed in this work is adapted from the existing in-house METU RF MEMS base-metallization process.

(a) Interdigital capacitor (IDC).　　　　(b) Planar spiral inductor (PSI).

(c) Microstrip patch (MP).
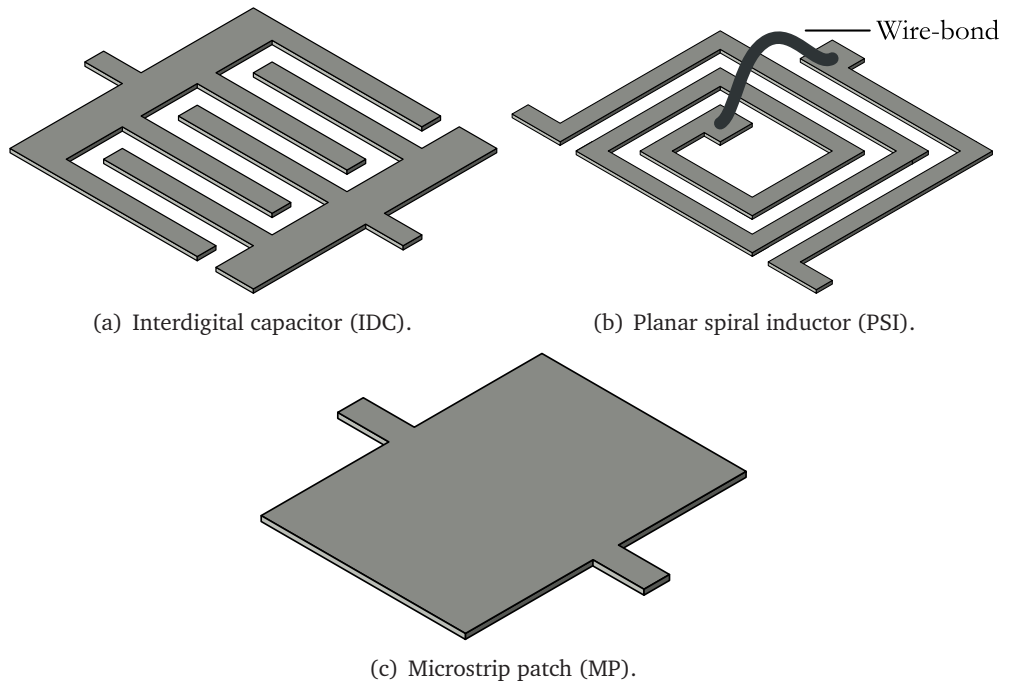
Figure 1.1: *Developed microwave lumped elements in this thesis. Substrate material and bottom ground plane is not shown for clarity.*
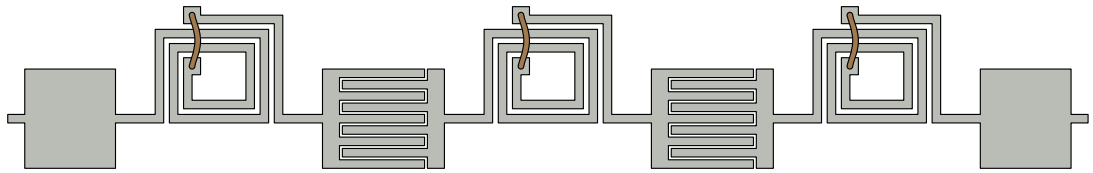
Figure 1.2: *Implemented monolithic filter structure using the developed microwave lumped elements. Components are not drawn to scale.*

Throughout this work, development of the microwave lumped elements is oriented towards an example filter application which not only serves as an effective test vehicle but also fulfills the monolithic integration goals of the fabrication technology. Figure 1.2 illustrates layout of the filter structure incorporating these lumped elements.

1.2.2　Mechanical Characterization of Fixed-Fixed Type Beam Structures

A fixed-fixed (or doubly-clamped) beam, as Figure 1.3 illustrates, is a structural component whose ends are built into restraints in order to constrain both the deflection and slope at those ends to zero. This particular component forms, or practically ap-
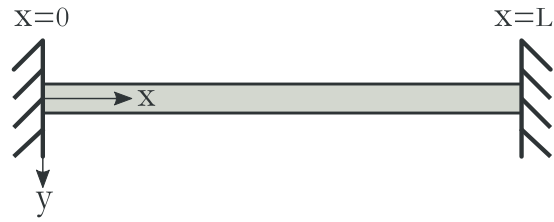
Figure 1.3: *An illustration of a fixed-fixed type beam.*

proximates, the micro-mechanical element in many MEMS applications including micro-resonators [70–72], mass-flow sensors [73], accelerometers [74] and for material property extraction purposes [75–77]. A sizeable portion of RF MEMS switches also belongs to this category [32, 36, 37]. Since those MEMS devices rely on mechanically actuated structures and operate with interdisciplinary principles, it follows that a proper characterization of fixed-fixed beams is crucial to the performance obtained in other domains.

This work attempts to establish a self-contained mechanical characterization of fixed-fixed type beams while devoting particular attention to electrostatical actuation. More specifically, this study constitutes the first stage for the characterization of Ka-band shunt, capacitive-contact RF MEMS shunt switch presented in Chapter 4 with the aim to understand and predict various associated electromechanical phenomena. Obtained results in this work can be applied to other similar MEMS devices as well.

Within the framework of this work, characterization attempts start with the determination of deflection profile for a fixed-fixed beam subject to a uniformly distributed load. This sample problem aims to form the basics of mechanical analyses and to build necessary experience to tackle with the more advanced problem of electrostatic actuation. In particular, relevant deflection properties are solved for analytically in a rigorous manner while incorporating the effects of axial stress resulting from both residual stress and bending-induced non-linear stretching. Obtained expressions moreover enable one to investigate the effects of partial load-span (load is distributed partially and symmetrically). These features provide the capability to investigate effective spring constant expressions with respect to parameters commonly involved in electrostatically actuated systems and distinguish this part of the work from the previously reported ones: In [76, 78] for in-

stance partial load-span and non-linear stretching effects are not considered. In [79], a derivation is made for the deflection profile while taking into account stretching effects rigorously similar to this work, but full load-span is assumed. [80] takes into account both partial load-span and non-linear stretching, but utilizes a simplifying assumption in the axial relation in order to have a closed-form spring constant. Noting the importance of closed-form spring constant expressions, in this work, a further derivation is performed for small-argument and large-argument closed-form spring constant expressions. Validities of the these latter expressions together with [78] and [80] are furthermore assessed with respect to the implicit expression of this work.

After solving for the analytical problem, this work then attempts to characterize electro-statically actuated fixed-fixed beams via the Finite Difference (FD) method by extending the formulation given in [81] to fixed-fixed beams incorporating axial effects (due to both residual stress and non-linear stretching). Having failed to solve for the resulting system of FD equations initially, an own shooting solution method is developed which is an improved version of the one provided in [82]. Proposed solution is observed to work seamlessly, except for voltages near the pull-in voltage [83–85].

Due to problems related with the previous FD equation set, pull-in phenomenon could not be located properly and to compensate for this, a one-dimensional pull-in analysis is conducted. Spring constant expression developed in the first part of this work is utilized to obtain pull-in voltages which are later corrected with coefficients extracted empirically from a simplified electrostatic problem (wherein axial tension is ignored). Upon a comparison with the Finite Element Analysis (FEA) results appearing in [80] and [86], it is observed that results obtained from developed pull-in expressions are comparable to the ones calculated with [76, 80, 87–89] for several test cases.

Final part of this work focuses on the post-pull-in problem, i.e. contact analysis of the collapsed beam. This latter analysis ignores adhesion and surface roughness effects and aims to understand the electromechanical behavior in the contact state. Using a similar approach with the previous problem but with different boundary conditions, FD solu-

tions are obtained. Contact improvement (zipping) phenomena [90, 91] with voltage is observed and investigated with respect to several problem parameters. To complete the characterization, release phenomenon [91, 92] is analyzed and hold voltages are calculated.

With the described accomplishments, an ability is gained to investigate the two-dimensional problem of electrostatically actuated fixed-fixed beams. This ability is exploited in Chapter 4 for analyzing and predicting mechanical aspects of switch designs.

1.2.3 Realization of an RF MEMS Switch

As explained in §1.1, switches are key building blocks of RF MEMS technology offering potential for high-performance and reconfigurable microwave and millimeter-wave circuits. Relevant switches can be implemented in various circuit configurations, with different contact-types and actuation means [8]. For a brief review of those concepts reader is referred to §4.1.

Since their first introduction in 1990 [93], RF MEMS switches have continually received interest by researches from several universities, government labs and companies [10]. Today, highly reliable commercial state-of-the-art switches are being offered on the market; RadantMEMS [94], MIT-LL [95], Raytheon [96] switches are some of the prominent ones exhibiting low insertion loss ($< 0.1 - 0.5$ dB), good return loss (< -20 dB) and high isolation ($> 15 - 20$ dB) in 10-40 GHz band while demonstrating lifetimes of > 200 billion cycles, switching times of $5 - 20 \, \mu s$ and requiring actuation voltages of $30 - 90 \, V$.

The last work of this thesis focuses on implementation of a shunt, capacitive-contact RF MEMS switch for millimeter-wave applications. Relevant switch constitutes the first RF MEMS switch to be explored by METU in Ka-band frequencies: Previous studies conducted by METU RF MEMS Group include development of RF MEMS components and systems up to K-band, and this work aims to extend the latter band up to 40 GHz [97–100].

1.3 Research Objectives and Organization of the Thesis

The primary aim of this dissertation is to develop microwave and millimeter-wave components which are based on the in-house RF MEMS technology of Middle East Technical University. Relevant specific objectives can be summarized as follows:

- Analysis, design and implementation of microwave lumped elements for a specific surface micromachining based technology. An easy and low-cost fabrication process is aimed along with monolithic integration and mass-production capabilities by utilizing a single metallization layer.

- Performing the design, fabrication and measurements of a filter structure serving as a test vehicle for the developed microwave lumped elements.

- Conducting a mechanical characterization of fixed-fixed type beams: Starting from a fairly simple analytical problem to derive useful mechanical properties and extending the accumulated knowledge by devoting particular attention to electrostatic actuator systems.

- Extending the capabilities of METU RF MEMS technology by realizing a successful RF MEMS building block at millimeter-wave frequencies: Carrying out electromagnetic and mechanical design, fabrication and measurements of a shunt, capacitive-contact RF MEMS switch tailored for Ka-band.

This thesis consists of five chapters which include the accomplishments attained up to date.

Following this introductory chapter, Chapter 2 explains development of microwave lumped elements fulfilling the stated fabrication goals. Analysis and implementation of these elements are oriented towards an example filter application serving as an effective test vehicle. Proceeding in a proper flow; design, fabrication and measurements of the monolithic filter structure are provided.

Chapter 3 then continues with a mechanical characterization for fixed-fixed type beams. This self-contained theoretical study primarily seeks to establish the link between electrical and mechanical domains of one class of MEMS devices including, but not limited to, the RF MEMS switch described in Chapter 4. Beginning with the rather simple mechanical problem for a uniform distributed load, deflection characteristics and effective spring constant of fixed-fixed beams are derived analytically. That analysis is later followed by numerical investigations of electrostatically actuated fixed-fixed type beams. Semi-empirical pull-in voltage expressions are also derived by employing the results of previous analyses.

Next, Chapter 4 details realization of a shunt, capacitive-contact RF MEMS switch for Ka-band frequencies. Design stage of the switch is presented in both electromagnetic and mechanical domains, the latter using the knowledge developed in Chapter 3. Fabrication aspects and measurement results of the implemented switch are discussed.

Finally, Chapter 5 lists the accomplishments achieved within the frame of this thesis and suggests future work demanding further research.

CHAPTER 2

A MONOLITHIC S-BAND BANDPASS FILTER IMPLEMENTED WITH SURFACE MICROMACHINED MICROWAVE LUMPED ELEMENTS

This chapter deals with analysis, design and development of basic lumped microwave elements tailored for a custom surface micromachining based fabrication technology and describes implementation of a monolithic S-band bandpass filter structure which is used as a test vehicle during this study. §2.1 establishes the design goals for the studied filter application and focuses on the pre-design using ideal circuit elements. §2.2 provides an overview of the selected fabrication technology and identifies the microwave lumped elements utilized in this work. §2.3 explains the design procedure of the developed lumped components and their subsequent tuning for satisfying filter design requirements. Following the design stage, §2.4 provides fabrication details of the relevant filter structures. Finally, §2.5 presents results of the microwave measurements and explores various factors affecting obtained filter performance.

2.1 Filter Specifications and Pre-Design using Ideal Components

The filter considered in this work is selected to be of bandpass type having its passband located in the S-band (2-4 GHz) and centered at 3 GHz. In-band return loss is specified to be better than -20 dB. Moreover, stop-band is required to extend up to 20 GHz with an associated suppression better than 20 dB at 6 GHz.

Design of the filter possessing the specifications given above is initiated with a pre-design
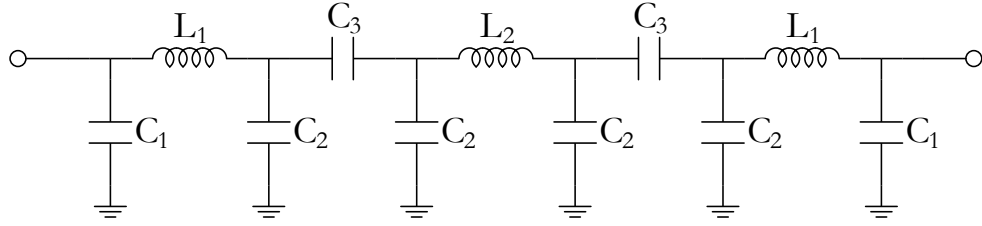
Figure 2.1: *Tubular bandpass filter topology adopted in this work (N=3).*

Table 2.1: *Optimized circuit element values for the ideal tubular bandpass filter with N=3.*

CIRCUIT ELEMENT	OPTIMIZED VALUE
C_1	0.60 pF
C_2	0.54 pF
C_3	2.37 pF
L_1	3.48 nH
L_2	4.65 nH

stage, which is carried out using ideal circuit components. For this purpose, a tubular bandpass filter topology is adopted which enables a convenient realization means for microstrip-based configurations [101, 102]. Figure 2.1 depicts utilized topology for the order of N=3. In particular, shown network is a symmetric one consisting of series inductors separated with capacitive π-networks and terminated with shunt capacitances. Element values C_i and L_i are determined using an optimization routine in Agilent ADS 2008 circuit simulator with the relevant filter specifications. Table 2.1 and Figure 2.2 provide obtained element values and associated magnitude S-parameter responses for the ideal tubular bandpass filter with N=3.

2.2 Overview of the Fabrication Technology and Introduction to Developed Microwave Lumped Elements

It is aimed to fabricate the filter structures using a cost-effective and simple fabrication process that would enable seamless monolithic integration and permit mass production with standard techniques. A surface micromachining process using a single metalization layer readily accomplishes these latter goals: Only a single photolithographic mask will be required for patterning relevant devices which will minimize fabrication costs as well
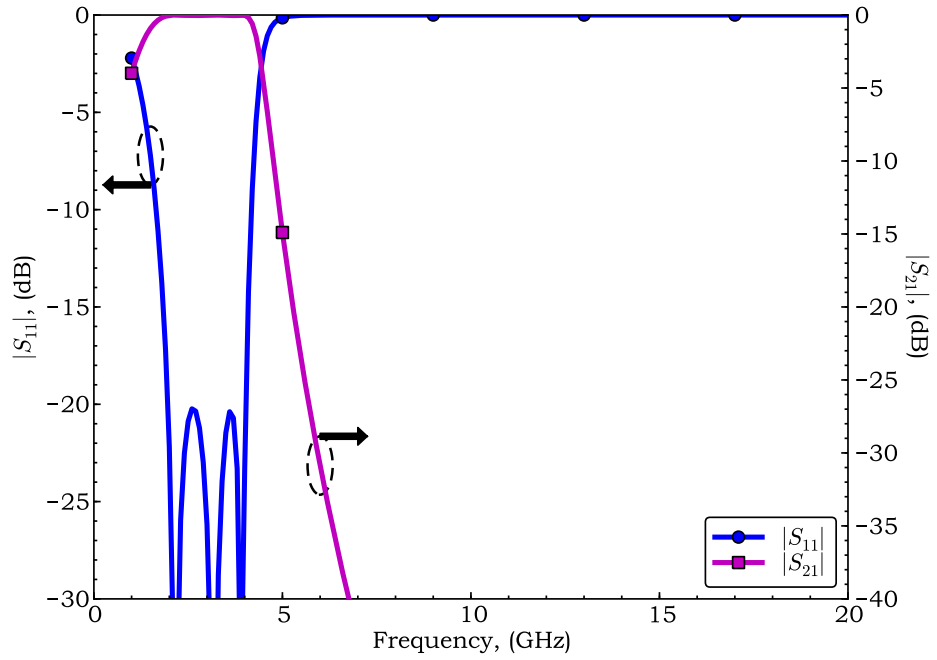
Figure 2.2: *Magnitude response of the optimized ideal tubular bandpass filter with N=3.*

as the manual effort for batch processing. Moreover, a microstrip-based topology is opted for the filters and the latter would call for an additional unprocessed ground layer metalization at the bottom of the substrates, a step posing no apparent fabrication difficulty.

Having established the design and fabrication goals of the filter structures, let us now turn the attention to specific implementation details. It was mentioned in the previous section that tubular nature of the chosen filter topology would allow a convenient means for a microstrip-based realization, which happens to be the intended configuration from a fabrication point of view. Accordingly, the elements L_i and C_i shown in Figure 2.1 will be implemented with microstrip lumped components. Figure 2.3 gives a more practical filter circuit configuration and suggests in addition physical implementation methods for those components.

It is observed from Figure 2.3 that filter structure at hand can be realized physically using three distinct microstrip-based lumped components, which are identified as follows:
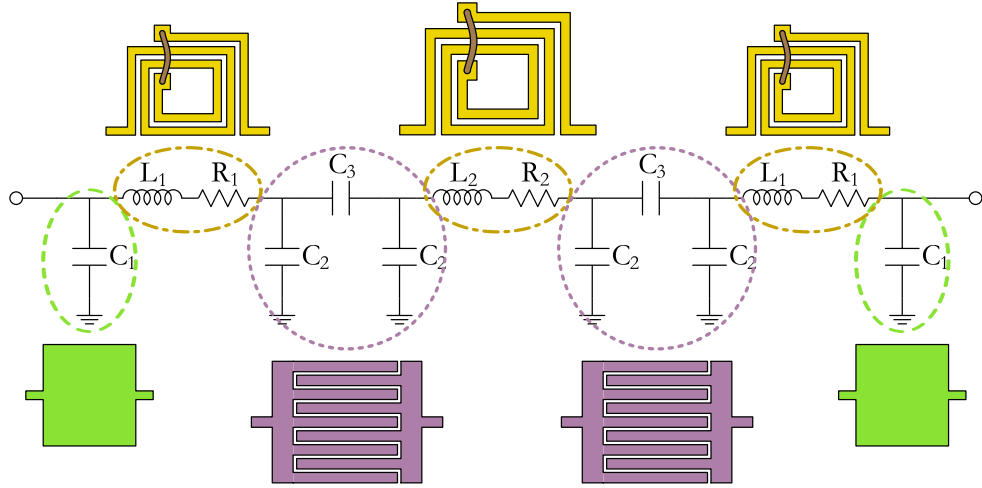
Figure 2.3: *A practical filter circuit showing how individual circuit elements can be realized physically.*

- Shunt capacitors at the input/output ports of the network (C_1) can be implemented via *microstrip patches*, which essentially form a parallel-plate capacitor with the microstrip ground plane.

- Series inductors L_1 and L_2 can be implemented with *planar spiral inductors* [103]. Notice that those practical inductors would also exhibit losses, which can be represented by series resistors R_1 and R_2.

- Capacitive π-networks can be realized with *interdigital capacitors* [104], which provide series and shunt capacitance elements in a compact layout at the same time.

Properties of the introduced microstrip lumped components together with their design methods are explored in the next section.

2.3 Design of the Microwave Lumped Components

Microwave lumped components introduced in the previous section are designed using full-wave electromagnetic analyses in conjunction with appropriate circuit models, in the light of the ideal circuit and associated element values given in Figure 2.1 and Table 2.1. For this purpose, Ansoft HFSS $^{\text{TM}}$ (v9.2) Finite Element Analysis (FEA) software and AWR Microwave Office $^{\text{TM}}$ (v2006) circuit simulator are utilized in collaboration. Design

of the lumped components are attempted in two main stages with a systematic approach: In the first stage, ideal element values are tried to be established for the corresponding components without paying attention to (yet observing the trends for) the associated parasitics. After establishing the required layouts satisfying those ideal element values, individually designed components are cascaded in the circuit simulator and are tuned with an iterative procedure in order to meet filter design requirements. In order to gain speed during the relevant design stages, layout estimation methods are developed for each lumped component through simple intuitive relations and educated guesses.

2.3.1 Design Stage I: Realization of Ideal Element Values

2.3.1.1 Interdigital Capacitor (IDC)

Figure 2.4 illustrates physical layout of the interdigital capacitor (IDC) together with its associated circuit model. It is noted from Figure 2.4(a) that the IDC component is formed by N interlaced fingers of length/width of L_f / W_f separated with a gap spacing of G_f. The fingers stem from two main stubs having a length of L_s, which are in turn connected to microstrip feed extensions of length/width L_e / W_e. Utilized circuit model shown in Figure 2.4(b) is a slightly modified version of the one reported in [105]. Relevant model is a physical one and its parameters can be interpreted as follows:

- C_s is the effective inter-finger series capacitance,

- L_s is the parasitic effective inductance associated with finger structures, main stubs and feed extensions,

- R_s represents the effective loss of the IDC,

- C_sh stands for the halved shunt capacitance of the IDC formed with the ground plane lying underneath,

- Z_0 and θ account for electrical length of the IDC and are responsible for its distributed nature, which becomes prominent at higher operating frequencies. Specifically, Z_0 is chosen as the reference impedance of the system and it is conveniently picked as 50 Ω.

(a) Layout
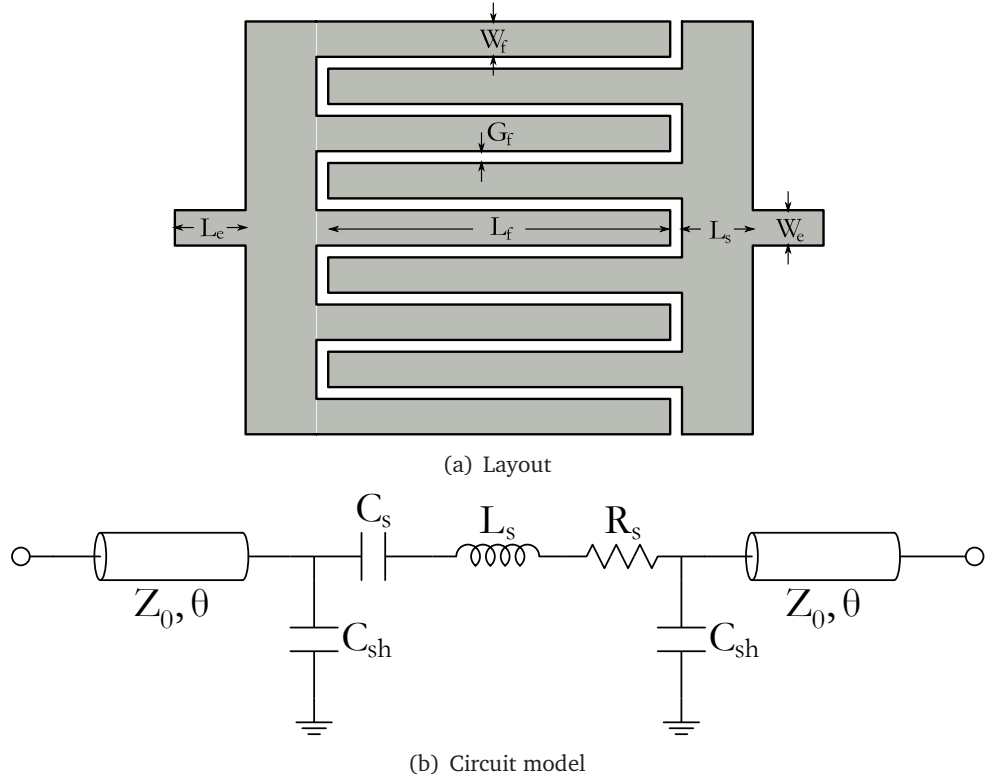
(b) Circuit model

Figure 2.4: *Illustration of the interdigital capacitor (IDC) layout and its associated circuit model.*

In particular, the lossless delay lines appearing at input/output ports of the IDC provide an improved description of the IDC frequency characteristics obtained from EM simulations and they distinguish the presented model from the ones reported in the literature.

Microwave performance and size considerations dictate certain geometrical and material constraints for the IDC component. First of these constraints is imposed on G_f: In order to maximize series capacitance per finger, G_f must be minimized. Such an approach also implies reduced device length as L_f may be taken smaller for a given C_s. Another constraint is on substrate parameters: For reasonable device dimensions, area of the IDC must be lowered as much as possible and selection of a substrate with a low thickness and high permittivity accomplishes such a goal for a given C_{sh} value. A last restriction is on finger dimensions: In order to prevent harmful effects of the transverse-resonance and effective loss of the IDC on microwave performance of the filter, effective inductance and resistance must be reduced. The latter can be achieved by employing shorter and wider fingers. Furthermore, increasing the finger number N is also an effective solution

for the latter purpose as doing so not only reduces those effective quantities by paralleling individual contributions but also permits realization of a higher C_s.

According to the discussion above, it is preferred to pick G_f as the fabrication tolerance of 5 μm. Moreover, fabrication-related preferences are also influenced and it is opted to utilize a thin (250 μm) alumina substrate which features a high relative permittivity and low dielectric loss ($\varepsilon_r = 9.6$, $\tan\delta = 0.001$). In addition, finger properties are adjusted with the goals of a high series-resonance frequency and low ohmic losses kept in mind.

During the design of the IDC component, number of conducted EM simulation iterations for attaining given values of C_s and C_{sh} are are reduced significantly through simple estimation means. Specifically, based on the extracted data of previous simulations, required layout parameters for next iterations are guessed using the following relations:

- C_s is taken proportional to L_f and N according to analytical approximations given in [67].

- C_{sh} is assumed to be a linear combination of a parallel-plate component proportional to the overall IDC area and a fringing component proportional to total device perimeter with associated coefficients c_{pp} and c_{fr}.

The estimation procedure can be explained as follows: First, required L_f or N value is determined for the desired C_s value through the proportionality relation. Then using the extracted model data from two similar simulations, the coefficients c_{pp} and c_{fr} are solved from the resulting linear equation set in C_{sh}. Next, this equation is solved for remaining layout parameters (typically for the main stub length L_s) in order to satisfy a desired C_{sh}. This method, although a crude one, indeed proved helpful during the EM simulation iterations.

Following a number of simulation iterations, it is arrived at the IDC configuration summarized in Table 2.2. Associated S-parameters obtained from EM simulations and the circuit model are provided in Figure 2.5.

Table 2.2: *Obtained layout and circuit model parameters for the IDC configuration in design stage I ($H_{sub} = 250\ \mu m$, $\varepsilon_r = 9.6$, $\tan\delta = 0.001$, $t_{metal} = 1\ \mu m$, $\sigma_{metal} = 3 \times 10^7\ S/m$).*

LAYOUT DIMENSIONS	CIRCUIT MODEL PARAMETERS
$N = 21$, $L_f = 740\ \mu m$	$C_s = 2.38$ pF
$W_f = 55\ \mu m$, $G_f = 5\ \mu m$	$C_{sh} = 0.48$ pF
$L_s = 500\ \mu m$, $W_e = 50\ \mu m$	$L_s = 0.21$ nH, $R_s = 0.36\ \Omega$
$L_e = 100\ \mu m$	$\theta = 1.95^o$ (@ 3 GHz)

(a) Magnitude S-parameters

(b) Phase S-parameters

Figure 2.5: *Simulated and modeled S-parameters of the IDC configuration arrived at the end of design stage I.*

It is recognized from Figure 2.5 that transverse-resonance occurs at approximately 12.5 GHz. This resonance could not be avoided due to the fairly large value of C_s and constraints on device height. Parameter extraction is consequently performed between 1-10 GHz, where S-parameters are not affected appreciably.

2.3.1.2 Planar Spiral Inductor (PSI)

The layout and circuit model for the planar spiral inductor (PSI) is provided in Figure 2.6. It is noted from Figure 2.6(a) that PSI is constructed with 2.75 turns and a wirebond is required in order to transfer the signal outside the loop center due to single-layer nature of the fabrication process. The PSI is wound with a strip of width W and track separation of G leading to a total device length of L_x and height of L_y. Connections to other components are established via microstrip feeds of length/width L_e/W_e. The wirebond is modeled as a torus with a cross-section diameter of 25 μm, which is specified by the fabrication requirements. Circuit model of the PSI is illustrated in Figure 2.6 and is

(a) Layout
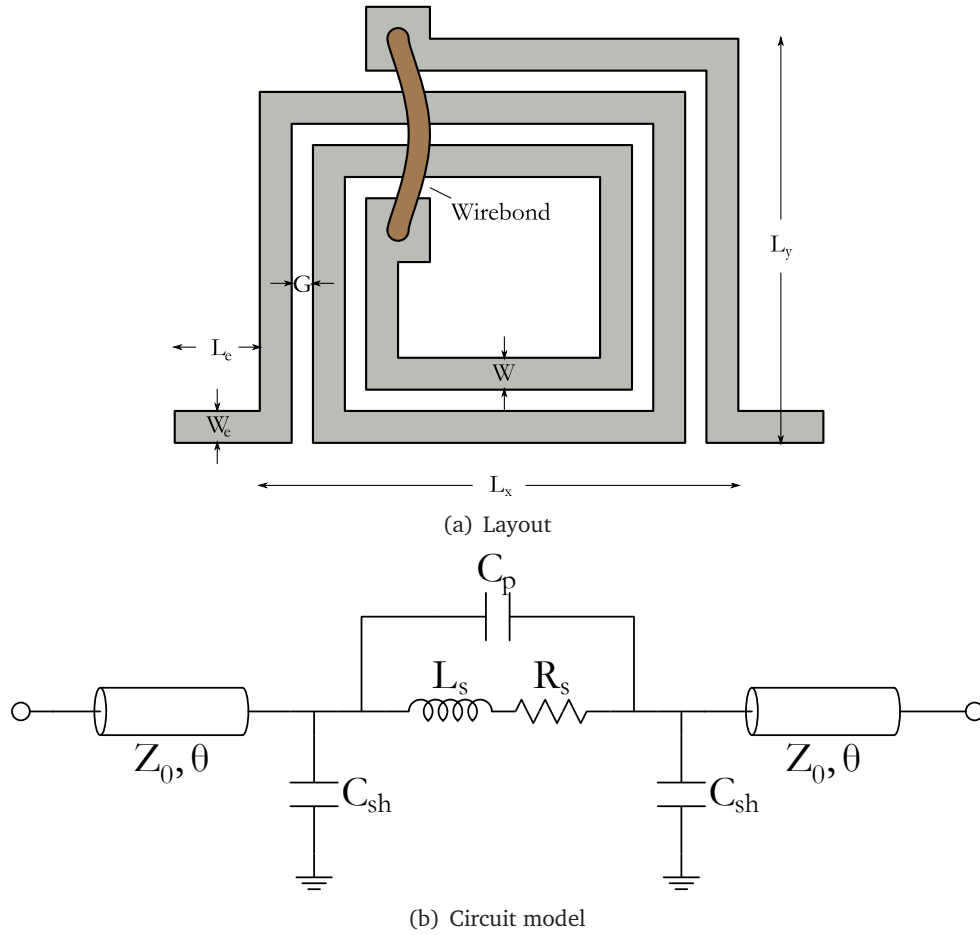
(b) Circuit model

Figure 2.6: *Illustration of the planar spiral inductor (PSI) layout and its associated circuit model.*

observed to contain following model elements:

- Effective inductance L_s,

- Effective loss component R_s,

- Inter-turn parasitic capacitance C_p,

- Shunt capacitance component (halved) C_{sh},

- Delay line parameters Z_0 and θ.

Similarly with the IDC case, delay lines are introduced in the conventional inductor model [105] and the parameter Z_0 is fixed to 50 Ω system reference impedance.

(a) Correlation for L_s

(b) Correlation for R_s
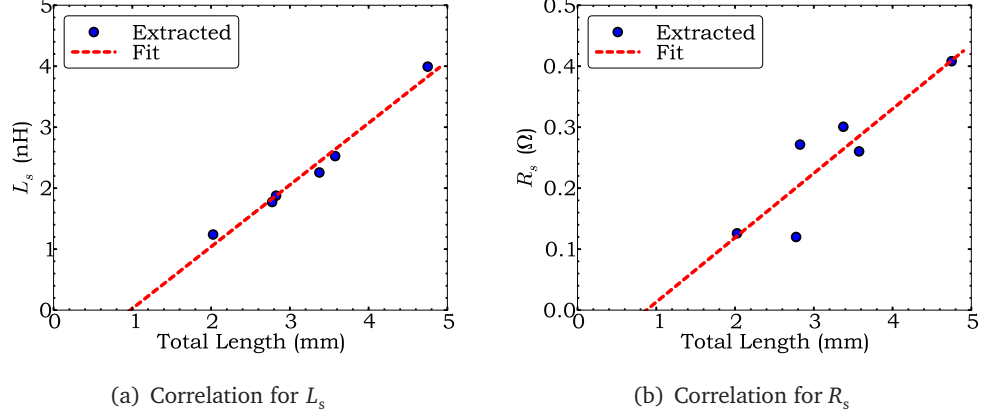
Figure 2.7: *Effective inductance and resistance versus mean PSI length emphasizing corresponding linear correlations.*

During the design of the PSI devices, a few parameters are fixed in order to reduce the number of variables to play with. In particular, W and G are determined as 50 μm and 25 μm respectively, which yield reasonable device dimensions. Moreover, microstrip feed width W_f is chosen to be equal to W in order to avoid any step discontinuities. Substrate parameters, which are set for the IDC configuration, are also retained for PSI devices.

In order to reduce the number of EM simulation iterations during design of PSI devices, an empirically determined relation is utilized for estimating inductance of a given layout. Mentioned relation is based on observed linear dependence of the extracted inductance value on mean path length of the PSI as depicted in Figure 2.7(a). Educated guesses then employed by determining the slope and offset of the fitted line and solving for the device dimension of interest that will yield a desired inductance value. Figure 2.7(b) shows a similar correlation for the effective resistance component, which however is not estimated between simulation runs.

PSI configurations arrived at the end of design stage I are listed in Table 2.3. Comparisons between simulated and modeled S-parameters are provided in Figure 2.8 and Figure 2.9 respectively for first and second PSI devices.

(a) Magnitude S-parameters

(b) Phase S-parameters
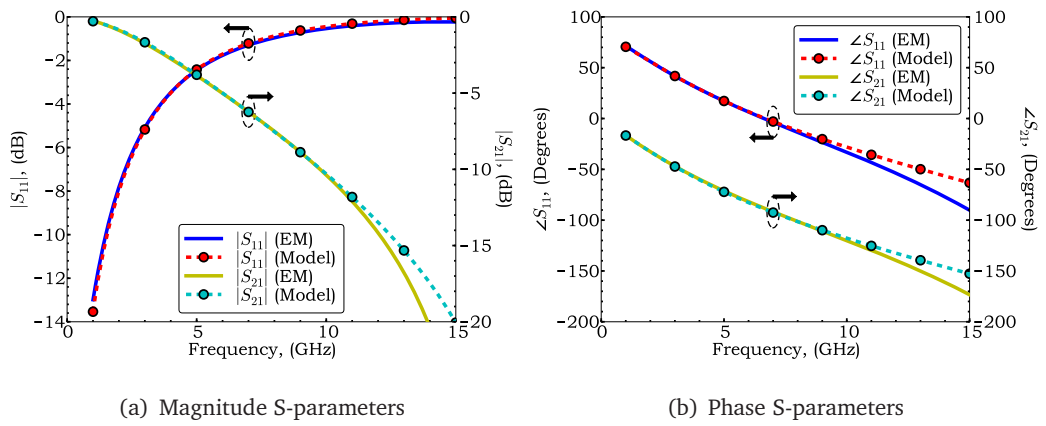
Figure 2.8: *Simulated and modeled S-parameters of the first PSI configuration arrived at the end of design stage I.*

(a) Magnitude S-parameters

(b) Phase S-parameters
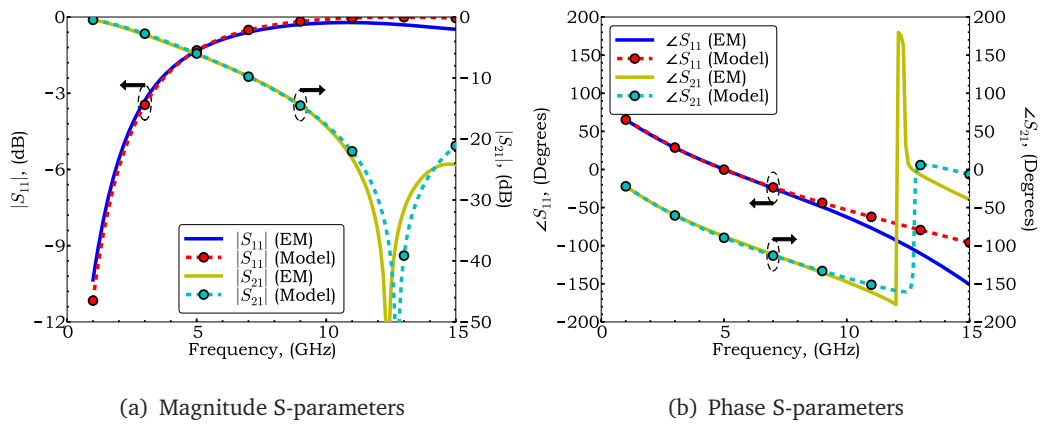
Figure 2.9: *Simulated and modeled S-parameters of the second PSI configuration arrived at the end of design stage I.*

23

Table 2.3: *Obtained layout and circuit model parameters for two PSI configurations in design stage I ($H_{sub} = 250 \ \mu m$, $\varepsilon_r = 9.6$, $\tan \delta = 0.001$, $t_{metal} = 1 \ \mu m$, $\sigma_{metal} = 3 \times 10^7 \ S/m$).*

PSI DEVICE	LAYOUT DIMENSIONS	CIRCUIT MODEL PARAMETERS
PSI #1	$N = 2.75$, $L_x = 880 \ \mu m$ $L_y = 440 \ \mu m$, $W = 50 \ \mu m$ $G = 25 \ \mu m$, $W_e = 50 \ \mu m$ $L_e = 100 \ \mu m$	$L_s = 3.52$ nH $R_s = 1.03; \ \Omega$ $C_p = 21.37$ fF, $C_{sh} = 15.35$ fF $\theta = 6.07^o$ (@ 3 GHz)
PSI #2	$N = 2.75$, $L_x = 1030 \ \mu m$ $L_y = 515 \ \mu m$, $W = 50 \ \mu m$ $G = 25 \ \mu m$, $W_e = 50 \ \mu m$ $L_e = 100 \ \mu m$	$L_s = 4.63$ nH $R_s = 1.31; \ \Omega$ $C_p = 33.73$ fF, $C_{sh} = 4.17$ fF $\theta = 8.87^o$ (@ 3 GHz)

It is noted from Figures 2.8-2.9 that designed PSI devices have visible parallel self-resonances at about 15.0 GHz and 12.5 GHz respectively. Model optimizations are confined to 1-10 GHz in order to properly capture the device behavior near passband of the filter. It is moreover observed that resonance frequency decreases with increased inductance, which is actually an expected trend.

2.3.1.3 Microstrip Patches (MPs)

The final lumped component pending for design is the microstrip patch (MP) as illustrated in Figure 2.10(a). Here, the designer has the liberty to adjust the length L_p and width W_p of the patch in order to obtain desired shunt capacitance value. As with the other lumped components, microstrip feed lines of length L_e and width W_e connect the patch to the other device terminals. Proposed circuit model for the patch is provided in Figure 2.10(b), which is essentially the familiar lumped transmission line model extended with delay lines. Here, C_{sh} represents the effective shunt capacitance, L_s and R_s stand for halved parasitic inductance and resistance, and θ denotes halved electrical length of the MP. Following the convention with the other lumped elements, Z_0 is set to 50 Ω system reference impedance.

For the MP component, the only design constraint is to obtain a reasonable device area, which is actually already facilitated by the previously established substrate specifications.

(a) Layout
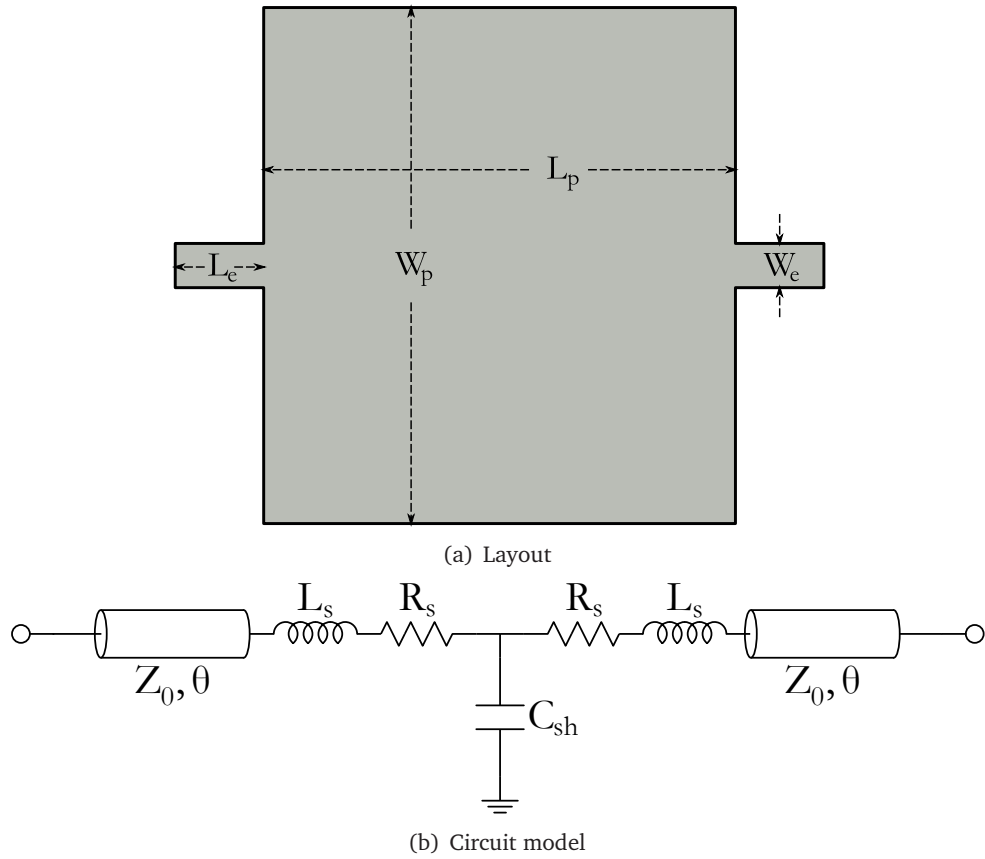
(b) Circuit model

Figure 2.10: *Illustration of the microstrip patch (MP) layout and its associated circuit model.*

The MP lumped component is designed rather quickly compared to the other ones due to its predictable characteristics. In order to estimate a given shunt capacitance in a single trial, C_{sh} is treated to be a linear combination of parallel-plate and fringing components, which are in turn assumed proportional to total patch area and perimeter respectively. Proceeding along the estimation method developed for the IDC component, desired C_{sh} value is then estimated accurately using previous extracted capacitance data.

Table 2.4 summarizes the arrived configuration for the MP component as well as the extracted circuit model parameters. Electromagnetically simulated and modeled S-parameters are provided in Figure 2.11.

An inspection of Table 2.4 would reveal that C_{sh} is not close to its intended value of 0.61 pF unlike the other lumped components. Moreover, one would realize from Figure

Table 2.4: *Obtained layout and circuit model parameters for the MP configuration in design stage I ($H_{sub} = 250~\mu m$, $\varepsilon_r = 9.6$, $\tan\delta = 0.001$, $t_{metal} = 1~\mu m$, $\sigma_{metal} = 3 \times 10^7 S/m$).*

LAYOUT DIMENSIONS	CIRCUIT MODEL PARAMETERS
$W_p = 1200~\mu m$	$C_{sh} = 0.56$ pF
$L_p = 1370~\mu m$	$L_s = 0.32$ pH
$W_e = 50~\mu m$	$R_s = 17.36~m\Omega$
$L_e = 100~\mu m$	$\theta = 5.03^o$ (@ 3 GHz)

(a) Magnitude S-parameters

(b) Phase S-parameters
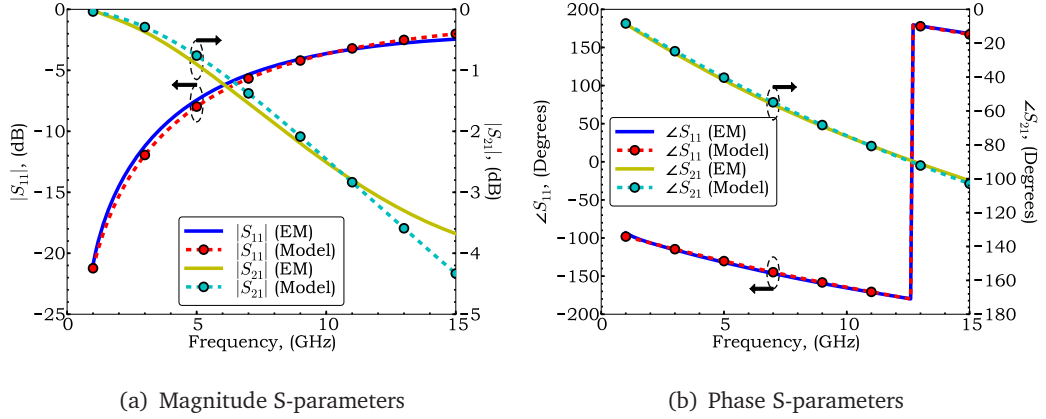
Figure 2.11: *Simulated and modeled S-parameters of the MP configuration arrived at the end of design stage I.*

2.11 that simulated and modeled S-parameters do not agree well in general. Actually, in the previous studies, relevant MP configuration was modeled with an additional parasitic series inductor attached to C_{sh} and it was found that a *negative* value for that inductor had improved modeling results dramatically while elevating the C_{sh} value to precisely 0.61 pF. However, it is not opted to utilize that model due to the non-physical quantities involved and accordingly it is adhered to the current one.

2.3.2 Design Stage II: Cascading of the Developed Elements and Tuning

Having realized and characterized each of the microstrip-based lumped components at the end of the design stage I, next, these components are cascaded in circuit simulation environment as shown in Figure 2.3. Figure 2.12 presents a comparison of S-parameters between cascaded lumped components and the ideal filter topology established in §2.1. It is noticed from the provided plots that cascaded model responses agree well with that of the cascaded EM simulation blocks, an observation validating the modeling approach

26

established in the previous section. When cascaded results are compared to the ideal filter response, however, it is noticed that filter design specifications are not met with the current components at hand: In particular; passband seems to narrow down and shift somewhat to lower frequencies, and in-band return loss is observed to exceed -20 dB.

Previous observations are actually not surprising: The effect of component parasitics on the filter response was not considered in design stage I, but it was only proved that it is possible to realize the component values with the proposed configurations. Naturally, next design stage encompasses the tuning of those components in order to meet filter design specifications. Following an iterative tuning stage that involves repeated component value estimation and physical realization steps for each lumped component, it is arrived at a final filter configuration that successfully meets the design specifications. Table 2.5 lists the determined layouts and extracted model parameters for each lumped component. Figures 2.13 to 2.16 present electromagnetically simulated and modeled S-parameters for those redesigned lumped components. S-parameters of the resulting cascaded filter structure is plotted in Figure 2.17.

An examination of Figure 2.17 shows that tuned filter successfully satisfies the design requirements: In-band return loss is better than -20 dB and passband is found in 1.94-4.00 GHz frequency band according to -20 dB reflection criterion. Moreover, suppression at 6 GHz is 25 dB, which is larger than the specified 20 dB value. Furthermore, insertion loss within the passband is determined as 0.5 dB, however this is regarded as an underestimation due to skin-effect related surface approximations in EM simulations.

(a) $|S_{11}|$

(b) $|S_{21}|$

(c) $\angle S_{11}$

(d) $\angle S_{21}$
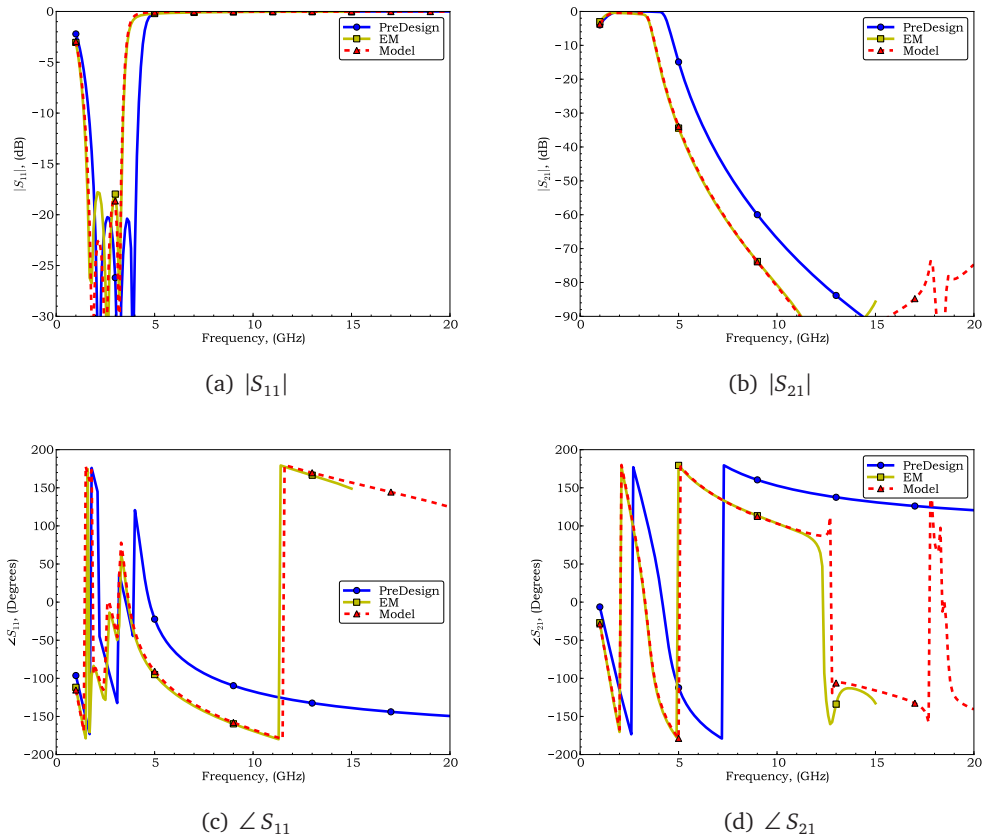
Figure 2.12: *Filter S-parameters obtained from cascade connection of EM simulation results and circuit models together with the ideal pre-design characteristics.*

(a) Magnitude S-parameters

(b) Phase S-parameters
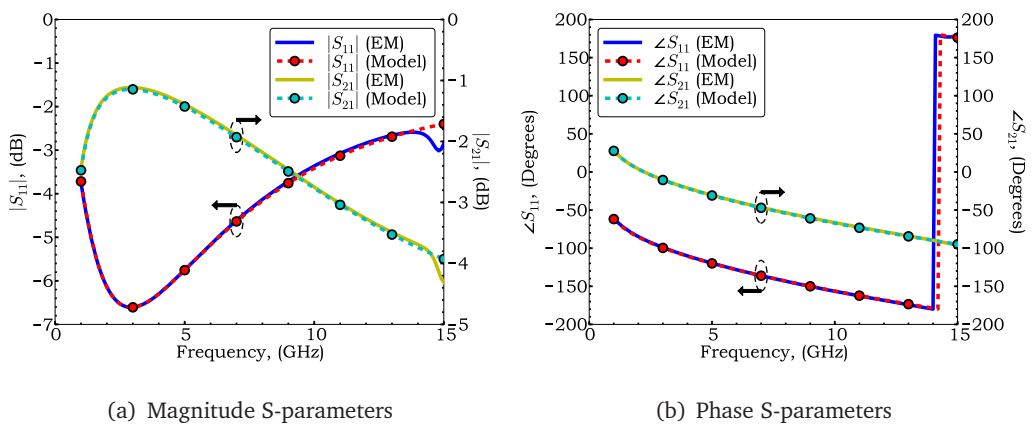
Figure 2.13: *Simulated and modeled S-parameters of the IDC configuration arrived at the end of design stage II.*

(a) Magnitude S-parameters

(b) Phase S-parameters
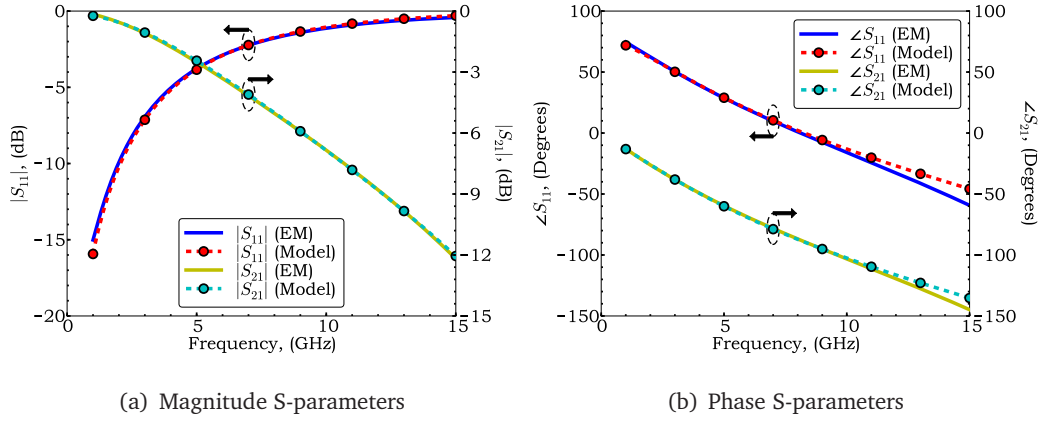
Figure 2.14: *Simulated and modeled S-parameters of the first PSI configuration arrived at the end of design stage II.*

(a) Magnitude S-parameters

(b) Phase S-parameters
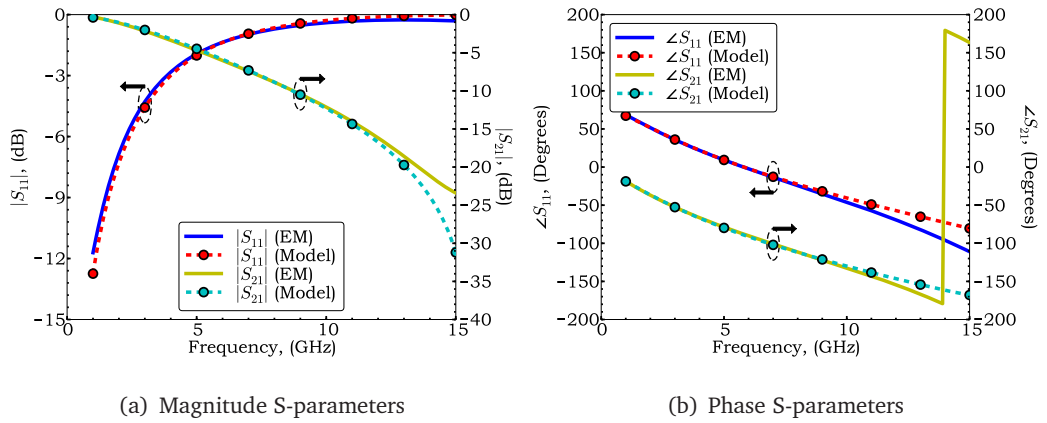
Figure 2.15: *Simulated and modeled S-parameters of the second PSI configuration arrived at the end of design stage II.*

(a) Magnitude S-parameters

(b) Phase S-parameters
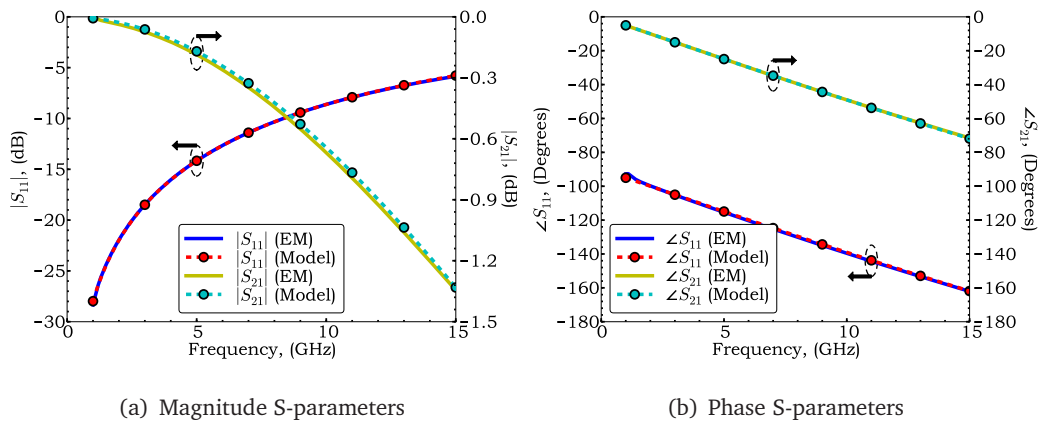
Figure 2.16: *Simulated and modeled S-parameters of the MP configuration arrived at the end of design stage II.*

(a) Magnitude S-parameters

(b) Phase S-parameters

(c) Passband magnitude S-parameters

(d) Passband phase S-parameters
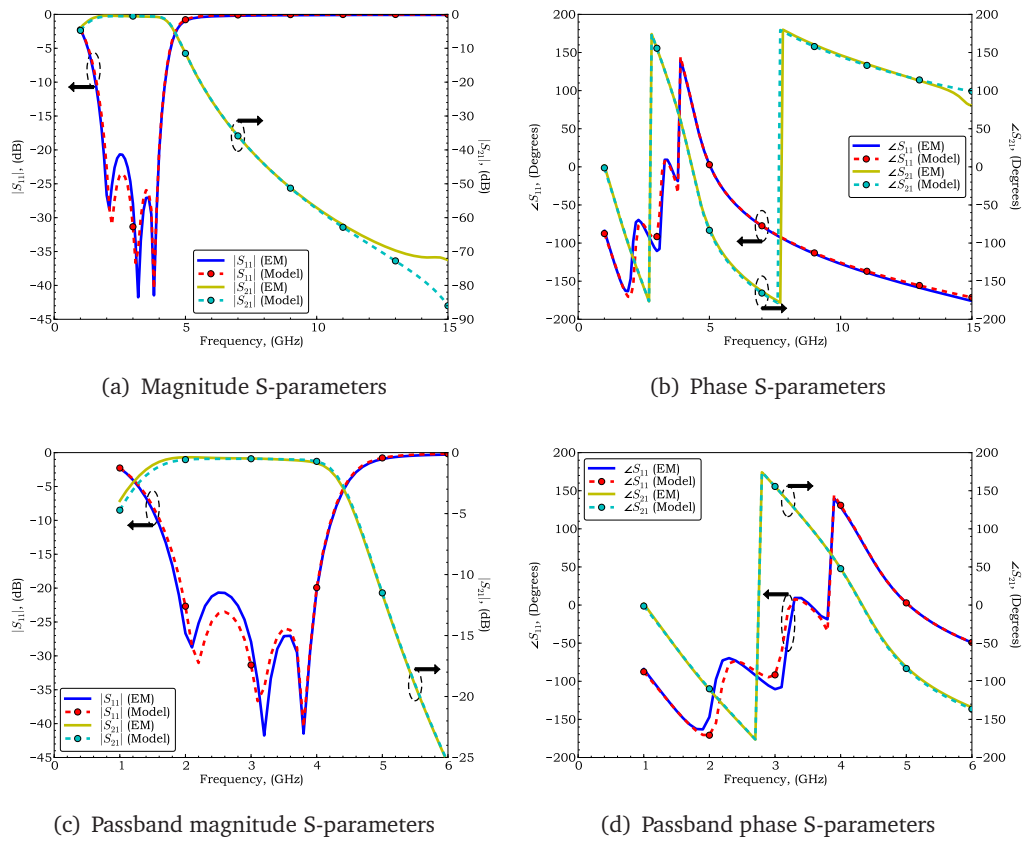
Figure 2.17: *Filter S-parameters obtained from cascade connection of EM simulation results and circuit models at the end of design stage II.*

Table 2.5: *Obtained layout and circuit model parameters for each of the lumped components at the end of design stage II ($H_{\mathrm{sub}} = 250\ \mu m$, $\varepsilon_r = 9.6$, $\tan\delta = 0.001$, $t_{\mathrm{metal}} = 1\ \mu m$, $\sigma_{\mathrm{metal}} = 3 \times 10^7\,S/m$).*

DEVICE	LAYOUT DIMENSIONS	CIRCUIT MODEL PARAMETERS
IDC	$N = 21$, $L_{\mathrm{f}} = 630\ \mu m$ $W_{\mathrm{f}} = 50\ \mu m$, $G_{\mathrm{f}} = 5\ \mu m$ $L_{\mathrm{s}} = 315\ \mu m$, $W_{\mathrm{e}} = 50\ \mu m$ $L_{\mathrm{e}} = 100\ \mu m$	$C_{\mathrm{s}} = 2.06$ pF $C_{\mathrm{sh}} = 0.30$ pF $L_{\mathrm{s}} = 0.13$ nH, $R_{\mathrm{s}} = 0.81\ \Omega$ $\theta = 3.51^o$ (@ 3 GHz)
PSI #1	$N = 2.75$, $L_{\mathrm{x}} = 560\ \mu m$ $L_{\mathrm{y}} = 560\ \mu m$, $W = 50\ \mu m$ $G = 25\ \mu m$, $W_{\mathrm{e}} = 50\ \mu m$ $L_{\mathrm{e}} = 100\ \mu m$	$L_{\mathrm{s}} = 2.60$ nH $R_{\mathrm{s}} = 1.40;\ \Omega$ $C_{\mathrm{p}} = 15.92$ fF, $C_{\mathrm{sh}} = 7.4x10^{-4}$ fF $\theta = 6.03^o$ (@ 3 GHz)
PSI #2	$N = 2.75$, $L_{\mathrm{x}} = 675\ \mu m$ $L_{\mathrm{y}} = 675\ \mu m$, $W = 50\ \mu m$ $G = 25\ \mu m$, $W_{\mathrm{e}} = 50\ \mu m$ $L_{\mathrm{e}} = 100\ \mu m$	$L_{\mathrm{s}} = 3.81$ nH $R_{\mathrm{s}} = 1.61;\ \Omega$ $C_{\mathrm{p}} = 26.64$ fF, $C_{\mathrm{sh}} = 3.18x10^{-3}$ fF $\theta = 8.20^o$ (@ 3 GHz)
MP	$W_{\mathrm{p}} = 900\ \mu m$ $L_{\mathrm{p}} = 820\ \mu m$ $W_{\mathrm{e}} = 50\ \mu m$ $L_{\mathrm{e}} = 100\ \mu m$	$C_{\mathrm{sh}} = 0.26$ pF $L_{\mathrm{s}} = 0.41$ pH $R_{\mathrm{s}} = 1.45x10^{-2}\ m\Omega$ $\theta = 4.09^o$ (@ 3 GHz)

2.4 Fabrication of the Filter Structures

Having successfully completed the design of the filters using developed lumped elements, next, these structures were fabricated at METU MEMS Center Facilities using the high-conductivity base-metal recipe developed by the RF MEMS Group. Relevant process steps were applied on a 250 μm thick alumina substrate ($\varepsilon_r = 9.6$, $\tan\delta = 0.001$) in the following order[1]:

- 1.2 μm thick gold layer was sputtered on the top wafer surface ($\sigma_0 = 3x10^7$ S/m).

- Devices were patterned on the gold layer through a photolithography step.

- Bottom of the wafer was covered with a 1.2 μm thick sputtered gold layer to form the microstrip ground plane ($\sigma_0 = 3x10^7$ S/m).

- Following the process steps, individual samples were diced.

Figure 2.4 shows a photograph of a successfully fabricated filter structure and indicates the final filter dimensions. It is realized from the same figure that filter terminals are

---

[1] Explained steps were performed by Dr. Kağan Topallı, Dr. Mehmet Ünlü and Orhan Akar.

connected to Coplanar Waveguide (CPW) ports. Relevant CPW launches are required for measurement purposes and are adjusted to the reference impedance of 50 Ω with G/W/G=50/120/50 μm transverse dimensions.
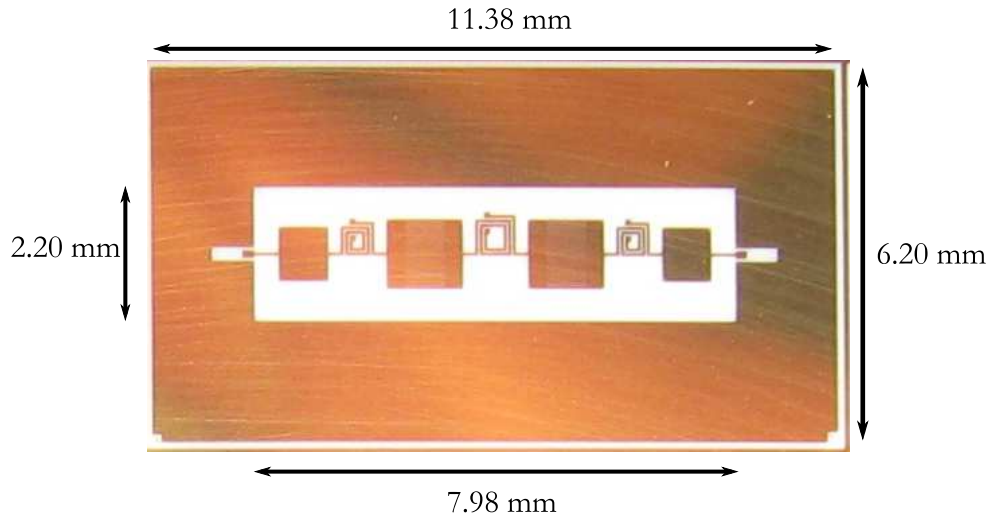
Figure 2.18: *Photograph of a successfully fabricated filter structure. Device dimensions are indicated.*

2.5   Microwave Measurements of Fabricated Filter Structures

Measurements of the fabricated filter structures were conducted utilizing Cascade Summit 9000 CPW Probe Station in conjunction with Agilent E8361A Vector Network Analyzer. Prior to the measurements; wire-bonds of the PSI devices were completed using 25 μm-diameter aluminum wires [2], filters were mounted on a clean copper surface and electrical contact between CPW side grounds and microstrip ground plane was established through conductive silver epoxy. After setting the reference planes at the Cascade ACP40-GSG-150 CPW Probe tips via an SOLT calibration performed in 1-20 GHz band using Cascade ISS 101-190 Calibration Kit, S-parameters of the filters were measured. Figure 2.19 provides measured S-parameters of a sample filter die.

It is observed from Figure 2.19 that fabricated filter sample exhibits an acceptable performance in the low frequency region: In particular, return loss in the passband is noted to be

---

[2] Relevant wire-bonds were performed by Dr. Mehmet Ünlü
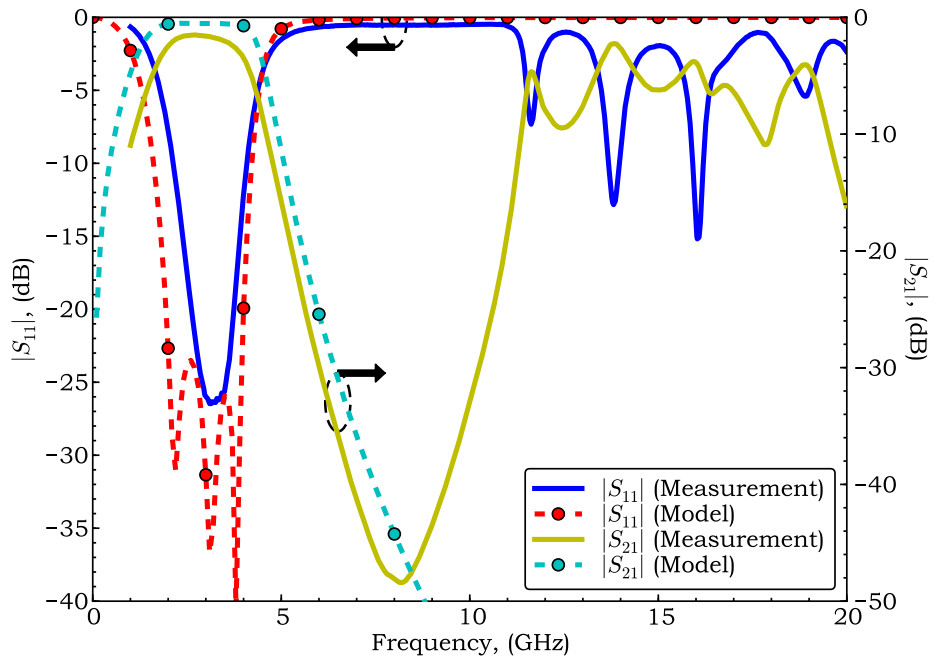
(a) Magnitude S-parameters
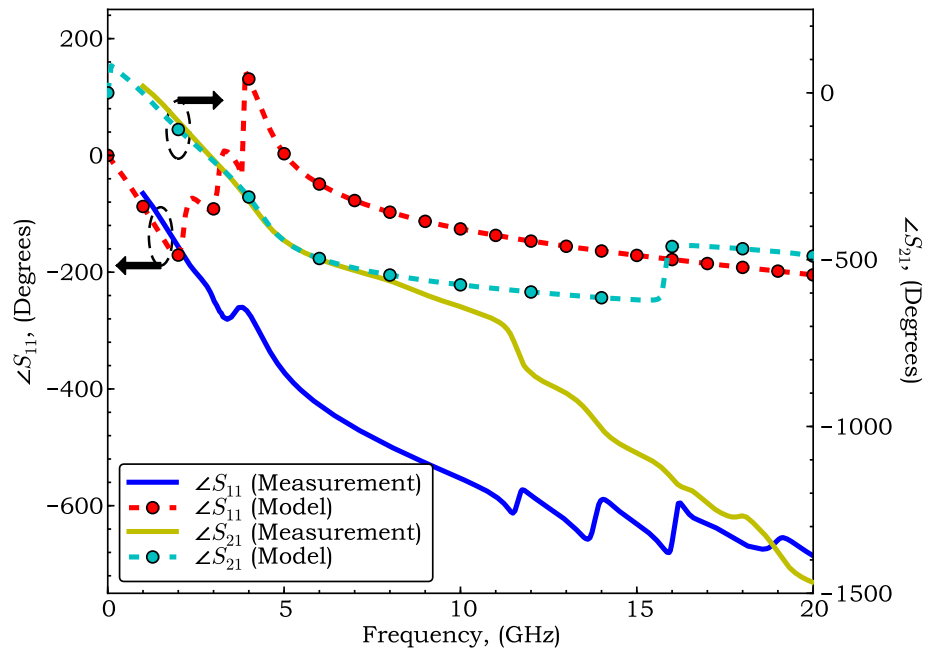
(b) Phase S-parameters

Figure 2.19: *Measured S-parameters of a sample filter structure utilizing epoxy as ground interconnection means. Circuit model S-parameters are also provided for comparison purposes.*

better than -20 dB and passband is defined as 2.62-3.75 GHz (@ RL=-20 dB), 2.39-3.90 GHz (@ RL= -15 dB) and 2.14-4.09 GHz (@ RL=-10 dB), which are somewhat narrower than the intended 2-4 GHz band. Insertion loss in the passband is noted to be 1.5 dB at 2.67 GHz, which confirms the loss-underestimation issue claimed for the EM simulations. Moreover, suppression at 6 GHz is observed to be better than 25 dB, satisfying the last design criterion. These acceptable results, however, degrade significantly when frequency is increased above 11 GHz: For the relevant frequency range $|S_{21}|$ increases dramatically, allowing formation of a virtual passband. Furthermore, spurious responses are noticed, the reasons for which are not currently evident but appears to indicate a systematic error with the DUT. Due to these latter observations, microwave performance of the filter is rendered unacceptable in its stop-band. Nevertheless, proposed design methodology seems to be verified in that utilized circuit model is in fair agreement with measurement results, at least below 8 GHz.

The resonance problem mentioned above triggered a separate study subsequently. In order to investigate the source of this interesting phenomenon, measurements were performed on a test structure fabricated along with the filter samples. Relevant structure is identical to the filter samples with the filter section replaced by a pure microstrip line (thru) of width equal to $W_e = 50 \ \mu m$. After mounting the latter structure on a copper base and establishing its CPW-to-microstrip ground connections via the same conductive epoxy[3], S-parameters shown in Figure 2.20 were obtained. In order to facilitate interpretation of the results, previous magnitude filter response is overlaid on the relevant curves. It is observed from Figure 2.20 that same resonance phenomenon also persists for the microstrip thru structure at the exact frequencies with the filter structure. This observation therefore suggests grounding problems that can be traced to utilized conductive epoxy.

In order further to justify whether the resonance problem actually stems from insufficient grounding due to improper epoxy microwave characteristics, simulation of the microstrip thru structure is attempted in Ansoft HFSS ^{TM} (v10.0). Replacing thick metal lines with two dimensional PECs, utilizing lumped excitation ports and employing a lumped boundary at the CPW-to-microstrip ground interconnections; S-parameters of the relevant struc-

---

[3] These manual steps were performed by İlker Comart.

(a) $|S_{11}|$　　　　(b) $|S_{21}|$
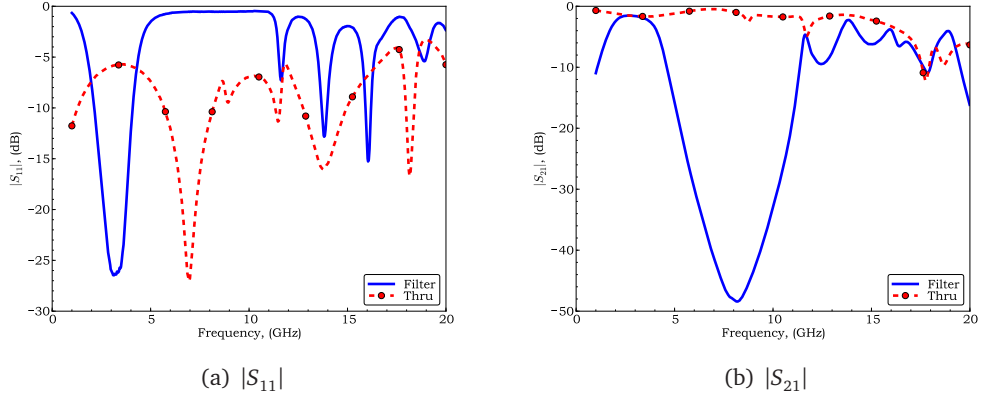
Figure 2.20: *Measured S-parameters of the microstrip thru structure employing the same epoxy based ground interconnection scheme. Measured filter response is also provided for comparison purposes.*

(a) $|S_{11}|$　　　　(b) $|S_{21}|$
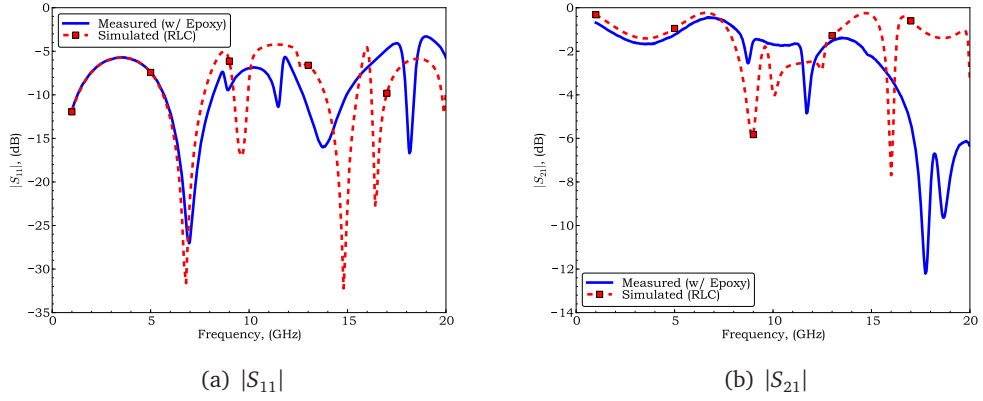
Figure 2.21: *Measured and simulated S-parameters of the microstrip thru structure. Simulated response is obtained by assigning a RLC boundary to ground interconnections ($L = 50$ pH, $R = 0.25\ \Omega$)*

ture is simulated. Figure 2.21 compares measured and simulated S-parameters of this test structure. It is noted that for an imperfect boundary featuring a series connection of $L = 50$ pH and $R = 0.25\ \Omega$ results in nearly identical resonance behavior. In order to shed more light into the matter, surface current density plots on the microstrip ground plane are plotted in Figure 2.22 for three distinct resonant frequencies.

An investigation of Figure 2.22 shows that at the resonance frequencies, field gets trapped under the CPW ground planes. This behavior is in fact well studied in the literature and it is known to arise from Parallel-Plate Mode (PPMs) guided by the Finite Width Conductor

35

(a) 9.4 GHz

(b) 12.0 GHz

(c) 15.6 GHz
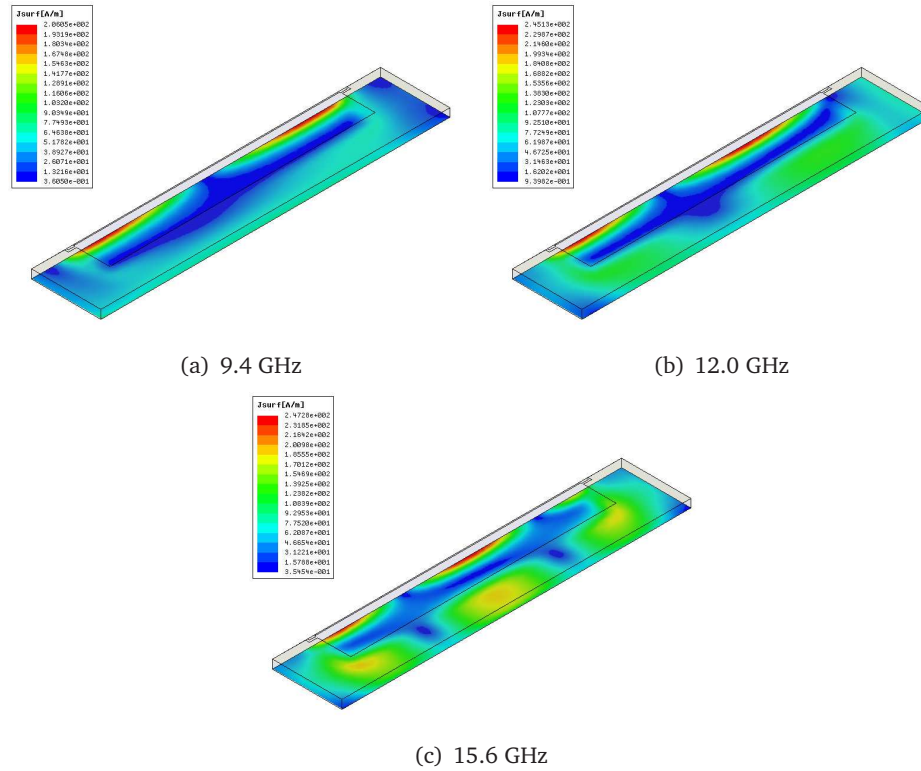
Figure 2.22: *Surface current density plots of the simulated microstrip thru structure at its bottom ground plate and at three resonance frequencies.*

Backed Coplanar Waveguides (FW-CBCPWs) [106, 107]. Due to strong coupling of the energy to those modes at the resonance frequencies, energy cannot reach the terminating CPW port which is accompanied with a significant decrease in $|S_{21}|$. Moreover, for reflective terminations, sent energy cannot return back due to this reason and a similar decrease in $|S_{11}|$ is experienced, as in the measured filter in its stop-band.

Having identified the reason for the malfunction of the fabricated filters after 11 GHz, it was decided to conduct another measurement using bonding strips instead of the conductive epoxy. Figure 2.23 shows the obtained improved filter response, validating the conclusion drawn earlier. It is observed that the latter filter sample exhibits an in-band return loss better than -20 dB. Passband is found as 2.03-4.22 GHz (@ RL=-10 dB), 2.27-4.07 GHz (@ RL=-15 dB) and 2.50-3.97 GHz (@ RL=-20 dB), which are once again a bit narrower than the intended band. Insertion loss is determined to be 1.2 dB and suppression at 6 GHz is noted as 25 dB. In the light of these results, performance of this particular filter sample is regarded as satisfactory.
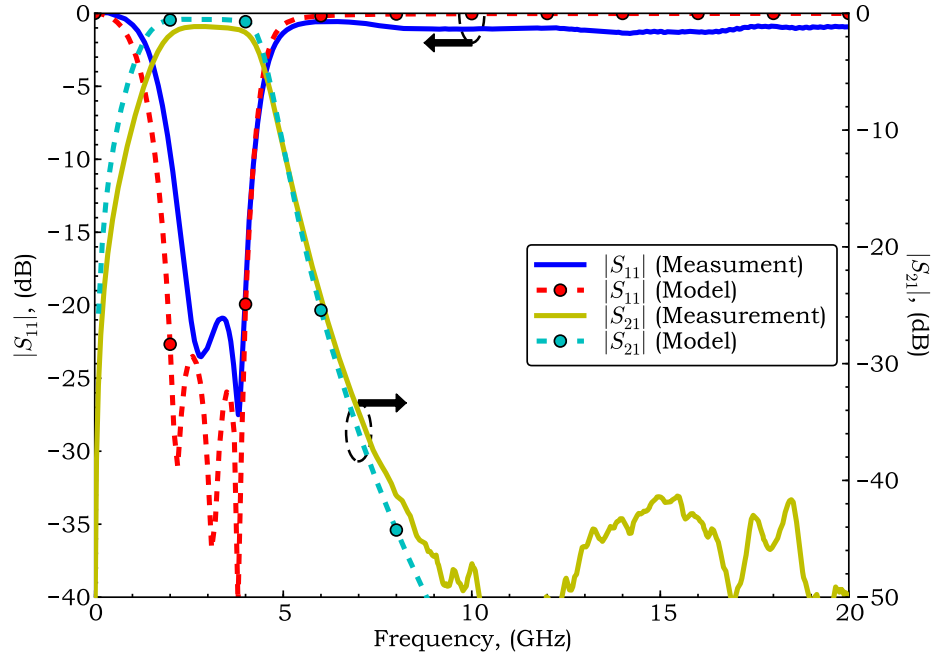
(a) $|S_{11}|$
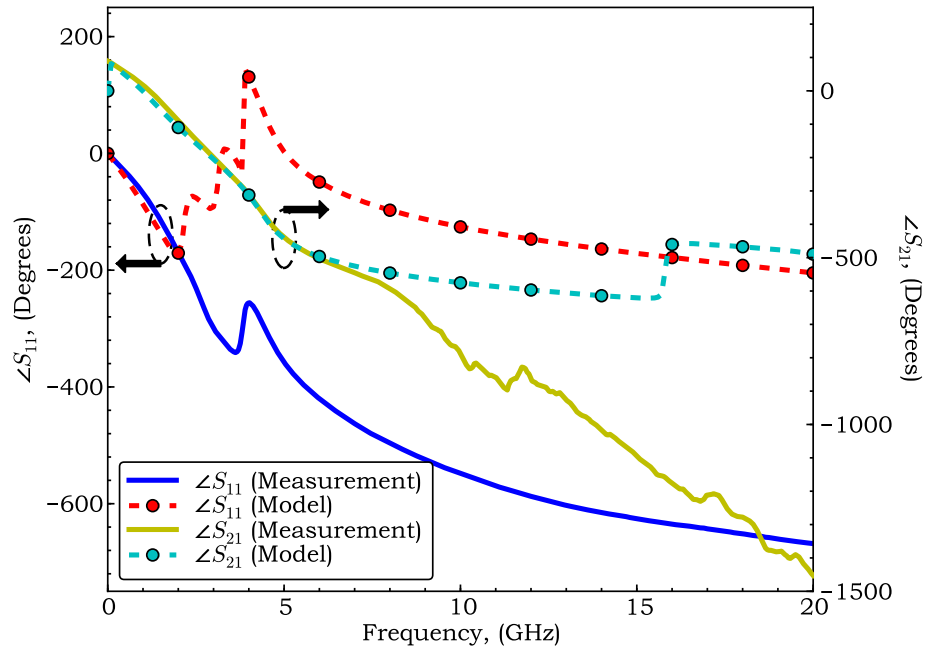
(b) $|S_{21}|$

Figure 2.23: *Measured S-parameters of a sample filter structure utilizing bonding strips as ground interconnection means. Circuit model S-parameters are also provided for comparison purposes.*

2.6 Conclusion

In this chapter, microwave lumped components are analyzed, designed and developed for a specific surface-micromachining based fabrication technology. Developed components are successfully employed to realize a bandpass filter in a cost-effective and monolithic manner. Designed filter structure is fabricated and characterized with microwave measurements. Peculiar phenomena observed in the measurement results are investigated further and filter samples are verified to work properly after solving grounding issues.

CHAPTER 3

MECHANICAL CHARACTERIZATION OF FIXED-FIXED TYPE BEAM STRUCTURES

3.1 Introduction

Fixed-fixed type beam structures are commonly encountered in MEMS applications such as switches [32, 36, 37], micro-resonators [70–72], mass-flow sensors [73], accelerometers [74] and material property extraction kits [75–77]. A proper mechanical characterization of such structures hence holds an essential role for a successful design of a wide class of devices. The inherent link between performance parameters in one domain to the mechanical ones further pronounces the latter argument.

This chapter focuses on mechanical aspects of fixed-fixed type beam structures and aims to establish a proper understanding from a statics perspective. Section 3.2 presents a rigorous treatment of fixed-fixed type beams subject to a uniform distributed transverse load and provides derivations for the effective spring constant expressions while taking axial effects into account. §3.3 then deals with the electrostatic actuation problem in a distributed sense and §3.4 outlines development of a numerical procedure for analyzing it. Next, §3.5 investigates the pull-in phenomenon for the electrostatic actuation problem and concerns with the construction of a pull-in voltage expression. Finally, §3.6 covers the problem of capacitive-contact electromechanics.

3.2 Mechanical Analysis of Fixed-Fixed Beams Subject to a Uniform Distributed Transverse Load

Investigation of fixed-fixed type beams for a given transverse load is essentially equivalent to determination of the deflection profile through governing beam differential equations under certain boundary conditions. For the particular case of a uniform distributed transverse load, it is possible to obtain analytical solutions for the deflection profile. This attribute not only facilitates development of physical insight into the mechanical problem, but also provides a good starting point for subsequent mechanical analyses.

In the following subsections, deflection profile expressions will be constructed first for a fixed-fixed type beam subject to a uniform distributed transverse load. During the derivations, axial effects will be taken into account and this latter property will render the analyses somewhat involved. In particular, axial tension will be considered first and results will be applied to a beam in compression through simple transformations. Having calculated the sought deflection characteristics, next, it will be concentrated on development of an effective spring constant expression which will prove useful hereafter.

3.2.1 Derivation for Tensile Axial Loading

In order to obtain the deflection profile of the fixed-fixed type beam for a uniform distributed transverse load under axial tension, one might begin with the determination of the relevant profile for a concentrated transverse load and then apply superposition. A rigorous treatment of the described method is provided in the following articles.

3.2.1.1 Deflection Characteristics for a Concentrated Transverse Load

Configuration for the concentrated-load problem at hand is illustrated in Figure 3.1. Governing differential equation for the system can be expressed as [108]:

$$\frac{\mathrm{d}^4 y(x)}{\mathrm{d}x^4} - k^2 \frac{\mathrm{d}^2 y(x)}{\mathrm{d}x^2} = \frac{q(x)}{E'I} \tag{3.1}$$

with

$$k^2 \triangleq \frac{P}{E'I} \tag{3.2}$$
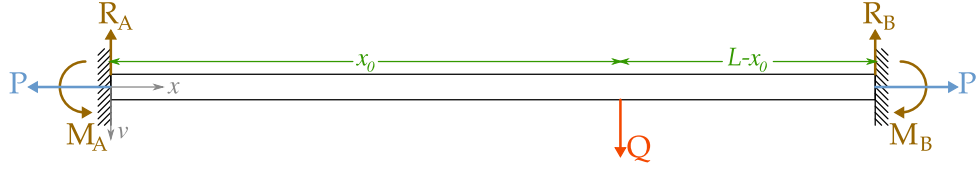
Figure 3.1: *Illustration of the mechanical problem for an arbitrary concentrated transverse load.*

In Equation (3.1); E' and I represent elastic modulus and moment of inertia of the beam, whereas $y(x)$ and $q(x)$ stand for the deflection at a given position and applied force density respectively. Owing to the concentrated nature of the force, $q(x)$ can be written as;

$$q(x) = Q\,\delta(x - x_0) \tag{3.3}$$

where $\delta(x)$ is the Dirac delta function. Substitution of Equation (3.3) into Equation (3.1) yields;

$$\frac{d^4 y(x)}{dx^4} - k^2 \frac{d^2 y(x)}{dx^2} = \frac{Q}{E'I}\,\delta(x - x_0) \tag{3.4}$$

Solution of Equation (3.4) is detailed in Appendix A. Resulting expression for the deflection profile is given by;

$$y(x) = g(x - x_0)\,u(x - x_0) + A\left[\cosh(kx) - 1\right] + B\left[\sinh(kx) - kx\right] \tag{3.5}$$

where

$$\begin{aligned}
A &= \frac{Q}{E'Ik^3}\,\frac{\sinh\left[k(L-x_0)\right] - kL\cosh\left[k(L-x_0)\right] + k(L-x_0)\cosh(kL) + \sinh(kx_0) + kx_0 - \sinh(kL)}{kL\sinh(kL) - 2\cosh(kL) + 2} \\
B &= \frac{Q}{E'Ik^3}\,\frac{\cosh\left[k(L-x_0)\right] - k(L-x_0)\sinh(kL) - \cosh(kx_0) + \cosh(kL) - 1}{kL\sinh(kL) - 2\cosh(kL) + 2}
\end{aligned} \tag{3.6}$$

and

$$g(x) = \frac{Q}{E'Ik^3}\left[\sinh(kx) - kx\right] \tag{3.7}$$

3.2.1.2 Deflection Characteristics for a General Distributed Transverse Load

Using previously derived concentrated-load formulation in conjunction with the principle of superposition, deflection characteristics for the beam at hand due to an arbitrary distributed load can be readily analyzed [109]. Let us consider the general case in which the
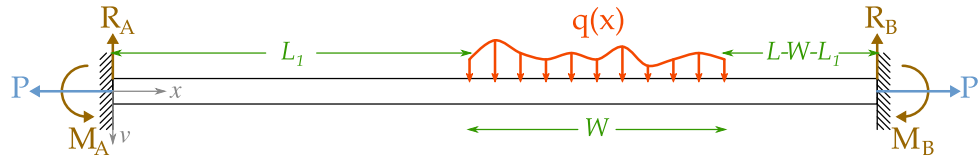
Figure 3.2: *Illustration of the mechanical problem for an arbitrary distributed load.*

span of loading is held variable and the loading is a given function of position as depicted in Figure 3.2. If the distributed load is investigated at a position, say, $x = x_0$ within an infinitesimal span of length dx_0, it is elementary to show that;

$$dQ = q(x_0)dx_0$$

Referring back to Equation (3.5), this concentrated force element results in an infinitesimal displacement at the position x as:

$$
\begin{aligned}
dy(x) &= [\cosh(kx) - 1] A(dQ, x_0) + [\sinh(kx) - kx] B(dQ, x_0) \\
&\quad + g(dQ, x - x_0)\, u(x - x_0) \\
&= [\cosh(kx) - 1] A(q(x_0), x_0)dx_0 + [\sinh(kx) - kx] B(q(x_0), x_0)dx_0 \\
&\quad + g(q(x_0), x - x_0)\, u(x - x_0)dx_0
\end{aligned}
$$

Superposing deflection contributions of such infinitesimal force components calls for an integration:

$$
\begin{aligned}
y(x) = \int dy &= [\cosh(kx) - 1] \int_{L_1}^{L_1+W} A(q(x_0), x_0)dx_0 \\
&+ [\sinh(kx) - kx] \int_{L_1}^{L_1+W} B(q(x_0), x_0)dx_0 \\
&+ \int_{L_1}^{L_1+W} g(q(x_0), x - x_0)\, u(x - x_0)dx_0
\end{aligned}
\qquad (3.8)
$$

It will be helpful to analyze the last integral term of Equation (3.8) in more detail. Utilizing the substitution $x_0' = x - x_0$, relevant integration becomes,

$$I_0 \triangleq \int_{L_1}^{L_1+W} g(q(x_0), x - x_0)\, \mathrm{u}(x - x_0)\mathrm{d}x_0$$

$$= \int_{x-L_1-W}^{x-L_1} g(q(x - x_0'), x_0')\, \mathrm{u}(x_0')\mathrm{d}x_0'$$

or more explicitly,

$$I_0 = \begin{cases} 0 & \text{if } x \leq L_1, \\ \int_0^{x-L_1} g(q(x - x_0'), x_0')\mathrm{d}x_0' & \text{if } L_1 \leq x \leq L_1 + W, \\ \int_{x-L_1-W}^{x-L_1} g(q(x - x_0'), x_0')\mathrm{d}x_0' & \text{if } x \geq L_1 + W. \end{cases} \qquad (3.9)$$

Hence, for an arbitrary distributed transverse load, deflection profile of the beam is expressed with,

$$y(x) = \begin{cases} y_I(x) & \text{if } x \leq L_1, \\ y_I(x) + \int_0^{x-L_1} g(q(x - x_0'), x_0')\mathrm{d}x_0' & \text{if } L_1 \leq x \leq L_1 + W, \\ y_I(x) + \int_{x-L_1-W}^{x-L_1} g(q(x - x_0'), x_0')\mathrm{d}x_0' & \text{if } x \geq L_1 + W. \end{cases} \qquad (3.10)$$

where $y_I(x)$ is the deflection profile corresponding to $x \leq L_1$ region and is given by,

$$y_I(x) = [\cosh(kx) - 1] \int_{L_1}^{L_1+W} A(q(x_0), x_0)\mathrm{d}x_0$$

$$+ [\sinh(kx) - kx] \int_{L_1}^{L_1+W} B(q(x_0), x_0)\mathrm{d}x_0 \qquad (3.11)$$

3.2.1.3 Deflection Characteristics for a Symmetrically and Uniformly Distributed Transverse Load

As a particular and common case of interest, let us now analyze the deflection problem when the applied load is distributed uniformly and symmetrically over a given span of
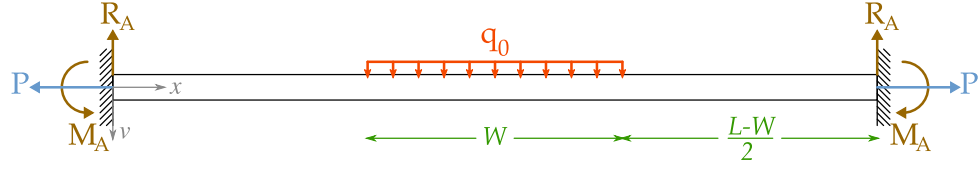
Figure 3.3: *Illustration of the problem configuration for a uniformly and symmetrically distributed load.*

the beam, as sketched in Figure 3.3. In terms of the mathematical notation adopted in the previous section, these properties are translated as

$$L_1 = \frac{L-W}{2}$$
$$q(x_0) = q_0$$

(3.12)

Moreover, it is expected by means of symmetry that,

$$y\left(\frac{L}{2} - x\right) = y\left(\frac{L}{2} + x\right)$$

so that it would suffice to carry out the analysis in two regions only, namely for $0 \leq x \leq \frac{L-W}{2}$ and $\frac{L-W}{2} \leq x \leq \frac{L}{2}$. Let us first evaluate $y_I(x)$ corresponding to the former. Utilizing Equation Set (3.12) in Equation (3.11) yields,

$$y_I(x) = [\cosh(kx) - 1] \int_{\frac{L-W}{2}}^{\frac{L+W}{2}} A(q_0, x_0) dx_0 + [\sinh(kx) - kx] \int_{\frac{L-W}{2}}^{\frac{L+W}{2}} B(q_0, x_0) dx_0 \quad (3.13)$$

Substituting the expressions for $A(q_0, x_0)$ and $B(q_0, x_0)$ from Equation Set (A.13) into Equation (3.13), integrating and performing subsequent simplification gives the following result:

$$\begin{aligned}
y_I(x) = &- \frac{q_0 W x^3}{12 E'I} \left\{ \frac{\sinh(kx) - kx}{(kx)^3/6} \right\} \\
&- \frac{q_0 L^2 x^2}{48 E'I} (\alpha^3 - 3\alpha) \left\{ \frac{\cosh(kx) - 1}{(kx)^2/2} \right\} \chi(u, \alpha)
\end{aligned}$$

(3.14)

with the auxiliary variables u, α and function $\chi(u, \alpha)$ defined as;

$$u \triangleq k\frac{L}{2} \tag{3.15a}$$

$$\alpha \triangleq \frac{W}{L} \tag{3.15b}$$

$$\chi(u, \alpha) \triangleq -6 \left\{ \frac{\alpha u \cosh(u) - \sinh(\alpha u)}{u^2 \sinh(u) \left[\alpha^3 - 3\alpha\right]} \right\} \tag{3.15c}$$

respectively.

Upon an inspection of Equation (3.14), one might notice curious arrangement of the rational factors being employed. Such organization of terms is favored as doing so enables one to quickly obtain relevant solution for the special case of zero axial force: Rational factors appearing in curly braces approach unity as k vanishes. In order to verify that claim, hyperbolic functions might be replaced with their corresponding Maclaurin series expansions to yield,

$$\lim_{k \to 0} \frac{\sinh(kx) - kx}{\frac{(kx)^3}{6}} \qquad\qquad \lim_{k \to 0} \frac{\cosh(kx) - 1}{\frac{(kx)^2}{2}}$$

$$= \lim_{k \to 0} \frac{kx + \frac{(kx)^3}{6} + O(k^5) - kx}{\frac{(kx)^3}{6}} \qquad\qquad = \lim_{k \to 0} \frac{1 + \frac{(kx)^2}{2} + O(k^4) - 1}{\frac{(kx)^2}{2}}$$

$$= \lim_{k \to 0} 1 + O(k^2) \qquad\qquad\qquad = \lim_{k \to 0} 1 + O(k^2)$$

$$= \quad 1 \qquad\qquad\qquad\qquad\qquad\qquad = \quad 1$$

In a similar manner, it can be shown that

$$\lim_{u \to 0} \chi(u, \alpha) = 1$$

Hence for zero axial loading, relevant deflection profile expression reduces to

$$y_{\mathrm{I}}(x)\Big|_{P=0} = -\frac{q_0 W x^3}{12 E' I} - \frac{q_0 L^2 x^2}{48 E' I} \left(\alpha^3 - 3\alpha\right) \tag{3.16}$$

Having obtained deflection characteristics of the beam in the first region, let us now proceed to the next one for which the solution will be denoted as $y_{\mathrm{II}}(x)$. A glance at Equations (3.10) and (3.12) reveals that,

$$y_{\mathrm{II}}(x) = y_{\mathrm{I}}(x) + \int_{0}^{x - \frac{L-W}{2}} g(q_0, x_0')\mathrm{d}x_0' \tag{3.17}$$

Substituting the expression for $g(q_0, x)$ defined in Equation (A.10) into Equation (3.17), integrating and performing subsequent manipulation yields,

$$y_{\mathrm{II}}(x) = y_{\mathrm{I}}(x) + \frac{q_0}{24 E' I} \left(x - \frac{L-W}{2}\right)^4$$

$$\times \left\{ \frac{8\left[\cosh\left(k\left(x - \frac{L-W}{2}\right)\right) - 1\right] - 4k^2\left(x - \frac{L-W}{2}\right)^2}{\frac{k^4}{3}\left(x - \frac{L-W}{2}\right)^4} \right\} \tag{3.18}$$

Maintaining the convention adopted in the previous region, Equation (3.18) is arranged so that the rational factor in curly braces becomes unity in the limit $k \to 0$. Consequently, relevant profile for zero axial loading can be easily determined as,

$$
\begin{aligned}
y_{\mathrm{II}}(x)\Big|_{P=0} &= y_{\mathrm{I}}(x)\Big|_{P=0} + \frac{q_0}{24E'I}\left(x - \frac{L-W}{2}\right)^4 \\
&= \frac{q_0}{48E'I}\left[2\left(x - \frac{L-W}{2}\right)^4 - 4Wx^3 - L^2\left(\alpha^3 - 3\alpha\right)x^2\right]
\end{aligned}
\tag{3.19}
$$

In most MEMS applications, a common quantity of interest is the center deflection of the beam, from which effective spring constants may be determined. Center deflection of the beam for the analyzed loading configuration can be found simply by substituting $x = \frac{L}{2}$ in Equation (3.18). Desired result is obtained as,

$$
\begin{aligned}
y_{\mathrm{max}} &= y_{\mathrm{II}}\left(\tfrac{L}{2}\right) \\
&= \frac{q_0 W L^3}{384 E'I}\left(\alpha^3 - 2\alpha^2 + 2\right)\zeta(u,\alpha)
\end{aligned}
\tag{3.20}
$$

with

$$
\zeta(u,\alpha) = \frac{2\cosh\left((2\alpha-1)\frac{u}{2}\right) - 2\alpha u \sinh\left(\frac{u}{2}\right) + \left[\alpha(2-\alpha)u^2 - 2\right]\cosh\left(\frac{u}{2}\right)}{\frac{1}{12}\left[\alpha^4 - 2\alpha^3 + 2\alpha\right]u^4 \cosh\left(\frac{u}{2}\right)}
\tag{3.21}
$$

Again, particular arrangement of the terms gives rise to

$$
\lim_{u \to 0}\zeta(u,\alpha) = 1
\tag{3.22}
$$

which is consistent with the adopted notation.

3.2.2 Derivation for Compressive Axial Loading

Deflection characteristics of a beam terminated with built-in ends and under the influence of compressive axial loading may be found through a similar analysis conducted in the previous section. Instead of that rigorous approach, however, one can readily obtain desired characteristics through a basic transformation applied to corresponding deflection expressions for tensile axial state as discussed in this section.

For a compressed beam, one immediately notices from Figures 3.1, 3.2 or 3.3 that P must act *into* the built-in ends and that its sign must be negative according to the adopted

convention. This observation actually implies that results determined for tensile axial loading are applicable to the compressed axial loading case with a reversed sign for P. Referring to Equation (3.2), this sign reversal implies,

$$k_c^2 = \frac{(-P)}{E'I}$$
$$= -k^2$$

or

$$k_c = \pm jk \tag{3.23a}$$
$$u_c = \pm ju \tag{3.23b}$$

where Equation (3.23b) follows from Equation (3.15a). Equation (3.23) indicates that deflection profile of the compressed beam due to a given transverse load may be obtained by merely replacing k and u with $\pm jk$ and $\pm ju$ respectively in the expressions associated with the beam in tension.

In the subsequent article, deflection profile of a compressed beam will be treated particularly for a uniformly and symmetrically distributed transverse load.

3.2.2.1 Deflection Characteristics for a Symmetrically and Uniformly Distributed Transverse Load

Substituting u and k with $\pm ju$ and $\pm jk$ respectively in Equations (3.14), (3.15c) and (3.18), deflection profile expressions of the compressed beam for a symmetrically and uniformly distributed transverse load can be determined as;

$$
\begin{aligned}
y_{\text{I,c}}(x) = & -\frac{q_0 W x^3}{12 E'I} \left\{ \frac{kx - \sin(kx)}{(kx)^3/6} \right\} \\
& -\frac{q_0 L^2 x^2}{48 E'I} \left(\alpha^3 - 3\alpha \right) \left\{ \frac{1 - \cos(kx)}{(kx)^2/2} \right\} \chi_c(u, \alpha)
\end{aligned}
\tag{3.24a}
$$

$$
\chi_c(u, \alpha) = 6 \left\{ \frac{\alpha u \cos(u) - \sin(\alpha u)}{u^2 \sin(u) \left(\alpha^3 - 3\alpha \right)} \right\}
\tag{3.24b}
$$

$$
\begin{aligned}
y_{\text{II,c}}(x) = & \, y_{\text{I,c}}(x) + \frac{q_0}{24 E'I} \left(x - \frac{L-W}{2} \right)^4 \\
& \times \left\{ \frac{8 \left[\cos \left(k \left(x - \frac{L-W}{2} \right) \right) - 1 \right] + 4k^2 \left(x - \frac{L-W}{2} \right)^2}{\frac{k^4}{3} \left(x - \frac{L-W}{2} \right)^4} \right\}
\end{aligned}
\tag{3.24c}
$$

Rational weighting factors appearing in Equation (3.24) are simplified through the use of identities

$$\sinh(\pm j\, x) = \pm j\, \sin(x)$$

$$\cosh(\pm j\, x) = \cos(x)$$

and by exploiting the even character of the original expressions.

Center deflection of the beam can be likewise found as,

$$
\begin{aligned}
y_{\mathrm{max,c}} &= y_{\mathrm{II,c}}\left(\tfrac{L}{2}\right) \\
&= \frac{q_0 W L^3}{384 E'I}\left(\alpha^3 - 2\alpha^2 + 2\right)\zeta_{\mathrm{c}}\left(u,\alpha\right)
\end{aligned}
\tag{3.25}
$$

where

$$
\begin{aligned}
\zeta_{\mathrm{c}}(u,\alpha) &= \zeta\left(ju,\alpha\right) \\
&= \frac{2\cos\left((2\alpha-1)\tfrac{u}{2}\right) + 2\alpha u \sin\left(\tfrac{u}{2}\right) + \left[\alpha(2-\alpha)u^2 - 2\right]\cos\left(\tfrac{u}{2}\right)}{\tfrac{1}{12}\left[\alpha^4 - 2\alpha^3 + 2\alpha\right]u^4 \cos\left(\tfrac{u}{2}\right)}
\end{aligned}
\tag{3.26}
$$

It is observed from Equation (3.26) that, unlike the beam in tension, there exists a critical axial load for the compressed beam at which the center deflection grows indefinitely for an arbitrary transverse force density q_0. Indeed, it is elementary to show that mentioned *critical buckling* occurs when

$$\sin(u_{\mathrm{cr}}) = 0$$

or at

$$u_{\mathrm{cr}} = n\pi \tag{3.27}$$

Taking $n = 1$ for the first mode, Equation (3.27) becomes equivalent to

$$\sqrt{\frac{|P_{\mathrm{cr}}|}{E'I}}\frac{L}{2} = \pi$$

$$\therefore |P_{\mathrm{cr}}| = \frac{4\pi^2 E'I}{L^2}$$

which is precisely the *Euler-load* or *buckling-load* expression for slender column members having built-in ends.

3.2.3 Calculation of the Parameter u

It is noted from the deflection profile expressions derived in the previous section that the effect of axial tension or compression in the beam is incorporated into rather complicated functions of the parameter u. Thus far, the value of this parameter has been assumed to be known for a given axial force P. In reality, however, P must itself be related to physical constraints of the problem. Specifically, P can be decomposed into two components [110]:

- Tension introduced in the beam due to non-linear stretching during bending,

- Residual tension/compression associated with the beam material.

Mathematically, these statements can be expressed as,

$$P = E' \frac{\Delta L}{L} A + \sigma A \tag{3.28}$$

where ΔL, A and σ represent bending related elongation, cross-sectional area and uniaxial residual stress of the beam respectively. With the aid of Equation (3.15a), Equation (3.28) can be transformed into,

$$\frac{4E'I}{AL^2} u^2 = E' \frac{\Delta L}{L} + \sigma \tag{3.29}$$

Beam elongation due to bending (ΔL) can be determined from the basic relation [111],

$$\Delta L = \int_{x=0}^{x=L} (\mathrm{d}s - \mathrm{d}x)$$

where

$$\mathrm{d}s = \mathrm{d}x \sqrt{1 + \left(\frac{\mathrm{d}y}{\mathrm{d}x}\right)^2}$$

Under small deflection assumption, the approximation

$$\sqrt{1 + \left(\frac{\mathrm{d}y}{\mathrm{d}x}\right)^2} \approx 1 + \frac{1}{2}\left(\frac{\mathrm{d}y}{\mathrm{d}x}\right)^2$$

remains valid and hence ΔL can be expressed as

$$\Delta L \approx \frac{1}{2} \int_0^L \left(\frac{\mathrm{d}y}{\mathrm{d}x}\right)^2 \mathrm{d}x \tag{3.30}$$

Substituting the deflection profile expression for a uniformly and symmetrically distributed transverse load described by Equations (3.14) and (3.18) into Equation (3.30), one obtains

$$\Delta L = \int_0^{\frac{L-W}{2}} \left(\frac{\mathrm{d}y_{\mathrm{I}}(x)}{\mathrm{d}x} \right)^2 \mathrm{d}x + \frac{1}{2} \int_{\frac{L-W}{2}}^{\frac{L+W}{2}} \left(\frac{\mathrm{d}y_{\mathrm{II}}(x)}{\mathrm{d}x} \right)^2 \mathrm{d}x$$

$$= \left(\frac{q_0^2 L^7}{E'^2 I^2} \right) \mathrm{h}(u, \alpha)$$

(3.31)

where

$$\begin{aligned}
\mathrm{h}(u, \alpha) =\ & \frac{1}{384} \frac{3\alpha^2 - 2\alpha^3}{u^4} - \frac{1}{256} \frac{\alpha^2}{u^4 \sinh^2(u)} \\
& - \frac{1}{256} \frac{3\alpha^2 \cosh(u)\sinh(u) - 2\alpha \cosh(u)\sinh(\alpha u) + 2\alpha^2 \cosh(\alpha u)\sinh(u)}{u^5 \sinh^2(u)} \\
& - \frac{1}{256} \frac{3\alpha \sinh^2(u) + \sinh^2(\alpha u) - 8\alpha \sinh(\alpha u)\sinh(u)}{u^6 \sinh^2(u)} \\
& + \frac{1}{256} \sinh((1-\alpha)u) \frac{5\sinh(\alpha u) - 2\alpha u \cosh(\alpha u)}{u^7 \sinh(u)}
\end{aligned}$$

(3.32)

In typical MEMS applications, thin-film materials are utilized as the beam material and patterned beams can be regarded as plates or slender elements depending on the ratio of beam thickness to width; the distinction being incorporated into the definition of effective elastic modulus. For a beam element having a rectangular cross-section, effective elastic modulus (E') and moment of inertia (I) expressions are given as [76, 110]:

$$E' = \begin{cases} E & \text{if } w < 5t \\ \frac{E}{1-v^2} & \text{if } w \geq 5t \end{cases}$$

(3.33a)

$$I = \frac{1}{12} w t^3$$

(3.33b)

where v, E denote the Poisson's ratio and Young's modulus of the relevant material while t, w indicate beam thickness and width respectively. Moreover, it would be proper to relate uniaxial residual stress of the beam (σ) to *biaxial* residual stress of the thin-film material as [76]:

$$\sigma = \sigma_0(1 - v)$$

(3.34)

50

with σ_0 standing for the biaxial residual stress. Inserting Equations (3.31), (3.33) and (3.34) into Equation (3.29) then yields,

$$u^2 = \frac{432}{E'^2} \left(\frac{L}{t}\right)^8 \left(\frac{q_0}{w}\right)^2 h(u, \alpha) + 3 \left(\frac{L}{t}\right)^2 \frac{\sigma_0(1-\nu)}{E'} \tag{3.35}$$

which is a characteristic equation for u in terms of geometrical/material parameters and the distributed transverse load q_0.

In order to shed more light into physical interpretation of the axial relation given in Equation (3.35), let us express distributed transverse load q_0 in terms of maximum deflection of the beam $y_{\max}$. For that purpose, Equation (3.20) can be re-arranged to yield,

$$\frac{q_0}{w} = \frac{32E't^3}{L^4 \, \overline{\zeta}(u, \alpha)} \, y_{\max} \tag{3.36a}$$

where,

$$\overline{\zeta}(u, \alpha) \triangleq \left[\alpha^4 - 2\alpha^3 + 2\alpha\right] \zeta(u, \alpha) \tag{3.36b}$$

Employing Equation (3.36a) in Equation (3.35) and performing subsequent simplification establishes the desired result;

$$u^2 = \left(\frac{y_{\max}}{t}\right)^2 \Psi(u, \alpha) + 3 \left(\frac{L}{t}\right)^2 \frac{\sigma_0(1-\nu)}{E'} \tag{3.37a}$$

with

$$\Psi(u, \alpha) \triangleq 442368 \times \frac{h(u, \alpha)}{\overline{\zeta}^2(u, \alpha)} \tag{3.37b}$$

This second form of the axial relation presented in Equation (3.37a) happens to be a more compact representation and it will prove more useful for spring constant determination purposes due to its explicit dependence on $y_{\max}$. Figure 3.4 provides a plot of the newly introduced function $\Psi(u, \alpha)$ as a function of u for a range of α values.

Having formulated an alternative expression for the axial relation in terms of maximum deflection of the beam, a physical interpretation may now follow. It is observed from Figure 3.4 that $\Psi(u, \alpha)$ is a slowly-varying function of u and it can be regarded as an α-dependent constant with $6.4 \leq \Psi(u, \alpha) \leq 8.0$ as a first-order approximation. Using this fact, it is immediately noticed from Equation (3.37a) that non-linear stretching effects can be ignored as long as $y_{\max}$ remains sufficiently small compared to beam thickness.
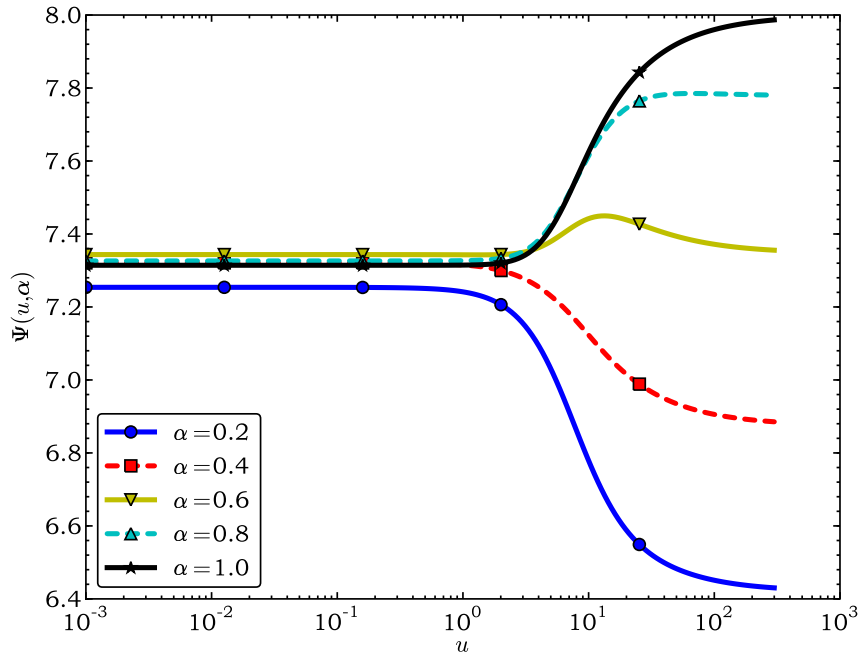
Figure 3.4: *Plot of $\Psi(u, \alpha)$ versus u with α as a parameter.*

In other words, axial state of the beam becomes (tensile) residual stress-dominated provided that $y_{\max}/t$ is small, a condition valid for low q_0 values. Conversely, the effect of non-linear stretching becomes more pronounced as $y_{\max}$ becomes comparable to or larger than t, for which the beam is said to be in *large-deflection* region[1].

In general, Equation (3.35) or (3.37a), being transcendental in nature, must be solved by numerical or graphical means in order to determine the exact value of u for a particular problem configuration. Closed-form expressions for u, however, *can* be derived for certain asymptotic cases; but relevant analyses are postponed until next section wherein closed-form spring constant expressions are sought for the beam configuration at hand.

Another useful property that might be deduced from Equation (3.37a) concerns with the residual stress level below (above) which compressive (tensile) deflection profile expressions apply. Mentioned tensile/compressive state transition occurs when u begins to

---

[1] This term should not be confused with the *small-deflection assumption* adopted throughout the derivations so far. The latter term pertains to the relation of $y_{\max}$ to t, whereas the former concerns with the magnitude of $\mathrm{d}y/\mathrm{d}x$ compared to unity. In fact, it can be shown that a beam in large-deflection region can still satisfy small-deflection assumption.

take on purely imaginary values below a certain $\sigma_0 = \sigma_{0,\mathrm{t}}$. It is apparent from tensile contribution of the non-linear beam stretching that $\sigma_{0,\mathrm{t}}$ is negative and its value can be readily determined by setting $u = 0$ in Equation (3.37a):

$$0 = \left(\frac{y_{\max}}{t}\right)^2 \Psi\left(0, \alpha\right) + 3 \left(\frac{L}{t}\right)^2 \frac{\sigma_{0,\mathrm{t}}(1 - \nu)}{E'}$$

which can be manipulated to obtain

$$
\begin{aligned}
\sigma_{0,\mathrm{t}} &= -\frac{E'}{3(1 - \nu)} \left(\frac{y_{\max}}{L}\right)^2 \Psi(0, \alpha) \\
&= -\frac{16}{105} \frac{E'}{(1 - \nu)} \left(\frac{y_{\max}}{L}\right)^2 \frac{21\alpha^6 - 96\alpha^5 + 133\alpha^4 - 105\alpha^2 + 63}{(\alpha^3 - 2\alpha^2 + 2)^2}
\end{aligned}
\tag{3.38}
$$

For $\sigma_0 < \sigma_{0,\mathrm{t}}$, beam under consideration admits a compressive state and accordingly u must be replaced with $\mathrm{j}u$ in the relevant expressions. Applying this transformation to Equation (3.37a) results in

$$-u^2 = \left(\frac{y_{\max}}{t}\right)^2 \Psi_{\mathrm{c}}\left(u, \alpha\right) + 3 \left(\frac{L}{t}\right)^2 \frac{\sigma_0(1 - \nu)}{E'} \tag{3.39a}$$

with

$$\Psi_{\mathrm{c}}\left(u, \alpha\right) = \Psi\left(\mathrm{j}u, \alpha\right) \tag{3.39b}$$

The transformed function $\Psi_{\mathrm{c}}\left(u, \alpha\right)$ is plotted in Figure 3.5.

Caution must be exercised when using Equation (3.39) to calculate u in compressive axial state: It was demonstrated earlier that deflection problem for compressive axial state is singular and this singularity manifests itself in the unbounded growth of $y_{\max}$ and associated break-down of the small deflection assumption. Recalling the fact that mentioned singularity occurs at $u = u_{\mathrm{cr}} = \pi$, it follows that one must consider only those values of u in $[0, \pi)$ range for compressive axial state. Described singularity, however, is not evident from Figure 3.5 due to cancellation of the relevant pole during the division of $\mathrm{h}\left(\mathrm{j}u, \alpha\right)$ by $\overline{\zeta}^2\left(\mathrm{j}u, \alpha\right)$.

Table 3.1 summarizes the axial relations to utilize in order to quantify u and their associated validity ranges at tensile and compressive axial states of the beam.
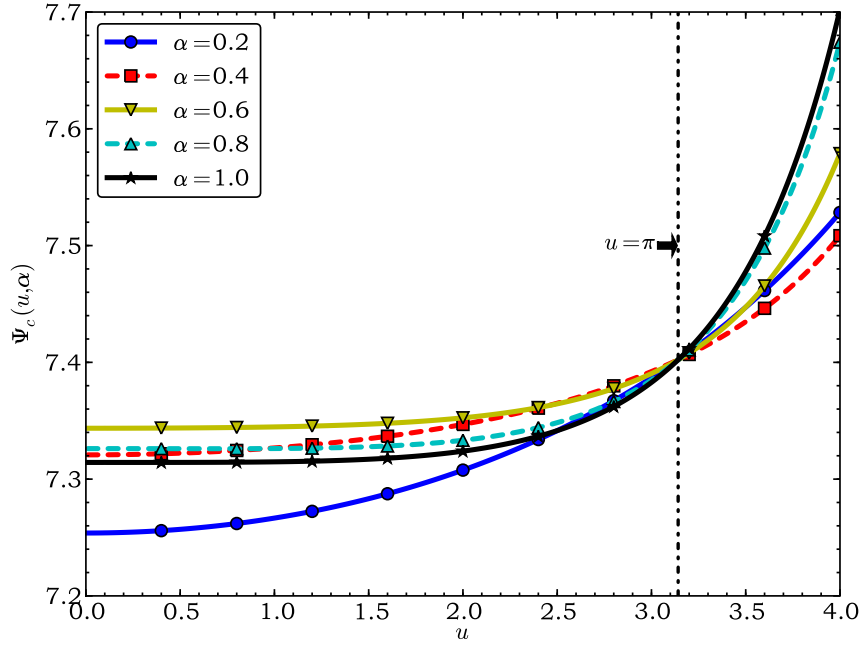
Figure 3.5: *Plot of $\Psi_c(u, \alpha)$ versus u with α as a parameter.*

Table 3.1: *A summary of the axial relations characterizing u and their corresponding validity ranges at different axial states of the beam.*

AXIAL STATE	RANGE OF σ_0	EXPRESSION FOR u	VALIDITY RANGE OF u
TENSILE	$\sigma_{0,t} \leq \sigma_0$	Equation (3.37)	$0 \leq u$
COMPRESSIVE	$\sigma_0 < \sigma_{0,t} < 0$	Equation (3.39)	$0 \leq u < \pi$

3.2.4 Spring Constant Evaluation

In previous sections, a rigorous treatment has been carried out in order to characterize the mechanical system of a fixed-fixed type beam subject to a constant distributed transverse load in the presence of axial forces. Conducted analysis has been of *distributed* nature and consequently sought quantities have been obtained as a function of position along the beam length. From a modeling perspective, however, it is often convenient to represent such a distributed mechanical system with a *lumped* spring as doing so greatly simplifies any further investigation wherein the beam is involved. It is the aim of this section to establish an adequate description of the equivalent lumped spring corresponding to the distributed mechanical system at hand.

According to Hooke's law, elongation Δx of an idealized spring is proportional to the externally exerted force F according to the relation [112];

$$F = k\Delta x \tag{3.40}$$

with the constant of proportionality equal to the *spring constant* (or *stiffness*) k, which is actually a characteristic property for a given spring. In other words, the spring constant effectively models a given spring provided that its force-displacement curve remains in the linear-elastic region[2]. It is thus deduced from this discussion that in order to represent the distributed fixed-fixed beam system as a lumped spring, it would be sufficient to formulate an *effective* spring constant expression.

Prior to any derivation attempt, a simple reasoning reveals that effective spring constant of the fixed-fixed beam system is actually position-dependent since beam deflection varies along the beam length. A convenient way to circumvent mentioned position-dependence is to define the effective spring constant at the beam center, i.e. effective displacement is set to y_{max}. Using this convention and the elementary relation

$$F = \int_{\frac{L-W}{2}}^{\frac{L+W}{2}} q(x_0)\mathrm{d}x_0 = \int_{\frac{L-W}{2}}^{\frac{L+W}{2}} q_0\mathrm{d}x_0 = q_0 W$$

an expression for the effective spring constant k_{q} can be developed through manipulation of Equation (3.20):

$$\begin{aligned} k_{\mathrm{q}} &= \frac{(q_0 W)}{y_{\mathrm{max}}} \\ &= \frac{32E'\alpha w}{\left(\frac{L}{t}\right)^3 \overline{\zeta}(u,\alpha)} \end{aligned} \tag{3.41}$$

As a notational preference, it is opted to eliminate beam width dependence by considering spring constant per unit width in the remainder of the text and consequently Equation (3.41) is re-written as,

$$\frac{k_{\mathrm{q}}}{w} = \frac{32E'\alpha}{\left(\frac{L}{t}\right)^3 \overline{\zeta}(u,\alpha)} \tag{3.42}$$

---

[2] This concept is analogous to modulus of elasticity (E') characterizing a specific material within the linear portion of the associated stress-strain curve [111].

It is realized from Equation (3.42) that per unit width stiffness of the fixed-fixed beam system is a function of u, which in turn depends on y_{max} according to Equation (3.37a). Thus, force-displacement relation of the equivalent lumped spring turns out to be non-linear contrary to the assumed linear trend. Although at this point it would make sense to extend the definition of stiffness to an incremental one by considering $\frac{\partial F}{\partial y_{max}}$, such a procedure will not be attempted as it is desired to retain a simple expression for force calculation purposes. Accordingly, it will be adhered to the current spring constant definition and the implicit non-linearity will be incorporated into the word "effective".

Another attribute of the effective spring constant k_q can be deduced from the above discussion: In order to determine k_q for a given maximum deflection y_{max}, it is required to calculate the corresponding u from Equation (3.37a) for which an explicit solution cannot be formulated in general. Hence, it follows that a general closed-form expression cannot be developed for k_q in terms of y_{max}. It is possible, however, to accomplish the latter for extreme values of the parameter u, which will lead to *small-argument* and *large-argument* forms of the effective spring constant k_q as next subsections demonstrate.

3.2.4.1 Small-argument Form of k_q

For small values of the parameter u, a closed-form expression for the effective spring constant k_q can be derived by utilizing truncated Maclaurin series expansions of the relevant functions containing u. Following the usual convention, tensile axial state will be considered first and results will be extended for the compressive axial state via the transformation $u \to j\, u$.

Tensile Axial State Case

Let us consider the axial relation Equation (3.37a) first. For small values of u, it can be shown that the function $\Psi(u, \alpha)$ appearing in the relevant expression can be represented as,

$$\Psi(u, \alpha) = p_0(\alpha) + O\left(u^2\right) \tag{3.43a}$$

where

$$p_0(\alpha) = \frac{16}{35} \frac{21\alpha^6 - 96\alpha^5 + 133\alpha^4 - 105\alpha^2 + 63}{(\alpha^3 - 2\alpha^2 + 2)^2} \tag{3.43b}$$

Truncation of Equation (3.43a) after its first term is permissible for $0 \leq u \leq 4$ and $0.25 \leq \alpha \leq 1.0$ with an accuracy better than 2%. Substituting this approximate form of $\Psi(u, \alpha)$ in Equation (3.37a) results in

$$u^2 \approx \left(\frac{y_{\text{max}}}{t}\right)^2 p_0(\alpha) + 3 \left(\frac{L}{t}\right)^2 \frac{\sigma_0(1-v)}{E'} \tag{3.44}$$

A small-argument approximation can be also applied to the function $\alpha/\overline{\zeta}(u, \alpha)$ appearing in Equation (3.42) by using the associated Maclaurin series expansion,

$$\frac{\alpha}{\overline{\zeta}(u, \alpha)} = q_0(\alpha) + q_2(\alpha)u^2 + O(u^4) \tag{3.45a}$$

where the coefficients $q_i(\alpha)$ are given by

$$
\begin{aligned}
q_0(\alpha) &= \frac{1}{\alpha^3 - 2\alpha^2 + 2} \\
q_2(\alpha) &= -\frac{1}{30} \frac{\alpha^5 - 3\alpha^4 + 5\alpha^2 - 6}{(\alpha^3 - 2\alpha^2 + 2)^2}
\end{aligned}
\tag{3.45b}
$$

Equation (3.45a) can be accurately represented as a second order polynomial of u with an error less than 1.2% for $0 \leq u \leq 4$ and $0 \leq \alpha \leq 1$. Employing this latter approximation in Equation (3.42) yields,

$$\frac{k_q}{w} \approx \frac{32E'}{\left(\frac{L}{t}\right)^3} \left[q_0(\alpha) + q_2(\alpha)u^2\right] \tag{3.46}$$

After plugging Equation (3.44) into Equation (3.46) and performing subsequent simplification, one then obtains,

$$
\begin{aligned}
\frac{k_q}{w} &\approx \frac{32E'\,\beta_{\text{b}}(\alpha)}{\left(\frac{L}{t}\right)^3} + \frac{4096}{175} \frac{E'\,\beta_{\text{nl}}(\alpha)}{\left(\frac{L}{t}\right)^3} \left(\frac{y_{\text{max}}}{t}\right)^2 + \frac{48}{5} \frac{\beta_\sigma(\alpha)}{\left(\frac{L}{t}\right)} \sigma_0(1-v) \\
&= \frac{k_{\text{q,b}}}{w} + \frac{k_{\text{q,nl}}}{w} + \frac{k_{\text{q},\sigma}}{w}
\end{aligned}
\tag{3.47a}
$$

where

$$
\begin{aligned}
\beta_{\text{b}}(\alpha) &= q_0(\alpha) \\
\beta_{\text{nl}}(\alpha) &= \frac{175}{128} p_0(\alpha)q_2(\alpha) \\
\beta_\sigma(\alpha) &= 10\, q_2(\alpha)
\end{aligned}
\tag{3.47b}
$$

It is noted from Equation (3.47a) that obtained small-argument spring constant expression can be decomposed into three components: Stiffness associated with bending ($k_{q,b} = k_q|_{u=0}$), non-linear membrane stretching ($k_{q,nl}$) and the residual stress of the beam ($k_{q,\sigma}$). Moreover, it is realized that each stiffness term is scaled with seemingly distinct span-dependent functions $\beta_i(\alpha)$ whose definitions are provided in Equation (3.47b). A simple analysis reveals that these latter functions are nearly indistinguishable in $0 \leq \alpha \leq 1$ interval as Figure 3.6 illustrates. Thus, one can utilize the fairly simpler $\beta_b(\alpha)$ expression to accurately represent $\beta_{nl}(\alpha)$ and $\beta_\sigma(\alpha)$ with associated errors less than 1% for $0.13 \leq \alpha \leq 1$ and 0.7% for $0 \leq \alpha \leq 1$ respectively. Using this information, k_q can be re-arranged as,
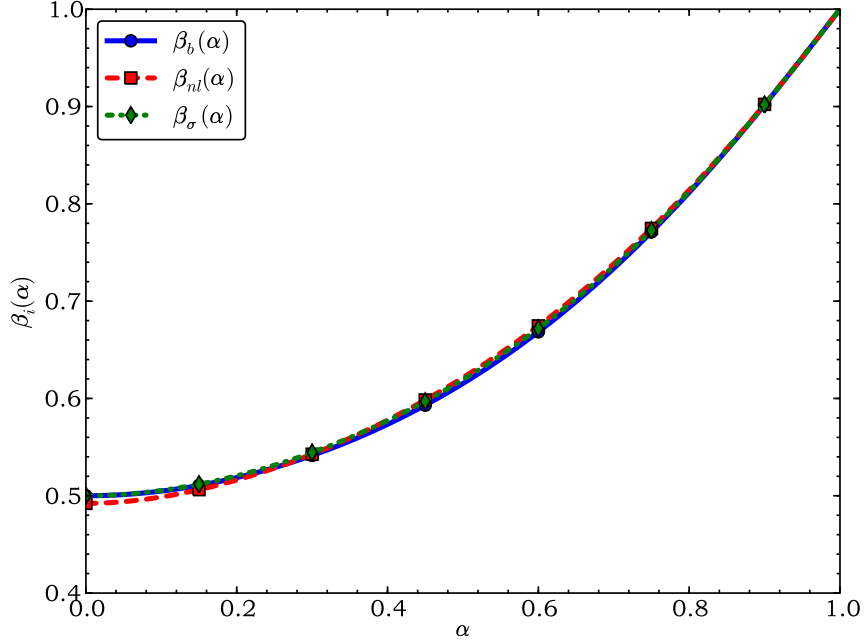
Figure 3.6: *Plot of $\beta_i(\alpha)$ for $0 \leq \alpha \leq 1$.*

$$\frac{k_q}{w} \approx \left[\frac{32E'}{\left(\frac{L}{t}\right)^3} + \frac{4096}{175} \frac{E'}{\left(\frac{L}{t}\right)^3} \left(\frac{y_{max}}{t}\right)^2 + \frac{48}{5} \frac{\sigma_0(1-\nu)}{\left(\frac{L}{t}\right)} \right] \beta_b(\alpha) \qquad (3.48)$$

Equation (3.48) is identical to the corresponding expression provided in [80] for $\alpha = 1$ with the exception of the scalar constant included in $k_{q,nl}$ ($12\pi^2/5$ versus $4096/175$, with

1.2% error). In particular, noted difference is due to the deflection profile estimation of

$$y(x) \approx y_{\max} \sin\left(\frac{\pi}{L}x\right)$$

adopted by the authors during the evaluation of beam elongation and this assumption is equivalent to

$$\Psi(u,\alpha) \approx \frac{3\pi^2}{4} \tag{3.49}$$

which actually happens to be a good approximation for small values of u^3.

Compressive Axial State Case

Small-argument form of the spring constant for the beam in compression may be found simply by replacing the parameter u with ju in the Maclaurin series expansions formulated previously for the beam in tension. An application of this transformation to Equations (3.44) and (3.46) yields the following equation set:

$$-u^2 \approx \left(\frac{y_{\max}}{t}\right)^2 p_0(\alpha) + 3\left(\frac{L}{t}\right)^2 \frac{\sigma_0(1-v)}{E'} \tag{3.50a}$$

$$\frac{k_{q,c}}{w} \approx \frac{32E'}{\left(\frac{L}{t}\right)^3}\left[q_0(\alpha) - q_2(\alpha)u^2\right] \tag{3.50b}$$

Upon an inspection of Equation Set (3.50), one recognizes that

$$k_{q,c} = k_q \tag{3.51}$$

that is, spring constant expression for the compressed beam is identical to that of a taut one for small u argument. Notice that the distinction between tensile and compressive axial states is inherent in the relation of σ_0 with σ_t: In particular, the condition $\sigma_0 < \sigma_{0,t}$ is implied for the latter axial state.

It must be stressed once again that deflection results obtained earlier for the compressive axial state are valid only for $0 \leq u < \pi$. Although this information might initially suggest that effective spring constant for the beam in compression entirely falls in the small-argument region, this is not the actual case: Accuracy of the Maclaurin series expansion provided in Equation (3.50b) rapidly degrades as $u \rightarrow \pi$. In order to maintain

---

[3] It can be shown that $\Psi(u,\alpha) \approx p_0(\alpha) \approx 7.30$ with an error better than 2.5% for $0 \leq u \leq 4$ and $0.25 \leq \alpha \leq 1$. For the same parameter range, the error involved in Equation (3.49) is 4%.

a reasonable accuracy, u can be restricted to $[0, 2.5]$ interval and doing so yields a maximum error of 1.4% for Equation (3.50b) in $0 \leq \alpha \leq 1$ range. It is moreover informative to point out that accuracy of the expansion in Equation (3.50a) is better than 1.8% for $0 \leq u \leq \pi$ and $0.25 \leq \alpha \leq 1$, a result consistent with the fact that $\Psi_c(u, \alpha)$ has no poles at $u = \pi$.

3.2.4.2 Large-argument Form of k_q

A closed-form expression for the effective spring constant k_q can be also developed for large values of the parameter u. The procedure is to utilize asymptotic expansions of the relevant functions containing u. As opposed to the small-argument case, it will *not* be attempted to derive a large-argument spring constant for the compressive axial state due to the following reasons:

- Range of u is limited to $[0, \pi)$ and accordingly a considerable number of terms would be required in the associated asymptotic series to attain a desired accuracy, rendering the chances of obtaining a closed-form expression very low.

- Although it is possible to circumvent the previous issue by employing Taylor series expansions around $u = \pi$, validity of the obtained expressions would be in question since beam slope would become comparable to unity in the large-argument region, violating the small-deflection assumption.

An application of the mentioned asymptotic expansion approach to the beam in tension is detailed in the following subsection.

Tensile Axial State Case

Asymptotic expansions of the functions $\Psi(u, \alpha)$ and $\frac{\alpha}{\overline{\zeta}(u,\alpha)}$ appearing in Equations (3.37a) and (3.42) can be shown to be:

$$\Psi(u, \alpha) = p_{a,0}(\alpha) + \frac{p_{a,1}(\alpha)}{u} + O\left(u^{-2}\right) \tag{3.52a}$$

$$\frac{\alpha}{\overline{\zeta}(u,\alpha)} = q_{a,0}(\alpha) u^2 + q_{a,1}(\alpha) u + q_{a,2}(\alpha) + O\left(u^{-1}\right) \tag{3.52b}$$

where

$$p_{a,0}(\alpha) = \frac{8(3 - 2\alpha)}{(2 - \alpha)^2} \tag{3.53a}$$

$$p_{a,1}(\alpha) = \frac{4(6 - 7\alpha)}{(2 - \alpha)^3} \tag{3.53b}$$

$$q_{a,0}(\alpha) = \frac{1}{12(2 - \alpha)} \tag{3.53c}$$

$$q_{a,1}(\alpha) = \frac{1}{6(2 - \alpha)^2} \tag{3.53d}$$

$$q_{a,2}(\alpha) = \frac{(2 + \alpha)}{6(2 - \alpha)^3 \alpha} \tag{3.53e}$$

Upon truncation of the higher order terms, Equations (3.52a) and (3.52b) remain accurate within 2% and 1.2% for $u \geq 15$ and $0.15 \leq \alpha \leq 1$ respectively. Substitution of these asymptotic forms into Equations (3.37a) and (3.42) yields,

$$u^2 \approx \left(\frac{y_{\max}}{t}\right)^2 p_{a,0}(\alpha) \left[1 + \frac{p_{a,1}(\alpha)}{p_{a,0}(\alpha)} \frac{1}{u}\right] + 3\left(\frac{L}{t}\right)^2 \frac{\sigma_0(1 - v)}{E'} \tag{3.54a}$$

$$\frac{k_q}{w} \approx \frac{32E'}{\left(\frac{L}{t}\right)^3} \left[q_{a,0}(\alpha) u^2 + q_{a,1}(\alpha) u + q_{a,2}(\alpha)\right] \tag{3.54b}$$

leading to the following spring constant expression:

$$\begin{aligned}
\frac{k_q}{w} &\approx \frac{32E'}{\left(\frac{L}{t}\right)^3} \frac{(2 + \alpha)}{6(2 - \alpha)^3 \alpha} \left[1 + \frac{(2 - \alpha)\alpha}{2 + \alpha} u\right] \\
&+ \frac{64}{3} \frac{E'}{\left(\frac{L}{t}\right)^3} \left(\frac{y_{\max}}{t}\right)^2 \frac{(3 - 2\alpha)}{(2 - \alpha)^3} \left[1 + \frac{p_{a,1}(\alpha)}{p_{a,0}(\alpha)} \frac{1}{u}\right] \\
&+ \frac{8}{\left(\frac{L}{t}\right)} \sigma_0(1 - v) \frac{1}{(2 - \alpha)} \\
&= \frac{k_{q,b}}{w} + \frac{k_{q,nl}}{w} + \frac{k_{q,\sigma}}{w}
\end{aligned} \tag{3.55}$$

Equation (3.55) shows that obtained large-argument spring constant expression comprises three components, similar to the small-argument case. Unlike the previous formulation, however, $k_{q,b}$ and $k_{q,nl}$ are noted to *depend* on u; a fact which emphasizes non-linear dependence of the spring constant on membrane stiffness mechanisms. In addition, a simple closed-form solution of u for a given $y_{\max}/t$ and σ_0 is not available according to Equation (3.54a), so one has to resort to numerical techniques for calculation of k_q.

An approximate closed-form solution for the large-argument spring constant may yet be found at the expense of somewhat reduced accuracy at the lower u bound. In order to determine this solution, one first considers the particular term,

$$\frac{p_{a,1}(\alpha)}{p_{a,0}(\alpha)}\frac{1}{u} = \frac{(6-7\alpha)}{2(2-\alpha)(3-2\alpha)}\frac{1}{u}$$

appearing in Equations (3.54) and (3.55). It is easy to prove that

$$\left|\frac{p_{a,1}(\alpha)}{p_{a,0}(\alpha)}\frac{1}{u}\right| \le \frac{1}{2u}$$

Moreover, validity range of the current derivation requires

$$\left|\frac{p_{a,1}(\alpha)}{p_{a,0}(\alpha)}\frac{1}{u}\right| \le \frac{1}{2u} \le \frac{1}{30}$$

Hence, one might utilize the additional approximation [4]

$$1 + \frac{p_{a,1}(\alpha)}{p_{a,0}(\alpha)}\frac{1}{u} \approx 1$$

to promote further simplification of the derived formulation as:

$$u^2 \approx 8\left(\frac{y_{\max}}{t}\right)^2 \frac{(3-2\alpha)}{(2-a)^2} + 3\left(\frac{L}{t}\right)^2 \frac{\sigma_0(1-v)}{E'} \tag{3.56a}$$

$$\begin{aligned}
\frac{k_q}{w} &\approx \frac{32E'}{\left(\frac{L}{t}\right)^3}\frac{(2+\alpha)}{6(2-\alpha)^3\alpha}\left[1 + \frac{(2-\alpha)\alpha}{2+\alpha}u\right] \\
&+ \frac{64}{3}\frac{E'}{\left(\frac{L}{t}\right)^3}\left(\frac{y_{\max}}{t}\right)^2\frac{(3-2\alpha)}{(2-\alpha)^3} \\
&+ \frac{8}{\left(\frac{L}{t}\right)}\sigma_0(1-v)\frac{1}{(2-\alpha)}
\end{aligned} \tag{3.56b}$$

It can be stated from Equation (3.56) that resulting large-argument spring constant expression is indeed of closed-form. It is also noted that $k_{q,nl}$ ceases to depend on u whereas $k_{q,b}$ still possesses a u-dependence. The latter observation reminds once again the non-linear spring constant contributions of membrane stiffness components.

---

[4] Notice that indicated approximation is actually equivalent to truncating Equation (3.52a) to its first term. Provided that $y_{\max}/t$ is not too high, accuracy of the resulting spring constant expression will not degrade significantly compared to its initial form.

In the literature, effective spring constant of a fixed-fixed type beam with full load-span is commonly reported as [36, 78, 113, 114]:

$$\frac{\widehat{k}_q}{w} = \frac{32E'}{\left(\frac{L}{t}\right)^3} + \frac{8}{\left(\frac{L}{t}\right)} \sigma_0(1-\nu) \tag{3.57}$$

which resembles Equation (3.56b) for $\alpha = 1$, but apparently lacks a non-linear stretching term. The absence of a non-linear stretching term in the effective spring constant $\widehat{k}_q$ is compensated in [80] by incorporating the latter axial force component calculated from an assumed sinusoidal deflection profile (see §3.2.4.1) and it is arrived at

$$\frac{\widehat{k}_q}{w} \approx \frac{32E'}{\left(\frac{L}{t}\right)^3} + \frac{2\pi^2 E'}{\left(\frac{L}{t}\right)^3} \left(\frac{y_{\text{max}}}{t}\right)^2 + \frac{8}{\left(\frac{L}{t}\right)} \sigma_0(1-\nu) \tag{3.58}$$

which is remarked to be a large-argument spring constant expression. For comparison purposes, Equation (3.56b) is re-written for $\alpha = 1$ below:

$$\frac{k_q}{w} \approx \frac{16E'}{\left(\frac{L}{t}\right)^3} \left[1 + \frac{u}{3}\right] + \frac{64}{3} \frac{E'}{\left(\frac{L}{t}\right)^3} \left(\frac{y_{\text{max}}}{t}\right)^2 + \frac{8}{\left(\frac{L}{t}\right)} \sigma_0(1-\nu) \tag{3.59}$$

Upon an examination of Equations (3.58) and (3.59), it is noted that two large-argument spring constant expressions are similar in form. In particular, $k_{q,\sigma}$ components are identical and $k_{q,nl}$ terms differ only in the corresponding scalar multiplier ($2\pi^2$ versus 64/3, with -7.5% error). The difference between $k_{q,b}$ terms, however, can be readily spotted: Bending-related stiffness component of Equation (3.59) appears to be *raised* by a factor of $\frac{1+u/3}{2} \geq 3$ compared to the corresponding term in Equation (3.58) via the contribution of membrane stiffness mechanisms. In the light of these observations, it can be stated that Equation (3.58) *underestimates* the large-argument effective spring constant due to failure of the assumed deflection profile to accurately represent the actual one.

3.2.4.3   Accuracy Assessment of Small and Large-Argument Forms of k_q

During the derivations for small and large-argument forms of k_q, accuracies for the utilized series expansions were indicated individually; but combined accuracies of the obtained forms were not investigated. To ensure that provided extreme-argument approximations indeed satisfy intended accuracy levels, numerical error analyses are carried out over corresponding valid parameter ranges. A brief description of the adopted error analysis method and obtained numerical results are provided in this section.

Accuracy of the extreme-argument k_q forms are assessed by considering the fractional error between exact and approximated k_q values, which is defined as:

$$\text{Error} = \frac{k_{q,\text{app}} - k_{q,\text{exact}}}{k_{q,\text{exact}}} \tag{3.60}$$

In order to facilitate the on-going analysis, dimension of parameter domain is reduced to a minimum by introduction of the following normalized quantities:

$$K_q \triangleq \frac{k_q \left(\frac{L}{t}\right)^3}{wE'} \tag{3.61a}$$

$$Y_t \triangleq \frac{y_{\max}}{t} \tag{3.61b}$$

$$\Sigma_0 \triangleq \left(\frac{L}{t}\right)^2 \frac{\sigma_0(1-v)}{E'} \tag{3.61c}$$

Using the dimensionless quantities provided in Equation (3.61), axial relation (Equation (3.37a)) and exact k_q expression (Equation (3.42)) are transformed to

$$K_q = \frac{32\alpha}{\overline{\zeta}(u,\alpha)} \tag{3.62a}$$

$$u^2 = Y_t{}^2 \Psi(u,\alpha) + 3\Sigma_0 \tag{3.62b}$$

A similar normalization is also applied to extreme argument spring constant forms and relevant expressions are re-written as,

$$K_{q,\text{small}} = \left[32 + \frac{4096}{175}Y_t{}^2 + \frac{48}{5}\Sigma_0\right] q_0(\alpha) \tag{3.63a}$$

$$u^2 \approx Y_t{}^2 p_0(\alpha) + 3\Sigma_0 \tag{3.63b}$$

$$K_{q,\text{large}} = \frac{16}{3}\frac{(2+\alpha)}{(2-\alpha)^3 \alpha}\left[1 + \frac{(2-\alpha)\alpha}{2+\alpha}u\right] + \frac{64}{3}\frac{(3-2\alpha)}{(2-\alpha)^3}Y_t{}^2 + \frac{8}{(2-\alpha)}\Sigma_0 \tag{3.64a}$$

$$u^2 \approx 8\frac{(3-2\alpha)}{(2-a)^2}Y_t{}^2 + 3\Sigma_0 \tag{3.64b}$$

It is noted from Equations (3.62)-(3.64) that only three parameters needs to be specified for numerical evaluation of the normalized spring constants: α and two parameters out of u, Y_t and Σ_0 (as the latter three are not independent). Keeping these information in mind, error analysis may then be outlined as follows:

64

i. A u value is picked.

ii. An α value is selected.

iii. Using the specified (u, α) pair, $K_{q,\text{exact}}$ is calculated.

iv. Y_t is swept in a predetermined range and corresponding Σ_0 is determined using Equation (3.62b) for the specified (u, α) pair.

v. Employing (Y_t, Σ_0) pairs, $K_{q,\text{small}}$ and $K_{q,\text{large}}$ are computed.

vi. Fractional error is evaluated between $K_{q,\text{app}}$ and $K_{q,\text{exact}}$.

vii. Maximum absolute fractional error is found and stored for the particular α.

viii. (ii-vii) is repeated for a range of α values.

ix. (i-viii) is repeated for a range of u values.

Obtained numerical results from a basic implementation of the described error analysis are presented in Figure 3.7 and Figure 3.8 for small and large-argument forms of k_q respectively.

It is observed from Figure 3.7 that derived small-argument forms of spring constant indeed satisfy the desired accuracy level within previously prescribed parameter ranges: At tensile axial state, accuracy of the proposed formulation is better than 2% for $0 \leq u \leq 4$, $0.25 \leq \alpha \leq 1$ and $Y_t \leq 1.5$; whereas at compressive axial state, identical expression provides an error less than 1.8% for $0 \leq u \leq 2.5$, $0.25 \leq \alpha \leq 1$ and $Y_t \leq 1.5$. It is moreover noted for both axial states that, error rapidly increases as α tends to values lower than 0.25, a result which is related to associated degradation of $\Psi(u, \alpha)$ approximation. Moreover, although not shown in these plots, accuracy of the small-argument forms grows worse when Y_t is increased beyond 1.5: Since the function $\Psi(u, \alpha)$ is scaled by Y_t^2 in the axial relation, an increase in Y_t^2 will render the error in the relevant approximation more prominent, especially for low residual stress levels. The latter behavior explains the additional range specification on Y_t.

An inspection of Figure 3.8 shows that accuracy of the derived large-argument form of
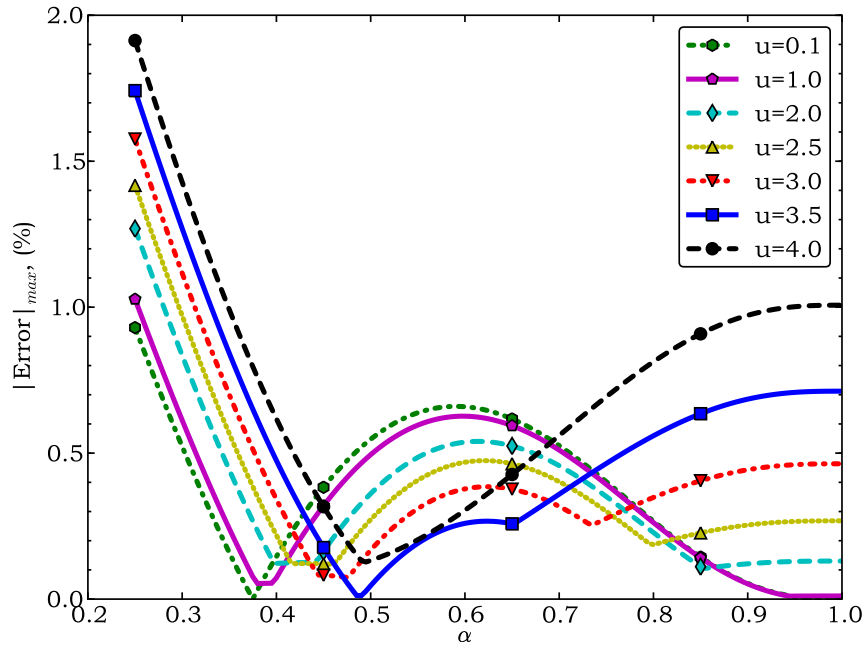
(a) Small-argument (tensile)
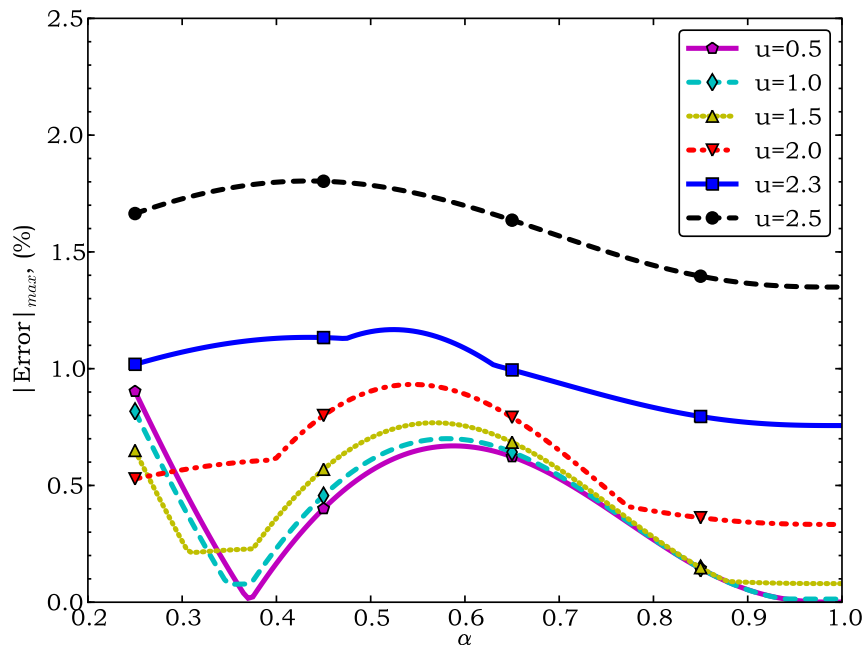
(b) Small-argument (compressive)

Figure 3.7: *Numerical error analysis results for small-argument form of k_q ($0.25 \leq \alpha \leq 1$, $0 \leq Y_t \leq 1.5$).*
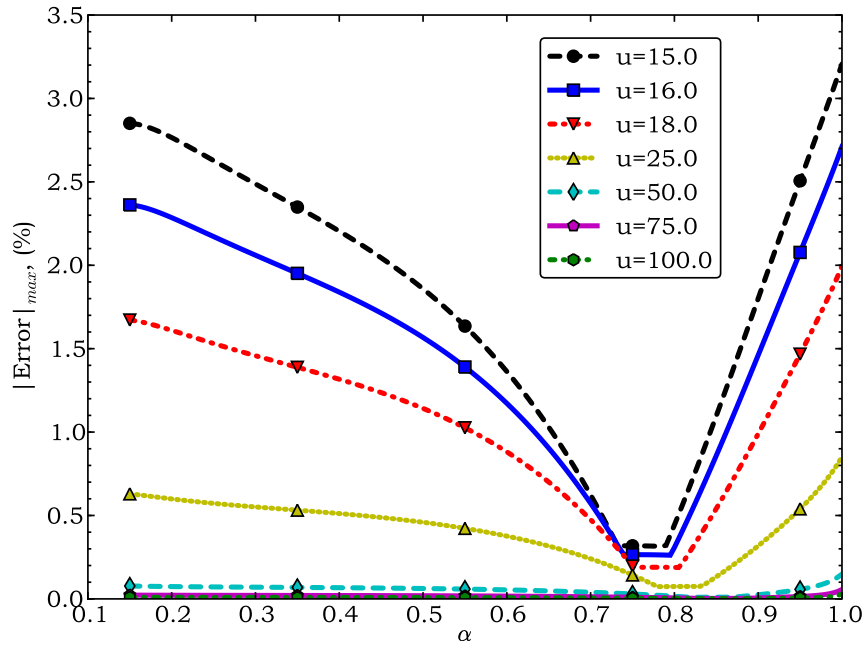
Figure 3.8: *Numerical error analysis results for large-argument form of k_q (0.15 ≤ α ≤ 1, 0 ≤ Y_t ≤ 5).*

spring constant deviates slightly from the intended one within previously set parameter limits: For $u \geq 15$, $0.15 \leq \alpha \leq 1$ and $Y_t \leq 5$, maximum absolute error is found as 3.2%, which is somewhat higher compared to the aimed 2% value. Nevertheless, targeted 2% accuracy can still be achieved by shifting the lower u bound from 15 to 18. Recall that mentioned accuracy deterioration at the lower u limit was previously anticipated in §3.2.4.2 when an additional approximation was made in order to arrive at a closed-form expression. Similar with the small-argument case, increasing Y_t above 5 causes a significant rise of the fractional error and due to this trend, the additional constraint of $Y_t \leq 5$ is imposed for the proposed large-argument form.

Before leaving the subject, it would be informative to investigate the accuracy of the effective spring constant expressions reported in the literature. Two of such expressions were noted earlier in §3.2.4.1 and §3.2.4.2, which were recognized to be small and large-argument forms respectively. Results obtained from an application of the numerical error analysis procedure to those forms are depicted in Figure 3.9. It is observed from Figure 3.9(a) that reported small-argument form displays a maximum error of 2.0% and 5.0%

at tensile and compressive axial states respectively within previously established parameter ranges for $\alpha = 1$. Referring back to Figure 3.7, corresponding maximum errors for the derived small-argument forms are read as 1.0% and 1.4% at tensile and compressive axial states respectively, apparently showing an accuracy improvement over the reported ones. A more dramatic improvement is noticed upon a comparison of Figure 3.9(b) with Figure 3.8: Over the parameter space of $u \geq 18$, $Y_t \leq 5$, $\alpha = 1$; reported large-argument form yields an error of about 10% whereas derived one exhibits a maximum error of 2%. It is moreover found out that for the reported large-argument form to attain an accuracy of 3% (2%), lower limit of u must be shifted to 60 (90); an attribute demonstrating once again superior accuracy of the derived large-argument spring constant form.

In addition to analyzed small and large-argument spring constant forms reported in the literature, it would be helpful to examine one more. It was pointed out earlier that both reported extreme-argument forms utilize the approximation $\Psi(u, \alpha) \approx \frac{3\pi^2}{4}$ in order to reduce analytical complexity of the problem. This approximation might be employed in a general context to explicitly calculate u from Equation (3.62b) and hence to arrive at a general closed-form solution for the effective spring constant, as proposed in [80]. It is known, however, from §3.2.3 that the function $\Psi(u, \alpha)$ exhibits weak dependencies on u and α so that some error is anticipated beforehand for such an approach. In order to quantify this error, a similar numerical error analysis is applied to the latter approximated form. Obtained results are presented in Figure 3.10.

Figure 3.10 shows that the assumption $\Psi(u, \alpha) \approx \frac{3\pi^2}{4}$ indeed causes the approximate closed-form effective spring constant to deviate from the exact one; but associated error remains below reasonable bounds over a wide parameter range. In particular, the error grows appreciably for high Y_t values, especially where Σ_0 is relatively low. Such a trend can be explained by the scaling effect of Y_t on $\Psi(u, \alpha)$ and reduced masking of the relevant error with lower Σ_0. Upon a comparison of Figures 3.10(a)-3.10(b), one moreover finds that error increases with decreasing α; a behavior which can be attributed to increased sensitivity of $\Psi(u, \alpha)$ for lower α values. In the light of these observations, it is realized that accuracy of the approximate closed-form solution is worst for the parameter zone in which α, Σ_0 are low and Y_t is high: In such a zone, relevant error might reach up to 10% as evidenced from Figure 3.10(b).
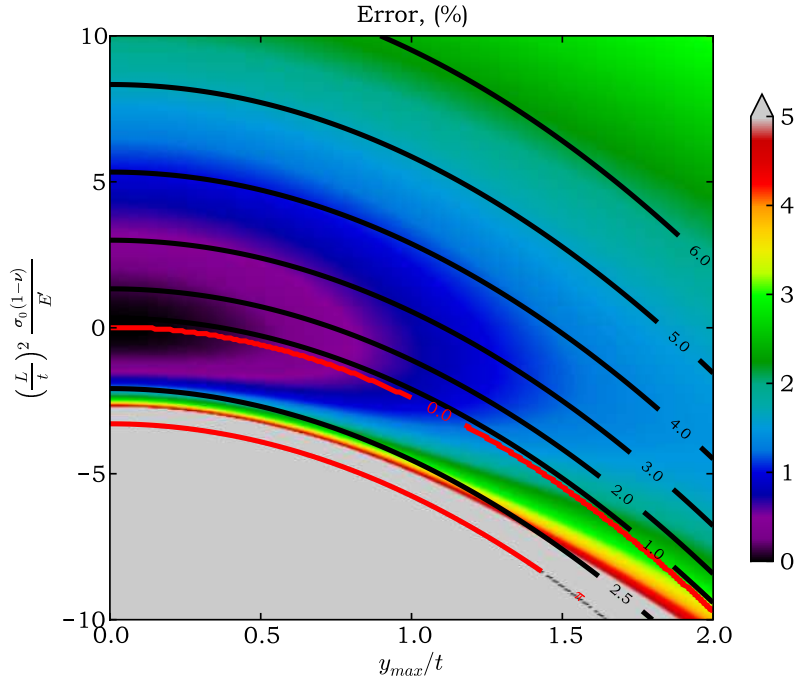
(a) Small-argument: $\widehat{K}_{q,\text{small}} = 32 + \frac{12\pi^2}{5}Y_t^2 + \frac{48}{5}\Sigma_0$
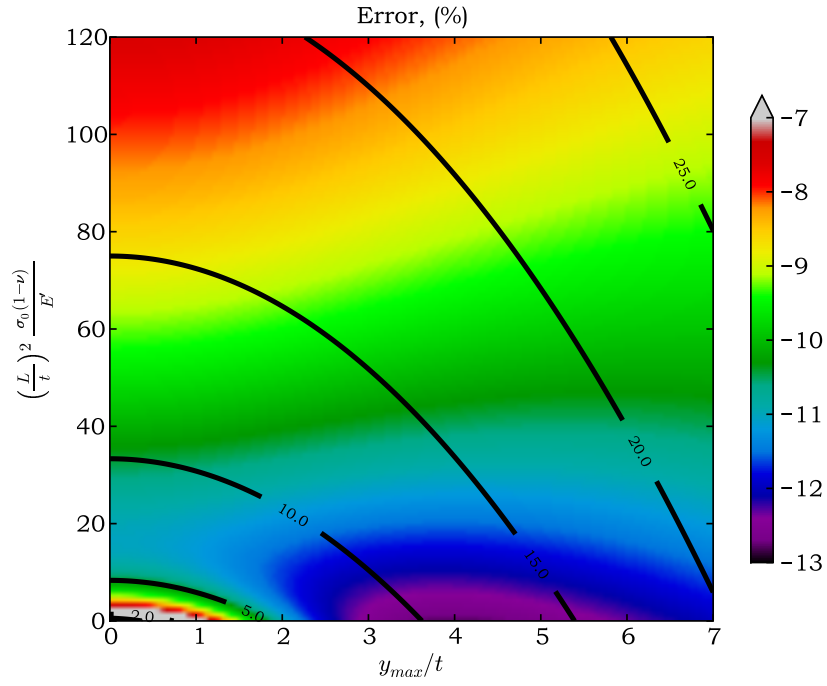
(b) Large-argument: $\widehat{K}_{q,\text{large}} = 32 + 2\pi^2 Y_t^2 + 8\Sigma_0$

Figure 3.9: *Numerical error analysis results for small and large-argument forms of effective spring constant reported in the literature. Contours of u are overlaid on the error plots.* $Y_t \leq 7$, $0 \leq \Sigma_0 \leq 120$, $\alpha = 1.00$.
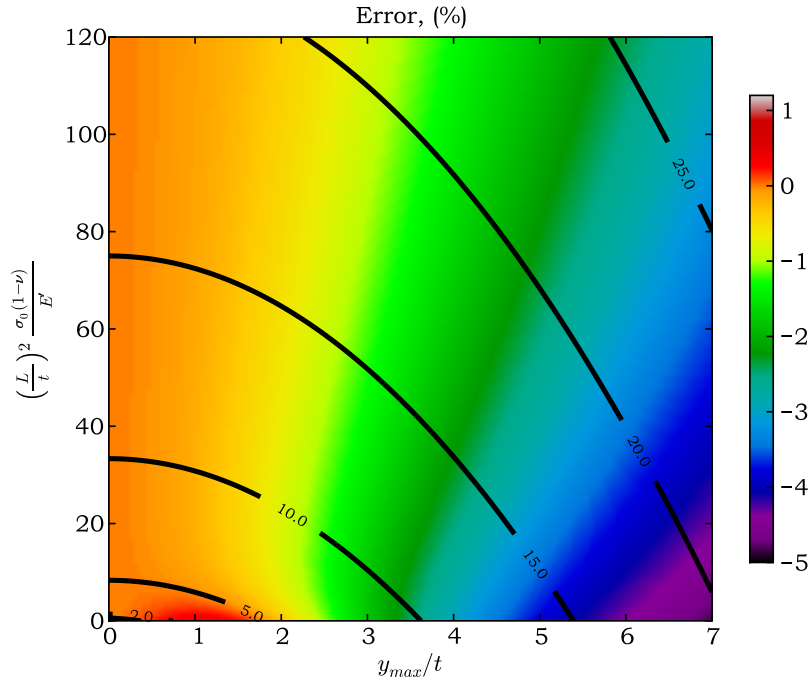
(a) $\alpha = 1.00$
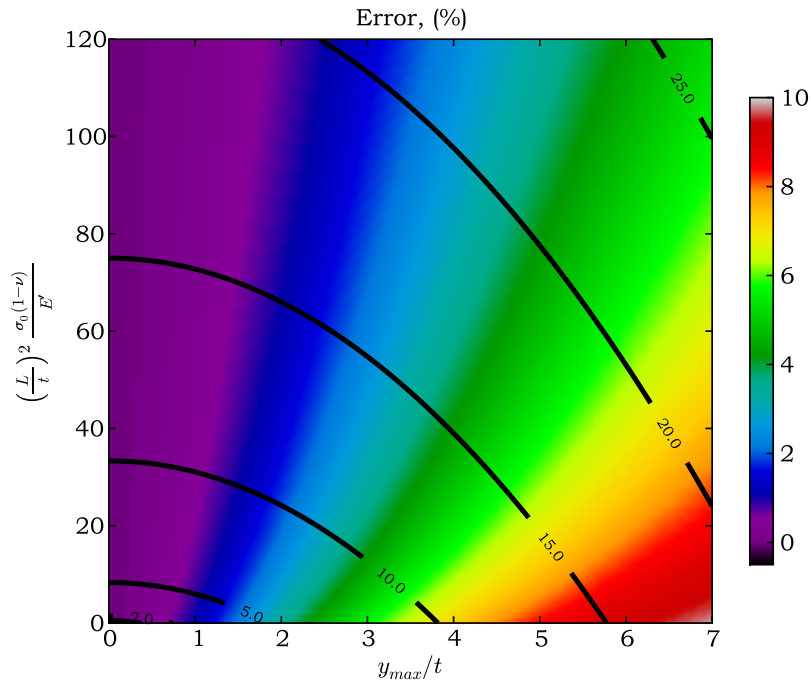
(b) $\alpha = 0.25$

Figure 3.10: *Numerical error analysis results for the approximate closed-form effective spring constant expression obtained by assuming $\Psi(u, \alpha) \approx \frac{3\pi^2}{4}$. Contours of u are overlaid on the error plots. $Y_t \leq 7$, $0 \leq \Sigma_0 \leq 120$, $\alpha = 1.00, 0.25$.*
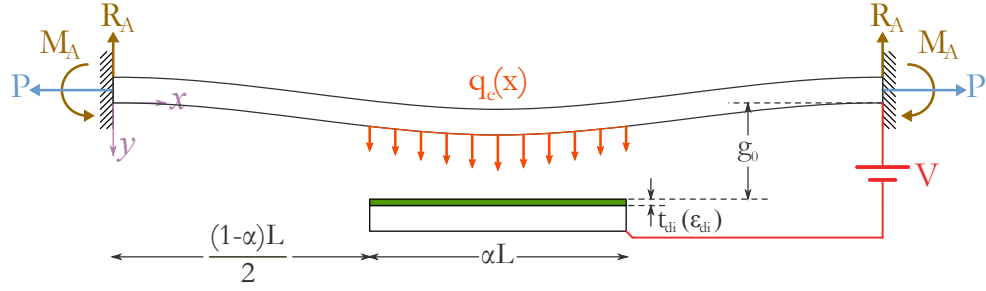
Figure 3.11: *Electrostatic actuation problem illustrated.*

A collective summary of the derived effective spring constant expressions, their valid parameter ranges and associated error analysis results is provided in Table 3.2 for reference purposes.

3.3 Distributed Mechanical Problem for Electrostatic Actuation

Previous section demonstrated an example of how mechanical analyses can be carried out for a relatively simple type of transverse load, and established useful analytical results such as deflection profile and spring constant expressions. Another wide class of transverse loading occurs for electrostatic actuation systems, which is treated next within the scope of this work.

3.3.1 Derivation of the Governing Integro-Differential Equation

Figure 3.11 illustrates the configuration for the electrostatic actuation problem of fixed-fixed type beams. The system is actuated by applying a DC potential across the beam and an electrode located underneath, which are separated with an air-gap spacing of g_0. The bottom electrode spans α fraction of the beam length and it is positioned symmetrically with respect to the beam. Moreover, a dielectric layer of thickness t_{di} and relative permittivity of ε_{di} covers the top of the bottom electrode for reasons which will become apparent in subsequent sections.

To analyze the presented system, one begins with the beam equation stated in §3.2.1.1

Table 3.2: *A summary of the derived effective spring constant expressions, valid parameter ranges and associated error analysis results.*

FORM OF k_q	DESCRIPTION	EXPRESSIONS
EXACT (TENSILE)	EXPRESSION FOR K_q	$K_q = \dfrac{32\alpha}{\overline{\zeta}(u,\alpha)}$
	EXPRESSION FOR u	$u^2 = \mathrm{Y_t}^2\,\Psi(u,\alpha) + 3\Sigma_0$
	VALIDITY RANGE	$u \geq 0,\ 0 < \alpha \leq 1,\ \Sigma_0 \geq \Sigma_{0,t}$
EXACT (COMPRESSIVE)	EXPRESSION FOR K_q	$K_q = \dfrac{32\alpha}{\overline{\zeta}_c(u,\alpha)}$
	EXPRESSION FOR u	$-u^2 = \mathrm{Y_t}^2\,\Psi_c(u,\alpha) + 3\Sigma_0$
	VALIDITY RANGE	$0 \leq u < \pi,\ 0 < \alpha \leq 1,\ \Sigma_0 < \Sigma_{0,t}$
SMALL ARGUMENT (TENSILE)	EXPRESSION FOR K_q	$K_q \approx \left[32 + \tfrac{4096}{175}\mathrm{Y_t}^2 + \tfrac{48}{5}\Sigma_0\right] q_0(\alpha)$
	EXPRESSION FOR u	$u^2 \approx \mathrm{Y_t}^2\,p_0(\alpha) + 3\Sigma_0$
	VALIDITY RANGE	$0 \leq u \leq 4,\ 0.25 \leq \alpha \leq 1,\ \mathrm{Y_t} \leq 1.5,\ \Sigma_0 \geq \Sigma_{0,t}$
	ACCURACY	$\leq 2.0\%$
SMALL ARGUMENT (COMPRESSIVE)	EXPRESSION FOR K_q	$K_q \approx \left[32 + \tfrac{4096}{175}\mathrm{Y_t}^2 + \tfrac{48}{5}\Sigma_0\right] q_0(\alpha)$
	EXPRESSION FOR u	$-u^2 \approx \mathrm{Y_t}^2\,p_0(\alpha) + 3\Sigma_0$
	VALIDITY RANGE	$0 \leq u \leq 2.5,\ 0.25 \leq \alpha \leq 1,\ \mathrm{Y_t} \leq 1.5,\ \Sigma_0 < \Sigma_{0,t}$
	ACCURACY	$\leq 1.8\%$
LARGE ARGUMENT (TENSILE)	EXPRESSION FOR K_q	$K_q \approx \dfrac{16}{3}\dfrac{(2+\alpha)}{(2-\alpha)^3\alpha}\left[1 + \dfrac{(2-\alpha)\alpha}{2+\alpha}u\right]$ $+ \dfrac{64}{3}\dfrac{(3-2\alpha)}{(2-\alpha)^3}\mathrm{Y_t}^2 + \dfrac{8}{(2-\alpha)}\Sigma_0$
	EXPRESSION FOR u	$u^2 \approx 8\dfrac{(3-2\alpha)}{(2-\alpha)^2}\mathrm{Y_t}^2 + 3\Sigma_0$
	VALIDITY RANGE	$u \geq 18,\ 0.15 \leq \alpha \leq 1,\ \mathrm{Y_t} \leq 5,\ \Sigma_0 \geq \Sigma_{0,t}$
	ACCURACY	$\leq 2.0\%$

$K_q = \dfrac{k_q\left(\frac{L}{t}\right)^3}{wE'}$, $\mathrm{Y_t} = \dfrac{y_{max}}{t}$, $\Sigma_0 = \left(\dfrac{L}{\xi}\right)^2\dfrac{\sigma_0(1-\nu)}{E'}$, $\Sigma_{0,t} = -\dfrac{p_0(\alpha)}{3}\mathrm{Y_t}^2$, $\alpha = \dfrac{W}{L}$

$p_0(\alpha) = \dfrac{16}{35}\dfrac{21\alpha^6 - 96\alpha^5 + 133\alpha^4 - 105\alpha^2 + 63}{(\alpha^3 - 2\alpha^2 + 2)^2}$, $q_0(\alpha) = \dfrac{1}{\alpha^3 - 2\alpha^2 + 2}$, $\overline{\zeta}(u,\alpha) = \alpha/q_0(\alpha)\zeta(u,\alpha)$

$\Psi(u,\alpha) = 442368\,h(u,\alpha)/\overline{\zeta}^2(u,\alpha)$

See Equations (3.21)-(3.32) for definitions of $\zeta(u,\alpha)$ and $h(u,\alpha)$.

for a general distributed transverse load $q(x)$:

$$\frac{d^4 y}{dx^4} - \frac{P}{E'I}\frac{d^2 y}{dx^2} = \frac{q(x)}{E'I} \tag{3.65}$$

Recall moreover from §3.2.3 that P is related to the problem variables via the axial relation:

$$\frac{P}{A} = \frac{E'}{2L}\int_0^L \left(\frac{dy}{dx'}\right)^2 dx' + \sigma_0(1 - v) \tag{3.66}$$

For the electrostatic actuation problem at hand, $q(x)$ is given by,

$$q(x) = \begin{cases} q_e(x) & \text{if} \quad \frac{(1-\alpha)L}{2} \leq x \leq \frac{1}{2} \\ 0 & \text{if} \quad 0 \leq x \leq \frac{(1-\alpha)L}{2} \end{cases} \tag{3.67}$$

The transverse distributed load $q_e(x)$ can be evaluated from the principle of virtual work, which expresses the electrostatic force in $+y$ direction in terms of the potential energy under constant potential as [115]:

$$\begin{aligned} F_e &= \frac{\partial U}{\partial y} \\ &= \frac{\partial}{\partial y}\left(\frac{1}{2}CV^2\right) \\ &= \frac{1}{2}V^2\frac{\partial C}{\partial y} \end{aligned} \tag{3.68}$$

where C, F_e and $U = \frac{1}{2}CV^2$ stand for inter-electrode capacitance, electrostatic force and potential energy respectively. Moreover, $q_e(x)$ and F_e are linked with

$$\begin{aligned} q_e(x) &= \frac{\partial F_e}{\partial x} \\ &= \frac{1}{2}V^2\frac{\partial^2 C}{\partial x \partial y} \end{aligned} \tag{3.69}$$

Neglecting fringing electric-field components, incremental inter-electrode capacitance may be written as,

$$\begin{aligned} \delta C &= \left[\frac{1}{\delta C_{air}} + \frac{1}{\delta C_{di}}\right]^{-1} \\ &= \left[\left(\frac{\varepsilon_0 w \delta x}{g_0 - y(x)}\right)^{-1} + \left(\frac{\varepsilon_0 \varepsilon_{di} w \delta x}{t_{di}}\right)^{-1}\right]^{-1} \\ &= \frac{\varepsilon_0 w \delta x}{g_0 + t_{di}/\varepsilon_{di} - y(x)} \end{aligned} \tag{3.70}$$

In the limit as $\delta x \to 0$, thus

$$\frac{\partial C}{\partial x} = \frac{\varepsilon_0 w}{g_0 + t_{\mathrm{di}}/\varepsilon_{\mathrm{di}} - y(x)} \tag{3.71}$$

Using Equation (3.71), Equation (3.69) becomes:

$$\begin{aligned} q_{\mathrm{e}}(x) &= \frac{1}{2} V^2 \frac{\partial}{\partial y} \frac{\partial C}{\partial x} \\ &= \frac{\varepsilon_0 w\, V^2}{2 \left[g_0 + t_{\mathrm{di}}/\varepsilon_{\mathrm{di}} - y(x) \right]^2} \end{aligned} \tag{3.72}$$

Substitution of Equation (3.72) into Equation (3.65) then yields,

$$\frac{\mathrm{d}^4 y}{\mathrm{d}x^4} - \frac{P}{E'I} \frac{\mathrm{d}^2 y}{\mathrm{d}x^2} = \begin{cases} \frac{\varepsilon_0 w\, V^2}{2E'I \left[g_0 + t_{\mathrm{di}}/\varepsilon_{\mathrm{di}} - y(x) \right]^2} & \text{if} \quad \frac{(1-\alpha)L}{2} \leq x \leq \frac{L}{2} \\ 0 & \text{if} \quad 0 \leq x \leq \frac{(1-\alpha)L}{2} \end{cases} \tag{3.73}$$

which is recognized to be a *non-linear* 4th order ODE for the loading span of the beam. Taking into account the dependence of P on the integral of squared beam slope from Equation (3.66), Equation (3.73) can actually be regarded as a non-linear integro-differential equation, which unfortunately cannot be solved through analytical means.

3.3.2 Normalization of the Governing Integro-Differential Equation

In order to reduce the number of parameters involved and hence to provide ease in the subsequent analysis steps, it is preferred to apply a normalization to Equations (3.66) and (3.73) along the guidelines of [82]. For this purpose, two dimensionless quantities are introduced:

$$\tilde{x} = \frac{x}{L} \tag{3.74a}$$

$$\tilde{y} = \frac{y}{g_0} \tag{3.74b}$$

Derivatives with respect to position x can be easily re-expressed in terms of the normalized position $\tilde{x}$ using the chain rule:

$$\frac{\partial}{\partial x} = \frac{\partial}{\partial \tilde{x}} \frac{\partial \tilde{x}}{\partial x} = \frac{1}{L} \frac{\partial}{\partial \tilde{x}}$$

which can be generalized to yield

$$\frac{\partial^n}{\partial x^n} = \frac{1}{L^n} \frac{\partial^n}{\partial \tilde{x}^n} \tag{3.75}$$

74

Employing Equations (3.74) and (3.75), Equation (3.73) can be transformed to,

$$\frac{g_0}{L^4}\frac{d^4\tilde{y}}{d\tilde{x}^4} - \frac{Pg_0}{E'IL^2}\frac{d^2\tilde{y}}{d\tilde{x}^2} = \begin{cases} \dfrac{\varepsilon_0 w\, V^2}{2E'Ig_0^2\left[1+\frac{t_{di}}{g_0\,\varepsilon_{di}}-\tilde{y}\right]^2} & \text{if } \frac{1-\alpha}{2} \le \tilde{x} \le \frac{1}{2} \\[2ex] 0 & \text{if } 0 \le \tilde{x} \le \frac{1-\alpha}{2} \end{cases} \tag{3.76}$$

which can be manipulated to obtain

$$\frac{d^4\tilde{y}}{d\tilde{x}^4} - 4u^2\frac{d^2\tilde{y}}{d\tilde{x}^2} = \begin{cases} \dfrac{\tilde{V}^2}{[1+\gamma-\tilde{y}]^2} & \text{if } \frac{1-\alpha}{2} \le \tilde{x} \le \frac{1}{2} \\[2ex] 0 & \text{if } 0 \le \tilde{x} \le \frac{1-\alpha}{2} \end{cases} \tag{3.77}$$

where

$$u = \frac{L}{2}\sqrt{\frac{P}{E'I}} = \sqrt{\frac{3PL^2}{E'wt^3}} \tag{3.78a}$$

$$\tilde{V} = \sqrt{\frac{\varepsilon_0 wL^4}{2g_0^3E'I}}\,V = \sqrt{\frac{6\varepsilon_0 L^4}{g_0^3 t^3 E'}}\,V \tag{3.78b}$$

$$\gamma = \frac{t_{di}}{g_0\,\varepsilon_{di}} \tag{3.78c}$$

A similar normalization can be applied to Equation (3.66) as follows. Employing Equation (3.78a), P can be expressed in terms of u to yield,

$$\frac{E't^2}{3L^2}u^2 = \frac{E'}{2L}\int_0^L \left(\frac{dy}{dx'}\right)^2 dx' + \sigma_0(1-v) \tag{3.79}$$

The integrand can be re-expressed in terms of normalized quantities through change of the integration variable by letting $\tilde{x}' = \frac{x'}{L}$ and by using Equation (3.74b);

$$\int_0^L \left(\frac{dy}{dx'}\right)^2 dx' = \int_0^1 \left(\frac{d(g_0\tilde{y})}{d\tilde{x}'}\frac{d\tilde{x}'}{dx'}\right)^2 (L\,d\tilde{x}')$$

$$= \frac{2g_0^2}{L}\int_0^{\frac{1}{2}}\left(\frac{d\tilde{y}}{d\tilde{x}'}\right)^2 d\tilde{x}' \tag{3.80}$$

where symmetry of the configuration is utilized in the last step. Substituting Equation (3.80) into Equation (3.79) and performing subsequent manipulation yields,

$$u^2 = 3\left(\frac{g_0}{t}\right)^2 \int_0^{\frac{1}{2}}\left(\frac{d\tilde{y}}{d\tilde{x}'}\right)^2 d\tilde{x}' + 3\Sigma_0 \tag{3.81a}$$

with

$$\Sigma_0 = \left(\frac{L}{t}\right)^2\frac{\sigma_0(1-v)}{E'} \tag{3.81b}$$

Notice that Equation (3.81) is similar in form to Equation (3.37a) formulated in §3.2.3. In particular, letting $\tilde{y} = \frac{y_{max}}{g_0}\sin(\pi\tilde{x})$ results in the identical expression with $\Psi(u,\alpha) \approx \frac{3\pi^2}{4}$.

3.3.3 Boundary Conditions and Continuity Relations

It is realized from Figure (3.11) that unless the electrostatic load $q_e(x)$ is not applied along the entire beam span; overall distributed load $q(x)$ will be a piecewise discontinuous function, taking on the value of zero outside the loading region. As it can be recalled from §sobek1, deflection solution can be expressed in an analytical form for this latter region with:

$$\tilde{y}_I(\tilde{x}) = A \cosh(2u\tilde{x}) + B \sinh(2u\tilde{x}) + C\tilde{x} + D \tag{3.82}$$

where A, B, C and D are four arbitrary constants yet to be found. In order to determine those constants unambiguously, a total of four equations are required two of which are obtained from the boundary conditions at $\tilde{x} = 0$. Setting deflection and beam slope at the clamped end to zero yields,

$$\tilde{y}_I(0) = 0 \quad \Rightarrow \quad D = -A \tag{3.83a}$$

$$\tilde{y}_I'(0) = 0 \quad \Rightarrow \quad C = -2uB \tag{3.83b}$$

which helps to re-express Equation (3.82) as

$$\tilde{y}_I(\tilde{x}) = A \left[\cosh(2u\tilde{x}) - 1\right] + B \left[\sinh(2u\tilde{x}) - 2u\tilde{x}\right] \tag{3.84}$$

In order to calculate remaining coefficients A and B, two additional equations are required. For this purpose, *continuity relations* across the boundary $\tilde{x} = \frac{1-\alpha}{2}$ can be utilized: Notice from Equation (3.77) that the piecewise transverse loading function $q(x)$ does not incorporate any impulsive term, implying that derivatives of $\tilde{y}$ up to third order must be continuous across $\tilde{x} = \frac{1-\alpha}{2}$. In mathematical terms, these statements can be translated as,

$$\tilde{y}_{II}(\beta) = A \left[\cosh(2u\beta) - 1\right] + B \left[\sinh(2u\beta) - 2u\beta\right] \tag{3.85a}$$

$$\tilde{y}_{II}'(\beta) = 2uA \sinh(2u\beta) + 2uB \left[\cosh(2u\beta) - 1\right] \tag{3.85b}$$

$$\tilde{y}_{II}''(\beta) = 4u^2 A \cosh(2u\beta) + 4u^2 B \sinh(2u\beta) \tag{3.85c}$$

$$\tilde{y}_{II}'''(\beta) = 8u^3 A \sinh(2u\beta) + 8u^3 B \cosh(2u\beta) \tag{3.85d}$$

where the auxiliary variable $\beta = \frac{1-\alpha}{2}$ is introduced to simplify notation.

It is noted from Equation (3.85) that continuity relations yield four equations, two of which might be regarded redundant at a quick glance. However, as it can be readily noticed, LHS of those equations are actually unknown. In fact, all four of these equations will be needed through the development of the numerical solution scheme as it will be shown in the next sections.

In addition to the boundary conditions and continuity relations concerning the first problem region, additional conditions are required at $\tilde{x} = \frac{1}{2}$ in order to set a proper *symmetry boundary*. Let us attempt to derive these conditions through the use of problem symmetry. Firstly, it is elementary to state by physical reasoning that maximum beam deflection must occur at the beam center, a condition which is equivalent to,

$$y'_{\text{II}}(1/2) = 0 \tag{3.86}$$

For other non-trivial properties, it might be helpful to resort to basic beam relations [108]:

$$\frac{\text{d}S}{\text{d}x} = -q(x) \tag{3.87a}$$

$$E'I \frac{\text{d}^3 y}{\text{d}x^3} = -S(x) + P \frac{\text{d}y}{\text{d}x} \tag{3.87b}$$

with $S(x)$ denoting the shear along the beam. Using Equation (3.87a), it is easy to write

$$S(x) = -\int_0^x q(x')\text{d}x' + S(0) \tag{3.88}$$

Moreover, by inspection, beam shear at $x = 0$ is equal to the vertical reaction R_{A} (see Figure 3.11) so that

$$S(L/2) = -\int_0^{\frac{L}{2}} q(x')\text{d}x' + R_{\text{A}} \tag{3.89}$$

$$= 0$$

In other words, shear at the beam center is found to be zero due to balance of symmetric forces. Using this latter fact together with Equation (3.86), Equation (3.87b) at $x = L/2$ can be evaluated as,

$$y'''_{\text{II}}(L/2) = 0 \tag{3.90}$$

77

Table 3.3: *Boundary conditions and continuity relations for the electrostatic actuation problem.*

TYPE OF CONDITION	POSITION	EXPRESSION
CONTINUITY RELATION	$\tilde{x} = \beta = \frac{1-\alpha}{2}$	Equation (3.85)
SYMMETRY	$\tilde{x} = \frac{1}{2}$	Equation (3.86) Equation (3.90)

establishing another symmetry condition.

Table 3.3 provides a summary of the boundary conditions and continuity relations for the electrostatic actuation problem.

3.4 Numerical Solution of the Electrostatic Actuation Problem

It was pointed out earlier that Equations (3.77) and (3.81a), forming a non-linear integro-differential equation system, cannot be solved analytically. Mentioned system, however, can still be investigated using numerical techniques. In particular, it is preferred to utilize Finite Difference (FD) method in this study due to its advantages such as relatively easy formulation construction, rapid simulation and good accuracy [77, 86]. Moreover, it is preferred to increase problem complexity gradually: Firstly, electrostatic actuation problem will be analyzed without any axial effects and next, building on the gained experience, axial effects will be incorporated into the solution.

3.4.1 Finite Difference Solution of the Zero-Tension Electrostatic Actuation Problem

Complexity of the electrostatic actuation problem can be reduced significantly by ignoring the axial effects of non-linear beam stretching and residual stress. Although such a simplification calls for a dramatic degradation in accuracy; it will be helpful to investigate this basic problem in that experience gained in Finite Difference formulation, simulation techniques and results will be utilized later for the non-zero axial effect case.

78

3.4.1.1 Transformation to Zero-Tension Electrostatic Problem

The non-linear integro-differential equation (3.77) can be transformed to the simpler zero-tension problem by setting $u = 0$, which amounts to letting $\sigma_0 = 0$ and ignoring the non-linear beam stretching. Under this assignment, Equation (3.77) becomes:

$$\frac{\mathrm{d}^4 \tilde{y}}{\mathrm{d}\tilde{x}^4} = \begin{cases} \dfrac{\tilde{V}^2}{\left[1+\gamma-\tilde{y}\right]^2} & \text{if } \beta \leq \tilde{x} \leq \frac{1}{2} \\ 0 & \text{if } 0 \leq \tilde{x} \leq \beta \end{cases} \tag{3.91}$$

It is clear from Equation (3.91) that continuity relations at $\tilde{x} = \beta$ boundary must be altered as the form of the analytical solution for the load-free region is modified as;

$$y_{\mathrm{I}}(\tilde{x}) = c_3 \tilde{x}^3 + c_2 \tilde{x}^2 \tag{3.92}$$

where two of the four unknown coefficients has been eliminated by utilizing the boundary condition at $\tilde{x} = 0$. Consequently, continuity relations at $\tilde{x} = \beta$ become

$$y_{\mathrm{II}}(\beta) = c_3 \beta^3 + c_2 \beta^2 \tag{3.93a}$$

$$y'_{\mathrm{II}}(\beta) = 3c_3 \beta^2 + 2c_2 \beta \tag{3.93b}$$

$$y''_{\mathrm{II}}(\beta) = 6c_3 \beta + 2c_2 \tag{3.93c}$$

$$y'''_{\mathrm{II}}(\beta) = 6c_3 \tag{3.93d}$$

3.4.1.2 Approximate Analytical Solution

A solution obtained from a numerical technique is not necessarily the correct one in some cases. In general, one has to validate the reliability of such numerical solutions to be able to *trust* in them. An analytical solution which is valid under specific conditions constitutes a typical validation means for this purpose. As it will be shown shortly, an approximate analytical solution is actually available for the zero-tension electrostatic actuation problem and this solution will aid in later steps to justify the correctness of associated numerical ones.

Remarked approximate analytical solution for the zero-tension electrostatic actuation problem can be obtained by expressing the source term of Equation (3.91) as a Maclaurin series:

$$\frac{\tilde{V}^2}{\left[1+\gamma-\tilde{y}\right]^2} = \frac{\tilde{V}^2}{(1+\gamma)^2} + \frac{2\tilde{V}^2}{(1+\gamma)^3}\tilde{y} + \mathrm{O}(\tilde{y}^2) \tag{3.94}$$

Equation (3.94) can be truncated after its second term for $\tilde{y} \leq \frac{1+\gamma}{10}$ with a corresponding worst case error of -2.8%. Substituting this approximation into Equation (3.91) yields,

$$\frac{\mathrm{d}^4 \tilde{y}_{\mathrm{II}}}{\mathrm{d}\tilde{x}^4} = \frac{\tilde{V}^2}{(1+\gamma)^2} + \frac{2\tilde{V}^2}{(1+\gamma)^3} \tilde{y}_{\mathrm{II}}, \quad \beta \leq \tilde{x} \leq \frac{1}{2}$$

which has an analytical solution of

$$\tilde{y}_{\mathrm{II}}(\tilde{x}) = D_0 \cos(\kappa\tilde{x}) + D_1 \sin(\kappa\tilde{x}) + D_2 \cosh(\kappa\tilde{x}) + D_3 \sinh(\kappa\tilde{x}) - \frac{1+\gamma}{2} \qquad (3.95a)$$

with

$$\kappa = \left[\frac{2\tilde{V}^2}{(1+\gamma)^3} \right]^{\frac{1}{4}} \qquad (3.95b)$$

The coefficients D_i ($i =$1, 2, 3, 4 for $\tilde{y}_{\mathrm{II}}$) and c_j ($j =$2, 3 for $\tilde{y}_{\mathrm{I}}$) can be solved simultaneously from the continuity relations (3.93) and the boundary conditions (3.86)-(3.90). Once these unknown coefficients are determined, it is straightforward to obtain an expression for the complete beam profile. Such a procedure, however, is omitted here due to significant complexity of the resulting formulation and it is preferred to consider maximum beam deflection $\tilde{y}_{\mathrm{max}}$ only. Upon evaluating $\tilde{y}_{\mathrm{II}}(1/2)$, desired result is found as,

$$\frac{\tilde{y}_{\mathrm{max}}}{1+\gamma} = -\frac{1}{2} + \frac{(6-3\mu^2)\sin(\upsilon) + (6+3\mu^2)\sinh(\upsilon) + 6\mu\left[\cos(\upsilon) + \cosh(\upsilon)\right]}{\mathrm{Den}(\mu,\upsilon)} \qquad (3.96a)$$

where

$$\mathrm{Den}(\mu,\upsilon) = \sin(\upsilon)\left[(12 - \mu^4 - 12\mu^2)\cosh(\upsilon) - 8\mu^3 \sinh(\upsilon)\right]$$
$$+ \cos(\upsilon)\left[(12 - \mu^4 + 12\mu^2)\sinh(\upsilon) + 24\mu\cosh(\upsilon)\right] \qquad (3.96b)$$

$$\mu \triangleq \beta\kappa \qquad (3.96c)$$

$$\upsilon \triangleq \frac{\alpha}{2}\kappa \qquad (3.96d)$$

Equation (3.96) is expected to be valid for deflections up to a tenth of the initial air-gap, a requirement dictated by Maclaurin series expansion of the non-linear load term. Consequently, comparisons with the numerical solutions must be made in $\tilde{y}_{\mathrm{max}} \leq \frac{1+\gamma}{10}$ range.

3.4.1.3 Finite Difference Formulation

In order to apply the Finite Difference technique to the zero-tension electrostatic actuation problem, firstly a discretization along the beam is required. A uniform discretization scheme consisting of N equi-spaced points is illustrated in Figure 3.12. It can be shown through method of undetermined coefficients that derivatives of $\tilde{y}(\tilde{x})$ can be approximated in terms of the discretized (nodal) deflections $\tilde{y}_i$ as [81, 116]:

$$\tilde{y}_i' = \frac{\tilde{y}_{i-2} - 8\tilde{y}_{i-1} + 8\tilde{y}_{i+1} - \tilde{y}_{i+2}}{12h} + O(h^4) \tag{3.97a}$$

$$\tilde{y}_i'' = \frac{-\tilde{y}_{i-2} + 16\tilde{y}_{i-1} - 30\tilde{y}_i + 16\tilde{y}_{i+1} - \tilde{y}_{i+2}}{12h^2} + O(h^4) \tag{3.97b}$$

$$\tilde{y}_i''' = \frac{-\tilde{y}_{i-2} + 2\tilde{y}_{i-1} - 2\tilde{y}_{i+1} + \tilde{y}_{i+2}}{2h^3} + O(h^2) \tag{3.97c}$$

$$\tilde{y}_i^{(iv)} = \frac{\tilde{y}_{i-2} - 4\tilde{y}_{i-1} + 6\tilde{y}_i - 4\tilde{y}_{i+1} + \tilde{y}_{i+2}}{h^4} + O(h^2) \tag{3.97d}$$

where h is the grid spacing given by

$$h = \frac{1/2 - \beta}{N - 1} = \frac{\alpha}{2(N - 1)} \tag{3.98}$$

It is realized from Equation (3.97) that a five-point stencil is needed in order to approximate the derivatives of $\tilde{y}(\tilde{x})$ with a worst case accuracy of $O(h^2)$. Employing Equation (3.97) in Equation (3.91) gives:

$$\tilde{y}_{i-2} - 4\tilde{y}_{i-1} + 6\tilde{y}_i - 4\tilde{y}_{i+1} + \tilde{y}_{i+2} - \frac{h^4\tilde{V}^2}{\left[1 + \gamma - \tilde{y}_i\right]^2} = 0, \quad \text{if} \quad \beta \le \tilde{x} \le \frac{1}{2} \tag{3.99}$$

Let us now restrict the problem domain to the second region, i.e. $\beta \le \tilde{x} \le \frac{1}{2}$. In order to proceed so, influence of first region must be incorporated into the solution via the continuity relations (3.93). For this purpose, nodal equation (3.99) can be written at nodes $i = 0$ and $i = 1$ to yield,

$$\tilde{y}_{-2} - 4\tilde{y}_{-1} + 6\tilde{y}_0 - 4\tilde{y}_1 + \tilde{y}_2 - \frac{h^4\tilde{V}^2}{\left[1 + \gamma - \tilde{y}_0\right]^2} = 0 \tag{3.100a}$$

$$\tilde{y}_{-1} - 4\tilde{y}_0 + 6\tilde{y}_1 - 4\tilde{y}_2 + \tilde{y}_3 - \frac{h^4\tilde{V}^2}{\left[1 + \gamma - \tilde{y}_1\right]^2} = 0 \tag{3.100b}$$

Notice from Equation (3.100) that two additional nodes, namely $\tilde{y}_{-2}$ and $\tilde{y}_{-1}$, appear in the list of unknowns. Such nodes are actually *fictitious* nodes whose values are to be determined from continuity relations at $\tilde{x} = \beta$. To see this, continuity relations (3.93)
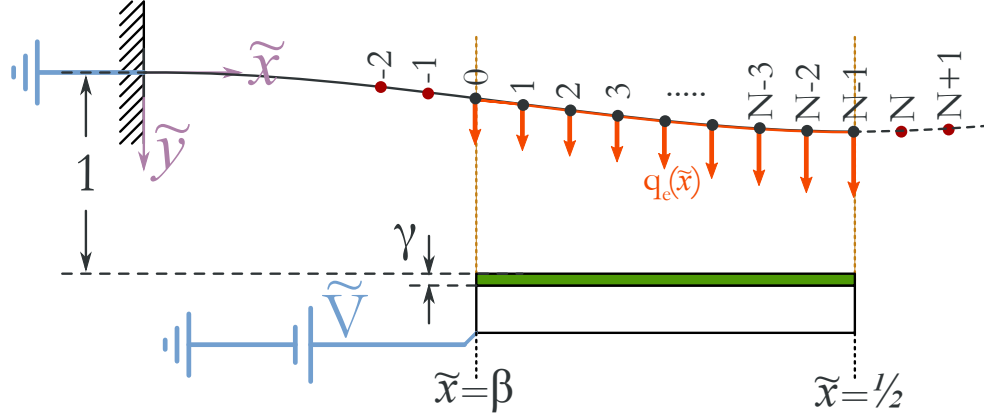
Figure 3.12: *An illustration of the zero-tension electrostatic actuation problem discretized for the application of Finite Difference method. Nodes are indicated with their indices.*

can be discretized with the aid of Equation (3.97) to obtain,

$$\tilde{y}_0 = c_3 \beta^3 + c_2 \beta^2 \tag{3.101a}$$

$$\frac{\tilde{y}_{-2} - 8\tilde{y}_{-1} + 8\tilde{y}_1 - \tilde{y}_2}{12h} = 3c_3\beta^2 + 2c_2\beta \tag{3.101b}$$

$$\frac{-\tilde{y}_{i-2} + 16\tilde{y}_{i-1} - 30\tilde{y}_i + 16\tilde{y}_{i+1} - \tilde{y}_{i+2}}{12h^2} = 6c_3\beta + 2c_2 \tag{3.101c}$$

$$\frac{-\tilde{y}_{i-2} + 2\tilde{y}_{i-1} - 2\tilde{y}_{i+1} + \tilde{y}_{i+2}}{2h^3} = 6c_3 \tag{3.101d}$$

Equation (3.101) is a linear equation set in c_3, c_2, $\tilde{y}_{-2}$, $\tilde{y}_{-1}$ and it can be simultaneously solved for these parameters as;

$$c_3 = \frac{-\beta^2 \tilde{y}_2 + 16\beta^2 \tilde{y}_1 - \left(12h^2 + 28\beta h + 15\beta^2\right)\tilde{y}_0}{2\beta^2 h \left(4h^2 + 12\beta h + 7\beta^2\right)} \tag{3.102a}$$

$$c_2 = \frac{\beta^3 \tilde{y}_2 - 16\beta^3 \tilde{y}_1 + \left(8h^3 + 36\beta h^2 + 42\beta^2 h + 15\beta^3\right)\tilde{y}_0}{2\beta^2 h \left(4h^2 + 12\beta h + 7\beta^2\right)} \tag{3.102b}$$

$$\tilde{y}_{-2} = \frac{3\left(4h^2 + 4\beta h + 3\beta^2\right)}{4h^2 + 12\beta h + 7\beta^2}\tilde{y}_2 - \frac{32\left(4h^2 + \beta^2\right)}{4h^2 + 12\beta h + 7\beta^2}\tilde{y}_1$$
$$+ \frac{6\left(16h^4 + 32\beta h^3 + 8\beta^2 h^2 + 5\beta^4\right)}{\beta^2 \left(4h^2 + 12\beta h + 7\beta^2\right)}\tilde{y}_0 \tag{3.102c}$$

$$\tilde{y}_{-1} = \frac{h^2 + \beta^2}{4h^2 + 12\beta h + 7\beta^2}\tilde{y}_2 - \frac{3\left(4h^2 - 4\beta h + 3\beta^2\right)}{4h^2 + 12\beta h + 7\beta^2}\tilde{y}_1$$
$$+ \frac{3\left(4h^4 + 4\beta h^3 - 7\beta^2 h^2 + 5\beta^4\right)}{\beta^2 \left(4h^2 + 12\beta h + 7\beta^2\right)}\tilde{y}_0 \tag{3.102d}$$

Substituting Equations (3.102c) and (3.102d) back into Equation (3.100) results in the following nodal expressions for $i = 0$ and $i = 1$;

$$P_0(\beta,h)\tilde{y}_0 + P_1(\beta,h)\tilde{y}_1 + P_2(\beta,h)\tilde{y}_2 - \frac{h^4\tilde{V}^2}{\left[1+\gamma-\tilde{y}_0\right]^2} = 0, \quad i{=}0 \qquad (3.103a)$$

$$Q_0(\beta,h)\tilde{y}_0 + Q_1(\beta,h)\tilde{y}_1 + Q_2(\beta,h)\tilde{y}_2 + \tilde{y}_3 - \frac{h^4\tilde{V}^2}{\left[1+\gamma-\tilde{y}_1\right]^2} = 0, \quad i{=}1 \qquad (3.103b)$$

where the functions $P_n(\beta,h)$ and $Q_n(\beta,h)$ ($n = 0$, 1, 2) are defined as:

$$P_0(\beta,h) = \frac{12\,(h+\beta)^2\,(2h+\beta)^2}{\beta^2\,(4h^2+12\,\beta\,h+7\,\beta^2)} \qquad (3.104a)$$

$$P_1(\beta,h) = -\frac{2\,\beta^2}{(h+\beta)^2}\,P_0(\beta,h) \qquad (3.104b)$$

$$P_2(\beta,h) = \frac{\beta^2}{(2h+\beta)^2}\,P_0(\beta,h) \qquad (3.104c)$$

$$Q_0(\beta,h) = \frac{12h^4+12\,\beta\,h^3-37\,\beta^2\,h^2-48\,\beta^3\,h-13\,\beta^4}{\beta^2\,(4h^2+12\,\beta\,h+7\,\beta^2)} \qquad (3.104d)$$

$$Q_1(\beta,h) = \frac{3\,\left(4h^2+28\,\beta\,h+11\,\beta^2\right)}{4h^2+12\,\beta\,h+7\,\beta^2} \qquad (3.104e)$$

$$Q_2(\beta,h) = -\frac{3\,\left(5h^2+16\,\beta\,h+9\,\beta^2\right)}{4h^2+12\,\beta\,h+7\,\beta^2} \qquad (3.104f)$$

Having derived the nodal equations for nodes at $\tilde{x} = \beta$ border, let us focus on the symmetry boundary next. In particular, problem symmetry implies

$$\tilde{y}_N = \tilde{y}_{N-2} \qquad (3.105a)$$

$$\tilde{y}_{N+1} = \tilde{y}_{N-3} \qquad (3.105b)$$

which can be obtained either by setting $\tilde{y}'_{N-1} = \tilde{y}'''_{N-1} = 0$ or using the symmetry directly. Hence, it is noticed that values of the fictitious nodes $\tilde{y}_N$ and $\tilde{y}_{N+1}$ can be obtained without any tedious formulation. Using this information and Equation (3.99), nodal equations at $i = N - 2$ and $i = N - 1$ can be determined as,

$$\tilde{y}_{N-4} - 4\tilde{y}_{N-3} + 7\tilde{y}_{N-2} - 4\tilde{y}_{N-1} - \frac{h^4\tilde{V}^2}{\left[1+\gamma-\tilde{y}_{N-2}\right]^2} = 0, \quad i{=}N{-}2 \qquad (3.106a)$$

$$2\tilde{y}_{N-3} - 8\tilde{y}_{N-2} + 6\tilde{y}_{N-1} - \frac{h^4\tilde{V}^2}{\left[1+\gamma-\tilde{y}_{N-1}\right]^2} = 0, \quad i{=}N{-}1 \qquad (3.106b)$$

Table 3.4: *Nodal Finite Difference equations for the zero-tension electrostatic actuation problem.*

INDEX	FD EQUATION
$i = 0$	$F_0(\vec{y}) = P_0(\beta, h)\tilde{y}_0 + P_1(\beta, h)\tilde{y}_1 + P_2(\beta, h)\tilde{y}_2 - \dfrac{h^4 \tilde{V}^2}{\left[1 + \gamma - \tilde{y}_0\right]^2} = 0$
$i = 1$	$F_1(\vec{y}) = Q_0(\beta, h)\tilde{y}_0 + Q_1(\beta, h)\tilde{y}_1 + Q_2(\beta, h)\tilde{y}_2 + \tilde{y}_3 - \dfrac{h^4 \tilde{V}^2}{\left[1 + \gamma - \tilde{y}_1\right]^2} = 0$
$2 \leq i \leq N - 3$	$F_i(\vec{y}) = \tilde{y}_{i-2} - 4\tilde{y}_{i-1} + 6\tilde{y}_i - 4\tilde{y}_{i+1} + \tilde{y}_{i+2} - \dfrac{h^4 \tilde{V}^2}{\left[1 + \gamma - \tilde{y}_i\right]^2} = 0$
$i = N - 2$	$F_{N-2}(\vec{y}) = \tilde{y}_{N-4} - 4\tilde{y}_{N-3} + 7\tilde{y}_{N-2} - 4\tilde{y}_{N-1} - \dfrac{h^4 \tilde{V}^2}{\left[1 + \gamma - \tilde{y}_{N-2}\right]^2} = 0$
$i = N - 1$	$F_{N-1}(\vec{y}) = 2\tilde{y}_{N-3} - 8\tilde{y}_{N-2} + 6\tilde{y}_{N-1} - \dfrac{h^4 \tilde{V}^2}{\left[1 + \gamma - \tilde{y}_{N-1}\right]^2} = 0$

For the sake of clarity, nodal Finite Difference equations for $i = 0, 1, \ldots, N - 1$ are summarized in Table 3.4 for the zero-tension electrostatic actuation problem.

Correction for the Case $\alpha = 1$

When the electrostatic load $q_e(\tilde{x})$ is applied along the entire beam span (i.e. for $\alpha = 1$), continuity interface $\tilde{x} = \beta$ coincides with the clamped beam end ($\tilde{x} = 0$) and hence previously derived Finite Difference equations become invalid for the relevant neighboring nodes. Moreover, $\tilde{y}_0$ is set to zero as dictated by the clamped boundary condition so that number of unknowns actually decreases by one. It is clear from these observations that Finite Difference equations for $\alpha = 1$ must be modified for nodes in the neighborhood of $\tilde{x} = 0$.

Initial intuition is that Finite Difference equations depicted in Table 3.4 must tend to the ones corresponding to $\alpha = 1$ by considering the limit as $\beta \to 0$. There is, however, a problem with such an approach as the functions $P_0(\beta, h)$ and $Q_0(\beta, h)$ are noted to have poles at $\beta = 0$ which in turn render Equations (3.103) singular. In fact, mentioned singularity can be eliminated by constructing a linear combination of Equations (3.103) in such a way to cancel the offending terms. If moreover, resulting regular equation is treated as the Finite Difference equation for node $i = 1$, one redundant equation will be eliminated and the equation system will cease to be overdetermined.

Table 3.5: *Nodal Finite Difference equations for the zero-tension electrostatic actuation problem for $\alpha = 1$.*

INDEX	FD EQUATION
$i = 1$	$F_1(\vec{y}) = 9\tilde{y}_1 - \frac{9}{2}\tilde{y}_2 + \tilde{y}_3 + \frac{h^4\tilde{V}^2}{4(1+\gamma)^2} - \frac{h^4\tilde{V}^2}{\left[1+\gamma-\tilde{y}_1\right]^2} = 0$
$i = 2$	$F_2(\vec{y}) = -4\tilde{y}_1 + 6\tilde{y}_2 - 4\tilde{y}_3 + \tilde{y}_4 - \frac{h^4\tilde{V}^2}{\left[1+\gamma-\tilde{y}_2\right]^2} = 0$
$3 \leq i \leq N-3$	$F_i(\vec{y}) = \tilde{y}_{i-2} - 4\tilde{y}_{i-1} + 6\tilde{y}_i - 4\tilde{y}_{i+1} + \tilde{y}_{i+2} - \frac{h^4\tilde{V}^2}{\left[1+\gamma-\tilde{y}_i\right]^2} = 0$
$i = N-2$	$F_{N-2}(\vec{y}) = \tilde{y}_{N-4} - 4\tilde{y}_{N-3} + 7\tilde{y}_{N-2} - 4\tilde{y}_{N-1} - \frac{h^4\tilde{V}^2}{\left[1+\gamma-\tilde{y}_{N-2}\right]^2} = 0$
$i = N-1$	$F_{N-1}(\vec{y}) = 2\tilde{y}_{N-3} - 8\tilde{y}_{N-2} + 6\tilde{y}_{N-1} - \frac{h^4\tilde{V}^2}{\left[1+\gamma-\tilde{y}_{N-1}\right]^2} = 0$

An application of the discussed approach may proceed as follows. If β is assumed to be very small compared to h, Equations (3.103) can be re-written as,

$$\frac{12h^2}{\beta^2}\tilde{y}_0 - 24\tilde{y}_1 + 3\tilde{y}_2 - \frac{h^4\tilde{V}^2}{\left[1+\gamma-\tilde{y}_0\right]^2} = 0$$

$$\frac{3h^2}{\beta^2}\tilde{y}_0 + 3\tilde{y}_1 - \frac{15}{4}\tilde{y}_2 + \tilde{y}_3 - \frac{h^4\tilde{V}^2}{\left[1+\gamma-\tilde{y}_1\right]^2} = 0$$

Eliminating the first terms and evaluating the limit as $\beta \to 0$ (hence $\tilde{y}_0 \to 0$) yields,

$$9\tilde{y}_1 - \frac{9}{2}\tilde{y}_2 + \tilde{y}_3 + \frac{h^4\tilde{V}^2}{4(1+\gamma)^2} - \frac{h^4\tilde{V}^2}{\left[1+\gamma-\tilde{y}_1\right]^2} = 0 \qquad (3.108)$$

which can be regarded as the Finite Difference equation for node $i = 1$.

In addition to the previous modification, it will be also required to alter the nodal equation for $i = 2$ since corresponding stencil makes use of the nodal deflection $\tilde{y}_0$ which is left out of the list of unknowns. Substituting $\tilde{y}_0 = 0$ in Equation (3.99) for $i = 2$ establishes the desired expression,

$$-4\tilde{y}_1 + 6\tilde{y}_2 - 4\tilde{y}_3 + \tilde{y}_4 - \frac{h^4\tilde{V}^2}{\left[1+\gamma-\tilde{y}_2\right]^2} = 0 \qquad (3.109)$$

In order to maintain clarity, Table 3.5 lists Finite Difference equations for the zero-tension, entire-span electrostatic actuation problem.

3.4.1.4   Solution of the Finite Difference Equations

Nodal equations presented in Table 3.4 constitute a non-linear equation system of N equations for the unknown vector $\vec{y} = \left[\tilde{y}_0, \tilde{y}_1, \ldots \tilde{y}_{N-1} \right]$ of length N[5]. Unlike linear equation systems, existence of a unique solution for such a non-linear equation system cannot be ascertained in general. Nevertheless, a solution (if it exists) can be obtained by multidimensional root-finding algorithms and its validity may be justified through physical reasoning [117]. In what follows, solution procedure of the Finite Difference equations will be described for the zero-tension electrostatic actuation problem and obtained results will be discussed.

In order to solve Finite Difference equations given in Table 3.4 (or 3.5 for $\alpha = 1$), Jacobian matrix J of the system is evaluated first. The entries J_{ij} of the Jacobian matrix are calculated analytically from,

$$J_{ij} = \frac{\partial F_i}{\partial \tilde{y}_j}$$

which can be shown to yield a 5-band diagonally-dominant matrix. Next, the equation system together with its Jacobian matrix are implemented as separate subroutines in Numpy-extended Python environment [118]. Then, those subroutines are fed to `fsolve` function of SciPy module [119] which is actually a wrapper around MINPACK's multi-dimensional root solver algorithm `hybrj` [120]. Finally, nodal deflection vector $\vec{y}$ is obtained as an output from `fsolve` for a given α, γ and $\tilde{V}$.

Selection of the number of grid points N is a general concern for any Finite Difference implementation, as picking a low N might cause an inaccurate representation of derivatives involved. In order to select a suitable N for the proposed Finite Difference algorithm, a convergence study is performed which can be described as follows:

- For given values of the parameters α and γ, unknown vector $\vec{y}$ is solved in a certain $\tilde{V}$ range.

- Previous step is repeated for various N values and $\tilde{y}_{max} - \tilde{V}$ curves are stored at each N.

---

[5]   A similar argument holds for equation system depicted in Table 3.5 with N replaced by N-1.
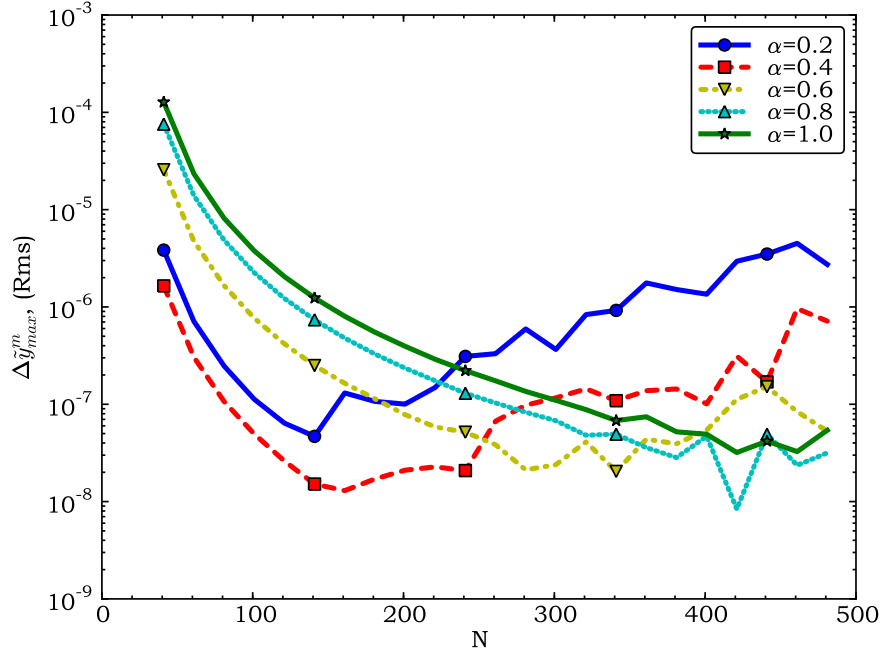
Figure 3.13: *Rms convergence error in $\tilde{y}_{\max}$ versus N for the zero-tension electrostatic actuation problem with α as a parameter ($\gamma = 0.03$).*

- Root-mean-square (rms) error between $\tilde{y}_{\max} - \tilde{V}$ curves of consecutive N's are evaluated from

$$\Delta\tilde{y}_{\max,m} = \sqrt{\frac{1}{P}\sum_{p=1}^{P}\left(\tilde{y}_{\max,p}^{m} - \tilde{y}_{\max,p}^{m-1}\right)^2}$$

where the subscript p indexes the points on $\tilde{y}_{\max} - \tilde{V}$ curves and the superscript m represents the particular curve for the m$^{\text{th}}$ N value.

Figure 3.13 depicts the results of explained convergence study for $\gamma = 0.03$ with α as a parameter. It is observed from Figure 3.13 that proposed Finite Difference implementation indeed converges with increasing N, as evident from decreasing rms error trend. For lower α values error seems to increase slightly after a certain N value, however, such a trend can be regarded insignificant as the error levels stay below 10^{-5} within the focused N range. Moreover, although not presented here, it is verified through a separate parametric analysis that γ-dependence of the rms error is too weak to be discerned compared to that of α. According to these results, it is preferred to pick $N = 251$ for the on-going
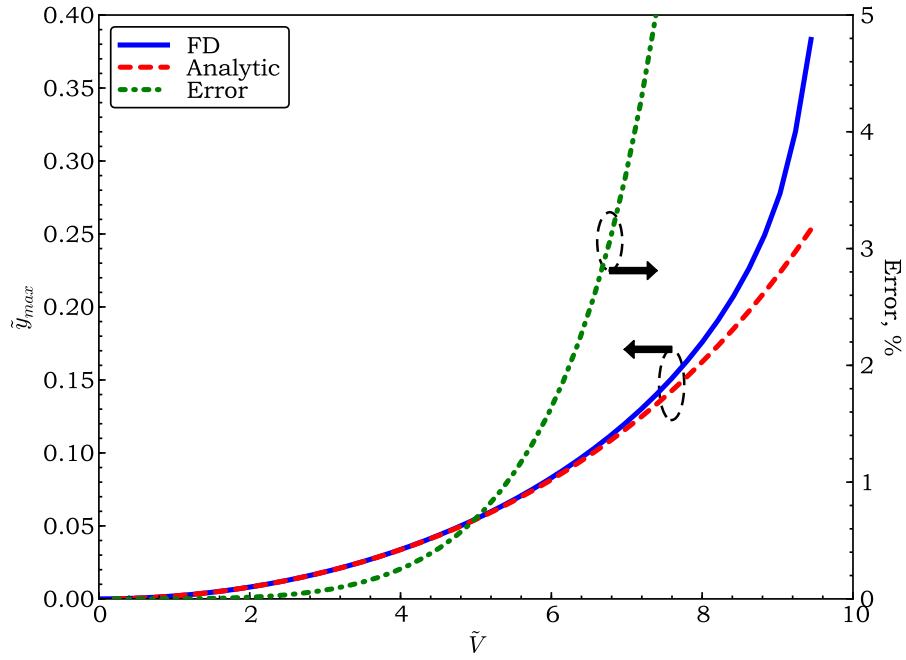
Figure 3.14: *A comparison between (approximate) analytical and Finite Difference solutions for the zero-tension electrostatic actuation problem ($\alpha = 0.5$, $\gamma = 0.03$, $N = 251$).*

analyses, whose rms error is noted to be lower than 10^{-6} for the considered α range, thus establishing sufficient accuracy.

Having determined a proper number of grid points, next, consistency of the solution must be investigated since convergence to a solution does not necessarily imply that relevant solution is a correct one. In order to verify that the solutions are consistent with the problem at hand, they are compared with the approximate analytical solution (3.96) determined in §3.4.1.2. Figure 3.14 presents the results of that comparison for a sample configuration with $\alpha = 0.5$, $\gamma = 0.03$ and $N = 251$. It is noticed from Figure 3.14 that the agreement between two solutions is excellent for $\tilde{y}_{\max} \leq \frac{1+\gamma}{10}$, with the associated error (referenced to the analytical results) less than 2.5%[6]. From these observations, consistency of the Finite Difference solutions can be clearly justified.

---

[6] It must be remarked that noted error is attributed to inaccurate representation of the non-linear loading term in Equation (3.96) with increasing $\tilde{y}_{\max}$ and hence it does not indicate the accuracy of the Finite Difference solution.
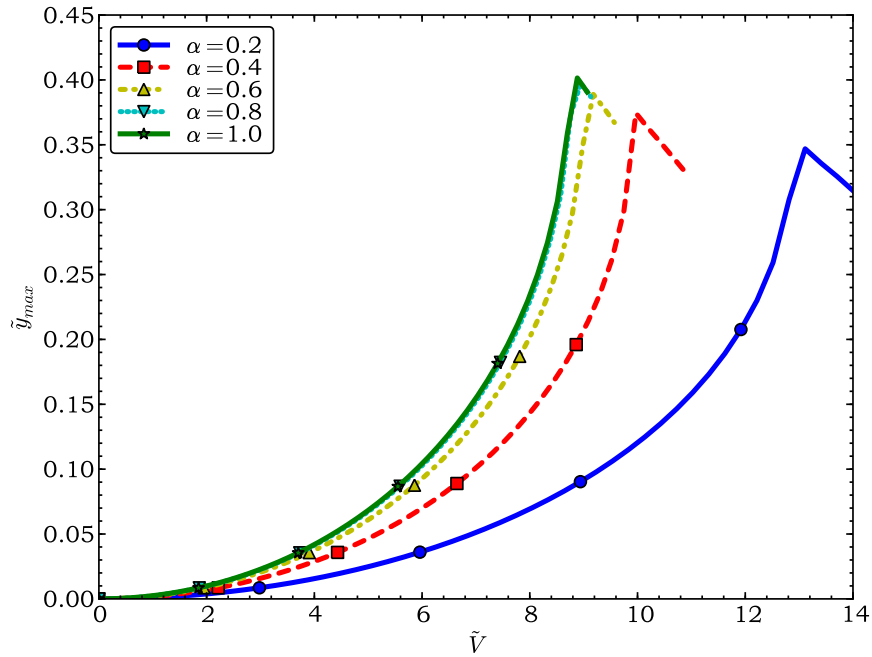
Figure 3.15: *Typical $\tilde{y}_{\max}$ versus $\tilde{V}$ characteristics for the zero-tension electrostatic actuation problem ($\gamma = 0.03$, $N = 251$).*

3.4.1.5 Pull-In Phenomenon and Extraction of Pull-in Voltage

Numerical analyses conducted in the previous section for the zero-tension electrostatic actuation problem were limited to a maximum deflection of a certain fraction of the air-gap. The reason for such a preference can be realized when $\tilde{y}_{\max} - \tilde{V}$ characteristic is considered in a wider sweep range: As depicted in Figure 3.15, relevant characteristic exhibits a sharp cusp at a particular $\tilde{V}$ after which the maximum deflection seems to *decrease* with increasing voltage. This apparent non-physical trend is moreover found to be linked with inability of the Finite Difference equation system to possess a solution. These observations suggest that the actuator system at hand undergoes a sharp behavior change at the very location where the mentioned cusp occur.

The peculiar feature described above is actually a well-known characteristic of voltage-controlled electrostatic actuator systems termed as "pull-in instability" [83–85]: Due to inherent positive feedback in the actuator system, mechanical restoring force of the move-able electrode fails to counterbalance the electrostatic attraction force beyond a specific

voltage (denoted as the "pull-in voltage" (V_{PI})), causing the moveable electrode to *snap down* to the stationary one. Pull-in mechanism thus limits the stable operation range of electrostatic actuator systems and an accurate determination of the pull-in voltage is hence crucial for a proper actuator design.

It is one of the goals of the on-going study to establish an accurate, simulation-based pull-in voltage expression for the electrostatically actuated fixed-fixed beam system at hand. In order to accomplish so, it is necessary to extract pull-in voltages reliably from numerical simulation data, a topic which is covered here in some detail. It is noted earlier that Finite Difference equation set ceases to have a solution once $\tilde{V}$ grows past a certain border. Physical reasoning suggests that $\tilde{V} = \tilde{V}_{PI}$ must hold at this border since absence of a stable solution beyond the relevant border complies with the snapping-down behavior of the beam. Assuming such a reasoning is correct, pull-in voltage determination then boils down to finding the lowest $\tilde{V}$ causing the residue of the Finite Difference equation set to jump from machine precision to a considerably higher value. The latter task can be easily automated through a binary search algorithm and $\tilde{V}_{PI}$ can be extracted easily within a prescribed precision.

Dynamic Stability Analysis to Verify Pull-in

In order to justify the proposed pull-in voltage extraction method from a physical stand point, a dynamic stability analysis is conducted following the guidelines of [81]. Relevant analysis starts from the normalized 1-D Euler-Bernoulli beam equation without any axial effects [82]:

$$\frac{\partial^4 \tilde{y}}{\partial \tilde{x}^4} + \frac{\partial^2 \tilde{y}}{\partial \tilde{t}^2} = \frac{\tilde{V}^2}{\left[1 + \gamma - \tilde{y}(\tilde{x}, \tilde{t})\right]^2} \Pi(\tilde{x}) \tag{3.110a}$$

where

$$\Pi(\tilde{x}) = \begin{cases} 1, & \text{if } \beta \leq \tilde{x} \leq 1 - \beta \\ 0, & \text{otherwise} \end{cases} \tag{3.110b}$$

A perturbation is then introduced to the static deflection solution by letting,

$$\tilde{y}(\tilde{x}) = \tilde{y}_s(\tilde{x}) + \tilde{\eta}(\tilde{x}, \tilde{t}) \tag{3.111}$$

After substituting Equation (3.111) into (3.110a), linearizing RHS and canceling the static terms, one is left with;

$$\frac{\partial^4 \tilde{\eta}}{\partial \tilde{x}^4} + \frac{\partial^2 \tilde{\eta}}{\partial \tilde{t}^2} = \frac{2\tilde{V}^2}{\left[1 + \gamma - \tilde{y}_s(\tilde{x})\right]^3} \, \Pi(\tilde{x}) \, \tilde{\eta}(\tilde{x}, \tilde{t}) \tag{3.112}$$

Next, following a separation of variables approach $\tilde{\eta}(\tilde{x}, \tilde{t})$ is expressed as a series:

$$\tilde{\eta}(\tilde{x}, \tilde{t}) = \sum_{p=1}^{P} \omega_p(\tilde{t}) \phi_p(\tilde{x}) \tag{3.113}$$

In Equation (3.113), P is the number of terms in the series expansion, $\omega_p(\tilde{t})$ is p^{th} time-dependent function and $\phi_p(\tilde{x})$ is the pth natural mode of the doubly clamped beam without axial effects. The latter is given by [121];

$$\phi_p(\tilde{x}) = \cosh(\lambda_p \tilde{x}) - \cos(\lambda_p \tilde{x}) - \frac{\cosh(\lambda_p) - \cos(\lambda_p)}{\sinh(\lambda_p) - \sin(\lambda_p)} \left[\sinh(\lambda_p \tilde{x}) - \sin(\lambda_p \tilde{x})\right]$$

where the eigenmode λ_p is a solution of

$$\cosh(\lambda_p) \cos(\lambda_p) - 1 = 0, \quad \lambda_p \neq 0$$

Employing Equation (3.113) in (3.112), taking the inner product of both sides with $\phi_q(\tilde{x})$ and using the following properties of natural modes;

$$\frac{d^4 \phi_p}{d\tilde{x}^4} = \lambda_p^4 \phi_p(\tilde{x})$$

$$\int_0^1 \phi_p(\tilde{x}) \phi_q(\tilde{x}) \, d\tilde{x} = \delta_{pq}$$

it is arrived at

$$\lambda_q^4 \omega_q(\tilde{t}) + \frac{d^2 \omega_q}{d\tilde{t}^2} = \sum_{p=1}^{P} \omega_p(\tilde{t}) \int_0^1 \frac{2\tilde{V}^2}{\left[1 + \gamma - \tilde{y}_s(\tilde{x})\right]^3} \, \Pi(\tilde{x}) \phi_p(\tilde{x}) \phi_q(\tilde{x}) \, d\tilde{x} \tag{3.115}$$

Equation (3.115) can be cast into a matrix equation as,

$$\frac{d^2 \Omega}{d\tilde{t}^2} + \Lambda^4 \Omega = M\Omega \tag{3.116}$$

with

$$\Omega = \begin{bmatrix} \omega_1(\tilde{t}) & \omega_2(\tilde{t}) & \cdots & \omega_P(\tilde{t}) \end{bmatrix}_{1 \times P}^{T}$$

$$\Lambda = \mathrm{Diag}(\lambda_1, \, \lambda_2, \, \cdots, \lambda_P)$$

$$\mathbf{M} = \left[\mathrm{M}_{\mathrm{pq}} \right]_{\mathrm{P \times P}}$$

The entries of the matrix $\mathbf{M}$ are given by,

$$\mathrm{M}_{\mathrm{pq}} = \mathrm{M}_{\mathrm{qp}} = \int_{\beta}^{1-\beta} \frac{2\tilde{V}^2}{\left[1 + \gamma - \tilde{y}_{\mathrm{s}}(\tilde{x})\right]^3} \, \phi_{\mathrm{p}}(\tilde{x}) \phi_{\mathrm{q}}(\tilde{x}) \, \mathrm{d}\tilde{x}$$

$$= \int_{\beta}^{\frac{1}{2}} \frac{2\tilde{V}^2}{\left[1 + \gamma - \tilde{y}_{\mathrm{s}}(\tilde{x})\right]^3} \left[\phi_{\mathrm{p}}(\tilde{x}) \phi_{\mathrm{q}}(\tilde{x}) + \phi_{\mathrm{p}}(1 - \tilde{x}) \phi_{\mathrm{q}}(1 - \tilde{x}) \right] \mathrm{d}\tilde{x} \quad (3.118)$$

$$= \left[1 + (-1)^{\mathrm{p+q}} \right] \int_{\beta}^{\frac{1}{2}} \frac{2\tilde{V}^2}{\left[1 + \gamma - \tilde{y}_{\mathrm{s}}(\tilde{x})\right]^3} \, \phi_{\mathrm{p}}(\tilde{x}) \phi_{\mathrm{q}}(\tilde{x}) \, \mathrm{d}\tilde{x}$$

where symmetry of the static configuration together with the property

$$\phi_{\mathrm{p}}(1 - \tilde{x}) = (-1)^{\mathrm{p}} \, \phi_{\mathrm{q}}(\tilde{x})$$

are utilized during the intermediate integration steps. Using the final integral form, M_{pq} can be computed on the Finite Difference grid by Simpson's integral approximation, the details of which are omitted here.

Letting $\boldsymbol{\Omega} = \mathbf{v} e^{a\tilde{t}}$ transforms Equation (3.116) into an eigen-problem,

$$\left(\mathbf{M} - \boldsymbol{\Lambda}^4 \right) \mathbf{v} = a^2 \mathbf{v} \qquad (3.119)$$

whose eigenvalues a^2 are noticed to be real due to symmetric nature of $\mathbf{M} - \boldsymbol{\Lambda}^4$. Stability of the zero-tension electrostatic actuation problem can now be assessed by monitoring the values of a^2 for a particular $\tilde{V}$: If the maximum eigenvalue a_{max}^2 happens to be positive, $\tilde{\eta}(\tilde{x}, \tilde{t})$ would grow indefinitely over time, implying a dynamic instability. Conversely, $\tilde{\eta}(\tilde{x}, \tilde{t})$ remains as a linear combination of purely oscillatory terms, hence satisfies a dynamically stable state, provided that a_{max}^2 is non-positive.

Figure 3.16 presents plots of $\tilde{y}_{\mathrm{max}}$ and a_{max}^2 versus $\tilde{V}$ for a sample problem configuration. An inspection of the provided curves validates the physical reasoning stated at the beginning of this section: For voltages smaller than the one corresponding to the sharp cusp on $\tilde{y}_{\mathrm{max}} - \tilde{V}$ curve, a_{max}^2 is observed to be negative and an increasing function of $\tilde{V}$. At
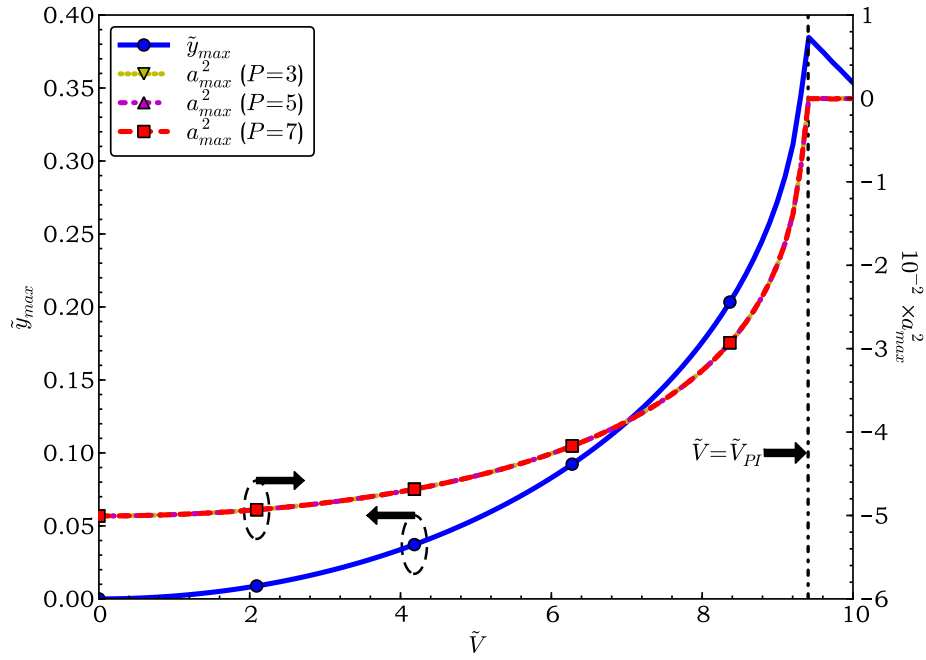
Figure 3.16: *Stability analysis results for the zero-tension electrostatic actuation problem ($\gamma = 0.03$, $\alpha = 0.5$, $N = 251$, P $= 3, 5, 7$).*

the very point where the relevant cusp occurs, $a^2_{\max}$ assumes the value of zero implying that the system is on the verge of pull-in at that voltage. Notice moreover that obtained stability results are virtually independent of the number of terms (P) employed in the modal expansion of $\tilde{\eta}(\tilde{x}, \tilde{t})$, an attribute ensuring that relevant results are not clouded by convergence related errors. These observations therefore justify the utilization of the proposed error monitoring approach for the extraction of V_{PI}.

Development of a pull-in voltage expression based on analytical and numerical results will be covered later in a dedicated section.

3.4.2 Finite Difference Solution of Non-zero Tension Electrostatic Actuation Problem

Having successfully characterized the simplified problem of zero-tension electrostatic actuation, next, a more complete analysis is attempted that will include previously neglected

93

axial effects of residual stress and non-linear stretching. Proceeding similarly with the previous section; Finite Difference formulation will be established first, solution of the resulting equations will be described next and obtained results will be discussed in the end.

3.4.2.1 Finite Difference Formulation

Figure 3.17 delineates the non-zero tension electrostatic actuation configuration which is discretized uniformly for the application of Finite Difference method. It was established in §3.3.2 and §3.3.3 that non-zero tension electrostatic actuation problem is governed by the following relations:

$$\frac{d^4 \tilde{y}}{d \tilde{x}^4} - 4u^2 \frac{d^2 \tilde{y}}{d \tilde{x}^2} = \begin{cases} \dfrac{\tilde{V}^2}{\left[1+\gamma-\tilde{y}\right]^2} & \text{if } \beta \leq \tilde{x} \leq \frac{1}{2} \\[2mm] 0 & \text{if } 0 \leq \tilde{x} \leq \beta \end{cases} \tag{3.120a}$$

$$u^2 = 3 \left(\frac{g_0}{t}\right)^2 \int\limits_{0}^{\frac{1}{2}} \left(\frac{d \tilde{y}}{d \tilde{x}'}\right)^2 d \tilde{x}' + 3 \Sigma_0 \tag{3.120b}$$

together with the edge conditions (3.85), (3.86) and (3.90). Let us begin with the discretization of Equation (3.120a) within the loading span. Unlike the zero-tension problem, it is preferred to utilize the following set of derivative approximations for the latter configuration:

$$\tilde{y}_i' = \frac{-\tilde{y}_{i-1} + \tilde{y}_{i+1}}{2h} + O(h^2) \tag{3.121a}$$

$$\tilde{y}_i'' = \frac{\tilde{y}_{i-1} - 2\tilde{y}_i + \tilde{y}_{i+1}}{h^2} + O(h^2) \tag{3.121b}$$

$$\tilde{y}_i''' = \frac{-\tilde{y}_{i-2} + 2\tilde{y}_{i-1} - 2\tilde{y}_{i+1} + \tilde{y}_{i+2}}{2h^3} + O(h^2) \tag{3.121c}$$

$$\tilde{y}_i'''' = \frac{\tilde{y}_{i-2} - 4\tilde{y}_{i-1} + 6\tilde{y}_i - 4\tilde{y}_{i+1} + \tilde{y}_{i+2}}{h^4} + O(h^2) \tag{3.121d}$$

A comparison of Equation (3.121) with (3.97) reveals that first and second order derivative approximations are replaced with three-point counterparts. Such a preference can be readily justified from an accuracy point of view: Since five-point third and fourth order derivative approximations have an associated error of $O(h^2)$, overall accuracy of
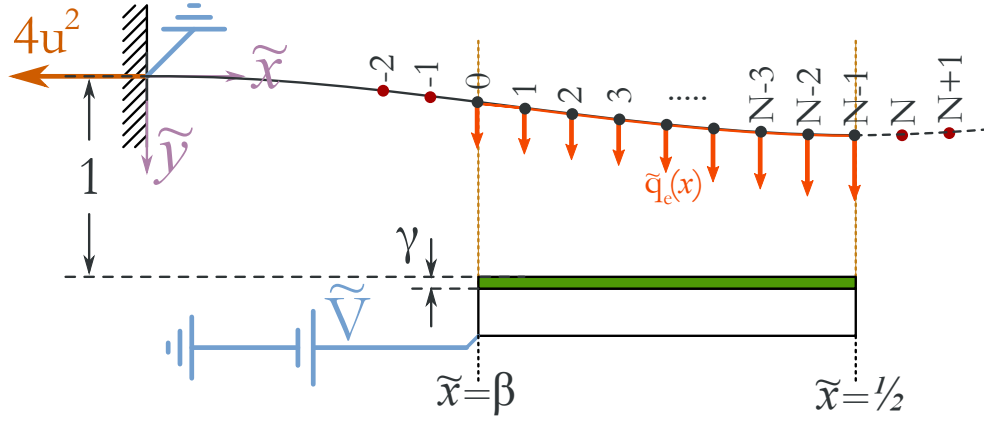
Figure 3.17: *An illustration of the non-zero tension electrostatic actuation problem discretized for the application of Finite Difference method. Nodes are indicated with their indices.*

the Finite Difference formulation will be limited by those terms even if $O(h^4)$ accurate approximations are utilized for the first and second order derivatives. Hence, it is unnecessary to utilize more accurate expressions for first and second order derivatives and doing so would only serve to complicate the analysis. As it will be shown shortly, this is especially true for the axial relation (3.120b) where an integration over square of the first order derivatives comes into play.

Employing the modified derivative approximations (3.121) in Equation (3.120a) yields the interior-node Finite Difference equation for the non-zero tension electrostatic actuation problem:

$$F_i = \tilde{y}_{i-2} + \tilde{y}_{i+2} - 4(1 + u^2 h^2)(\tilde{y}_{i-1} + \tilde{y}_{i+1}) + (6 + 8u^2 h^2)\tilde{y}_i - \frac{h^4 \tilde{V}^2}{\left[1 + \gamma - \tilde{y}_i\right]^2} = 0 \quad (3.122)$$

which is valid for $2 \leq i \leq N - 3$. For the nodes in the neighborhood of continuity and symmetry borders, Equation (3.122) needs to be modified in order to incorporate corresponding edge conditions.

Nodes Near the Continuity Border

Writing Equation (3.122) for the nodes $i = 0$ and $i = 1$ leads to

$$\tilde{y}_{-2} + \tilde{y}_2 - 4(1 + u^2 h^2)(\tilde{y}_{-1} + \tilde{y}_1) + (6 + 8u^2 h^2)\tilde{y}_0 - \frac{h^4 \tilde{V}^2}{\left[1 + \gamma - \tilde{y}_0\right]^2} = 0 \quad (3.123a)$$

$$\tilde{y}_{-1} + \tilde{y}_3 - 4(1 + u^2 h^2)(\tilde{y}_0 + \tilde{y}_2) + (6 + 8u^2 h^2)\tilde{y}_1 - \frac{h^4 \tilde{V}^2}{\left[1 + \gamma - \tilde{y}_1\right]^2} = 0 \qquad (3.123b)$$

Equation (3.123) is noted to include the fictitious nodal deflections $\tilde{y}_{-2}$ and $\tilde{y}_{-1}$ as additional unknowns. These extra unknowns can be eliminated by replacing the derivatives in Equation (3.85) with the corresponding approximations (3.121) and solving the resulting system of four linear equations for $\tilde{y}_{-2}$, $\tilde{y}_{-1}$, A and B in terms of $\tilde{y}_0$, $\tilde{y}_1$, $\tilde{y}_2$ and u. These fictitious nodal deflections can then be substituted back in Equation (3.123) to establish the desired Finite Difference equations for nodes i = 0 and i = 1. Carrying out relevant calculations, one arrives at the result:

$$F_0 = c_{00}(u,\beta,h)\tilde{y}_0 + c_{01}(u,\beta,h)\tilde{y}_1 + 2\tilde{y}_2 - \frac{h^4 \tilde{V}^2}{\left[1 + \gamma - \tilde{y}_0\right]^2} = 0 \qquad (3.124a)$$

$$F_1 = c_{10}(u,\beta,h)\tilde{y}_0 + c_{11}(u,\beta,h)\tilde{y}_1 - 4\left[1 + u^2 h^2\right]\tilde{y}_2 + \tilde{y}_3 - \frac{h^4 \tilde{V}^2}{\left[1 + \gamma - \tilde{y}_1\right]^2} = 0 \quad (3.124b)$$

where the functions $c_{ij}(u,\beta,h)$ are defined as

$$c_{00}(u,\beta,h) = -\left\{ \left[\left(8h^3 + 16\beta h^2\right)u^3 + (4\beta - 6h)u\right]\sinh(2\beta u) \right.$$
$$\left. + \left[\left(16h^4 + 16\beta h^3\right)u^4 + 12\beta h u^2 - 4\right]\cosh(2\beta u) + 4\right\}/Q(u,\beta,h) \qquad (3.125a)$$

$$c_{01}(u,\beta,h) = 8\left\{ \left[\left(2\beta h^2 - h^3\right)u^3 + (\beta - h)u\right]\sinh(2\beta u) \right.$$
$$\left. + \left[2\beta h^3 u^4 + \left(2\beta h - h^2\right)u^2 - 1\right]\cosh(2\beta u) + h^2 u^2 + 1\right\}/Q(u,\beta,h)$$

$$(3.125b)$$

$$c_{10}(u,\beta,h) = \frac{1}{2}c_{01}(u,\beta,h) \qquad (3.125c)$$

$$c_{11}(u,\beta,h) = \left\{ \left[\left(8h^3 - 16\beta h^2\right)u^3 + (7h - 10\beta)u\right]\sinh(2\beta u) \right.$$
$$+ \left[-16\beta h^3 u^4 + \left(16h^2 - 14\beta h\right)u^2 + 10\right]\cosh(2\beta u) \qquad (3.125d)$$
$$\left. - 16h^2 u^2 - 10\right\}/Q(u,\beta,h)$$

$$Q(u, \beta, h) = (h - 2\beta)\, u \sinh(2\beta u) + \left[2 - 2\beta h u^2\right] \cosh(2\beta u) - 2 \qquad \text{(3.125e)}$$

For the sake of completeness, expressions for the coefficients A and B are also provided:

$$\begin{aligned}
A &= \frac{\left[\sinh(2\beta u) - 2\beta u\right]\tilde{y}_1 - \left[(1 + 2h^2 u^2)\sinh(2\beta u) + 2hu\cosh(2\beta u) - (2h + 2\beta)u\right]\tilde{y}_0}{2uh\, Q(u,\beta,h)} \\
B &= \frac{\left[1 - \cosh(2\beta u)\right]\tilde{y}_1 + \left[2hu\sinh(2\beta u) + (1 + 2h^2 u^2)\cosh(2\beta u) - 1\right]\tilde{y}_0}{2uh\, Q(u,\beta,h)}
\end{aligned} \qquad \text{(3.126)}$$

Nodes Near the Symmetry Boundary

From Equation (3.122), nodal expressions for the nodes $i = N - 2$ and $i = N - 1$ are

$$\begin{aligned}
\tilde{y}_{N-4} + \tilde{y}_N - 4(1 + u^2 h^2)(\tilde{y}_{N-3} + \tilde{y}_{N-1}) + (6 + 8u^2 h^2)\tilde{y}_{N-2} - \frac{h^4 \tilde{V}^2}{\left[1 + \gamma - \tilde{y}_{N-2}\right]^2} &= 0 \\
\tilde{y}_{N-3} + \tilde{y}_{N+1} - 4(1 + u^2 h^2)(\tilde{y}_{N-2} + \tilde{y}_N) + (6 + 8u^2 h^2)\tilde{y}_{N-1} - \frac{h^4 \tilde{V}^2}{\left[1 + \gamma - \tilde{y}_{N-1}\right]^2} &= 0
\end{aligned} \qquad \text{(3.127)}$$

After translating the boundary conditions (3.86) and (3.90) to the discretized domain via Equation (3.121), one obtains

$$\begin{aligned}
\tilde{y}_N &= \tilde{y}_{N-2} \\
\tilde{y}_{N+1} &= \tilde{y}_{N-3}
\end{aligned} \qquad \text{(3.128)}$$

Substitution of Equation (3.128) back into (3.127) then gives the desired expressions:

$$\begin{aligned}
F_{N-2} &= \tilde{y}_{N-4} - 4(1 + u^2 h^2)(\tilde{y}_{N-3} + \tilde{y}_{N-1}) + (7 + 8u^2 h^2)\tilde{y}_{N-2} - \frac{h^4 \tilde{V}^2}{\left[1 + \gamma - \tilde{y}_{N-2}\right]^2} = 0 \\
F_{N-1} &= 2\tilde{y}_{N-3} - 8(1 + u^2 h^2)\tilde{y}_{N-2} + (6 + 8u^2 h^2)\tilde{y}_{N-1} - \frac{h^4 \tilde{V}^2}{\left[1 + \gamma - \tilde{y}_{N-1}\right]^2} = 0
\end{aligned} \qquad \text{(3.129)}$$

Equations (3.122), (3.124) and (3.129) form N Finite Difference equations for the unknown nodal deflection vector $\vec{y} = \left[\tilde{y}_0\ \tilde{y}_1\ \cdots\ \tilde{y}_{N-1}\right]$ of length N. Notice, however, that there exists one more unknown for the non-zero electrostatic actuation problem unlike the zero-tension one: The variable u, which is assumed to be known so far, is actually yet to be determined from the axial relation (3.120b). Next part explores this topic.

Discretization of the Axial Relation

Let us now elaborate on the axial relation (3.120b) to furnish one more Finite Difference equation for the unknowns $\tilde{y}$ and u. Relevant relation can be discretized by approximating the integral term with a summation and employing the derivative approximation (3.121a) for the integrand. In order to successfully apply the former, range of the integration must be first split into two regions since the Finite Difference grid is only valid for the region with $\beta \leq \tilde{x} \leq \frac{1}{2}$:

$$\int_0^{\frac{1}{2}} \left(\frac{d\tilde{y}}{d\tilde{x}'} \right)^2 d\tilde{x}' = \int_0^{\beta} \left(\frac{d\tilde{y}_{\mathrm{I}}}{d\tilde{x}'} \right)^2 d\tilde{x}' + \int_\beta^{\frac{1}{2}} \left(\frac{d\tilde{y}_{\mathrm{II}}}{d\tilde{x}'} \right)^2 d\tilde{x}' \tag{3.130}$$

The first integration in Equation (3.130) can be carried out analytically: Employing the expression of $\tilde{y}_{\mathrm{I}}(\tilde{x})$ from Equation (3.84), substituting A and B from Equation (3.126) and evaluating the integral gives,

$$\int_0^{\beta} \left(\frac{d\tilde{y}_{\mathrm{I}}}{d\tilde{x}'} \right)^2 d\tilde{x}' = w_{00}(u,\beta,h)\tilde{y}_0^2 + w_{01}(u,\beta,h)\tilde{y}_0\tilde{y}_1 + w_{11}(u,\beta,h)\tilde{y}_1^2 \tag{3.131}$$

For the sake of brevity, definitions of the functions $w_{\mathrm{ij}}(u,\beta,h)$ are omitted due to their highly complicated nature.

Remaining integral in Equation (3.130) can be approximated as a summation through Simpson's integral rule [122]:

$$\int_\beta^{\frac{1}{2}} \left(\frac{d\tilde{y}_{\mathrm{II}}}{d\tilde{x}'} \right)^2 d\tilde{x}' \approx \frac{h}{3} \left\{ \tilde{y}_0'^2 + \tilde{y}_{N-1}'^2 + 4\tilde{y}_1'^2 + 2 \sum_{n=1}^{\frac{N-3}{2}} \left[\tilde{y}_{2n}'^2 + 2\tilde{y}_{2n+1}'^2 \right] \right\} \tag{3.132}$$

where it is assumed that N is odd. After utilizing the derivative approximation (3.121a) and re-arranging, one obtains

$$\begin{aligned} \int_\beta^{\frac{1}{2}} \left(\frac{d\tilde{y}_{\mathrm{II}}}{d\tilde{x}'} \right)^2 d\tilde{x}' \approx \frac{1}{3h} \Bigg\{ & \left[\phi_0^2(u,\beta,h) + 1 \right] \tilde{y}_0^2 + \left[\phi_1^2(u,\beta,h) - \frac{1}{2} \right] \tilde{y}_1^2 \\ & + 2\phi_0(u,\beta,h)\phi_1(u,\beta,h)\tilde{y}_0\tilde{y}_1 - 2\tilde{y}_0\tilde{y}_2 + \frac{1}{2}\tilde{y}_{N-2}^2 + \tilde{y}_{N-1}^2 \\ & + \sum_{n=1}^{\frac{N-3}{2}} \tilde{y}_{2n-1}(\tilde{y}_{2n-1} - \tilde{y}_{2n+1}) + 2\tilde{y}_{2n}(\tilde{y}_{2n} - \tilde{y}_{2n+2}) \Bigg\} \end{aligned} \tag{3.133}$$

In Equation (3.133), the functions $\phi_i(u, \beta, h)$ stem from the representation

$$\tilde{y}_0' = \tilde{y}_1'(\beta) = \frac{\phi_0(u, \beta, h)\tilde{y}_0 + \phi_1(u, \beta, h)\tilde{y}_1}{h} \tag{3.134}$$

Expressions for these latter functions, which are omitted here for the sake of clarity, can be obtained by substituting Equation (3.126) into (3.85b). Combining Equations (3.131) and (3.133), the final Finite Difference equation can be formulated as

$$
F_u = 3\Sigma_0 - u^2 + \frac{(g_0/t)^2}{h}\left\{ R_{00}(u, \beta, h)\tilde{y}_0^2 + R_{11}(u, \beta, h)\tilde{y}_1^2 + R_{01}(u, \beta, h)\tilde{y}_0\tilde{y}_1 \right.
$$

$$
\left. -2\tilde{y}_0\tilde{y}_2 + \frac{1}{2}\tilde{y}_{N-2}^2 + \tilde{y}_{N-1}^2 + \sum_{n=1}^{\frac{N-3}{2}} \tilde{y}_{2n-1}(\tilde{y}_{2n-1} - \tilde{y}_{2n+1}) + 2\tilde{y}_{2n}(\tilde{y}_{2n} - \tilde{y}_{2n+2}) \right\} = 0
$$

$$\tag{3.135}$$

with

$$R_{00}(u, \beta, h) = \phi_0^2(u, \beta, h) + 3hw_{00}(u, \beta, h) + 1$$

$$R_{01}(u, \beta, h) = 2\phi_0(u, \beta, h)\phi_1(u, \beta, h) + 3hw_{01}(u, \beta, h)$$

$$R_{11}(u, \beta, h) = \phi_1^2(u, \beta, h) + 3hw_{11}(u, \beta, h) - \frac{1}{2}$$

For reference purposes, Table 3.6 summarizes the Finite Difference equations derived so far for the non-zero tension electrostatic actuation problem.

Correction for the Case $\alpha = 1$

As with the zero-tension electrostatic actuation problem, when the electrostatic load is applied along the entire beam span, Finite Difference equations must be modified due to the vanishing continuity border. Once again, letting simply $\beta \to 0$ does not yield regular expressions for the nodes in the relevant neighborhood so that a separate analysis must be conducted in order to remove corresponding singularities. For this purpose, Equation (3.125) is considered for $\beta \ll h$:

$$\frac{6h^3}{\beta^3}\tilde{y}_0 - \frac{6h}{\beta}\tilde{y}_1 + 2\tilde{y}_2 - \frac{h^4\tilde{V}^2}{(1+\gamma)^2} = 0$$

$$-\frac{3h}{\beta}\tilde{y}_0 + (7 + 8u^2h^2)\tilde{y}_1 - 4(1 + u^2h^2)\tilde{y}_2 + \tilde{y}_3 - \frac{h^4\tilde{V}^2}{\left[1 + \gamma - \tilde{y}_1\right]^2} = 0$$

Table 3.6: *Finite Difference equations for the nonzero-tension electrostatic actuation problem.*

<table>
<tr><td colspan="1" align="center">NODES NEAR THE CONTINUITY BORDER (i=0, 1)</td></tr>
<tr><td>

$$F_0 = c_{00}(u,\beta,h)\tilde{y}_0 + c_{01}(u,\beta,h)\tilde{y}_1 + 2\tilde{y}_2 - \frac{h^4\tilde{V}^2}{\left[1+\gamma-\tilde{y}_0\right]^2} = 0$$

$$F_1 = c_{10}(u,\beta,h)\tilde{y}_0 + c_{11}(u,\beta,h)\tilde{y}_1 - 4\left[1+u^2h^2\right]\tilde{y}_2 + \tilde{y}_3 - \frac{h^4\tilde{V}^2}{\left[1+\gamma-\tilde{y}_1\right]^2} = 0$$

</td></tr>
<tr><td align="center">INTERIOR NODES (2 ≤ i ≤ N-3)</td></tr>
<tr><td>

$$F_i = \tilde{y}_{i-2} + \tilde{y}_{i+2} - 4(1+u^2h^2)(\tilde{y}_{i-1}+\tilde{y}_{i+1}) + (6+8u^2h^2)\tilde{y}_i - \frac{h^4\tilde{V}^2}{\left[1+\gamma-\tilde{y}_i\right]^2} = 0$$

</td></tr>
<tr><td align="center">NODES NEAR THE SYMMETRY BORDER (i=N-2, N-1)</td></tr>
<tr><td>

$$F_{N-2} = \tilde{y}_{N-4} - 4(1+u^2h^2)(\tilde{y}_{N-3}+\tilde{y}_{N-1}) + (7+8u^2h^2)\tilde{y}_{N-2} - \frac{h^4\tilde{V}^2}{\left[1+\gamma-\tilde{y}_{N-2}\right]^2} = 0$$

$$F_{N-1} = 2\tilde{y}_{N-3} - 8(1+u^2h^2)\tilde{y}_{N-2} + (6+8u^2h^2)\tilde{y}_{N-1} - \frac{h^4\tilde{V}^2}{\left[1+\gamma-\tilde{y}_{N-1}\right]^2} = 0$$

</td></tr>
<tr><td align="center">AXIAL RELATION</td></tr>
<tr><td>

$$F_u = 3\Sigma_0 - u^2 + \frac{(g_0/t)^2}{h}\left\{R_{00}(u,\beta,h)\tilde{y}_0^2 + R_{11}(u,\beta,h)\tilde{y}_1^2 + R_{01}(u,\beta,h)\tilde{y}_0\tilde{y}_1\right.$$

$$\left. -2\tilde{y}_0\tilde{y}_2 + \frac{1}{2}\tilde{y}_{N-2}^2 + \tilde{y}_{N-1}^2 + \sum_{n=1}^{\frac{N-3}{2}} \tilde{y}_{2n-1}(\tilde{y}_{2n-1} - \tilde{y}_{2n+1}) + 2\tilde{y}_{2n}(\tilde{y}_{2n} - \tilde{y}_{2n+2})\right\} = 0$$

</td></tr>
</table>

Multiplying the first equation by $\frac{\beta^2}{2h^2}$ and adding it to the second one gives,

$$\left[7 + 8u^2h^2 - \frac{3\beta}{h}\right]\tilde{y}_1 - \left[4 + 4u^2h^2 - \frac{\beta^2}{h^2}\right]\tilde{y}_2 + \tilde{y}_3 - \frac{\beta^2h^2\tilde{V}^2}{2\left[1+\gamma-\tilde{y}_0\right]^2} - \frac{h^4\tilde{V}^2}{\left[1+\gamma-\tilde{y}_1\right]^2} = 0$$

Taking the limit as $\beta \to 0$ (hence $\tilde{y}_0 \to 0$) then yields a regular equation for the node $i = 1$:

$$F_1 = \left(7+8u^2h^2\right)\tilde{y}_1 - 4\left(1+u^2h^2\right)\tilde{y}_2 + \tilde{y}_3 - \frac{h^4\tilde{V}^2}{\left[1+\gamma-\tilde{y}_1\right]^2} = 0 \qquad (3.136)$$

Nodal equation for the $i = 2$ node must be also modified as its stencil includes $i = 0$ node. This issue is solved merely by letting $\tilde{y}_0 = 0$ in the corresponding expression:

$$F_2 = -4(1+u^2h^2)(\tilde{y}_1+\tilde{y}_3) + (6+8u^2h^2)\tilde{y}_2 + \tilde{y}_4 - \frac{h^4\tilde{V}^2}{\left[1+\gamma-\tilde{y}_2\right]^2} = 0 \qquad (3.137)$$

A final modification must be made for the axial relation (3.135) as the latter expression

Table 3.7: *Finite Difference equations for the nonzero-tension electrostatic actuation problem with $\alpha = 1$.*

NODES NEAR THE CLAMPED END (i=1, 2)
$$F_1 = \left(7 + 8u^2h^2\right)\tilde{y}_1 - 4\left(1 + u^2h^2\right)\tilde{y}_2 + \tilde{y}_3 - \frac{h^4\tilde{V}^2}{\left[1+\gamma-\tilde{y}_1\right]^2} = 0$$ $$F_2 = -4(1 + u^2h^2)(\tilde{y}_1 + \tilde{y}_3) + (6 + 8u^2h^2)\tilde{y}_2 + \tilde{y}_4 - \frac{h^4\tilde{V}^2}{\left[1+\gamma-\tilde{y}_2\right]^2} = 0$$
INTERIOR NODES ($3 \leq i \leq$ N-3)
$$F_i = \tilde{y}_{i-2} + \tilde{y}_{i+2} - 4(1 + u^2h^2)(\tilde{y}_{i-1} + \tilde{y}_{i+1}) + (6 + 8u^2h^2)\tilde{y}_i - \frac{h^4\tilde{V}^2}{\left[1+\gamma-\tilde{y}_i\right]^2} = 0$$
NODES NEAR THE SYMMETRY BORDER (i=N-2, N-1)
$$F_{N-2} = \tilde{y}_{N-4} - 4(1 + u^2h^2)(\tilde{y}_{N-3} + \tilde{y}_{N-1}) + (7 + 8u^2h^2)\tilde{y}_{N-2} - \frac{h^4\tilde{V}^2}{\left[1+\gamma-\tilde{y}_{N-2}\right]^2} = 0$$ $$F_{N-1} = 2\tilde{y}_{N-3} - 8(1 + u^2h^2)\tilde{y}_{N-2} + (6 + 8u^2h^2)\tilde{y}_{N-1} - \frac{h^4\tilde{V}^2}{\left[1+\gamma-\tilde{y}_{N-1}\right]^2} = 0$$
AXIAL RELATION
$$F_u = 3\Sigma_0 - u^2 + \frac{(g_0/t)^2}{h}\left\{ -\frac{1}{2}\tilde{y}_1^2 + \frac{1}{2}\tilde{y}_{N-2}^2 + \tilde{y}_{N-1}^2 \right.$$ $$\left. + \sum_{n=1}^{\frac{N-3}{2}} \tilde{y}_{2n-1}(\tilde{y}_{2n-1} - \tilde{y}_{2n+1}) + 2\tilde{y}_{2n}(\tilde{y}_{2n} - \tilde{y}_{2n+2}) \right\} = 0$$

also becomes singular when α tends to unity. Referring to Equation (3.130), it is noticed that first integral vanishes for $\alpha = 1$, so that only the second integral needs consideration. Since $\tilde{y}_0' = 0$ for $\alpha = 1$, it follows from Equation (3.134) that the functions $\phi_i(u, \beta, h)$ must be excluded from Equation (3.133). If furthermore $\tilde{y}_0$ is set to zero, Equation (3.135) is then transformed to,

$$F_u = 3\Sigma_0 - u^2 + \frac{(g_0/t)^2}{h}\left\{ -\frac{1}{2}\tilde{y}_1^2 + \frac{1}{2}\tilde{y}_{N-2}^2 + \tilde{y}_{N-1}^2 \right.$$
$$\left. + \sum_{n=1}^{\frac{N-3}{2}} \tilde{y}_{2n-1}(\tilde{y}_{2n-1} - \tilde{y}_{2n+1}) + 2\tilde{y}_{2n}(\tilde{y}_{2n} - \tilde{y}_{2n+2}) \right\} = 0 \tag{3.138}$$

Table 3.7 lists corrected Finite Difference equations for the nonzero-tension electrostatic actuation problem with $\alpha = 1$.

3.4.2.2 Solution of the Finite Difference Equations

Finite Difference equations shown in Table (3.6) compose $N+1$ equations in the unknown nodal deflection vector $\vec{y} = \begin{bmatrix} \tilde{y}_0, & \tilde{y}_1, & \cdots \tilde{y}_{N-1} \end{bmatrix}$ and the axial variable u. In order to solve these equations for the depicted unknowns, different strategies are tried in succession which are discussed next.

Direct Solution Approach:

In the direct solution approach, the method outlined in §3.4.1.4 is extended by concatenating the unknowns $\vec{y}$ and u into a new array $\vec{v}$. Jacobian matrix is then evaluated from

$$J_{ij} = \frac{\partial F_i}{\partial v_j}$$

It can verified trivially that J ceases to be a 5-band diagonally-dominant one due to global dependence of u on $\vec{y}$. After implementing subroutines for the equations F_i and the Jacobian matrix J, it is attempted to solve the relevant system of equations by calling `fsolve`. Unfortunately, a uniform convergence could not be attained and solutions are noted to be very sensitive to the supplied initial guess. Providing *smart* initial guesses (like analytical solutions of approximate equivalent problems) also proved fruitless.

Shooting Approach with Direct Substitution:

Having become unsuccessful with the previous method, a shooting approach described in [82] is adapted for the current problem next. In this approach, nodal equations F_i and the discretized axial relation F_u are handled separately: The problem is treated to be consisting of two distinct systems, $\vec{F}$ and F_u, whose corresponding unknowns $\vec{y}$ and u are assumed known from the viewpoint of the other one. In other words, u is assumed known when solving $\vec{F}$ and vice versa[7]. A solution is then attempted with the following procedure:

i. An initial guess is calculated for the unknowns $\vec{y}$ and u from the approximate uni-

---

[7] Note that Jacobian matrix of the system $\vec{F}$ becomes a 5-band diagonally-dominant matrix in this case.

form distributed load problem: Employing $q_e(\tilde{x})$ in the undeflected position, which is in fact a uniform distributed load, deflection profile $\vec{y}_{const}$ and u_{const} are calculated using the analytical derivation established in §3.2.1.3.

ii. $\vec{y}_1$ is evaluated for $u = u_{const}$ by calling `fsolve` with an associated initial guess $\vec{y}_{const}$.

iii. u_1 is calculated from F_u using $\vec{y}_1$ determined in the previous step.

iv. $\vec{y}_2$ is computed for $u = u_1$ by calling `fsolve` with the initial guess $\vec{y}_1$.

v. Steps (iii)-(iv) are repeated until $\tilde{y}_{max} = \tilde{y}_{N-1}$ and u converge within a prescribed tolerance.

Presented algorithm is demonstrated to work well for medium to large tensile residual stress levels. For low tensile stresses and higher $\frac{g_0}{t}$ ratios, however, convergence is noted to slow down considerably (and even break down for the stress-free case). The cause for such a phenomenon is later identified as an inherent positive feedback, which may be exemplified qualitatively for the stress-free case as follows: Suppose a small value of u is generated in an iteration step. For a small u, $\tilde{y}_{max}$ tends to be large (since smaller tension would enable larger deflections physically) and when the relevant profile is substituted back to F_u, u is updated to a considerably large value. In the next iteration, $\tilde{y}_{max}$ becomes too small (as excessive tension reduces deflections appreciably), causing the next u value to be even smaller. Hence for the case of $\Sigma_0 = 0$, u and $\tilde{y}_{max}$ stagnate between two extreme values. A positive Σ_0 serves to introduce a means of damping into the iterations by weakening the feedback cycle in F_u, thus allowing convergence to be attained.

Perceived deficiency of the current method soon led to development of an improved one, as explained subsequently.

Shooting Approach with Interpolation:

Poor convergence attributes of the previous method can be improved dramatically when direct substitution approach is replaced with an interpolation-based one. This argument

(a) Linear   (b) Quadratic
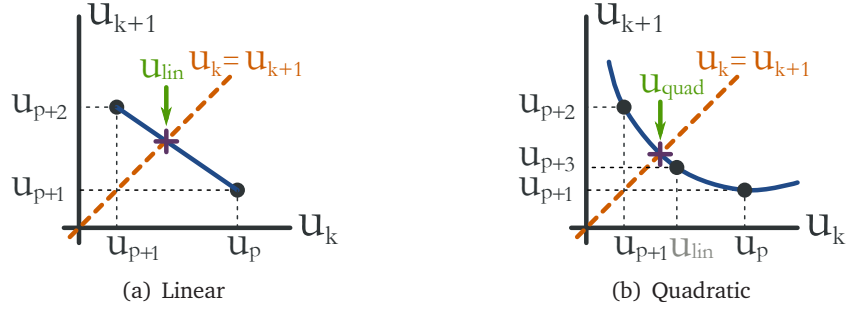
Figure 3.18: *An illustration of the proposed linear and quadratic interpolation approaches employed in the shooting method.*

has its roots in the following idea: It is wiser to monitor the outcomes in previous iterations and *shoot* a value based on those results rather than blindly using the outcome itself. Proposed approach makes use of the variable u for this purpose. Notice that convergence in u implies, u_k fed into the kth iteration step must generate an outcome u_{k+1} (from $u_k \rightarrow \vec{y}_{k+1} \rightarrow u_{k+1}$ cycle in the previous method) that is close to u_k. From a graphical point of view, if fed and generated values of u are plotted in u_k-u_{k+1} coordinates, these points must lie close to $u_k = u_{k+1}$ line. Exploiting the offset data of those points from this line, one can then estimate a proper u value that should be located *on* that line, i.e. the converged u value.

Figure 3.18 illustrates two methods for calculating a proper u estimate. The simpler linear interpolation method requires two $u_k - u_{k+1}$ pairs and returns the particular u value at the intersection of $u_k = u_{k+1}$ line and the line connecting the points. Note that such an approach inherently solves the stagnation problem occurring with the previous method by forcing u values away from the extreme bounds. The quadratic interpolation method employs three $u_k - u_{k+1}$ pairs and determines relevant u estimate from the intersection of $u_k = u_{k+1}$ line with the second order polynomial passing through these points. This latter interpolation method can be applied just after the linear interpolation and $u_k \rightarrow \vec{y}_{k+1} \rightarrow u_{k+1}$ iteration cycle in order to yield an improved u estimate.

Having established useful estimation means, skeleton of the improved shooting algorithm is then constructed as follows:

i. Initial guesses $\vec{y}_0 = \vec{y}_{\mathrm{const}}$ and $u_0 = u_{\mathrm{const}}$ are calculated from the approximate uniform distributed load problem by utilizing $q_{\mathrm{e}}(\tilde{x})$ in the undeflected position. In the case of a voltage sweep, however, those guesses are replaced with $\vec{y}$ and u of the nearest converged solution.

ii. $u_0 \to \vec{y}_1 \to u_1$ cycle is executed: $\vec{y}_1$ is evaluated for $u = u_0$ by calling `fsolve` with an associated initial guess $\vec{y}_0$. Subsequently, u_1 is calculated from F_{u} using $\vec{y}_1$.

iii. $u_1 \to \vec{y}_2 \to u_2$ cycle is executed.

iv. Having collected two $u_k - u_{k+1}$ pairs, a linear interpolation is conducted to obtain the next estimate $u = u_{\mathrm{lin},1}$. Subsequently, $u_{\mathrm{lin},1} \to \vec{y}_3 \to u_3$ cycle is executed.

v. With three $u_k - u_{k+1}$ pairs at hand, a quadratic interpolation is performed to determine the next estimate $u = u_{\mathrm{quad},1}$. Subsequently, $u_{\mathrm{quad},1} \to \vec{y}_4 \to u_4$ cycle is executed.

vi. Steps (iv)-(v) are repeated until $\tilde{y}_{\mathrm{max}} = \tilde{y}_{N-1}$ and u converge within a prescribed tolerance.

Proposed interpolation-based shooting algorithm is found to work successfully. In particular, not only previously mentioned stagnation problem is removed, but also convergence rate is increased substantially: It is observed that a fractional error of 10^{-6} is attainable in both $\tilde{y}_{\mathrm{max}}$ and u with only 2-3 iterations for the residual stress-free case.

Having realized an improved numerical solution algorithm, it is next continued to an investigation of convergence and consistency properties of obtained Finite Difference solutions.

Convergence and Consistency Analyses

Convergence of the Finite Difference formulation for the nonzero electrostatic actuation problem is analyzed using the method outlined in §3.4.1.4. For this purpose, problem parameters γ, g_0/t and α are fixed, a voltage sweep is performed up to the pull-in border with 10 points, and rms errors in $\tilde{y}_{\mathrm{max}}$ and u are monitored as a function of N for several Σ_0 values. Obtained results are presented in Figure 3.19.

105
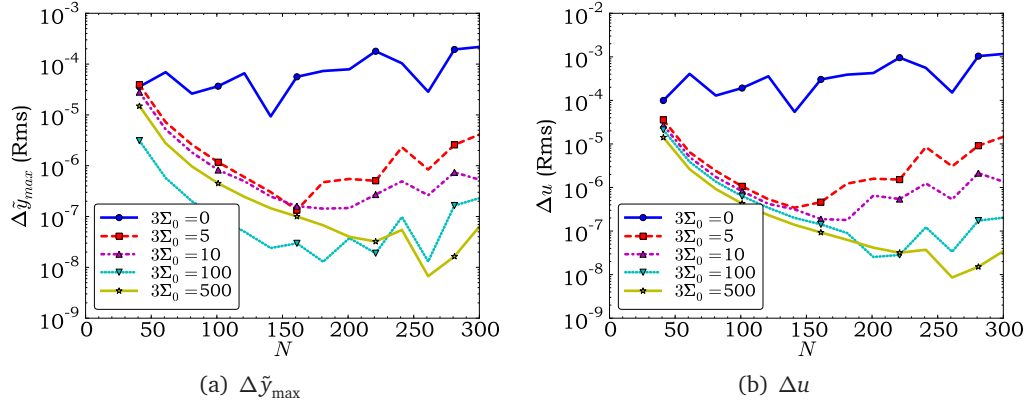
Figure 3.19: *Rms convergence error in $\tilde{y}_{\max}$ and u as a function of N for the non-zero tension electrostatic actuation problem with Σ_0 as a parameter ($\gamma = 0.03$, $\alpha = 0.5$, $g_0/t = 2.0$).*

It is observed from Figure 3.19(a) that worst rms error in $\tilde{y}_{\max}$ is about 2×10^{-4} which occurs for $\Sigma_0 = 0$. With increased Σ_0, the effect of N on convergence becomes prominent and relevant error decreases further. Rms error in u follows essentially the same trend with that of $\tilde{y}_{\max}$, except for a level shift: Figure 3.19(b) depicts that worst rms error in u is about 1.2×10^{-3}. Based on the obtained results and following the convention with the zero-tension problem, it becomes reasonable to pick $N = 251$ for the number of grid points, which yields an accuracy sufficient for simulation purposes.

In order to study consistency of the Finite Difference solutions for the non-zero tension electrostatic actuation problem, relevant solutions are compared with the zero-tension ones. Justification for such an approach can be described as follows: It was established in §3.4.1.4 that Finite Difference solutions of the zero-tension problem were consistent with the original system, which was demonstrated from the good agreement with the approximate analytical solution. It is moreover expected that nonzero-tension solutions must approach to the zero-tension ones for $\Sigma_0 = 0$ and small g_0/t ratios. Hence, one can assess consistency of the former by observing overlapping $\tilde{y}_{\max} - \tilde{V}$ traces of zero-tension and non-zero tension solutions (with $\Sigma_0 = 0$), at least for small deflections. Figure 3.20 provides such traces for a sample problem configuration. An inspection of Figure 3.20 shows that curves with $\Sigma_0 = 0$ indeed agree well with the corresponding zero-tension solution. Furthermore, the agreement range is noted to improve with smaller g_0/t ratios,

as expected. In the light of these observations, consistency of the Finite Difference solutions can be ascertained for the nonzero-tension electrostatic actuation problem.

It might be worthwhile to examine Figure 3.20 further. The effect of axial tension on deflection characteristics is readily noticed upon a comparison of zero-tension solution with nonzero-tension ones. In particular, as evidenced by $3\Sigma_0 = 10$ trace, introduction of a tensile residual stress into the system reduces the deflections considerably. Increasing g_0/t ratio, moreover, serves to amplify nonlinear stretching effects and thus to impede deflections as the voltage is increased. Therefore, ignoring the axial effects in a fixed-fixed beam system calls for a significant degradation in accuracy unless the operation is confined within a very small fraction of the air-gap ($\sim 10\%$ for $\Sigma_0 = 0$, even smaller for $\Sigma_0 > 0$).
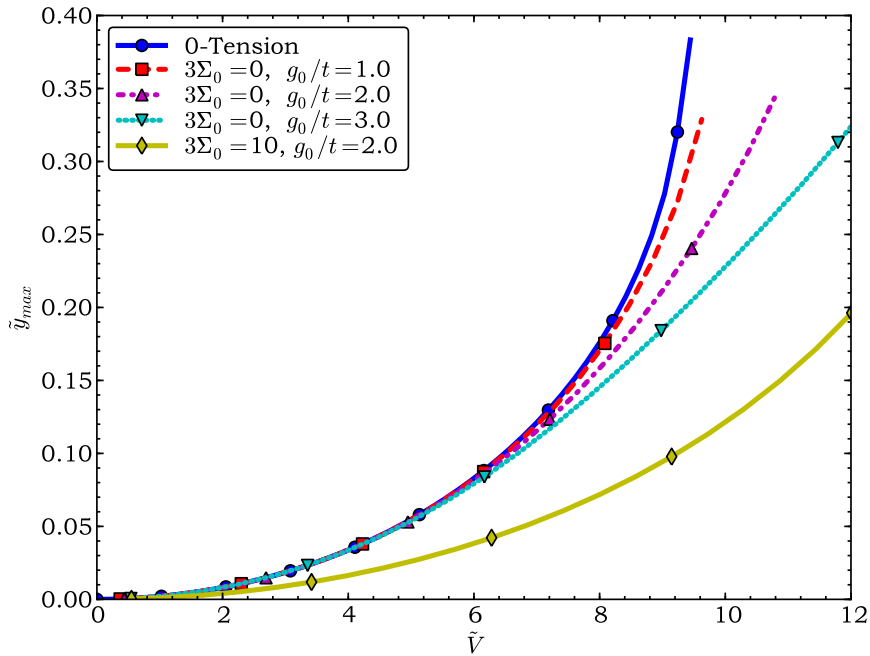
Figure 3.20: *A comparison between $\tilde{y}_{\max} - \tilde{V}$ characteristics of zero-tension and non-zero tension electrostatic actuation problems ($\gamma = 0.03$, $\alpha = 0.5$, $N = 251$).*

3.4.2.3 Pull-in Phenomenon

According to the experience gained in zero-tension electrostatic actuation problem, one would expect to observe pull-in phenomenon if the voltage range in Figure 3.20 is extended. Such a behavior is indeed present for the non-zero tension problem as Figure 3.21 demonstrates. A difference is noted, however, between zero-tension and nonzero-tension solutions around corresponding pull-in regions: For the zero-tension problem, the slope of the curve $\frac{\partial \tilde{y}_{\max}}{\partial \tilde{V}}$ tends to $+\infty$ at pull-in; while the nonzero-tension solutions exhibit a finite slope at their cusp. It is moreover recognized that pointed difference becomes more pronounced for increased g_0/t ratios. Furthermore, maximum deflection at the pull-in does not seem to exceed $0.4g_0$ even for high g_0/t ratios, which in reality should according to [113]. These observations actually indicate a weakness of the proposed Finite Difference algorithm for the nonzero-tension problem: Relevant solutions become unstable *prior to* actual pull-in. This discovered deficiency of implemented Finite Difference algorithm thus, unfortunately, precludes accurate pull-in voltage extraction for beams in axial tension.

In order to compensate for the lack of an accurate pull-in voltage extraction tool and to be able to predict pull-in voltages hereafter for beams in axial tension, analytical pull-in voltage expressions are investigated in the next section.

3.5 Pull-in Analyses and Development of Pull-in Voltage Expressions

In this section, mechanical knowledge accumulated throughout the previous sections is utilized in order to derive expressions for the pull-in voltage. On-going study starts with a one-dimensional pull-in analysis wherein analytical expressions are established for relevant parameters. Subsequently, corrections are applied to the proposed formulation using the results of Finite Difference simulations. Finally, obtained formulation is tested for sample configurations reported in the literature.

3.5.1 One-Dimensional Pull-in Analysis

Following derivation is based on the widely-known one-dimensional pull-in analysis, a good example of which can be found in [85]. Figure 3.22 illustrates the problem con-
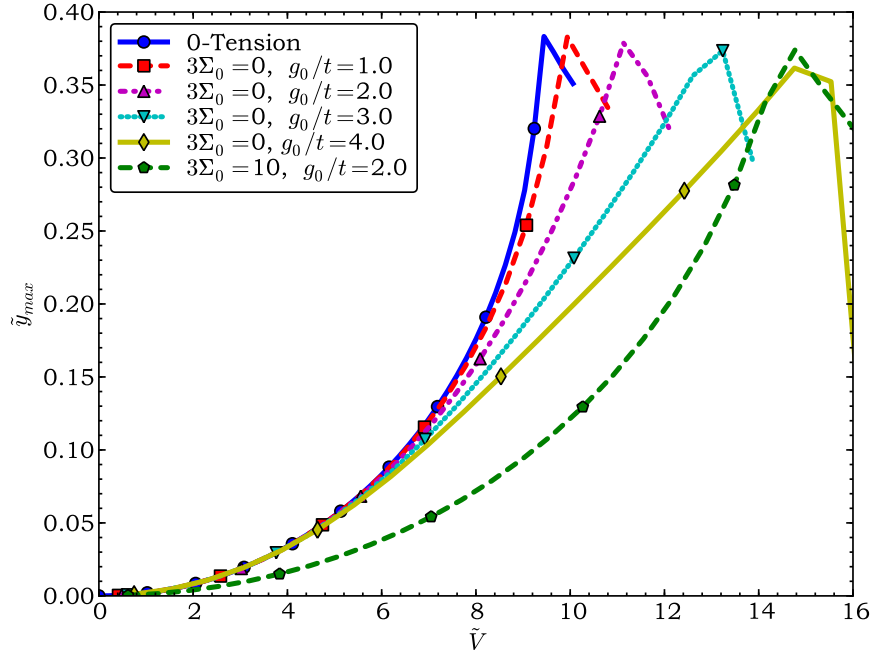
Figure 3.21: *Typical $\tilde{y}_{\max} - \tilde{V}$ characteristics for the non-zero tension electrostatic actuation problem depicting the pull-in instability ($\gamma = 0.03$, $\alpha = 0.5$, $N = 251$).*

figuration: A massless plate is attached to a lumped spring and is suspended above an electrode with an initial air-gap spacing of g_0. The electrode has a length/width of W/w respectively and is covered with a dielectric layer of thickness t_{di} and relative permittivity ε_{di}. The lumped spring has an effective stiffness of k_{eff} and its other end is affixed to an immobile support. As depicted in Figure 3.22(b), application of a non-zero voltage V between the plate and the electrode causes the plate to deflect by an amount y. In order to quantify the deflection-voltage characteristics of the presented system, one begins by writing the force-balance equation:

$$F_e = F_r$$

where F_e and F_r are the electrostatic attraction force and the restoring force of the spring acting on the plate respectively. Employing the expression for $q_e(x)$ derived in §3.3, it is easy to show that

$$F_e = \frac{\varepsilon_0 w W V^2}{2 \left[g_0 + t_{di}/\varepsilon_{di} - y \right]^2} \tag{3.139}$$

Moreover, F_r is given by

$$F_r = y k_{eff}(y) \tag{3.140}$$

(a) $V = 0$ (b) $V \neq 0$
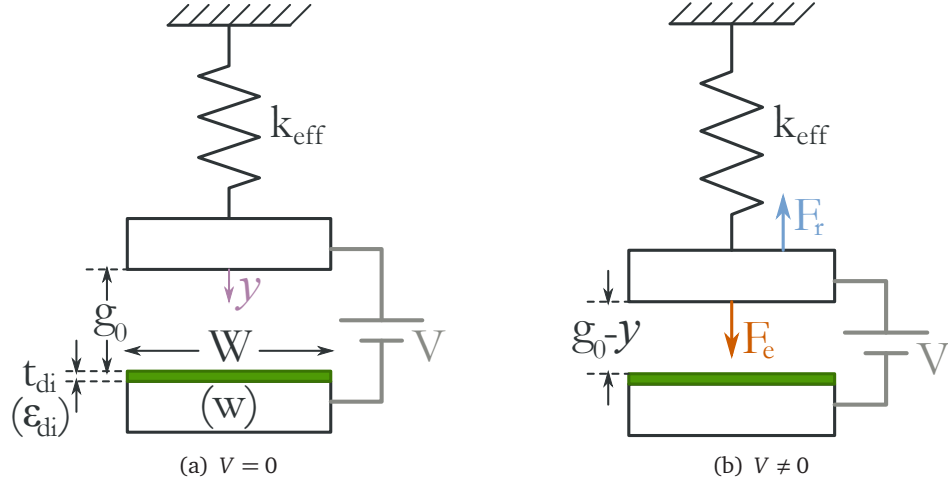
Figure 3.22: *An illustration of one-dimensional lumped model for pull-in analysis.*

In general, k_{eff} might depend on the deflection y and Equation (3.140) reflects this dependency explicitly. Combining Equations (3.139) and (3.140), one arrives at

$$y k_{\text{eff}}(y) = \frac{\varepsilon_0 w W V^2}{2 \left[g_0 + t_{\text{di}}/\varepsilon_{\text{di}} - y \right]^2} \tag{3.141}$$

It is convenient to normalize Equation (3.141) using previously defined dimensionless parameters $\tilde{y}$, γ, α and $\tilde{V}$ as:

$$\tilde{y} k_{\text{eff}}(\tilde{y}) = \frac{E' \alpha w \, \tilde{V}^2}{12 \left(L/t \right)^3 \left[1 + \gamma - \tilde{y} \right]^2} \tag{3.142}$$

The parameters E', α, L and t in Equation (3.142) actually pertain to beam properties; but they can be treated as parameters of k_{eff} owing to lumped representation of the actual structure.

Expressions for pull-in parameters can be found by setting the derivative of $\tilde{V}$ with respect to $\tilde{y}$ to zero. Taking derivatives of both sides of Equation (3.142) with respect to $\tilde{y}$ and re-arranging yields,

$$\frac{\partial \tilde{V}}{\partial \tilde{y}} = \frac{6 \left(L/t \right)^3}{E' \alpha w \tilde{V}} \frac{\partial}{\partial \tilde{y}} \left\{ \tilde{y} (1 + \gamma - \tilde{y})^2 \, k_{\text{eff}}(\tilde{y}) \right\} \tag{3.143}$$

Setting Equation (3.143) to zero gives the following characteristic equation for pull-in deflection $\tilde{y}_{\text{PI}}$:

$$(1 + \gamma - \tilde{y}_{\text{PI}}) \left[(1 + \gamma - 3\tilde{y}_{\text{PI}}) \, k_{\text{eff}}(\tilde{y}_{\text{PI}}) + \tilde{y}_{\text{PI}} (1 + \gamma - \tilde{y}_{\text{PI}}) \left. \frac{\partial k_{\text{eff}}}{\partial \tilde{y}} \right|_{\tilde{y} = \tilde{y}_{\text{PI}}} \right] = 0 \tag{3.144}$$

Since $\tilde{y} \leq 1$, first factor appearing in Equation (3.144) cannot be zero. Accordingly, $\tilde{y}_{\text{PI}}$ must satisfy:

$$(1 + \gamma - 3\tilde{y}_{\text{PI}}) \, k_{\text{eff}}(\tilde{y}_{\text{PI}}) + \tilde{y}_{\text{PI}}(1 + \gamma - \tilde{y}_{\text{PI}}) \left. \frac{\partial k_{\text{eff}}}{\partial \tilde{y}} \right|_{\tilde{y} = \tilde{y}_{\text{PI}}} = 0 \qquad (3.145)$$

Once a solution is found for $\tilde{y}_{\text{PI}}$ from Equation (3.145), pull-in voltage $\tilde{V}_{\text{PI}}$ can be determined from Equation (3.142) with $\tilde{y} = \tilde{y}_{\text{PI}}$.

It is informative to investigate characteristic equation (3.145) and associated $\tilde{V}_{\text{PI}}$ for zero-tension and nonzero-tension cases using the effective spring constant formulated in §3.2.4. These cases are discussed in the subsequent articles.

3.5.1.1 Pull-in Parameters for Zero-Tension Case

Letting $u \to 0$ in Equation (3.42) and using the property

$$\lim_{u \to 0} \overline{\zeta}(u, \alpha) = \alpha^4 - 2\alpha^3 + 2\alpha$$

effective spring constant for zero-tension case can be obtained as,

$$k_{\text{eff}} = \frac{32E'w}{(L/t)^3 (\alpha^3 - 2\alpha^2 + 2)} \qquad (3.146)$$

It is noticed from Equation (3.146) that k_{eff} is independent of $\tilde{y}$. Using this information in Equation (3.145) gives

$$(1 + \gamma - 3\tilde{y}_{\text{PI}}) \, k_{\text{eff}} = 0$$

or

$$\tilde{y}_{\text{PI}} = \frac{1 + \gamma}{3} \qquad (3.147)$$

Equation (3.147) states that normalized pull-in deflection solely depends on γ in a linear manner when axial effects are ignored. Substitution of Equations (3.146)-(3.147) in (3.142) then establishes the pull-in voltage expression for zero-tension case:

$$\tilde{V}_{\text{PI}} = \sqrt{\frac{512}{9} \frac{(1 + \gamma)^3}{\alpha^4 - 2\alpha^3 + 2\alpha}} \qquad (3.148)$$

111

3.5.1.2 Pull-in Parameters for Nonzero-Tension Case

For the nonzero-tension case, axial parameter u enters into the list of problem variables. Following Equation (3.42), effective stiffness of the spring can then be expressed as,

$$k_{\text{eff}} = \frac{32E'\alpha w}{(L/t)^3 \, \overline{\zeta}(u,\alpha)} \tag{3.149}$$

k_{eff} given in Equation (3.149) is noted to depend on $\tilde{y}$ *implicitly* through the axial relation:

$$u^2 = \tilde{y}^2 \left(\frac{g_0}{t}\right)^2 \Psi(u,\alpha) + 3\Sigma_0 \tag{3.150}$$

In order to calculate $\partial k_{\text{eff}}/\partial \tilde{y}$, one may apply chain rule

$$\frac{\partial k_{\text{eff}}}{\partial \tilde{y}} = \frac{\partial k_{\text{eff}}}{\partial u} \frac{\partial u}{\partial \tilde{y}} \tag{3.151}$$

Partial derivative of k_{eff} with respect to u can be evaluated from Equation (3.149):

$$\frac{\partial k_{\text{eff}}}{\partial u} = -\frac{32E'\alpha w}{(L/t)^3} \frac{\frac{\partial \overline{\zeta}(u,\alpha)}{\partial u}}{\overline{\zeta}^2(u,\alpha)} \tag{3.152}$$

In order to calculate $\partial u/\partial \tilde{y}$, one may differentiate both sides of Equation (3.150) with respect to u and re-arrange the terms to obtain,

$$\frac{\partial \tilde{y}}{\partial u} = \frac{2u - \tilde{y}^2 \left(\frac{g_0}{t}\right)^2 \frac{\partial \Psi}{\partial u}}{2\tilde{y} \left(\frac{g_0}{t}\right)^2 \Psi(u,\alpha)}$$

or

$$\frac{\partial u}{\partial \tilde{y}} = \frac{1}{\frac{\partial \tilde{y}}{\partial u}} = \frac{2\tilde{y} \left(\frac{g_0}{t}\right)^2 \Psi(u,\alpha)}{2u - \tilde{y}^2 \left(\frac{g_0}{t}\right)^2 \frac{\partial \Psi}{\partial u}} \tag{3.153}$$

Equations (3.152) and (3.153) can be combined to yield,

$$\frac{\partial k_{\text{eff}}}{\partial \tilde{y}} = -\frac{64E'\alpha w}{(L/t)^3} \frac{\frac{\partial \overline{\zeta}(u,\alpha)}{\partial u}}{\overline{\zeta}^2(u,\alpha)} \frac{\tilde{y} \left(\frac{g_0}{t}\right)^2 \Psi(u,\alpha)}{2u - \tilde{y}^2 \left(\frac{g_0}{t}\right)^2 \frac{\partial \Psi}{\partial u}} \tag{3.154}$$

Substituting Equation (3.154) into the characteristic equation (3.145) and performing subsequent manipulation then gives:

$$\frac{32E'\alpha w}{(L/t)^3 \overline{\zeta}^2(u_{\text{PI}},\alpha)} \left\{ (1 + \gamma - 3\tilde{y}_{\text{PI}}) \, \overline{\zeta}(u_{\text{PI}},\alpha) \right.$$

$$\left. - 2(1 + \gamma - \tilde{y}_{\text{PI}}) \frac{u_{\text{PI}}^2 - 3\Sigma_0}{2u_{\text{PI}} - \tilde{y}_{\text{PI}}^2 \left(g_0/t\right)^2 \left.\frac{\partial \Psi}{\partial u}\right|_{u=u_{\text{PI}}}} \left.\frac{\partial \overline{\zeta}}{\partial u}\right|_{u=u_{\text{PI}}} \right\} = 0$$

which in turn implies

$$(1 + \gamma - 3\tilde{y}_{\mathrm{PI}}) \left[2u_{\mathrm{PI}} - \tilde{y}_{\mathrm{PI}}^2 (g_0/t)^2 \left. \frac{\partial \Psi}{\partial u} \right|_{u=u_{\mathrm{PI}}} \right] \overline{\zeta}(u_{\mathrm{PI}}, \alpha)$$
$$= 2(1 + \gamma - \tilde{y}_{\mathrm{PI}}) \left(u_{\mathrm{PI}}^2 - 3\Sigma_0 \right) \left. \frac{\partial \overline{\zeta}}{\partial u} \right|_{u=u_{\mathrm{PI}}} \tag{3.155}$$

Notice that the quantities $\tilde{y}_{\mathrm{PI}}$ and u_{PI} are further related by the axial relation (3.150):

$$u_{\mathrm{PI}}^2 = \tilde{y}_{\mathrm{PI}}^2 \left(\frac{g_0}{t} \right)^2 \Psi(u_{\mathrm{PI}}, \alpha) + 3\Sigma_0 \tag{3.156}$$

The pull-in parameters $\tilde{y}_{\mathrm{PI}}$ and u_{PI} can be solved from Equations (3.155)-(3.156) via numerical means. Having determined those unknowns, pull-in voltage can be calculated from Equation (3.142) as,

$$\tilde{V}_{\mathrm{PI}} = \sqrt{384 \frac{\tilde{y}_{\mathrm{PI}} (1 + \gamma - \tilde{y}_{\mathrm{PI}})^2}{\overline{\zeta}(u_{\mathrm{PI}}, \alpha)}} \tag{3.157}$$

Equations (3.155)-(3.157) are valid for tensile axial state. If one is interested in compressive axial state instead, corresponding relations can be obtained via the transformation $u \to \mathrm{j}u$. Relevant results are

$$(1 + \gamma - 3\tilde{y}_{\mathrm{PI}}) \left[2u_{\mathrm{PI}} + \tilde{y}_{\mathrm{PI}}^2 (g_0/t)^2 \left. \frac{\partial \Psi_{\mathrm{c}}}{\partial u} \right|_{u=u_{\mathrm{PI}}} \right] \overline{\zeta}_{\mathrm{c}}(u_{\mathrm{PI}}, \alpha)$$
$$= 2(1 + \gamma - \tilde{y}_{\mathrm{PI}}) \left(u_{\mathrm{PI}}^2 + 3\Sigma_0 \right) \left. \frac{\partial \overline{\zeta}_{\mathrm{c}}}{\partial u} \right|_{u=u_{\mathrm{PI}}} \tag{3.158a}$$

$$-u_{\mathrm{PI}}^2 = \tilde{y}_{\mathrm{PI}}^2 \left(\frac{g_0}{t} \right)^2 \Psi_{\mathrm{c}}(u_{\mathrm{PI}}, \alpha) + 3\Sigma_0 \tag{3.158b}$$

$$\tilde{V}_{\mathrm{PI}} = \sqrt{384 \frac{\tilde{y}_{\mathrm{PI}} (1 + \gamma - \tilde{y}_{\mathrm{PI}})^2}{\overline{\zeta}_{\mathrm{c}}(u_{\mathrm{PI}}, \alpha)}} \tag{3.158c}$$

Figure 3.23 provides plots of the pull-in parameters $\tilde{y}_{\mathrm{PI}}$ and $\tilde{V}_{\mathrm{PI}}$ with respect to g_0/t for several Σ_0 values. It is observed from Figure 3.23(a) that stable travel range of the lumped system can be extended up to $0.6g_0$ for increased g_0/t ratios, a result which supports the argument in [113]. It is moreover noted that residual stress has an apparent impact on $\tilde{y}_{\mathrm{PI}}$: For $g_0/t = 2.0$ as an example, $\tilde{y}_{\mathrm{PI}}$ ranges between 0.36-0.55 as $3\Sigma_0$ is varied in $[-5, 100]$ interval. A comparison of these $\tilde{y}_{\mathrm{PI}}$ results with that of the zero-tension one clearly highlights the lack of accuracy of the latter formulation. Axial factors also have an appreciable effect on $\tilde{V}_{\mathrm{PI}}$ as depicted in Figure 3.23(b): Pull-in voltage is

113
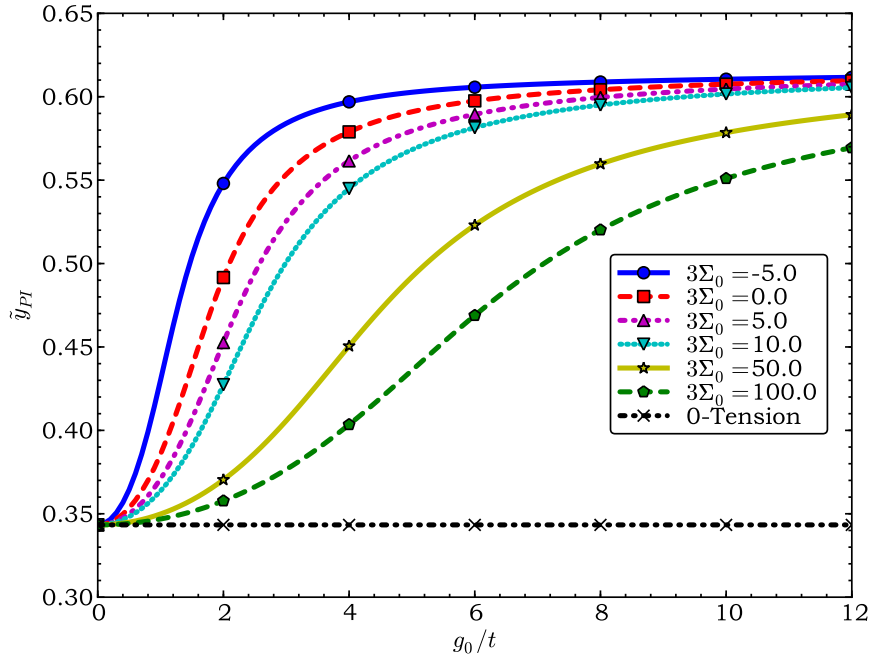
(a) Pull-in deflection ($\tilde{y}_{PI}$)
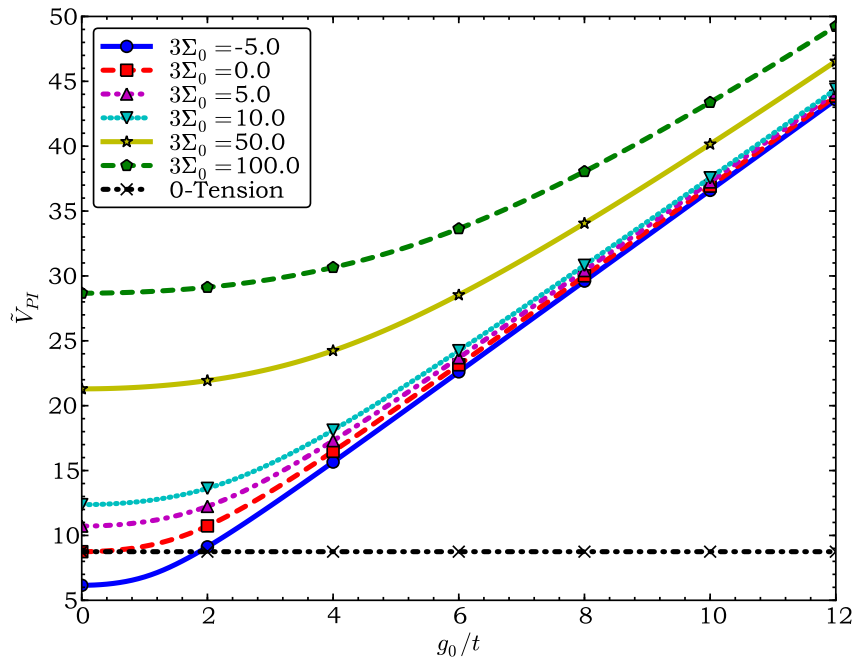
(b) Pull-in voltage ($\tilde{V}_{PI}$)

Figure 3.23: *A plot of pull-in parameters $\tilde{y}_{PI}$ and $\tilde{V}_{PI}$ as a function of g_0/t for several Σ_0 values ($\gamma = 0.03$, $\alpha = 0.5$).*

recognized to increase with higher g_0/t ratios and increasing Σ_0 values, a trend which confirms physical intuition. Notice furthermore from the same figure that zero-tension $\tilde{V}_{\mathrm{PI}}$ formulation appears to be applicable only to the particular case with $\Sigma_0 = 0$ and $g_0/t \leq 1$.

3.5.2 Corrections to Pull-in Formulation using Finite Difference Simulation Results

Pull-in parameter expressions derived in §3.5.1 do not account for some of the higher-dimensional properties of the actual fixed-fixed beam system and relevant formulation needs to be corrected in order to maintain a desired level of accuracy. Two main attributes one-dimensional model fails to capture are:

- *Charge-redistribution* resulting from position-dependent beam deflection profile,

- *Fringing capacitances* caused by out-of-plane and in-plane fringing electric fields.

First of these attributes yields a position-dependent electrostatic force and its effects can be characterized using results of the Finite Difference simulations detailed earlier in this chapter. The latter one, on the other hand, is not considered in this work as attention is particularly restricted to wide beams for which the effect of out-of-plane[8] fringing fields is negligible[9] [86].

In order to quantify the effect of charge-redistribution on pull-in parameters, relevant quantities must be extracted first from Finite Difference simulations. It was noted in §3.4.2.3 that such a task could not be accomplished with the nonzero-tension implementation at hand due to instability of the algorithm before the actual pull-in. Consequently, it is decided to rely on simulation results of the zero-tension implementation. One might argue at this point about the accuracy of such a partial characterization; however, relevant procedure turns out to yield acceptable results as it will be shown shortly.

---

[8] The effect of in-plane fringing fields for the case of partial electrodes ($\alpha \neq 1$) can be shown to be negligible for small g_0 [123].

[9] Relevant effect can be incorporated into Finite Difference simulations of narrow beams with an additional correction term; however, such a procedure is not attempted in this work for the sake of simplicity.

(a) $f_{\tilde{V}}(\alpha)$ (b) $f_{\tilde{y}}(\alpha)$
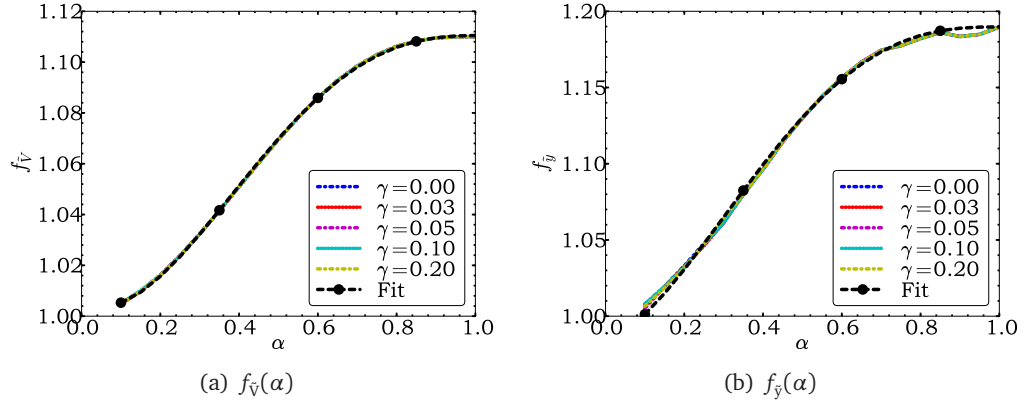
Figure 3.24: *Coefficients $f_{\tilde{V}}(\alpha)$ and $f_{\tilde{y}}(\alpha)$ describing the effect of charge re-distribution on $\tilde{V}_{\mathrm{PI}}$ and $\tilde{y}_{\mathrm{PI}}$. Fourth-order polynomials are fitted for each coefficient.*

3.5.2.1 Characterization of the Charge Re-distribution Effect

Charge re-distribution effect is characterized by exploring dependencies of simulated pull-in quantities $\tilde{V}_{\mathrm{PI}}$ and $\tilde{y}_{\mathrm{PI}}$ on zero-tension problem parameters γ and α in the light of the functional forms established in §3.5.1. For this purpose, $\tilde{V}_{\mathrm{PI}}$ and $\tilde{y}_{\mathrm{PI}}$ are first extracted for a wide range of γ and α parameters via a binary search algorithm mentioned in §3.4.1.5. Next, it is attempted to model the relevant effect as a simple multiplicative coefficient by letting

$$\tilde{y}_{\mathrm{PI,FD}} = f_{\tilde{y}}\, \tilde{y}_{\mathrm{PI,1D}}$$
$$\tilde{V}_{\mathrm{PI,FD}} = f_{\tilde{V}}\, \tilde{V}_{\mathrm{PI,1D}}$$

(3.159)

where subscripts FD and 1D denote quantities obtained from Finite Difference simulations and one-dimensional analysis respectively. Upon a survey of the coefficients $f_{\tilde{V}}$ and $f_{\tilde{y}}$, a univariate α dependence is discovered which can be described accurately as a fourth-order polynomial. Figure 3.24 presents obtained results. Figure 3.24(a) shows that pull-in voltage increases slightly due to charge re-distribution, with the effect growing as α tends to unity. A similar trend is noted for pull-in deflection as Figure 3.24(b) demonstrates. Physical reasoning supports these observations: As α gets smaller, electrostatic force gets confined to a smaller span in which position dependence would eventually cease for small enough α, thus making the coefficients $f_{\tilde{V}}$ and $f_{\tilde{y}}$ approach unity. Conversely, as α increases, beam center becomes subject to a higher electrostatic force and it becomes harder for the beam to reach pull-in since off-center sections experience less

116

Table 3.8: *Fourth-order polynomial fits for $f_{\tilde{V}}(\alpha)$ and $f_{\tilde{y}}(\alpha)$.*

FUNCTION	FITTED POLYNOMIAL	POLYNOMIAL COEFFICIENTS
$f_{\tilde{V}}(\alpha)$	$\sum_{n=0}^{4} a_n \alpha^n$	$a_4 = 0.338,\ a_3 = -0.960$ $a_2 = 0.801,\ a_1 = -0.074$ $a_0 = 1.006$
$f_{\tilde{y}}(\alpha)$	$\sum_{n=0}^{4} a_n \alpha^n$	$a_4 = 0.489,\ a_3 = -1.283$ $a_2 = 0.893,\ a_1 = \ \ \ 0.109$ $a_0 = 0.983$

overall attraction; a response which is equivalent to elevated $f_{\tilde{V}}$ and $f_{\tilde{y}}$ values.

Table 3.8 provides the coefficients of the fourth-order polynomials fitted for $f_{\tilde{V}}(\alpha)$ and $f_{\tilde{y}}(\alpha)$.

3.5.2.2 Modified Formulation for Pull-in Parameters

Having characterized charge re-distribution effect and established expressions for its correction, final forms of the pull-in quantities may now be formulated. At this point, it is preferred to develop two types of formulation: One which is prominently based on one-dimensional zero-tension model and hence simpler to employ, and another which includes intricate effects of axial tension/compression on $\tilde{y}_{\mathrm{PI}}$ and consequently more complex to utilize. These types are discussed below.

1D Zero-Tension Model Based (0AX) Formulation

This model does not account for the dependence of pull-in deflection on axial effects and assumes the following form for $\tilde{y}_{\mathrm{PI}}$:

$$\tilde{y}_{\mathrm{PI}} = f_{\tilde{y}}(\alpha)\,\frac{1+\gamma}{3} \tag{3.160}$$

For the pull-in voltage, on the other hand, the model incorporates axial effects by replacing zero-tension effective stiffness with the nonzero-tension one in Equation (3.142). After correcting for the charge re-distribution effect, assumed $\tilde{V}_{\mathrm{PI}}$ form becomes:

$$\tilde{V}_{\mathrm{PI}} = f_{\tilde{V},2}(\alpha)\sqrt{\frac{512}{9}\frac{(1+\gamma)^3}{\overline{\zeta}(u_{\mathrm{PI}},\alpha)}} \tag{3.161a}$$

where

$$f_{\tilde{V},2}(\alpha) = f_{\tilde{V}}(\alpha) \left[\frac{3 - f_{\tilde{y}}(\alpha)}{2} \right] \sqrt{f_{\tilde{y}}(\alpha)} \qquad (3.161b)$$

In Equation (3.161a), u_{PI} is determined from the axial relation (3.156) with the assumed form of $\tilde{y}_{\mathrm{PI}}$.

1D Nonzero-Tension Model Based (NAX) Formulation

This latter model is essentially a repetition of the corresponding one-dimensional one except for a correction term for charge re-distribution effects. Relevant formulation for tensile axial state is repeated below for convenience:

$$(1 + \gamma - 3\tilde{y}_{\mathrm{PI}}) \left[2u_{\mathrm{PI}} - \tilde{y}_{\mathrm{PI}}^2 (g_0/t)^2 \left. \frac{\partial \Psi}{\partial u} \right|_{u=u_{\mathrm{PI}}} \right] \overline{\zeta}(u_{\mathrm{PI}}, \alpha)$$
$$= 2(1 + \gamma - \tilde{y}_{\mathrm{PI}}) \left(u_{\mathrm{PI}}^2 - 3\Sigma_0 \right) \left. \frac{\partial \overline{\zeta}}{\partial u} \right|_{u=u_{\mathrm{PI}}} \qquad (3.162a)$$

$$u_{\mathrm{PI}}^2 = \tilde{y}_{\mathrm{PI}}^2 \left(\frac{g_0}{t} \right)^2 \Psi(u_{\mathrm{PI}}, \alpha) + 3\Sigma_0 \qquad (3.162b)$$

$$\tilde{V}_{\mathrm{PI}} = f_{\tilde{V}}(\alpha) \sqrt{384 \frac{\tilde{y}_{\mathrm{PI}} (1 + \gamma - \tilde{y}_{\mathrm{PI}})^2}{\overline{\zeta}(u_{\mathrm{PI}}, \alpha)}} \qquad (3.162c)$$

Results can be extended to compressive axial state via the transformation $u \to \mathrm{j}\,u$. It can be realized from Equation (3.162) that a correction is not applied to $\tilde{y}_{\mathrm{PI}}$. This choice is motivated partly by self-determined nature of the relevant parameter and mainly by observed overestimation of pull-in voltages.

3.5.3 Validation of the Proposed Pull-in Formulations

Having completed development of proposed pull-in formulations, their validity is investigated next. For this purpose, sample fixed-fixed beam configurations are surveyed in the literature whose pull-in characteristics are characterized accurately using Finite Element Analysis (FEA) software. In particular, thirteen such configurations are found and these are listed in Table 3.9 along with their geometrical/material parameters. Accuracy of the proposed formulations is then assessed by comparing calculated pull-in voltages of those

Table 3.9: *Fixed-fixed beam configurations employed for testing the proposed pull-in formulation. Configurations 1-7 and 8-13 are adopted from [86] and [80] respectively.*

CONFIGURATION NUMBER	PROBLEM PARAMETERS								
	E (GPa)	ν	σ_0 (MPa)	L (μm)	w (μm)	t (μm)	g_0 (μm)	α	γ
1	169	0.06	0	250	50	3.0	1.0	1	0
2	169	0.32	0	250	50	3.0	1.0	1	0
3	169	0.06	100	250	50	3.0	1.0	1	0
4	169	0.06	-25	250	50	3.0	1.0	1	0
5	169	0.06	0	350	50	3.0	1.0	1	0
6	169	0.06	100	350	50	3.0	1.0	1	0
7	169	0.06	-25	350	50	3.0	1.0	1	0
8	77	0.33	0	300	0.5	1.0	1.0	1	0
9	77	0.33	0	300	50	0.5	6.0	1	0
10	77	0.33	100	300	50	3.0	1.0	1	0
11	70	0.33	60	300	10	1.0	2.0	1	0
12	70	0.33	60	300	10	1.0	2.0	0.33	0
13	77	0.33	0	300	50	3.0	1.0	0.10	0

Table 3.10: *Pull-in voltage data for test configurations #1-7 calculated using various methods.*

CALCULATION METHOD	PULL-IN VOLTAGE (V)						
	# 1	#2	#3	#4	#5	#6	#7
CoSolve EM FEA [86]	40.10	41.20	57.60	33.60	20.30	35.80	13.70
[76]	39.46	41.58	56.83	33.66	20.13	35.37	13.72
[80]	40.37	42.53	58.85	34.11	20.59	36.75	13.63
[87]	35.54	37.45	51.94	30.08	18.13	32.57	12.08
[88]	39.31	41.42	57.44	33.27	20.06	36.02	13.36
[89]	39.11	41.20	57.80	32.81	19.95	36.36	12.93
This work (0AX)	39.09	41.19	57.00	33.03	19.95	35.60	13.19
This work (NAX)	39.53	41.64	57.68	33.38	20.17	36.04	13.31

configurations with the ones obtained from FEA tools. Moreover, for the sake of a richer comparison, pull-in voltage results determined with other formulations existing in the literature are also analyzed. Tables 3.10-3.11 and 3.12-3.13 provide relevant comparisons of pull-in voltages and associated fractional errors with respect to FEA results for configurations #1-7 and #8-13 respectively.

Upon an inspection of Table 3.11, it is realized that accuracy of the proposed pull-in formulations are indeed acceptable for configurations #1-7. In particular, worst case fractional errors for zero-tension (0AX) and nonzero-tension (NAX) formulations are found

119

Table 3.11: *Fractional error of the pull-in voltage data calculated using various formulations with respect to CoSolve EM Finite Element Analysis (FEA) results [86] for configurations #1-7.*

PULL-IN	PULL-IN VOLTAGE ERROR (%)							
FORMULATION	# 1	#2	#3	#4	#5	#6	#7	Rms
[76]	-1.59	0.92	-1.33	0.18	-0.81	-1.21	0.12	1.02
[80]	0.66	3.23	2.17	1.53	1.45	2.66	-0.54	1.98
[87]	-11.36	-9.11	-9.83	-10.48	-10.67	-9.03	-11.83	10.38
[88]	-1.97	0.52	-0.28	-0.99	-1.21	0.6	-2.48	1.37
[89]	-2.48	0.01	0.34	-2.35	-1.71	1.57	-5.65	2.65
This work (0AX)	-2.51	-0.03	-1.04	-1.68	-1.75	-0.56	-3.69	1.97
This work (NAX)	-1.43	1.08	0.15	-0.67	-0.66	0.67	-2.84	1.34

Table 3.12: *Pull-in voltage data for test configurations #8-13 calculated using various methods.*

CALCULATION	PULL-IN VOLTAGE (V)					
METHOD	# 8	#9	#10	#11	#12	#13
Coventorware FEA [80]	2.50	89.60	36.00	39.70	49.70	38.10
[76]	2.63	19.17	34.68	35.49	N/A	N/A
[80]	2.87	79.90	36.04	37.72	44.64	39.67
[87]	3.20	17.62	31.94	34.92	N/A	N/A
[88]	3.54	19.48	35.32	38.62	46.71	40.21
[89]	2.34	18.79	35.67	37.10	N/A	N/A
This work (0AX)	3.69	79.71	34.91	37.80	46.58	39.85
This work (NAX)	3.70	96.08	35.34	38.13	46.62	39.85

Table 3.13: *Fractional error of the pull-in voltage data calculated using various formulations with respect to Coventorware Finite Element Analysis (FEA) results [80] for configurations #8-13.*

PULL-IN	PULL-IN VOLTAGE (V)					
FORMULATION	# 8	#9	#10	#11	#12	#13
[76]	5.23	-78.61	-3.68	-10.60	N/A	N/A
[80]	14.94	-10.83	0.11	-4.98	-10.18	4.12
[87]	28.02	-80.34	-11.27	-12.04	N/A	N/A
[88]	41.59	-78.25	-1.88	-2.73	-6.02	5.54
[89]	-6.52	-79.03	-0.92	-6.55	N/A	N/A
This work (0AX)	47.74	-11.03	-3.03	-4.78	-6.27	4.58
This work (NAX)	47.99	7.23	-1.83	-3.95	-6.19	4.59

to be 3.70% and 2.84% respectively compared to CoSolve EM FEA results [86]. Furthermore, overall accuracy performance of these formulations are noted to be close to, if not superior than, other pull-in formulations as evidenced by the rms error tab in the same table: Rms errors for seven test cases are read as 1.97% and 1.34% for 0AX and NAX formulations, which are indeed comparable to the least error of 1.02% yielded by [76]. According to those results, it can be stated that 0AX and NAX pull-in formulations presented in this work perform well in terms of accuracy for the case of wide beams having a small g_0/t ratio.

Accuracy trends of all formulations change dramatically for configurations #8-13 as evidenced by Table 3.13. In particular, worst case fractional errors of 0AX and NAX formulations reach up to 50% compared to Coventorware FEA results [80], a behavior implying break-down of one of the fundamental assumptions: Relevant error occurs only for configuration #8, which actually describes an extreme case of a narrow beam ($w < t$ and $w < g_0$) permitting a significant fringing field contribution. Since a fringing field correction for narrow beams is not intended within the scope of this study and it is mainly focused on wide beams, relevant configuration therefore should not be regarded as a valid one for 0AX and NAX formulations. Accordingly, #8 is excluded from valid configurations in Table 3.13 in the remainder of this discussion, while noting that there exists formulations that successfully account for such fringing-effects ([76] and [80] specifically).

For configurations #9-13 in Table 3.13, proposed pull-in formulations yield comparable, if not improved, errors to those of other applicable ones. In particular, #9 appears as another extreme configuration for which 0AX and NAX formulations exhibit their next severe accuracy degradation with worst case errors of 11.03% and 7.23% respectively. This latter extreme case features a wide beam with a very high g_0/t ratio which in turn promotes nonlinear stretching effects considerably. Except for [80], other formulations do not account for this axial effect and this is the reason why they yield errors in the order of 80%. Notice that NAX formulation provides a better estimate for the pull-in voltage of this configuration (7.23% versus 10.83% of [80]), which is due to proper accounting of $\tilde{y}_{\mathrm{PI}}$ extension. Configuration #10 is similar to the ones provided in Table 3.11 and all formulations give corresponding similar results. Configuration #11 depicts a less prominent

121

case of a medium g_0/t ratio, which is handled well by formulations accounting for the associated nonlinear stretching effect. The final configurations #12-13 are distinguished by their partial electrode span (i.e. $\alpha \neq 1$) for which formulations of $[76, 87, 89]$ are not applicable and errors of the remaining ones resemble each other.

Previous observations serve to validate the proposed 0AX and NAX pull-in formulations for the case of wide beams featuring negligible fringing fields. Both formulations are found to yield accuracy levels comparable to existing pull-in expressions in the literature. For configurations having small to medium g_0/t ratios, it might be preferable to utilize 0AX formulation due to its reduced computational complexity, without sacrificing the accuracy too much. For increased g_0/t ratios however, NAX formulation seems to yield improved results.

3.6 Contact Electromechanics of Electrostatically Actuated Fixed-Fixed Beams

Previous sections covered the electrostatic actuation problem of fixed-fixed beams for stable deflections and investigated the pull-in phenomenon limiting this stable operation. In order to complete the discussion on electromechanics of relevant actuator systems, pre-pull-in characteristics established earlier are now complemented with the ones *beyond* pull-in in this section. Outline of this section resembles to that of the pre-pull-in case: Governing normalized equations are provided first, boundary conditions are examined second, a Finite Difference scheme for the contact problem is developed next and relevant numerical solutions are discussed at the end.

3.6.1 Normalized Governing Equations for the Electromechanical Contact Problem

Figure 3.25 illustrates the configuration for the electromechanical contact problem of fixed-fixed beams in terms of the normalized quantities developed in §3.3.2. It is assumed currently that the applied voltage $\tilde{V}$ is larger than the pull-in voltage $\tilde{V}_{\mathrm{PI}}$ so that the beam snaps down to the bottom electrode and subsequently forms a contact with the isolation dielectric in a contact length of $1 - 2\tilde{x}_0$. Contrary to the pre-pull-in configuration, there now exists three distinct problem regions with different transverse load distribution:
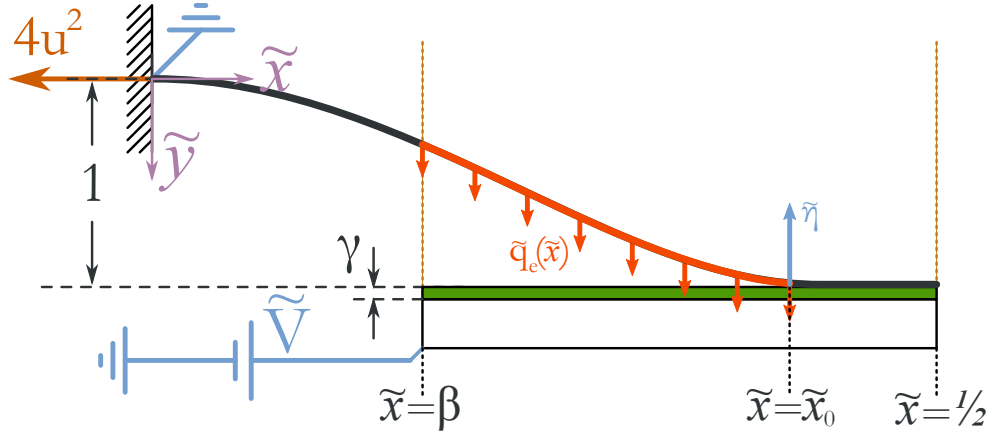
Figure 3.25: *Configuration for the electromechanical contact problem of fixed-fixed beams.*

- In the first region ($0 \leq \tilde{x} \leq \beta$), beam is not subject to any transverse load.

- In the second region ($\beta \leq \tilde{x} \leq \tilde{x}_0$), beam experiences a position-dependent electrostatic attraction force $\tilde{q}_e(\tilde{x})$.

- In the third region ($\tilde{x}_0 \leq \tilde{x} \leq 1/2$), the beam is in contact with the underlying dielectric and a distributed normal force counterbalances the electrostatic one, thereby setting the net force to zero.

Notice that first two regions are common to pre-pull-in and post-pull-in configurations while the contact region is specific to the latter one. Since the beam is flat in the contact region, one can state:

$$\tilde{y}_{\text{III}}(\tilde{x}) = 1$$
$$\tilde{y}'_{\text{III}}(\tilde{x}) = \tilde{y}''_{\text{III}}(\tilde{x}) = \tilde{y}'''_{\text{III}}(\tilde{x}) = 0$$

(3.163)

Combining the symmetry of the configuration with Equation (3.163), it becomes permissible to restrict the on-going analysis to regions I and II with appropriate edge conditions at $\tilde{x} = \tilde{x}_0$. Moreover, since $\tilde{y}_{\text{I}}(\tilde{x})$ and $\tilde{y}_{\text{II}}(\tilde{x})$ are actually related with each other through continuity relations at $\tilde{x} = \beta$, it suffices to focus only on region II. It follows from these observations that solution of the electromechanical contact problem is governed by a similar integro-differential equation set as with the pre-pull-in problem:

$$\frac{\mathrm{d}^4 \tilde{y}}{\mathrm{d}\tilde{x}^4} - 4u^2 \frac{\mathrm{d}^2 \tilde{y}}{\mathrm{d}\tilde{x}^2} = \frac{\tilde{V}^2}{\left[1 + \gamma - \tilde{y}\right]^2}, \quad \beta \leq \tilde{x} \leq \tilde{x}_0$$

(3.164a)

$$u^2 = 3\left(\frac{g_0}{t}\right)^2 \int_0^{\tilde{x}_0} \left(\frac{\mathrm{d}\tilde{y}}{\mathrm{d}\tilde{x}'}\right)^2 \mathrm{d}\tilde{x}' + 3\Sigma_0 \qquad (3.164b)$$

Equation (3.164) is an adapted version of Equation (3.120) for the current configuration with the right-hand boundary shifted from $1/2$ to $\tilde{x}_0$[10]. Before seeking solutions to this governing equation set, conditions at the problem boundaries must be specified, a task which is detailed in the next subsection.

3.6.2 Boundary Conditions and Continuity Relations

Edge conditions for the electromechanical contact problem closely follow that of the pre-pull-in problem at the boundary $\tilde{x} = \beta$ owing to identical configurations in regions I and II. Consequently, one can utilize the continuity relations (3.85) derived in §3.3.3 for the relevant boundary without any additional effort. A similar argument, however, does not hold for the boundary $\tilde{x} = \tilde{x}_0$ and one needs to perform a separate analysis in order to determine associated edge conditions. For this purpose, let us refer back to Figure 3.25 and consider the contact problem in the neighborhood of $\tilde{x} = \tilde{x}_0$. Although the net distributed transverse load in region III is zero, a concentrated force might arise at the initial contact point [109] and this force is denoted with $\tilde{\eta}$ in Figure 3.25. Taking into account this latter force component, Equation (3.164a) can be re-written around $\tilde{x} = \tilde{x}_0$ as,

$$\frac{\mathrm{d}^4\tilde{y}}{\mathrm{d}\tilde{x}^4} - 4u^2 \frac{\mathrm{d}^2\tilde{y}}{\mathrm{d}\tilde{x}^2} = -\tilde{\eta}\,\delta(\tilde{x} - \tilde{x}_0) + \tilde{q}_1(\tilde{x}) \qquad (3.165)$$

where

$$\tilde{q}_1(\tilde{x}) = \begin{cases} \dfrac{\tilde{V}^2}{\left[1+\gamma-\tilde{y}\right]^2}, & \tilde{x} < \tilde{x}_0 \\[2mm] 0, & \tilde{x} > \tilde{x}_0 \end{cases}$$

Recognizing that $\tilde{q}_1(\tilde{x})$ does not possess any impulsive component or its derivatives, it

---

[10] Notice that the integration limit in Equation (3.164b) can be shifted likewise since $\tilde{y}'_{\mathrm{III}}(\tilde{x}) = 0$ in region III.

follows from Equation (3.165) that

$$\tilde{y}(\tilde{x}_0^-) = \tilde{y}(\tilde{x}_0^+)$$

$$\left.\frac{\mathrm{d}\tilde{y}}{\mathrm{d}\tilde{x}}\right|_{\tilde{x}=\tilde{x}_0^-} = \left.\frac{\mathrm{d}\tilde{y}}{\mathrm{d}\tilde{x}}\right|_{\tilde{x}=\tilde{x}_0^+}$$

$$\left.\frac{\mathrm{d}^2\tilde{y}}{\mathrm{d}\tilde{x}^2}\right|_{\tilde{x}=\tilde{x}_0^-} = \left.\frac{\mathrm{d}^2\tilde{y}}{\mathrm{d}\tilde{x}^2}\right|_{\tilde{x}=\tilde{x}_0^+} \qquad (3.166)$$

$$\left.\frac{\mathrm{d}^3\tilde{y}}{\mathrm{d}\tilde{x}^3}\right|_{\tilde{x}=\tilde{x}_0^-} = \tilde{\eta} + \left.\frac{\mathrm{d}^3\tilde{y}}{\mathrm{d}\tilde{x}^3}\right|_{\tilde{x}=\tilde{x}_0^+}$$

Utilizing Equation (3.163) in (3.166), one thus obtains:

$$\tilde{y}_{\mathrm{II}}(\tilde{x}_0) = 1$$

$$\tilde{y}'_{\mathrm{II}}(\tilde{x}_0) = 0$$

$$\tilde{y}''_{\mathrm{II}}(\tilde{x}_0) = 0 \qquad (3.167)$$

$$\tilde{y}'''_{\mathrm{II}}(\tilde{x}_0) = \tilde{\eta}$$

Equation (3.167) establishes edge conditions for the boundary $\tilde{x} = \tilde{x}_0$. Since it is not possible to determine $\tilde{\eta}$ beforehand, first three of these equations actually serve as boundary conditions. The final equation, nevertheless, will prove to be useful as subsequent studies will demonstrate.

Table 3.14 provides a summary of the boundary conditions and continuity relations for the electromechanical contact problem.

Table 3.14: *Boundary conditions and continuity relations for the electromechanical contact problem.*

TYPE OF CONDITION	POSITION	EXPRESSION
CONTINUITY RELATION	$\tilde{x} = \beta$	Equation (3.85)
BOUNDARY CONDITION	$\tilde{x} = \tilde{x}_0$	Equation (3.167)

3.6.3 Finite Difference Solution of the Electromechanical Contact Problem

The boundary-value problem (3.164) subject to the edge conditions (3.85)-(3.167), unfortunately, cannot be solved through analytical means due to non-linear integro-differential
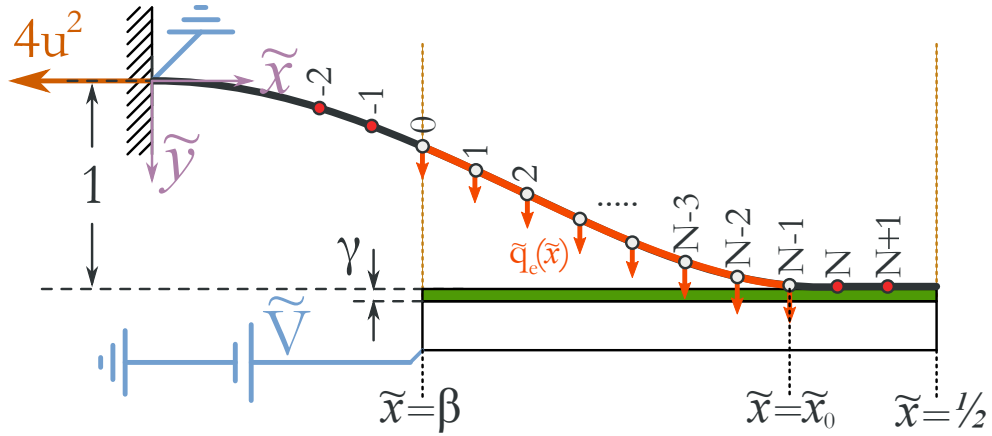
Figure 3.26: *An illustration for the electromechanical contact problem discretized for the application of Finite Difference method. Nodes are indicated with their indices.*

nature of the system. Consequently, one has to employ numerical techniques in order to approximate the relevant solution. As with the nonzero-tension electrostatic actuation problem, it is preferred to utilize Finite Difference method for this purpose. Such a choice bears the additional advantage of sparing most of the required derivations for Finite Difference equations and associated algorithm implementations: Similarity of the governing relations between two problems permits utilization of already established results as it will be shown shortly.

Subsequent articles elaborate on construction of the Finite Difference equations for the electromechanical contact problem, solution of the resulting equation system and interpretation of the obtained results.

3.6.3.1 Finite Difference Formulation

Figure 3.26 depicts the uniform discretization scheme employed for Finite Difference solution of the electromechanical contact problem. Utilizing the similarity of the current configuration with the nonzero-tension electrostatic actuation problem (see §3.4.2.1), one can directly adopt bulk of the Finite Difference equations except for the nodes in the neighborhood of the contact region. Consequently, relevant equations for interior nodes and nodes around the continuity border become:

$$F_0 = c_{00}(u,\beta,h)\tilde{y}_0 + c_{01}(u,\beta,h)\tilde{y}_1 + 2\tilde{y}_2 - \frac{h^4\tilde{V}^2}{\left[1+\gamma-\tilde{y}_0\right]^2} = 0 \qquad (3.168a)$$

$$F_1 = c_{10}(u,\beta,h)\tilde{y}_0 + c_{11}(u,\beta,h)\tilde{y}_1 - 4\left[1+u^2h^2\right]\tilde{y}_2 + \tilde{y}_3 - \frac{h^4\tilde{V}^2}{\left[1+\gamma-\tilde{y}_1\right]^2} = 0 \quad (3.168b)$$

$$F_i = \tilde{y}_{i-2} + \tilde{y}_{i+2} - 4(1+u^2h^2)(\tilde{y}_{i-1}+\tilde{y}_{i+1}) + (6+8u^2h^2)\tilde{y}_i - \frac{h^4\tilde{V}^2}{\left[1+\gamma-\tilde{y}_i\right]^2} = 0 \quad (3.168c)$$

For the nodes around the contact region, a separate analysis is conducted as follows. Substituting the derivative approximations (3.121) into Equation (3.167) gives

$$\tilde{y}_{N-1} = 1$$

$$\tilde{y}_N = \tilde{y}_{N-2}$$

$$\tilde{y}_{N-2} + \tilde{y}_N = 2\tilde{y}_{N-1}$$

$$-\tilde{y}_{N-3} + 2\tilde{y}_{N-2} - 2\tilde{y}_N + \tilde{y}_{N+1} = 2h^3\tilde{\eta}$$

leading to

$$\tilde{y}_{N-2} = \tilde{y}_{N-1} = \tilde{y}_N = 1 \qquad (3.170a)$$

$$\tilde{\eta} = \frac{\tilde{y}_{N+1} - \tilde{y}_{N-3}}{2h^3} \qquad (3.170b)$$

It is noticed from Equation (3.170a) that normalized deflections of the nodes $N-2$, $N-1$ and N are fixed to unity once the relevant boundary conditions are imposed. Writing the interior node equation (3.168c) for the former two nodes and subsequently using (3.170a) gives two additional nodal relations:

$$F_{N-2} = \tilde{y}_{N-4} - 4(1+u^2h^2)\tilde{y}_{N-3} + 3 + 4u^2h^2 - \frac{h^4\tilde{V}^2}{\gamma^2} = 0 \qquad (3.171a)$$

$$F_{N-1} = \tilde{y}_{N-3} + \tilde{y}_{N+1} - 2 - \frac{h^4\tilde{V}^2}{\gamma^2} = 0 \qquad (3.171b)$$

Equation (3.171b) serves to determine $\tilde{y}_{N+1}$, which is only required for the evaluation of $\tilde{\eta}$. Accordingly, employing Equation (3.171b) in (3.170b) gives:

$$\tilde{\eta} = \frac{1-\tilde{y}_{N-3}}{h^3} + \frac{h\tilde{V}^2}{2\gamma^2} \qquad (3.172)$$

Since Finite Difference stencils of the nodes $N-4$ and $N-3$ make use of the known quantities $\tilde{y}_{N-2}$ and $\tilde{y}_{N-1}$, interior nodal equations for the relevant nodes must be modified.

127

Letting i $= N- 4, N- 3$ in Equation (3.168c) and using (3.170a) establishes the desired relations:

$$
\begin{aligned}
F_{N-4} &= \tilde{y}_{N-6} - 4(1+u^2 h^2)(\tilde{y}_{N-5} + \tilde{y}_{N-3}) + (6 + 8u^2 h^2)\tilde{y}_{N-4} + 1 \\
&\quad - \frac{h^4 \tilde{v}^2}{\left[1+\gamma-\tilde{y}_{N-4}\right]^2} = 0 \\
F_{N-3} &= \tilde{y}_{N-5} - 4(1+u^2 h^2)\tilde{y}_{N-4} + (6 + 8u^2 h^2)\tilde{y}_{N-3} - (3 + 4u^2 h^2) \\
&\quad - \frac{h^4 \tilde{v}^2}{\left[1+\gamma-\tilde{y}_{N-3}\right]^2} = 0
\end{aligned}
\tag{3.173}
$$

Formulation of Finite Difference equations ends with a derivation for the discretized axial relation F_u. Notice, however, that identical continuity relations at $\tilde{x} = \beta$ and the property $\tilde{y}'_{N-1} = 0$ necessitates F_u derived in §3.4.2.1 to also hold for the current configuration. Hence, without any further effort, F_u can be stated as:

$$
\begin{aligned}
F_u = 3\Sigma_0 - u^2 + \frac{(g_0/t)^2}{h} &\Bigg\{ R_{00}(u,\beta,h)\tilde{y}_0^2 + R_{11}(u,\beta,h)\tilde{y}_1^2 + R_{01}(u,\beta,h)\tilde{y}_0\tilde{y}_1 \\
- 2\tilde{y}_0\tilde{y}_2 + \frac{1}{2}\tilde{y}_{N-2}^2 + \tilde{y}_{N-1}^2 &+ \sum_{n=1}^{\frac{N-3}{2}} \tilde{y}_{2n-1}(\tilde{y}_{2n-1} - \tilde{y}_{2n+1}) + 2\tilde{y}_{2n}(\tilde{y}_{2n} - \tilde{y}_{2n+2}) \Bigg\} = 0
\end{aligned}
\tag{3.174}
$$

along with the constraint $\tilde{y}_{N-2} = \tilde{y}_{N-1} = 1$.

Table 3.15 provides a summary of the Finite Difference equations for the electromechanical contact problem derived in this subsection.

Correction for the Case $\alpha = 1$

Finite Difference equations provided in Table 3.15 become invalid if fractional span α assumes the value of unity. Required correction for this particular case, however, can be instantly applied by using the results established in §3.4.2.1: Owing to identical configurations of nonzero-tension electrostatic actuation and electromechanical contact problems around $\tilde{x} = \beta$ boundary, corrected nodal equations are also expected to be the same for both problems. Corrected nodal equations for the electromechanical contact problem are listed in Table 3.16.

Table 3.15: *Finite Difference equations for the electromechanical contact problem.*

NODES NEAR THE CONTINUITY BORDER (i=0, 1)

$$F_0 = c_{00}(u,\beta,h)\tilde{y}_0 + c_{01}(u,\beta,h)\tilde{y}_1 + 2\tilde{y}_2 - \frac{h^4\tilde{V}^2}{\left[1+\gamma-\tilde{y}_0\right]^2} = 0$$

$$F_1 = c_{10}(u,\beta,h)\tilde{y}_0 + c_{11}(u,\beta,h)\tilde{y}_1 - 4\left[1+u^2h^2\right]\tilde{y}_2 + \tilde{y}_3 - \frac{h^4\tilde{V}^2}{\left[1+\gamma-\tilde{y}_1\right]^2} = 0$$

INTERIOR NODES ($2 \leq i \leq$ N-5)

$$F_i = \tilde{y}_{i-2} + \tilde{y}_{i+2} - 4(1+u^2h^2)(\tilde{y}_{i-1} + \tilde{y}_{i+1}) + (6 + 8u^2h^2)\tilde{y}_i - \frac{h^4\tilde{V}^2}{\left[1+\gamma-\tilde{y}_i\right]^2} = 0$$

NODES NEAR THE CONTACT REGION (N-4 $\leq$ i $\leq$ N-2)

$$F_{N-4} = \tilde{y}_{N-6} - 4(1+u^2h^2)(\tilde{y}_{N-5} + \tilde{y}_{N-3}) + (6 + 8u^2h^2)\tilde{y}_{N-4} + 1 - \frac{h^4\tilde{V}^2}{\left[1+\gamma-\tilde{y}_{N-4}\right]^2} = 0$$

$$F_{N-3} = \tilde{y}_{N-5} - 4(1+u^2h^2)\tilde{y}_{N-4} + (6 + 8u^2h^2)\tilde{y}_{N-3} - (3 + 4u^2h^2) - \frac{h^4\tilde{V}^2}{\left[1+\gamma-\tilde{y}_{N-3}\right]^2} = 0$$

$$F_{N-2} = \tilde{y}_{N-4} - 4(1+u^2h^2)\tilde{y}_{N-3} + 3 + 4u^2h^2 - \frac{h^4\tilde{V}^2}{\gamma^2} = 0$$

AXIAL RELATION

$$F_u = 3\Sigma_0 - u^2 + \frac{(g_0/t)^2}{h}\left\{ R_{00}(u,\beta,h)\tilde{y}_0^2 + R_{11}(u,\beta,h)\tilde{y}_1^2 + R_{01}(u,\beta,h)\tilde{y}_0\tilde{y}_1 \right.$$

$$\left. -2\tilde{y}_0\tilde{y}_2 + \frac{1}{2}\tilde{y}_{N-2}^2 + \tilde{y}_{N-1}^2 + \sum_{n=1}^{\frac{N-3}{2}} \tilde{y}_{2n-1}(\tilde{y}_{2n-1} - \tilde{y}_{2n+1}) + 2\tilde{y}_{2n}(\tilde{y}_{2n} - \tilde{y}_{2n+2}) \right\} = 0$$

$$(\tilde{y}_{N-2} = \tilde{y}_{N-1} = 1)$$

Table 3.16: *Finite Difference equations for the electromechanical contact problem with $\alpha = 1$.*

NODES NEAR THE CLAMPED END (i=1, 2)
$$F_1 = \left(7 + 8u^2h^2\right)\tilde{y}_1 - 4\left(1 + u^2h^2\right)\tilde{y}_2 + \tilde{y}_3 - \frac{h^4\tilde{V}^2}{\left[1+\gamma-\tilde{y}_1\right]^2} = 0$$ $$F_2 = -4(1 + u^2h^2)(\tilde{y}_1 + \tilde{y}_3) + (6 + 8u^2h^2)\tilde{y}_2 + \tilde{y}_4 - \frac{h^4\tilde{V}^2}{\left[1+\gamma-\tilde{y}_2\right]^2} = 0$$
INTERIOR NODES (3 ≤ i ≤ N-5)
$$F_i = \tilde{y}_{i-2} + \tilde{y}_{i+2} - 4(1 + u^2h^2)(\tilde{y}_{i-1} + \tilde{y}_{i+1}) + (6 + 8u^2h^2)\tilde{y}_i - \frac{h^4\tilde{V}^2}{\left[1+\gamma-\tilde{y}_i\right]^2} = 0$$
NODES NEAR THE CONTACT REGION (N-4 ≤ i ≤ N-2)
$$F_{N-4} = \tilde{y}_{N-6} - 4(1 + u^2h^2)(\tilde{y}_{N-5} + \tilde{y}_{N-3}) + (6 + 8u^2h^2)\tilde{y}_{N-4} + 1 - \frac{h^4\tilde{V}^2}{\left[1+\gamma-\tilde{y}_{N-4}\right]^2} = 0$$ $$F_{N-3} = \tilde{y}_{N-5} - 4(1 + u^2h^2)\tilde{y}_{N-4} + (6 + 8u^2h^2)\tilde{y}_{N-3} - (3 + 4u^2h^2) - \frac{h^4\tilde{V}^2}{\left[1+\gamma-\tilde{y}_{N-3}\right]^2} = 0$$ $$F_{N-2} = \tilde{y}_{N-4} - 4(1 + u^2h^2)\tilde{y}_{N-3} + 3 + 4u^2h^2 - \frac{h^4\tilde{V}^2}{\gamma^2} = 0$$
AXIAL RELATION
$$F_u = 3\Sigma_0 - u^2 + \frac{(g_0/t)^2}{h}\left\{-\frac{1}{2}\tilde{y}_1^2 + \frac{1}{2}\tilde{y}_{N-2}^2 + \tilde{y}_{N-1}^2\right.$$ $$\left. + \sum_{n=1}^{\frac{N-3}{2}}\tilde{y}_{2n-1}(\tilde{y}_{2n-1} - \tilde{y}_{2n+1}) + 2\tilde{y}_{2n}(\tilde{y}_{2n} - \tilde{y}_{2n+2})\right\} = 0$$ $$(\tilde{y}_{N-2} = \tilde{y}_{N-1} = 1)$$

3.6.3.2 Solution of the Finite Difference Equations

A quick glance at Table 3.15 might suggest that there exists a total of N Finite Difference equations for the seeming $N-1$ unknowns $\vec{y} = \begin{bmatrix} \tilde{y}_0 \tilde{y}_1 \cdots \tilde{y}_{N-3} \end{bmatrix}$ and u. Before identifying the missing unknown, let us formulate the grid spacing h first. From Figure 3.26, it is trivial to write,

$$h = \frac{\tilde{x}_0 - \beta}{N - 1} \qquad (3.175)$$

It is evident from Equation (3.175) that initial contact point $\tilde{x}_0$ enters into the Finite Difference equations as *embedded* in the grid spacing h. This observation implies that it might not feasible to treat $\tilde{x}_0$ as an unknown: In general, it is not desired to vary h in an uncontrolled manner. Having thus eliminated $\tilde{x}_0$ from the list of unknowns, one is left with the remaining variable $\tilde{V}$. In fact, this latter variable can be conveniently allowed as an unknown for a given $\tilde{x}_0$: Specifying $\tilde{V}$ instead of $\tilde{x}_0$ has the possible pitfall of obtaining non-physical solutions, whereas determining $\tilde{x}_0$ beforehand eliminates such a possibility by ensuring the presence of a contact. In the light of this mini discussion, N^{th} unknown for the Finite Difference equations is selected as $\tilde{V}$.

Having specified the N unknowns for N Finite Difference equations, it is then advanced to solution of the relevant equation system. For this purpose, the interpolation-based shooting algorithm developed in §3.4.2.2 is utilized. Unlike the nonzero-tension electrostatic actuation problem, stability issues are not encountered and the algorithm is thus enabled to work with its full potential. After demonstrating successful operation in trial runs for a given number of grid points, an investigation of convergence is attempted next. Proceeding along the lines of §3.4.1.4, rms errors in $\tilde{y}_0$, $\tilde{V}$ and u are evaluated as a function of N by sweeping $\tilde{x}_0$ for a sample configuration. Obtained convergence results are presented in Figure 3.27.

Figure 3.27 shows that convergence for the electromechanical contact problem is almost uniform for all outcomes of interest unlike the nonzero-tension electrostatic actuation one. For $N = 251$ in particular, rms errors in $\tilde{y}_0$, $\tilde{V}$ and u are found to be better than 3×10^{-7}, 2×10^{-4} and 2×10^{-6} respectively within the considered Σ_0 range. Hence, adopted convenience of 251 points for the Finite Difference grid is verified to be suffi-

131
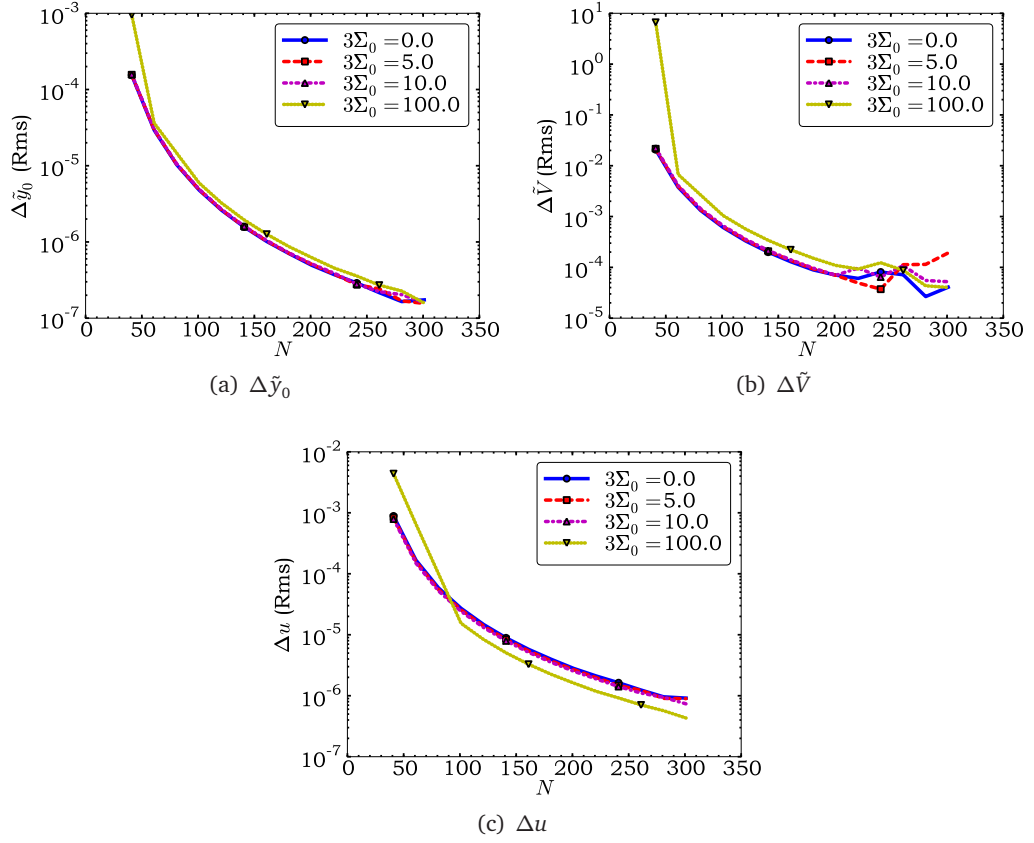
Figure 3.27: *Rms convergence errors in $\tilde{y}_0$, $\tilde{V}$ and u as a function of N for the electrome-chanical contact problem with Σ_0 as a parameter ($\gamma = 0.03$, $\alpha = 0.5$, $g_0/t = 2.0$).*

ciently accurate for further analyses.

3.6.3.3 Interpretation of Numerical Results

In the previous subsection, solution of Finite Difference equations for the electromechanical contact problem was addressed and confidence was built up in the relevant solutions by means of a convergence analysis. Having thus established a successful implementation for analyzing the electromechanical contact problem, a physical interpretation of obtained numerical results may now follow. For this purpose, multiple simulations are run for various combinations of problem variables γ, g_0/t, Σ_0 and α in order to investigate dependencies of the outcomes on those parameters. In particular, two outcomes are considered as a function of the applied voltage $\tilde{V}$:

- Fractional contact area, which is simply the contact area at a given $\tilde{V}$ normalized

with respect to the available electrode area. Note that it is trivial to write;

$$\text{Fractional contact area} = \frac{1 - 2\tilde{x}_0}{\alpha}$$

- Fractional capacitance C/C_{max} between the electrodes, which is an electrical manifestation of the previous item. Once a numerical solution is found for a given $\tilde{x}_0$, relevant capacitances can be calculated easily as (neglecting fringing fields);

$$C = 2 \times (C_{\text{II}} + C_{\text{III}}) = \frac{2\varepsilon_0 wL}{g_0} \left[\frac{0.5 - \tilde{x}_0}{\gamma} + \int_{\beta}^{\tilde{x}_0} \frac{\mathrm{d}\tilde{x}'}{1 + \gamma - \tilde{y}(\tilde{x}')} \right]$$

$$C_{\text{max}} = C\Big|_{\tilde{x}_0 = \beta} = \frac{2\varepsilon_0 wL}{g_0} \frac{0.5 - \beta}{\gamma}$$

which in turn gives

$$C/C_{\text{max}} = \frac{0.5 - \tilde{x}_0}{0.5 - \beta} + \frac{\gamma}{0.5 - \beta} \int_{\beta}^{\tilde{x}_0} \frac{\mathrm{d}\tilde{x}'}{1 + \gamma - \tilde{y}(\tilde{x}')}$$

Figures 3.28-3.29 present plots of the fractional contact area and fractional capacitance as a function of the applied voltage with each of the problem variables held as a parameter. In order to facilitate interpretation of the results, applied voltage is further normalized with respect to the corresponding pull-in voltage $\tilde{V}_{\text{PI}}$ calculated with the NAX pull-in formulation (see §3.5.2.2). Upon an examination of the provided results, one can draw the following conclusions:

- Increasing the applied voltage causes to fractional contact area to increase, a phenomenon which is termed as *zipping* [90,91]. Fractional capacitance closely follows the zipping trend of fractional contact area since the latter effectively defines the overlap area between the electrodes.

- The variable γ acts to decrease the fractional contact area at a given voltage level. Such a behavior can be explained readily by the fact that electrostatic load $\tilde{q}_e(\tilde{x})$ decreases with higher γ, which in turn necessitates a reduced stiffness (hence higher $\tilde{x}_0$) of the beam to counterbalance the effect.

- Changing nonlinear stretching multiplier g_0/t does not seem to affect fractional contact area appreciably at a certain fractional voltage $\tilde{V}/\tilde{V}_{\text{PI}}$. This observation

<div align="center">(a) γ as a parameter   (b) g_0/t as a parameter</div>

<div align="center">(c) $3\Sigma_0$ as a parameter   (d) α as a parameter</div>
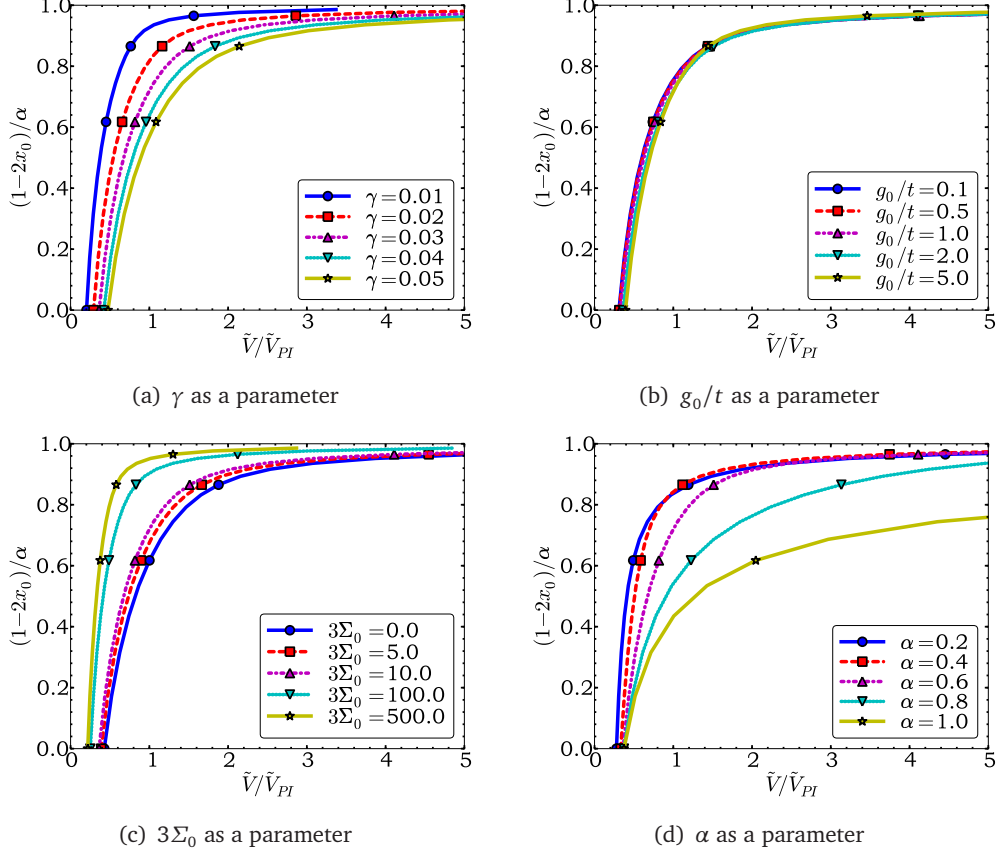
Figure 3.28: *Fractional contact area $(1 - 2\tilde{x}_0)/\alpha$ as a function of fractional voltage $\tilde{V}/\tilde{V}_{\mathrm{PI}}$ ($\gamma = 0.03$, $g_0/t = 2.0$, $3\Sigma_0 = 10.0$, $\alpha = 0.6$, $N = 251$ unless indicated).*

suggests that pull-in voltage $\tilde{V}_{\mathrm{PI}}$ and the voltage $\tilde{V}(\tilde{x}_0)$ required to establish a given contact area increase with similar rates as a function of g_0/t for a moderate Σ_0. Although not shown in these plots, the effects of g_0/t are noticed, albeit slightly, for smaller and higher Σ_0 values: For a smaller Σ_0, $\tilde{V}_{\mathrm{PI}}$ is noted to grow faster than $\tilde{V}(\tilde{x}_0)$ most probably due to pronounced effect of pull-in travel range extension (see Figure 3.23 in §3.5.1.2); whereas for larger Σ_0 the trend is recognized to reverse.

- Increasing the normalized residual stress Σ_0 improves the fractional contact area at a given fractional voltage. Such a trend can be explained from a converse stand-point as follows: $\tilde{V}(\tilde{x}_0)$ satisfying a given contact area is less sensitive to residual stress compared to $\tilde{V}_{\mathrm{PI}}$ since nonlinear stretching effects are prominent for the former. Consequently, fractional voltage $\tilde{V}(\tilde{x}_0)/\tilde{V}_{\mathrm{PI}}$ needs to decrease in order to maintain the same contact area for an elevated Σ_0.

- Fractional contact area appears to degrade with increased fractional span α at a

(a) γ as a parameter

(b) g_0/t as a parameter

(c) $3\Sigma_0$ as a parameter

(d) α as a parameter
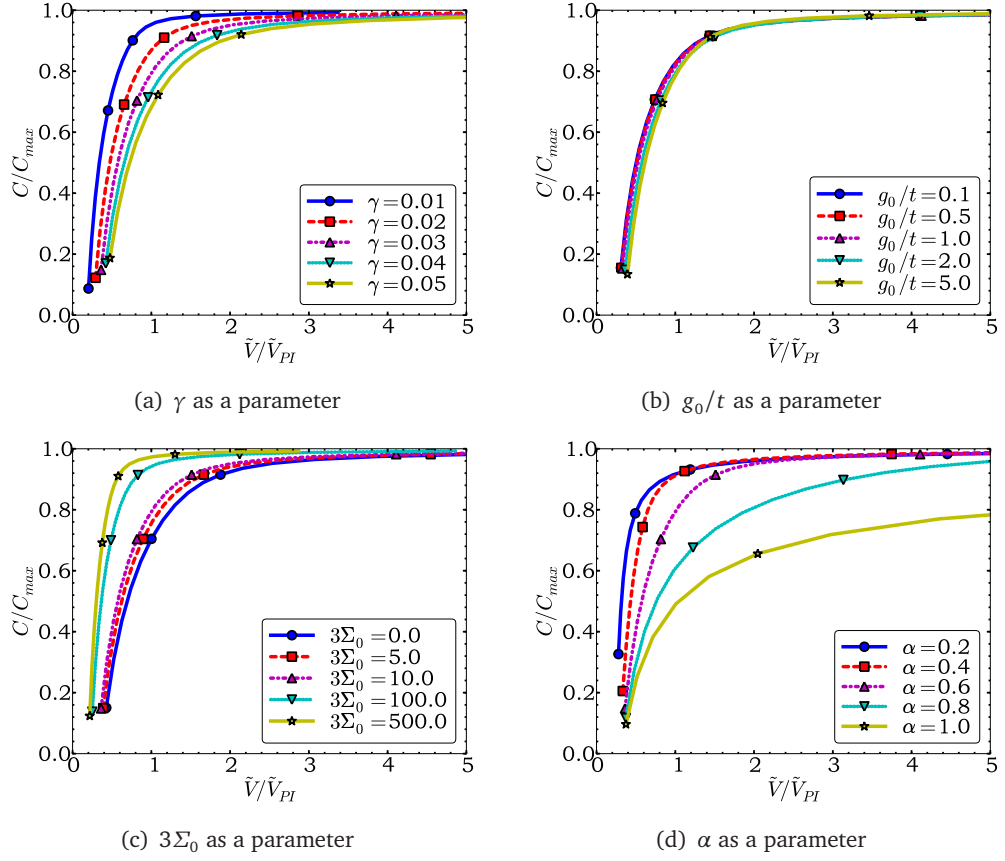
Figure 3.29: *Fractional capacitance $C/C_{\max}$ as a function of fractional voltage $\tilde{V}/\tilde{V}_{\mathrm{PI}}$ ($\gamma = 0.03$, $g_0/t = 2.0$, $3\Sigma_0 = 10.0$, $\alpha = 0.6$, $N = 251$ unless indicated).*

certain $\tilde{V}/\tilde{V}_{\mathrm{PI}}$. A qualitative reasoning might explain such a trend as follows: For a given fractional contact area, increasing α calls for an amplification of the nonlinear stretching effects due to increased beam slope in non-contact regions. Hence, the voltage required to maintain such contact area must increase with α.

Qualitative relations established above can be analyzed quantitatively by introducing appropriate fitting functions describing the effect of each problem variable on the $\tilde{x}_0 - \tilde{V}$ characteristics. Such a study, however, is left as a future work.

Before leaving the subject, it would be informative to analyze two more output quantities. The first one is the maximum normalized beam slope $g_0/t \times \tilde{y}'_{\max}$, which is plotted in Figure 3.30(a) as a function of $\tilde{V}/\tilde{V}_{\mathrm{PI}}$ for a sample configuration. The importance of this particular quantity can be understood more clearly if one relates it to absolute beam

(a) $g_0/t \times \tilde{y}'_{\text{max}}$

(b) $\tilde{\eta}$
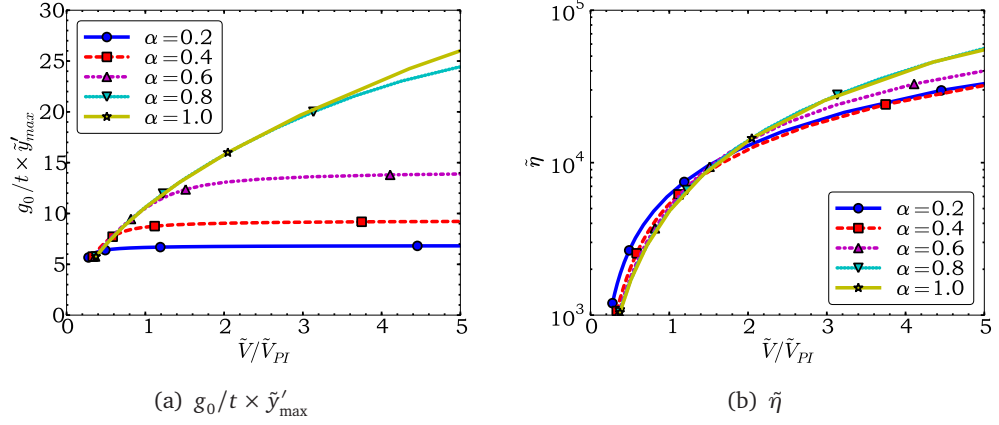
Figure 3.30: *Normalized maximum beam slope $g_0/t \times \tilde{y}'_{\text{max}}$ and concentrated contact force $\tilde{\eta}$ as a function of fractional voltage $\tilde{V}/\tilde{V}_{\text{PI}}$ ($\gamma = 0.03$, $g_0/t = 2.0$, $3\Sigma_0 = 10.0$, $N = 251$).*

slope:

$$y'_{\text{max}} = \frac{g_0}{L}\tilde{y}'_{\text{max}} = \frac{(g_0/t)}{(L/t)}\tilde{y}'_{\text{max}} \tag{3.176}$$

In order not to violate the small-deflection assumption inherently employed during the derivations, $y'^{\,2}_{\text{max}}$ must be sufficiently small compared to unity. An inspection of Equation (3.176) reveals that such a condition can be ensured if $(g_0/t)/(L/t)$ ratio is kept below a certain limit. For the particular case depicted in Figure 3.30(a), obtained results will rigorously hold if $L/t \gtrsim 185$, which corresponds to the condition

$$y'^{\,2}_{\text{max}} = 0.02$$

with $\alpha = 1$ and $\tilde{V}/\tilde{V}_{\text{PI}} = 5$. It can be deduced from these observations that care should be exercised when analyzing configurations featuring high g_0/t, low L/t and high $\alpha\tilde{V}/\tilde{V}_{\text{PI}}$ ratios in order not to distort physical consistency of the numerical solutions.

Remaining output quantity of interest is the normalized concentrated contact force $\tilde{\eta}$, whose plot with respect to $\tilde{V}/\tilde{V}_{\text{PI}}$ is given in Figure 3.30(b) for a sample configuration. It is noted from the provided curves that $\tilde{\eta}$ is always positive, a condition valid for a physical contact. In addition, $\tilde{\eta}$ tends to decrease sharply around a voltage that is a proper fraction of $\tilde{V}_{\text{PI}}$ and satisfying the condition $\tilde{x}_0 \to 0.5$. These comments suggest that contact of the beam with the underlying dielectric would diminish at a critical voltage that would simultaneously set $\tilde{x}_0 = 0.5$ and $\tilde{\eta} = 0$. This critical contact phenomenon actually

pertains to another well-known characteristic of electrostatic actuator systems, which is explored in more detail in the next article.

3.6.3.4 Analysis of the Critical Contact Problem and Determination of Hold Voltage

Previously described critical contact phenomenon is in fact a two-dimensional interpretation of the well-recognized *release* problem of electrostatic actuator systems: For a given nonzero contact area, electrostatic attraction exceeds the mechanical restoring force of the beam and a positive reaction $\tilde{\eta}$ balances the excess force. As the applied voltage $\tilde{V}$ is lowered gradually, contact area as well as $\tilde{\eta}$ starts to decrease due to reduced electrostatic attraction. When $\tilde{V}$ reaches a threshold known as the *hold* or *release voltage* $\tilde{V}_{\mathrm{H}}$ (with $\tilde{V}_{\mathrm{H}} < \tilde{V}_{\mathrm{PI}}$), electrostatic force can barely counteract the mechanical restoring force of the beam ($\tilde{\eta} = 0$) and a further reduction in voltage causes the beam to subsequently snap up to a stable non-contact state. This latter phenomenon therefore causes electrostatic actuator systems to exhibit a *hysteresis* behavior with abrupt state transitions at $\tilde{V}_{\mathrm{PI}}$ and $\tilde{V}_{\mathrm{H}}$ [91,92].

In order to complete the characterization of hysteresis exhibited by the electrostatic actuator system at hand, a final mechanical analysis is attempted for the determination of $\tilde{V}_{\mathrm{H}}$. It was suggested by the end of previous subsection that critical contact of the beam would occur when $\tilde{x}_0 = 0.5$ and $\tilde{\eta} = 0$ conditions are simultaneously met. Upon an inspection of the relevant configuration delineated in Figure 3.31, one might immediately notice that critical contact problem is actually equivalent to the non-zero tension electrostatic actuation problem with $\tilde{y}(1/2) = 1$. Thus without exerting any further effort, Finite Difference formulation for this latter problem can be established by merely setting $\tilde{y}_{\mathrm{N}-1} = 1$ in the expressions provided in Table 3.6. Performing so and solving the resulting equation system along the lines of §3.6.3.2 then yields the hold voltage $\tilde{V}_{\mathrm{H}}$.

The procedure described above is implemented in NumPy and hold voltages are obtained for various combinations of the problem variables. Figure 3.32 provides plots of the hold voltage as a function of the variable γ with each other variable held as a parameter. In order to facilitate understanding of these results $\tilde{V}_{\mathrm{H}}$ is normalized with respect to $\tilde{V}_{\mathrm{PI}}$ (cal-
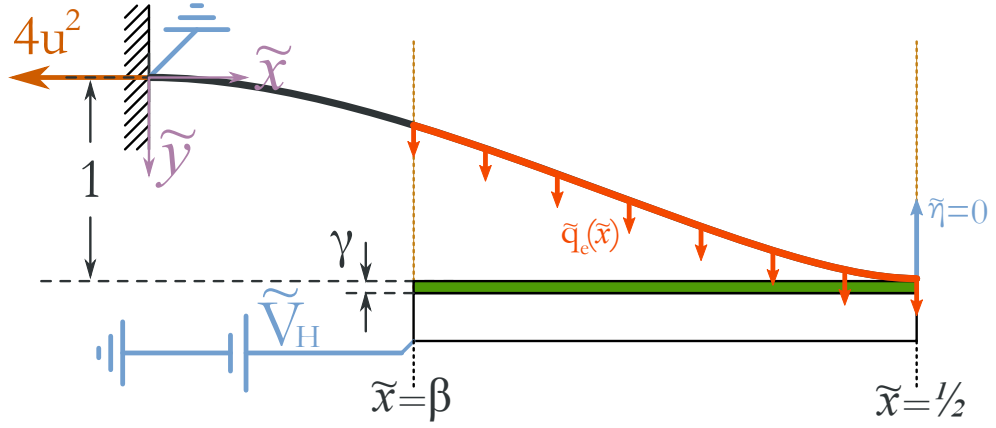
Figure 3.31: *Configuration for the critical contact problem of fixed-fixed beams.*

culated with the NAX pull-in formulation given in §3.5.2.2), a process which permits an interpretation in terms of the fractional hysteresis width $1 - \tilde{V}_{\mathrm{H}}/\tilde{V}_{\mathrm{PI}}$. It is observed from the provided curves that increasing the variable γ serves to reduce the hysteresis width: Decreasing the electrostatic force via a higher γ causes $\tilde{V}_{\mathrm{H}}$ to increase faster than $\tilde{V}_{\mathrm{PI}}$, which in turn narrows the hysteresis region. Dependencies of $\tilde{V}_{\mathrm{H}}/\tilde{V}_{\mathrm{PI}}$ on g_0/t, Σ_0 and α are moreover found consistent with the comments stated in §3.6.3.3: In particular; lowering g_0/t, reducing α or increasing Σ_0 is noted to enhance the fractional hysteresis width and those relations can be explained by relative effects of nonlinear stretching and residual stress.

As with the electromechanical contact problem, development of a semi-empirical hold voltage expression for the fixed-fixed beam actuator system is left as a future work.

3.7 Summary and Closing Comments

In this chapter, a mechanical characterization of fixed-fixed type beams is presented from a statics standpoint. Proceeding in a systematic manner, mechanical response of the relevant system to a uniform distributed transverse load is investigated first through a rigorous analytical treatment. Having established useful results such as the deflection profile and effective spring constant, and having set the background for more complicated analyses; attention is then focused on the problem of electrostatic actuation. Progressing

(a) g_0/t as a parameter

(b) Σ_0 as a parameter
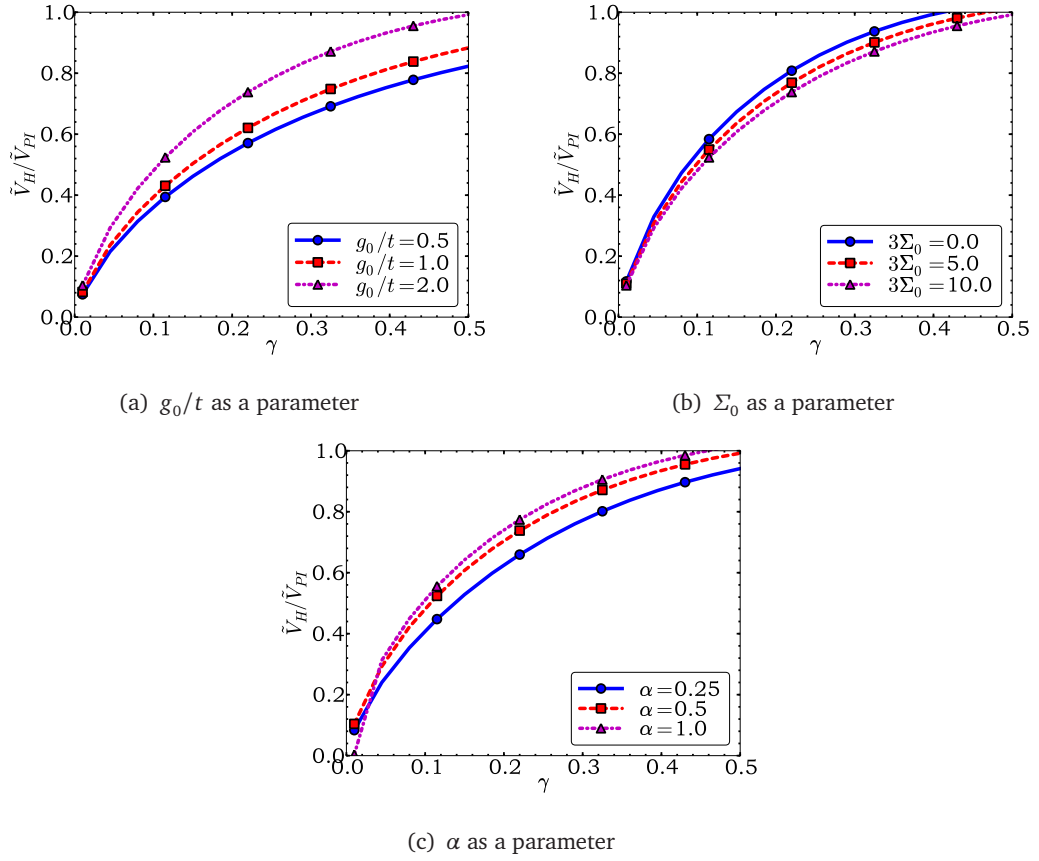
(c) α as a parameter

Figure 3.32: *Simulated $\tilde{V}_{\mathrm{H}}/\tilde{V}_{\mathrm{PI}}$ characteristics as a function of γ with each problem variable held as a parameter ($g_0/t = 2.0$, $3\Sigma_0 = 10.0$, $\alpha = 0.5$, $N = 251$ unless indicated).*

with increased difficulty, numerical analysis methods are developed and subsequently utilized in order to study the latter mechanical system. Using the obtained numerical results in conjunction with the accumulated mechanics knowledge, well-known pull-in phenomenon is investigated next and expressions are developed for the pull-in voltage. After evaluating various test configurations, accuracy of the developed pull-in formulation is demonstrated to be comparable to, if not better than, that of existing formulations in the literature. Advancing further, electromechanical characteristics of this actuator system is studied beyond pull-in as the next step. Adapting previously established numerical analysis methods to the electromechanical contact problem at hand, zipping phenomenon is successfully quantified and the effect of problem variables on the zipping behavior is studied in a qualitative sense. Finally, release phenomenon is examined in two dimensions and determination of the hold voltage is accomplished, which in turn completed the characterization of hysteresis exhibited by the relevant actuator system.

Before finishing this chapter, it is preferred to investigate a case study of a fixed-fixed type electrostatic actuator system lastly for a clear demonstration of the analysis and simulation capabilities established so far. For this purpose, the fixed-fixed beam configuration presented in [91] is selected and analyzed thoroughly. Figure 3.33 presents obtained results, which can be considered as a visual representation of the accomplishments described above.
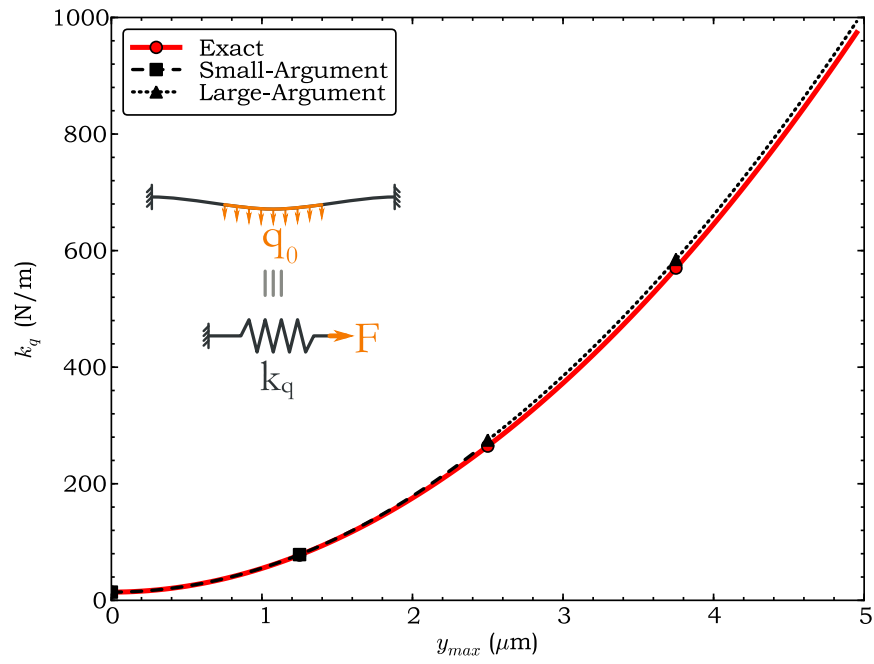
(a) Spring Constant k_q
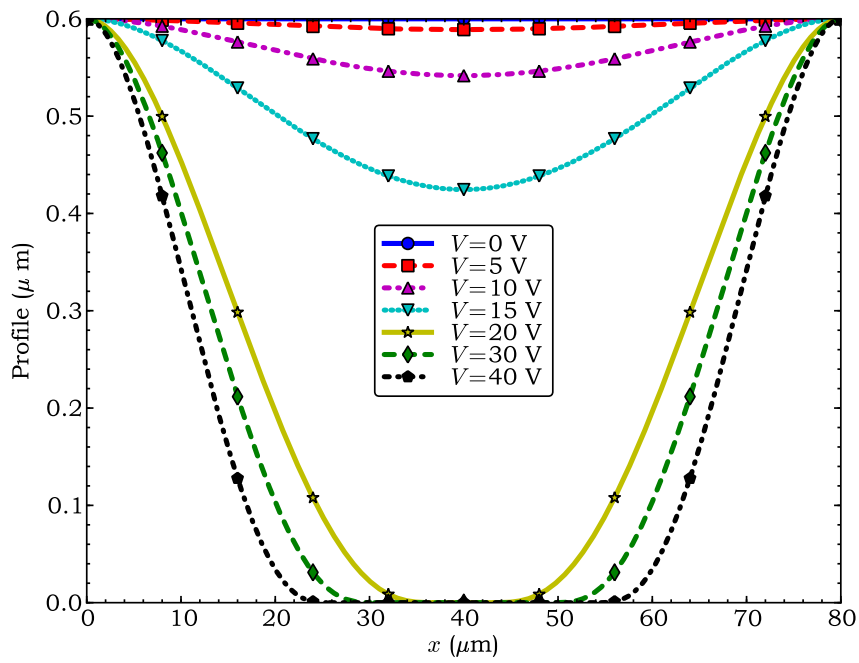
(b) Deflection profile for increasing V
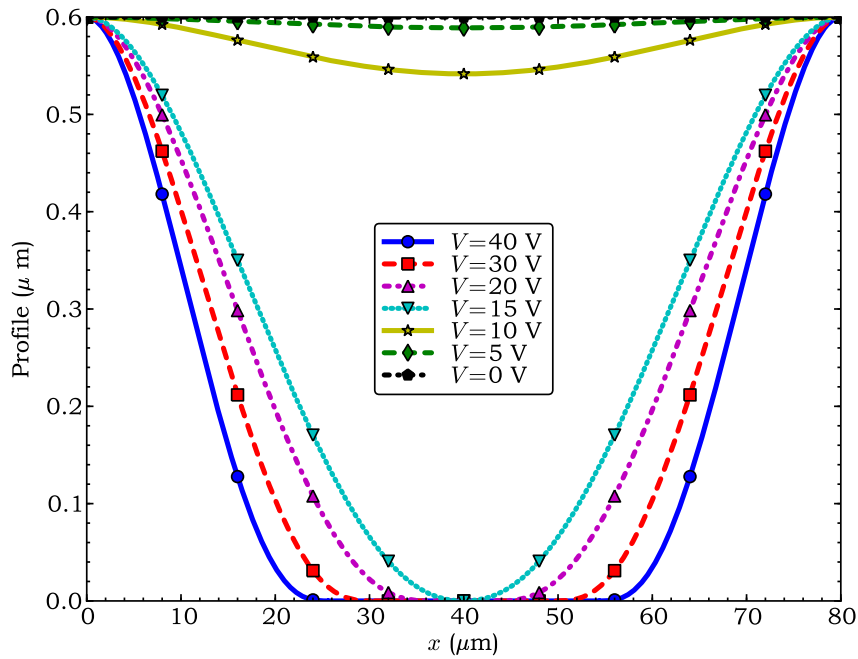
(c) Deflection profile for decreasing V
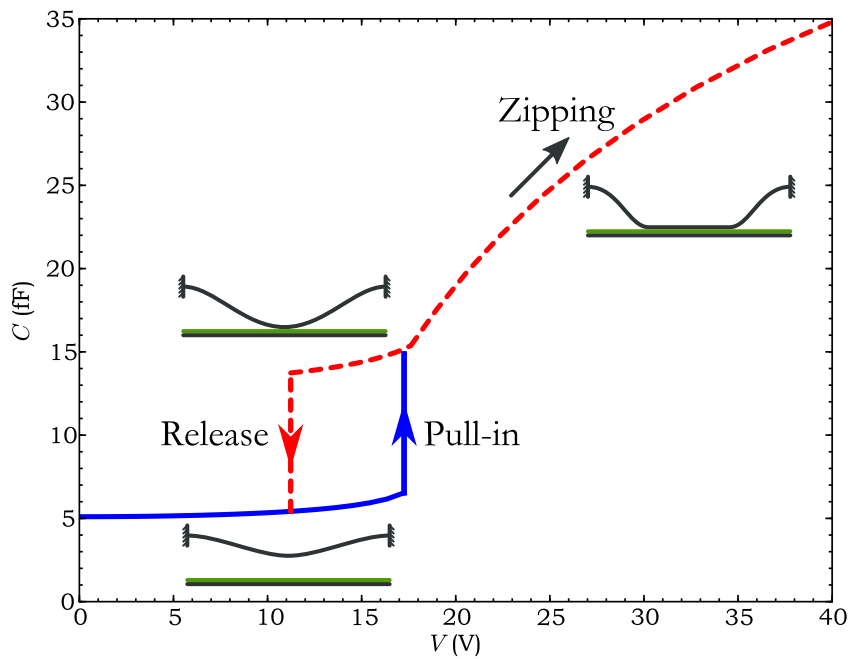
(d) Capacitance-voltage hysteresis characteristics

Figure 3.33: *Results of a case study for fixed-fixed type electrostatic actuator systems demonstrating an overview of analysis and simulation capabilities established in this chapter ($E = 169$ GPa, $v = 0.25$, $\sigma_0 = 0$ MPa, $L = 80$ μm, $w = 10$ μm, $g_0 = 0.6$ μm, $t = 0.5$ μm, $\gamma = 1/6$, $\alpha = 1$, $N = 251$).*

CHAPTER 4

REALIZATION OF A Ka-BAND SHUNT, CAPACITIVE-CONTACT RF MEMS SWITCH

This chapter investigates development of a primitive RF MEMS component, namely an RF MEMS switch, for millimeter-wave applications utilizing an in-house RF MEMS fabrication process. The chapter begins with an introduction section which explains operation principles of RF MEMS switches and their various configurations. Section §4.2 then explores electromagnetic design of the switch at Ka-band frequencies and provides two CPW-based shunt, capacitive-contact switch configurations satisfying the millimeter-wave design criteria. §4.3 next evaluates those switch configurations from a mechanical perspective using the knowledge established in Chapter 3 and elects one of the designs featuring better mechanical characteristics for implementation. Subsequently, §4.4 gives fabrication details of the selected switch configuration and presents associated measurement results. Having not met the design specifications in the first fabrication run, §4.5 examines the reasons for the observed discrepancy through post-fabrication related studies. After identifying problems with the fabricated switches, §4.6 continues with a design modification on the relevant device for improved millimeter-wave performance and immunity to fabrication-related issues. Finally, §4.7 details the second fabrication iteration and corresponding successful measurement results.

4.1 Introduction

RF MEMS (Radio Frequency Micro-Electro-Mechanical Systems) is an enabling technology that makes use of static or adjustable micro-mechanical structures to yield high-

(a) Series configuration.   (b) Shunt configuration.
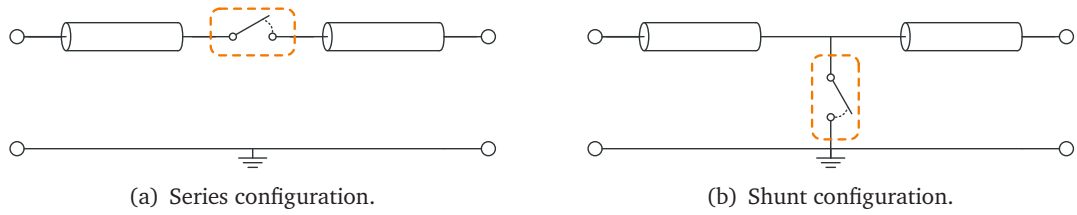
Figure 4.1: *Circuit configurations for the ideal RF MEMS switch.*

performance fixed or reconfigurable/tunable components and systems in high-frequency electrical domain [11–14]. Primitive building blocks of this technology bringing the ability of mentioned reconfigurability and tunability are RF MEMS switches and varactors, which can respond mechanically to a given form of actuation [8]. In particular, the former switch component gets the primary focus in this work and an overview of its types and associated properties would hence serve as a good starting point for the on-going discussions in the remainder of this chapter.

4.1.1   Overview of the RF MEMS Switch Component

4.1.1.1   Circuit Configuration Types

The RF MEMS switch may be regarded as a practical high-frequency version of the ideal switch element defined in the circuit theory. Maintaining the high-frequency analogy, ideally, the switch behaves either as an open-circuit or a short-circuit across a transmission line section in one of the two possible configurations as Figure 4.1 illustrates. For the *series* configuration; RF power can be fully transmitted from one port to the other when the switch is in ON (closed)-state, and ports are rendered isolated (i.e. no power can be transmitted to the output) when the switch assumes its OFF (open)-state. Converse statements hold for the *shunt* configuration: When the switch is ON, the path enabled to ground prevents RF power to reach to the output port, thereby causing infinite isolation; whereas RF power travels to the output port without any insertion loss for the OFF-state of the switch.

In practice, no switch can attain infinite isolation or zero insertion loss between its ports

(a) OFF-state.

(b) ON-state.
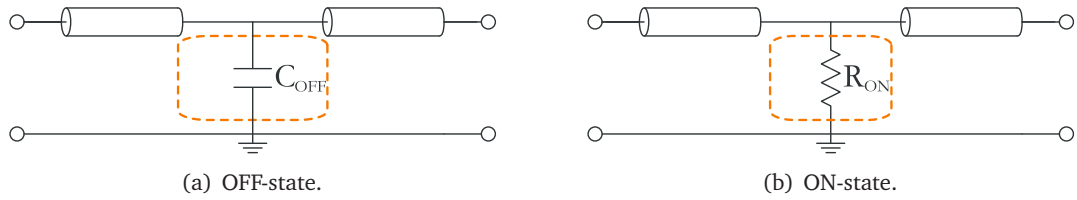
Figure 4.2: *Simplified equivalent circuits of a practical RF MEMS shunt switch implementation.*

and consequently previous discussion raised for the ideal switch can hardly apply to practical components. These non-idealities stem from inability of the practical switch to present a perfect open or short-circuit in its OFF and ON-states respectively: Due to physical structure of the practical component, an OFF-state capacitance and an ON-state impedance (resistance or capacitance depending on actual implementation) are always associated with the switch at hand. Figure 4.2 attempts to clarify the adverse effect of these imperfections for the case of a specific shunt switch implementation: For the OFF-state, parasitic capacitance C_{OFF} causes a part of the incident power to couple to the ground and results in a non-zero insertion loss; while parasitic resistance R_{ON} for the ON-state gives rise to limited coupling to ground, making the switch exhibit a finite isolation. Fortunately, mentioned parasitics for RF MEMS switches are in general too low compared to that of solid-state counterparts, a property which enables RF MEMS switches to achieve very low insertion losses and high isolation levels [124].

4.1.1.2 Utilized Contact Types

Aside from the utilized circuit configuration, RF MEMS switches can be also classified in terms of the contact type they employ. In order to shed some light for this latter classification, Figure 4.3 shows two possible implementations of practical RF MEMS switches. The first device depicted in Figure 4.3(a)-4.3(b) is a series implementation and utilizes an *ohmic-contact*, meaning that the switch establishes a direct physical connection of its input/output ports in its ON-state. Due to the direct connection involved, ohmic contact switches can successfully operate down to DC frequencies and the parasitic associated with the contact is essentially a series resistance. On the other hand, Figure 4.3(c)-4.3(d) shows a shunt implementation featuring a *capacitive-contact*. For the latter case, the switch makes an intimate contact with an overlaid dielectric material rather than

(a) Ohmic-contact OFF-state.   (b) Ohmic-contact ON-state.

(c) Capacitive-contact OFF-state.   (d) Capacitive-contact ON-state.
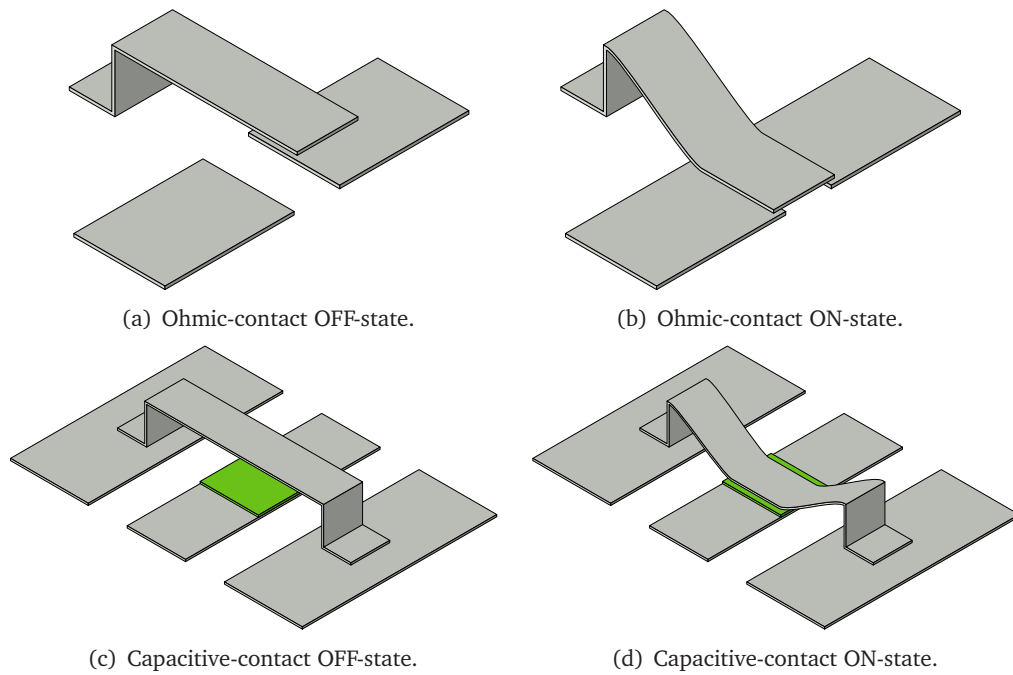
Figure 4.3: *Practical RF MEMS switch implementations featuring two different contact types.*

the transmission line itself in its ON-state and accordingly relevant contact is of capacitive nature. Because of this AC coupling, capacitive-contact switches cannot work properly at low frequencies at which ON-state parasitic capacitance presents a considerable impedance, and accordingly they are more suited to high frequencies.

4.1.1.3   Actuation Types

After having focused on categorization of RF MEMS switches in terms of their electrical properties, it might now be wondered how practical RF MEMS switches are controlled to attain their ON and OFF states. In fact, such a discussion leads to another classification of relevant devices, from a mechanical standpoint this time. Mechanical movement, hence state control, of RF MEMS switches can be achieved through various *actuation* means: RF MEMS switches utilizing electrostatic [29–37], magnetostatic [38], piezoelectric [39] and thermal actuation [40] can be found in the literature. In particular, electrostatic actuation is commonly preferred, as in this work, due to its advantages such as yielding a small device footprint, enabling faster switching and requiring nearly zero bias power [8].

In order to get a clear understanding of how electrostatic actuation works for RF MEMS switches, let us specifically consider the CPW-based shunt, capacitive-contact switch presented in Figure 4.4. For this particular configuration, CPW signal trace forms one of the electrodes and the MEMS bridge, which is electrically connected to the CPW ground planes, constitutes the other one. Having identified the actuation terminals, the operation principle can then be explained as follows:

- When there exists no potential difference between the electrodes (Figure 4.4(a)), lack of a downward directed electrostatic force causes the switch to assume its OFF-state.

- Conversely, if the potential difference between the electrodes exceeds the *pull-in* voltage[1] V_{PI} of the mechanical structure (Figure 4.4(b)), MEMS bridge collapses on the dielectric layer, setting the switch to its ON-state.

It is thus realized from the described actuation mechanism that, an RF signal superposed with a control voltage V can reach to the output port with a low insertion loss if $V = 0$ (OFF-state), and it is routed to ground to establish isolation of the ports if $V \geq V_{\mathrm{PI}}$ (ON-state).

For the electrostatic actuation scheme discussed above, RF signal itself also has an effect on the actuation mechanism along with the control voltage V, owing to the fact that electrostatic force is proportional to the *square* of the *total* applied voltage between the electrodes. The latter property is actually the source of a non-linearity between input and output power characteristics of the RF MEMS switch, analogous to the well-known trend occurring for solid-state components. It has been shown, however, that mentioned non-linearity of RF MEMS switches remains far negligible compared to that of solid-state counterparts [8].

---

[1] Pull-in phenomenon was treated in Chapter 3 for fixed-fixed type beams, which happens to be the same structure for the illustrated configuration.

(a) OFF-state.
(b) ON-state.
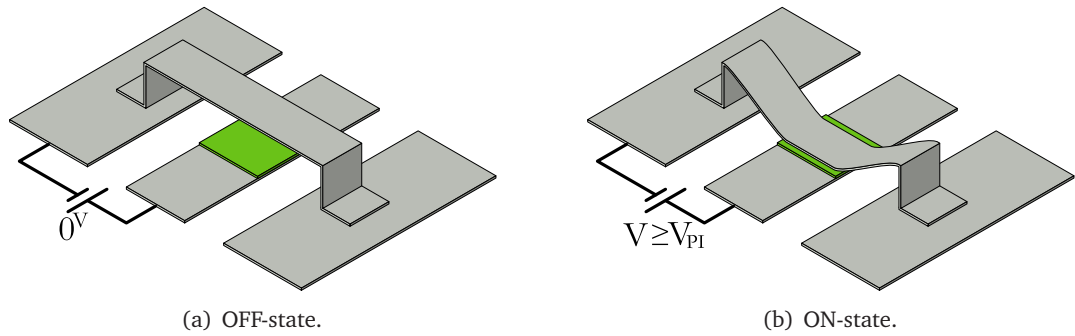
Figure 4.4: *Electrostatic actuation illustrated for a CPW-based shunt, capacitive-contact RF MEMS switch.*

4.1.2 RF MEMS Switch Considered in This Study

According to the classifications established in the previous subsection, the RF MEMS switch considered in this work belongs to the following categories:

- Circuit configuration : Shunt

- Contact-type: Capacitive-contact

- Actuation-type: Electrostatically actuated

It is moreover selected to implement the RF MEMS switch in a CPW transmission line topology. In the light of these properties, it can be recognized that Figure 4.4 provides a simplified illustration of the studied switch configuration.

The aim of the present work is to realize a CPW-based shunt, capacitive contact RF MEMS switch whose electrical characteristics are suited for Ka frequency band (25 - 40 GHz). Electromagnetic and mechanical design, fabrication through an in-house developed process and characterization of the implemented component through measurements are considered within the scope of this study.

4.2 Electromagnetic Design of the RF MEMS Switch

Design of the Ka-band shunt, capacitive-contact RF MEMS switch is pursued in two domains: First, electromagnetic design is completed with a given set of millimeter-wave

design specifications and two design candidates are obtained. Next, one of these candidates are eliminated from a survey of their mechanical characteristics. This section, in particular, focuses on electromagnetic part of the design stage. Proceeding in a regular flow; millimeter-wave design specifications are given initially, utilized physical layout and circuit models are provided next, employed design methodology is discussed subsequently and arrived configurations are listed at the end.

4.2.1 Millimeter-wave Design Specifications

During the electromagnetic design of the Ka-band shunt, capacitive-contact RF MEMS switch, a few millimeter-wave design specifications are adopted for both OFF and ON-states. Relevant specifications are as follows:

- For the OFF-state;

  - Return loss must be better than -20 dB over the Ka-band,

  - Insertion loss must be less than 0.5 dB over the Ka-band.

- For the ON-state;

  - Isolation between the input/output ports should be optimum at 35 GHz with an associated level better than 20 dB.

For reference purposes, Table 4.1 summarizes these millimeter-wave specifications collectively.

Table 4.1: *Millimeter-wave design specifications of the Ka-band shunt, capacitive-contact RF MEMS switch.*

SWITCH STATE	DESIGN SPECIFICATION
OFF	RETURN LOSS ≤ -20 dB in Ka-band INSERTION LOSS ≤ 0.5 dB in Ka-band
ON	OPTIMUM ISOLATION at 35 GHz ISOLATION at 35 GHz ≥ 20 dB
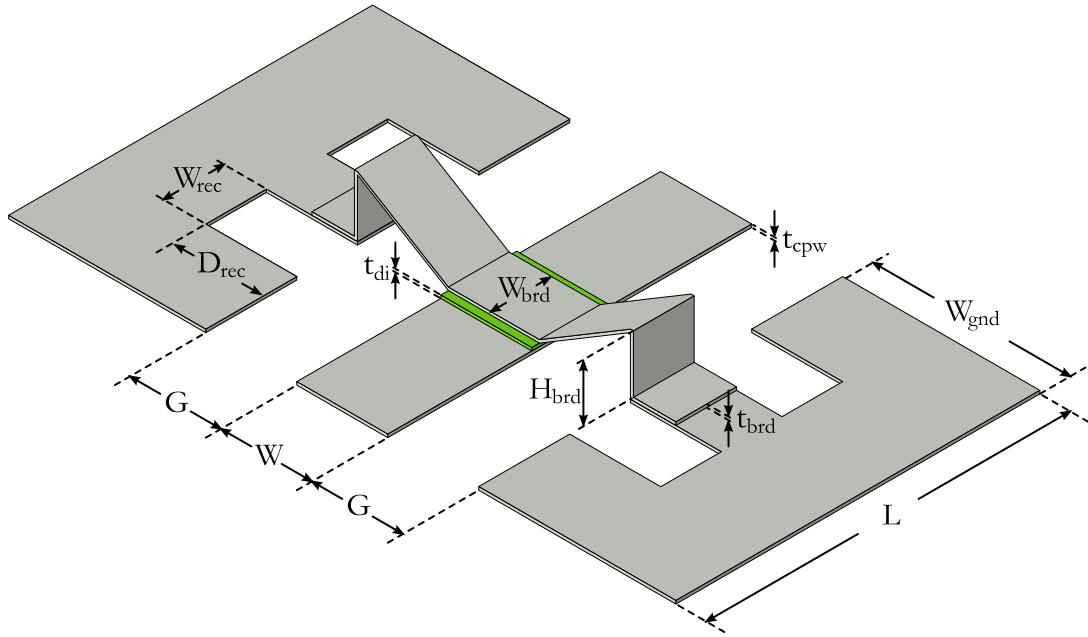
Figure 4.5: *Physical layout of the Ka-band shunt, capacitive-contact RF MEMS switch. Design variables are indicated.*

4.2.2 Physical Layout of the Switch

Figure 4.5 presents the physical layout for the Ka-band shunt, capacitive-contact RF MEMS switch adopted during the electromagnetic design stage and indicates relevant design variables. A quick glance at Figure 4.5 reveals that utilized layout is essentially a replica of the basic shunt layout given in Figure 4.4 with the exception of rectangular recesses located at CPW ground planes near the MEMS bridge. Originally proposed in [125], these recesses enable one to optimize the ON-state isolation performance of the switch for a given frequency band through *inductive tuning*, a method which is discussed in more detail in subsequent sections.

During the electromagnetic design stage of the Ka-band shunt, capacitive-contact RF MEMS switch; material properties and some of the design variables pertaining to physical layout are held fixed in order to reduce the dimension of problem space. Relevant assignments are done in accordance with fabrication plans and by considering typical values. The material properties and fixated design variables along with their descriptions and selected values are listed in Table 4.2. Remaining design variables, which are ad-

150

Table 4.2: *Fixated design variables and material properties for the Ka-band shunt, capacitive-contact RF MEMS switch.*

CATEGORY	PARAMETER	EXPLANATION	FIXED VALUE
SWITCH LAYOUT DIMENSIONS	L	SWITCH DEVICE LENGTH	$400\ \mu m$
	W_{gnd}	CPW GROUND PLANE WIDTH	$500\ \mu m$
	W_{brd}	BRIDGE WIDTH	$50\ \mu m$
	H_{brd}	BRIDGE HEIGHT[a]	$1.5, 2\ \mu m$
SUBSTRATE MATERIAL (QUARTZ)	H_{subs}	SUBSTRATE THICKNESS	$500\ \mu m$
	$\varepsilon_{\text{subs}}$	RELATIVE SUBSTRATE PERMITTIVITY	3.8
	$\tan \delta$	SUBSTRATE TANGENT LOSS	0.002
METALLIZATION (GOLD)	t_{CPW}	CPW METAL THICKNESS	$1.0\ \mu m$
	t_{brd}	BRIDGE METAL THICKNESS	$1.0\ \mu m$
	σ_{CPW}	METALLIZATION CONDUCTIVITY	30 MS/m
DIELECTRIC MATERIAL (SILICON NITRIDE)	t_{di}	DIELECTRIC LAYER THICKNESS	$0.3\ \mu m$
	ε_{di}	RELATIVE DIELECTRIC PERMITTIVITY	7.0
	f_{cont}	CONTACT DEGRADATION FACTOR[b]	0.37

[a] Bridge height is the spacing between the bottom of the bridge and top of the CPW signal trace.
[b] This factor takes into account the ON-state capacitance degradation due to surface roughness of the electrodes and etch holes in the bridge. Its value is inferred from previous measurement results [97]. In particular, contact degradation is incorporated in ON-state simulations by scaling ε_{di} by f_{cont}.

Table 4.3: *Adjusted design variables for the Ka-band shunt, capacitive-contact RF MEMS switch.*

CATEGORY	PARAMETER	EXPLANATION
SWITCH LAYOUT DIMENSIONS	G	CPW SLOT WIDTH
	W	CPW SIGNAL TRACE WIDTH
	W_{rec}	CPW GROUND PLANE RECESS WIDTH
	D_{rec}	CPW GROUND PLANE RECESS DEPTH

justed throughout the design procedure, are provided in Table 4.3 together with their explanations.

4.2.3 Circuit Model of the Switch

In order to set the design procedure on a systematic and predictable basis, a circuit model is utilized in conjunction with the EM simulations for the Ka-band shunt, capacitive-contact RF MEMS switch. Figure 4.6 presents the employed circuit model, which is actually a slightly modified version of the one proposed in [126]. Physical interpretation of each model element and their associated parameters are discussed briefly below:

1. Transmission line sections appearing at the input and output ports of the model represent CPW line sections up to the ground plane recesses in the physical layout. Consequently, one has

$$L_{\text{CPW}} = \frac{L - W_{\text{brd}}}{2} - W_{\text{rec}}$$

Characteristic impedance of these lines are denoted with Z_0 and associated propagation constant γ can be expressed as

$$\gamma = \alpha_{\text{CPW}} + \text{j} \frac{2\pi f \sqrt{\epsilon_{\text{eff}}}}{c}$$

where α_{CPW} is attenuation per unit length, f is the operating frequency, ϵ_{eff} is the effective relative permittivity and $c = 3x10^8$ m/s is the speed of light in vacuum. In particular, Z_0 and ϵ_{eff} can be accurately related to physical CPW dimensions through the quasi-TEM formulation found in [127,128] for a non-shielded topology without
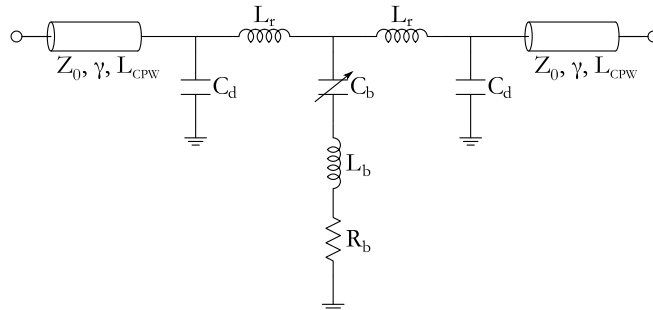
Figure 4.6: *Utilized circuit model for the Ka-band shunt, capacitive-contact RF MEMS switch.*

152

conductor-backing as:

$$Z_0 = \frac{30\pi}{\sqrt{\epsilon_{\mathrm{eff}}}\, K(k)/K(\sqrt{1-k^2})} \tag{4.1a}$$

$$\epsilon_{\mathrm{eff}} = 1 + q(\epsilon_{\mathrm{subs}} - 1) \tag{4.1b}$$

In Equation (4.1); q, k_3 and k are given by

$$q = \frac{K(k_3)/K(\sqrt{1-k_3^2})}{2\, K(k)/K(\sqrt{1-k^2})} \tag{4.2a}$$

$$k_3 = \frac{\sinh(\pi W/4H_{\mathrm{subs}})}{\sinh(\pi(W+2G)/4H_{\mathrm{subs}})} \tag{4.2b}$$

$$k = \frac{W}{W+2G} \tag{4.2c}$$

where $K(.)$ denotes the complete elliptic integral of the first kind. Although an analytical expression also exists for attenuation coefficient α_{CPW}, this quantity is best to be extracted from EM simulations since corresponding formulation is found to underestimate the conductor loss significantly.

2. Reactive elements C_{d} and L_{r} account for the step discontinuity in the CPW transmission line at the ground plane recess interfaces [129]. Notice also that, L_{r} has an additional component representing the high-impedance CPW line section of the recess zones featuring an increased slot width of $G + D_{\mathrm{rec}}$. Values for the relevant elements are extracted from EM simulation data during the course of modeling.

3. Shunt branch consisting of series connected C_{b}, L_{b} and R_{b} elements is an electrical manifestation of the MEMS bridge. Specifically,

   - C_{b} represents the capacitance between the MEMS bridge and the CPW signal trace, and it has two values corresponding to OFF and ON-states of the switch.

   - L_{b} is the bridge inductance and consists of two components: First component is responsible for the inductance due to the bridge itself[2], whereas the second one describes the short-circuited *transverse* CPW transmission line having cross-section dimensions of $W_{\mathrm{rec}}/W_{\mathrm{brd}}/W_{\mathrm{rec}}$ and a length of D_{rec} [125, 126]. It is in fact the latter component which enables one to accomplish aforementioned *inductive tuning*.

---

[2] This component can be thought of the total inductance of the inverted microstrip line section formed by the bridge and the CPW signal trace. Note that such an approximation is permissible due to the property $H_{\mathrm{brd}} \ll G$. C_{b} and R_{b} can be similarly envisioned.

- R_b stands for the loss associated with the bridge.

Values of these bridge-related elements are extracted from EM simulation data as well.

4.2.4 Design Procedure

Design procedure for the Ka-band shunt, capacitive-contact RF MEMS switch is an iterative based one and is composed of two main steps. First step encompasses determination of the CPW characteristic impedance Z_0 for the optimization of OFF-state return loss. Inductive tuning forms the second step, in which ON-state isolation is optimized for 35 GHz. Following subsections briefly describe mentioned design phases.

4.2.4.1 Optimization of OFF-State Return Loss

In order to optimize return loss for the OFF-state of the switch, an analytical approach is utilized to determine Z_0 of the CPW sections. Employed method is actually similar to the one developed in [130], the latter which attempts to obtain required unloaded line impedance Z_0 for optimum degree/dB performance of a loaded-line phase shifter. Adopted method proceeds as follows:

- For a given value of the CPW signal trace width W, CPW slot width G is swept.

- Using Equation 4.1, Z_0 and ϵ_{eff} are next determined for that sweep.

- Then, using the equivalent circuit model in Figure 4.6 together with empirical estimations for the associated circuit element values (based on EM simulation data), $|S_{11}|$ is monitored for each G at a number of frequency points (25 GHz, 35 GHz and 45 GHz to be specific).

Figure 4.7 presents sample plots for the OFF-state return loss as a function of Z_0 for two designs having different bridge heights (H_{brd}). It is noted for both designs that $|S_{11}|$ becomes sufficiently small for Z_0 values in 80-100 Ω range, an observation justifying the loaded-line concept: The MEMS bridge, which effectively acts as a shunt capacitor in the

154

(a) $H_{\mathrm{brd}} = 2.0 \ \mu m$, $W = 150 \ \mu m$.

(b) $H_{\mathrm{brd}} = 1.5 \ \mu m$, $W = 130 \ \mu m$.
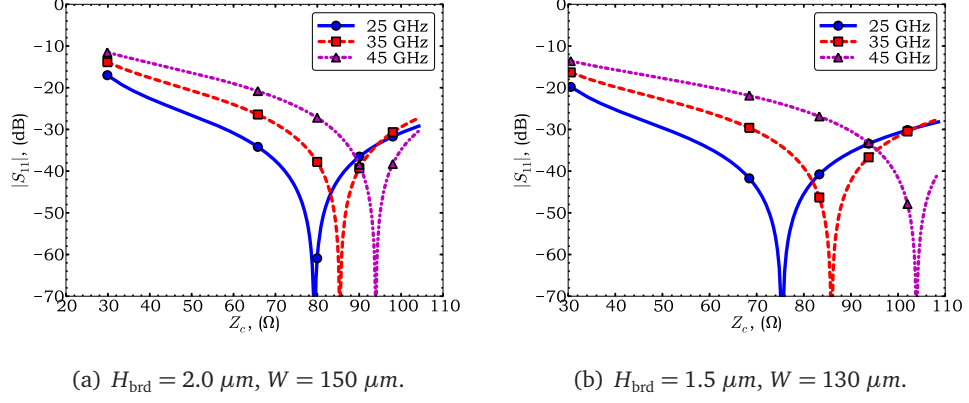
Figure 4.7: *Sample $|S_{11}|$ versus Z_0 plots for two different designs featuring different H_{brd} values.*

OFF-state, *loads* the underlying CPW transmission line and resulting *loaded* characteristic impedance can be brought close to the 50 Ω reference impedance if Z_0 assumes an appropriate high value. Frequency dependence of the return loss is moreover noticed from the provided curves. In particular, the design having $H_{\mathrm{brd}} = 1.5 \ \mu m$ seems to be more sensitive to frequency and this is a consequence of its higher OFF-state capacitance (as $Y_C = \mathrm{j}\omega C$). From bandwidth considerations, it is tried to pick Z_0 as the intersection of $f = 25$ GHz and $f = 45$ GHz curves for both designs during the design procedure.

4.2.4.2 Inductive Tuning and Optimization of ON-State Isolation

Referring back to the circuit model depicted in Figure 4.6, one notices that the shunt branch representing the MEMS bridge is actually a series RLC circuit. From elementary circuit theory, it is known that relevant circuit *resonates* at the particular frequency f_0, where

$$f_0 = \frac{1}{2\pi \ \sqrt{L_{\mathrm{b}} C_{\mathrm{b}}}} \tag{4.3}$$

Since the bridge capacitance C_{b} takes on different values for OFF and ON-states of the switch, it follows from Equation (4.3) that resonance frequency of the shunt arm changes up on state change. This property in turn can be exploited to optimize the isolation response around a particular frequency with proper tuning of L_{b}. For the sake of clarity, Figure 4.8 illustrates the concept. If one desires to optimize the ON-state isolation for a given angular frequency ω, it suffices to shift the ON-state resonance frequency $\omega_{0,\mathrm{ON}}$ to

155
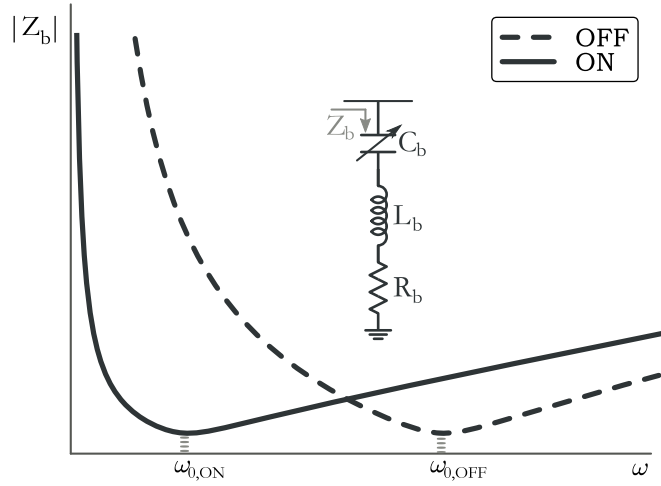
Figure 4.8: *Impedance characteristics of the MEMS bridge as a function of angular frequency for different switch states.*

ω as the impedance presented by the MEMS bridge becomes a minimum there. Since C_b usually cannot be altered due to previously determined device dimensions (from return loss optimization step in particular) and design/fabrication constraints, it follows that performance of the switch in ON-state can be significantly improved for a desired isolation center frequency by tuning L_b. Notice moreover that, performing so does not hinder the OFF-state performance as long as Z_b, whose magnitude switches to a much higher value in OFF-state, is properly compensated for.

In order to optimize the ON-state isolation for 35 GHz through inductive tuning, a semi-empirical approach is utilized. For that purpose, initially, L_b is expressed as the sum of two components as pointed in §4.2.3:

$$L_b = L_{b,0} + L_{b,rec} \tag{4.4}$$

where $L_{b,0}$ is the inductance component due to the MEMS bridge itself and $L_{b,rec}$ is associated with the short-circuited transverse CPW transmission line ($W_{rec}/W_{brd}/W_{rec}$) of length D_{rec}. For given values of bridge dimensions and CPW slot width G, $L_{b,0}$ is a constant [126]. $L_{b,rec}$, on the other hand, can be expressed with:

$$L_{b,rec} = a_{rec} \frac{Z_{0,rec}}{\omega} \tan\left(\beta_{rec} D_{rec}\right) \tag{4.5}$$

where β_{rec} and $Z_{0,rec}$ are the propagation constant and characteristic impedance of the short-circuited transverse CPW line respectively, and a_{rec} is a coefficient yet to be deter-

mined. For typical D_{rec} values, it is observed that $\beta_{rec}D_{rec} \ll 1$, an inequality permitting the following small-argument approximation:

$$L_{b,rec} = a_{rec}\frac{Z_{0,rec}\sqrt{\epsilon_{eff,rec}}}{c}D_{rec} \tag{4.6}$$

Employing Equation (4.6) into (4.4) thus gives;

$$L_b = L_{b,0} + a_{rec}\frac{Z_{0,rec}\sqrt{\epsilon_{eff,rec}}}{c}D_{rec} \tag{4.7}$$

The quantities $Z_{0,rec}$ and $\epsilon_{eff,rec}$ appearing in Equation (4.7) can be calculated from Equations (4.1) and (4.2) by letting $G = W_{rec}$ and $W = W_{brd}$. Unknowns $L_{b,0}$ and a_{rec} can then be solved from the two equations obtained after simulating two switch configurations differing only in their D_{rec} values. Having determined those unknowns, required recess depth for a desired bridge inductance, hence ON-state resonance frequency, can be easily obtained from Equation (4.7).

Utilized semi-empirical inductive tuning approach can be outlined as follows:

i. Electromagnetically simulate two switch configurations having different D_{rec} dimensions and extract corresponding bridge inductance values $L_{b,1}$ and $L_{b,2}$.

ii. Construct Equation (4.7) for the two configurations as:

$$L_{b,1} = L_{b,0} + a_{rec}\frac{Z_{0,rec}\sqrt{\epsilon_{eff,rec}}}{c}D_{rec,1} \tag{4.8}$$

$$L_{b,2} = L_{b,0} + a_{rec}\frac{Z_{0,rec}\sqrt{\epsilon_{eff,rec}}}{c}D_{rec,2} \tag{4.9}$$

iii. Solve Equation (4.8) for $L_{b,0}$ and a_{rec}.

iv. Determine the required bridge inductance to shift the ON-state resonance to 35 GHz from

$$L_{b,35} = L_{b,i}\left(\frac{f_{0,i}}{35\text{ GHz}}\right)^2, \quad i = 1 \text{ or } 2$$

v. Solve Equation (4.7) for $D_{rec,35}$ with $L_b = L_{b,35}$.

Proposed inductive tuning approach described above is found to achieve an excellent tuning of the ON-state resonance frequency to 35 GHz in only two iterations.

Table 4.4: *Switch configurations and corresponding circuit model parameters attained at the end of electromagnetic design cycle.*

DESIGN	LAYOUT PARAMETERS[a]	CIRCUIT MODEL PARAMETERS
DESIGN #1	$H_{\mathrm{brd}} = 2.0\ \mu m$ $W = 150\ \mu m$ $G = 120\ \mu m$ $W_{\mathrm{rec}} = 40\ \mu m$ $D_{\mathrm{rec}} = 100\ \mu m$	$Z_0 = 89.8\ \Omega,\ \epsilon_{\mathrm{eff}} = 2.37,\ L_{\mathrm{CPW}} = 135\ \mu m$ $\alpha_{\mathrm{CPW}} = 440.3\ \mathrm{dB/m}$ (@ 35 GHz) $C_{\mathrm{d}} = 6.66\ \mathrm{fF},\ L_{\mathrm{r}} = 42.25\ \mathrm{pH}$ $C_{\mathrm{b,OFF}} = 41.44\ \mathrm{fF},\ C_{\mathrm{b,ON}} = 561.6\ \mathrm{fF}$ $L_{\mathrm{b}} = 37.01\ \mathrm{pH},\ R_{\mathrm{b}} = 0.37\ \Omega$
DESIGN #2	$H_{\mathrm{brd}} = 1.5\ \mu m$ $W = 130\ \mu m$ $G = 90\ \mu m$ $W_{\mathrm{rec}} = 80\ \mu m$ $D_{\mathrm{rec}} = 145\ \mu m$	$Z_0 = 85.9\ \Omega,\ \epsilon_{\mathrm{eff}} = 2.38,\ L_{\mathrm{CPW}} = 95\ \mu m$ $\alpha_{\mathrm{CPW}} = 713.4\ \mathrm{dB/m}$ (@ 35 GHz) $C_{\mathrm{d}} = 7.19\ \mathrm{fF},\ L_{\mathrm{r}} = 73.24\ \mathrm{pH}$ $C_{\mathrm{b,OFF}} = 52.90\ \mathrm{fF},\ C_{\mathrm{b,ON}} = 472.5\ \mathrm{fF}$ $L_{\mathrm{b}} = 43.26\ \mathrm{pH},\ R_{\mathrm{b}} = 0.78\ \Omega$

[a] For material properties and other common layout parameters, refer to Table 4.2.

4.2.4.3 Attained Switch Configurations

The design steps detailed in the previous subsections are applied in an iterative cycle to arrive at two switch configurations. During the process, Ansoft HFSS™v9.2 Finite Element Analysis (FEA) software is utilized to perform EM simulations of the switch device and AWR Microwave Office™v2006 circuit simulator is employed to extract circuit model parameters through built-in optimization routines. Table 4.4 lists the attained switch configurations for Design #1 (with $H_{\mathrm{brd}} = 2.0\ \mu m$) and Design #2 (with $H_{\mathrm{brd}} = 1.5\ \mu m$) along with their extracted circuit model parameters. Electromagnetically simulated and modeled magnitude S-parameters are provided in Figures 4.9 and 4.10 for Design #1 and Design #2 respectively.

A quick inspection of Figures 4.9 and 4.10 shows that attained switch configurations successfully satisfy the millimeter-wave design specifications listed in Table 4.1. In particular, Design #1 is observed to perform slightly better than Design #2 in both OFF and ON states. It is moreover noted that the agreement between EM simulation and circuit model results is reasonable. For the sake of completeness, Table 4.5 summarizes the performance of both designs based on corresponding EM simulation data.
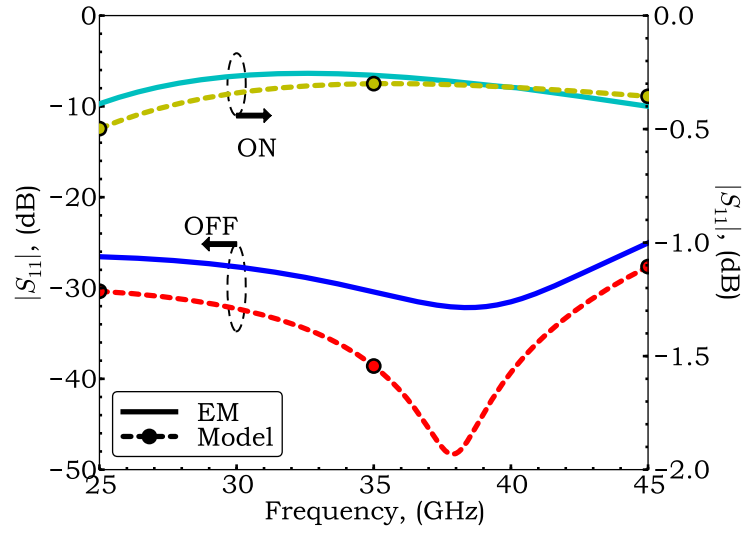
(a) $|S_{11}|$ for both states.
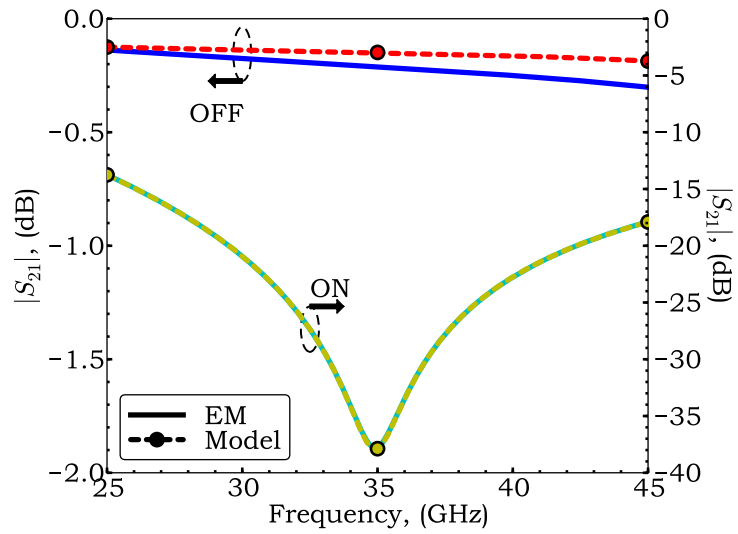
(b) $|S_{21}|$ for both states.

Figure 4.9: *Electromagnetically simulated and modeled magnitude S-parameters for Design #1 ($H_{\mathrm{brd}} = 2.0\ \mu m$).*
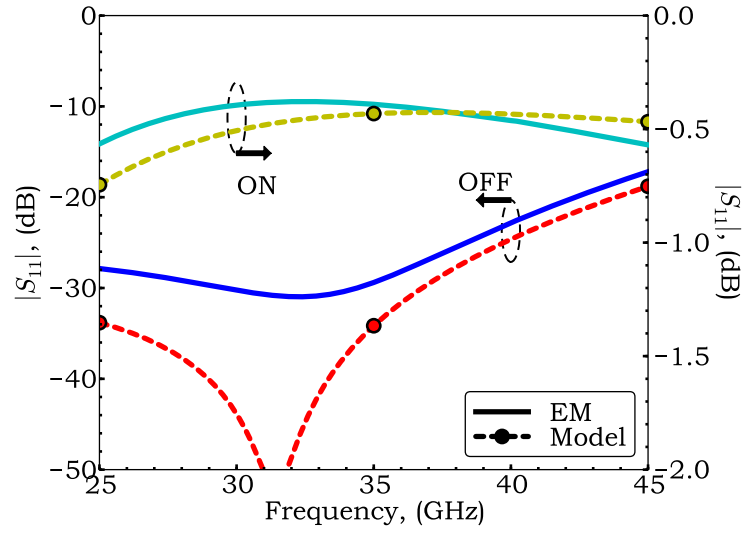
(a) $|S_{11}|$ for both states.
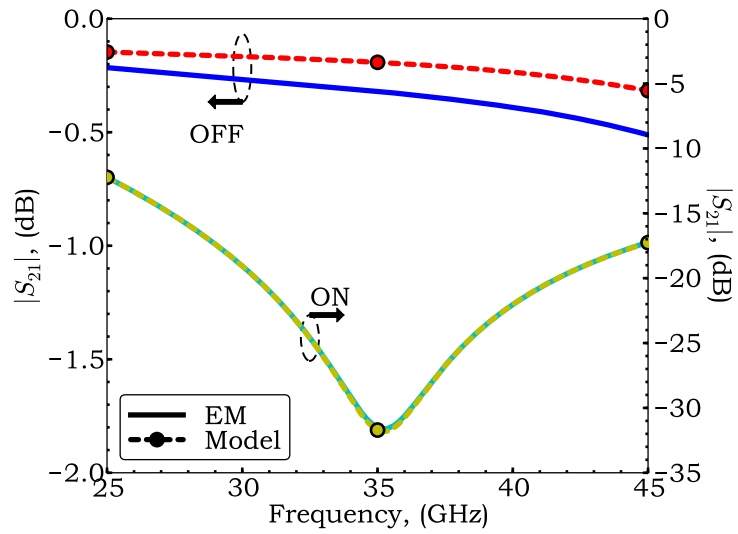
(b) $|S_{21}|$ for both states.

Figure 4.10: *Electromagnetically simulated and modeled magnitude S-parameters for Design #2 ($H_{\mathrm{brd}} = 1.5\ \mu m$).*

Table 4.5: *Millimeter-wave performance summary of Design #1 and Design #2 obtained from corresponding EM simulation data.*

DESIGN	PERFORMANCE DATA	
	OFF-STATE	ON-STATE
DESIGN #1	INSERTION LOSS ≤ 0.25 dB, $f \leq 40.0$ GHz ≤ 0.30 dB, $f \leq 45.0$ GHz RETURN LOSS ≤ -26.6 dB, 25.0–40.0 GHz ≤ -25.0 dB, 25.0–45.0 GHz	ISOLATION OPTIMUM LEVEL: 37.8 dB ($f_0 = 34.9$ GHz) ≥ 20 dB, 29.5–42.4 GHz ≥ 30 dB, 33.2–36.8 GHz
DESIGN #2	INSERTION LOSS ≤ 0.39 dB, $f \leq 40.0$ GHz ≤ 0.50 dB, $f \leq 44.6$ GHz RETURN LOSS ≤ -22.8 dB, 25.0–40.0 GHz ≤ -20.0 dB, 25.0–42.3 GHz	ISOLATION OPTIMUM LEVEL: 31.6 dB ($f_0 = 35.2$ GHz) ≥ 20 dB, 30.5–41.7 GHz ≥ 30 dB, 34.3–36.3 GHz

4.2.4.4 Integration of CPW Transitions to Switch Configurations

Finalized switch configurations provided in §4.2.4.3 utilize high-impedance CPW lines in order to optimize their return loss performance, which in turn necessitates a high CPW slot width G according to Equations (4.1)-(4.2). This requirement in turn lends itself to high CPW pitch dimensions (i.e. 2G+W), which might not be desired in practice due to measurement related restrictions. In particular, CPW probes found in the inventory of METU Dept. of EE Millimeter-wave Laboratory posed such a restriction: Pitch spacing of the available CPW probes were about 220 μm so that it was not possible to measure designed switch devices (having CPW pitch spacings of 390 μm and 310 μm) unless the layouts were modified in a compatible fashion.

In order to circumvent described CPW pitch problem, it is opted to employ CPW transitions at the input and output ports of the switch designs, which would establish the interconnection between measurement-dictated low-pitch and design-dictated high-pitch CPW lines. For that purpose, linear type transitions are employed as illustrated in Figure 4.11. Introduction of these CPW transitions calls for four additional design parameters, which are indicated in Table 4.6 along with their explanations. In particular, three of these parameters are determined readily: Since switch devices are designed for a 50 Ω system, it is desirable to set the characteristic impedance of outer CPW lines to 50 Ω by adjusting
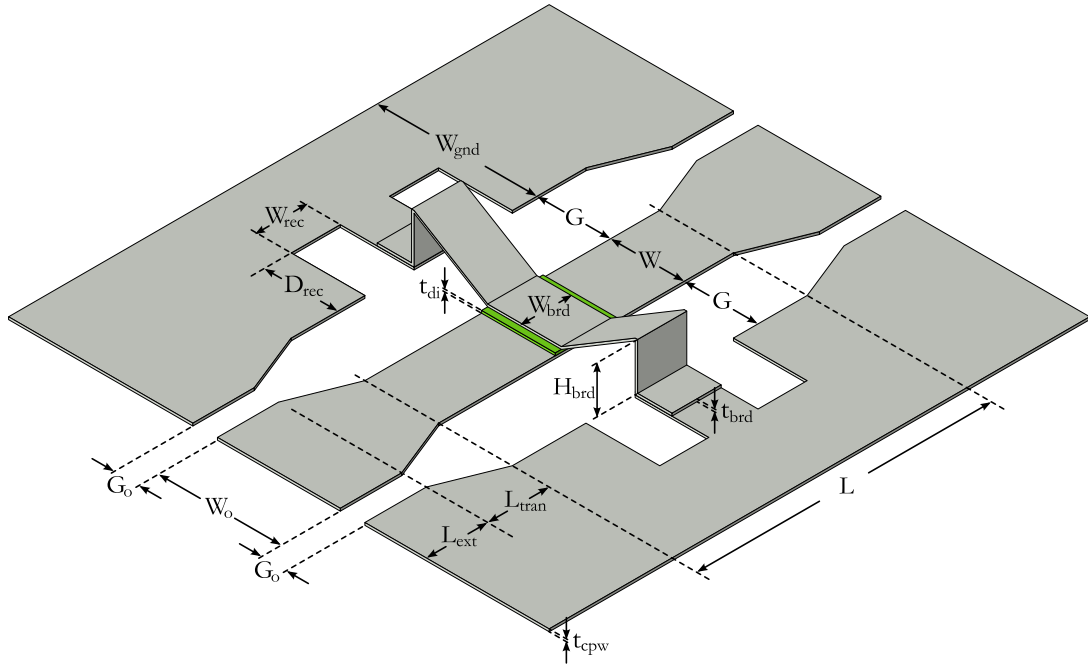
Figure 4.11: *Physical layout of the Ka-band shunt, capacitive-contact RF MEMS switch with integrated CPW transitions. Design variables are indicated.*

G_0 and W_0. Imposing this latter condition together with the pitch spacing constraint (i.e. $2G_0 + W_0 \leq 220 \ \mu m$) in Equation (4.1) yields a possible solution of $G_0 = 17 \ \mu m$ and $W_0 = 180 \ \mu m$. L_{ext} dimension is moreover set to 50 μm as this value is a good compromise between minimum probe landing area and maximum device length trade-offs. These three assignments leave L_{tran} as the only unknown.

Determination of the dimension L_{tran} is accomplished by monitoring the effect of that parameter on overall OFF-state return loss of two switch designs. For that purpose, reasonable values of 50 μm and 100 μm are assigned to L_{tran} and simulated return losses are compared. Figure 4.12 provides the relevant comparison for Design #1 and Design #2.

Table 4.6: *Design variables for the CPW transitions of Ka-band shunt, capacitive-contact RF MEMS switch.*

CATEGORY	PARAMETER	EXPLANATION
CPW TRANSITION DIMENSIONS	G_0	OUTER CPW SLOT WIDTH ($= 17 \ \mu m$)
	W_0	OUTER CPW SIGNAL TRACE WIDTH ($= 180 \ \mu m$)
	L_{ext}	OUTER CPW LINE LENGTH ($= 50 \ \mu m$)
	L_{tran}	CPW TRANSITION LENGTH

(a) Design #1   (b) Design #2
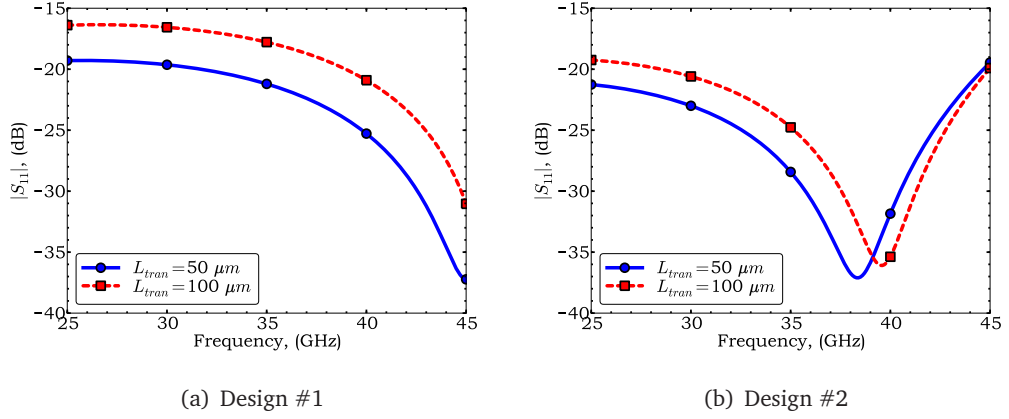
Figure 4.12: *Return loss performance of the switch configurations compared for two different L_{tran} values.*

It is observed from Figures 4.12(a) and 4.12(b) that reducing L_{tran} improves the return loss performance for both switch configurations and that $L_{\text{tran}} = 50 \ \mu m$ is an acceptable selection considering the -20 dB reflection specification.

Having set the design parameters related to the CPW transitions, Table 4.7 presents the final forms of the switch configurations. From the same table, four additional circuit model parameters are noticed: As delineated in Figure 4.13, relevant parameters pertain to a transmission line section of length $L_{\text{t}} = L_{\text{tran}} + L_{\text{ext}}$ which represents the CPW transition in the physical layout. Figures 4.14 and 4.15 plot simulated and modeled magnitude S-parameters for the final forms of Design #1 and Design #2 respectively. Millimeter-wave performance aspects of both designs is summarized in Table 4.8.
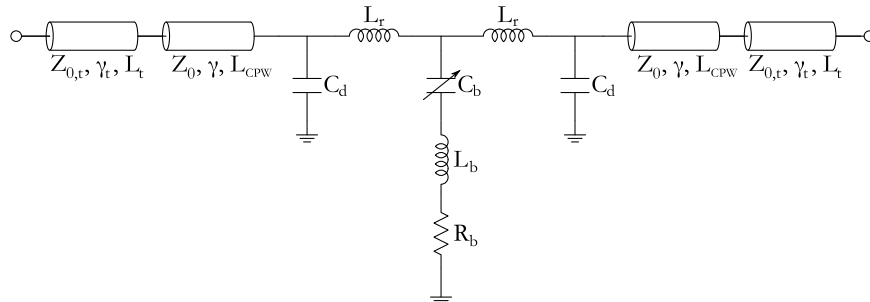
Figure 4.13: *Circuit model for the Ka-band shunt, capacitive-contact RF MEMS switch integrated with CPW transitions.*
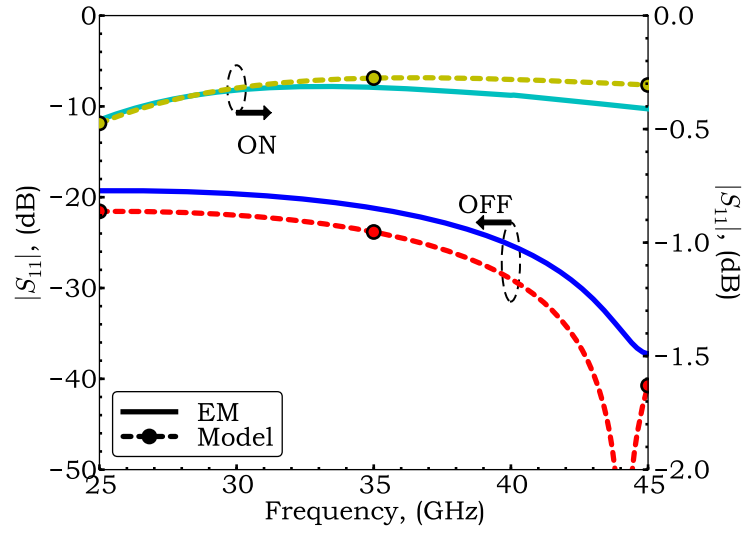
(a) $|S_{11}|$ for both states.
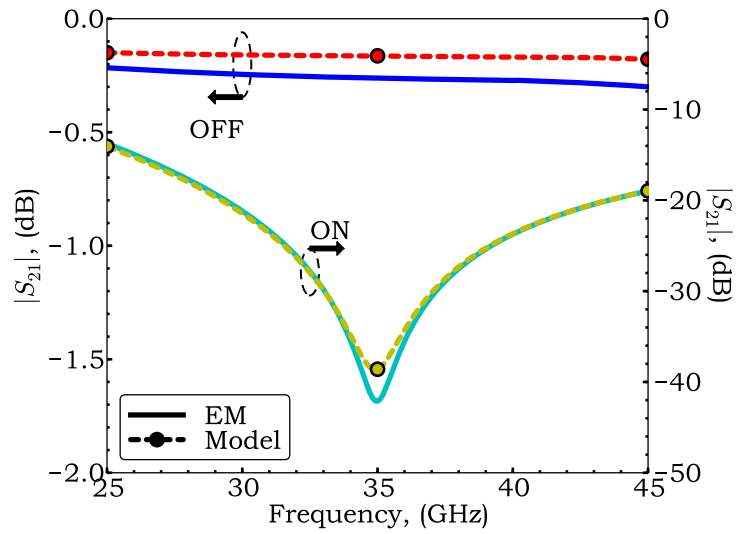
(b) $|S_{21}|$ for both states.

Figure 4.14: *Electromagnetically simulated and modeled magnitude S-parameters for Design #1 after integration of CPW transitions ($H_{\text{brd}} = 2.0\ \mu m$).*
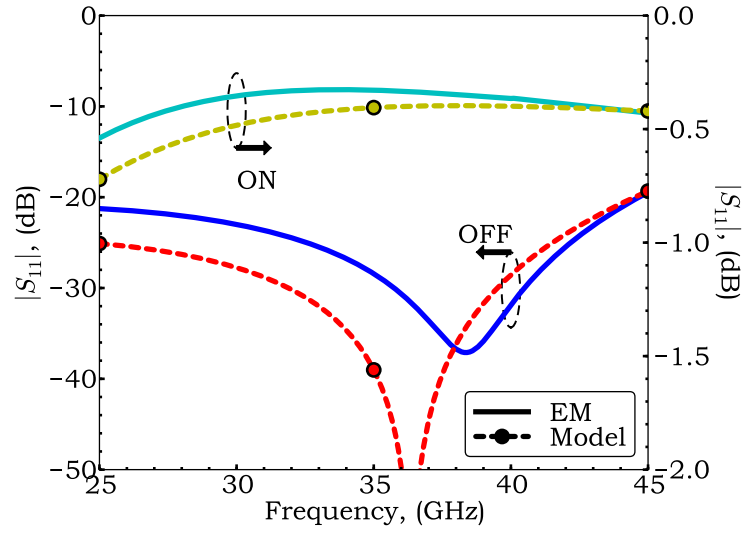
(a) $|S_{11}|$ for both states.
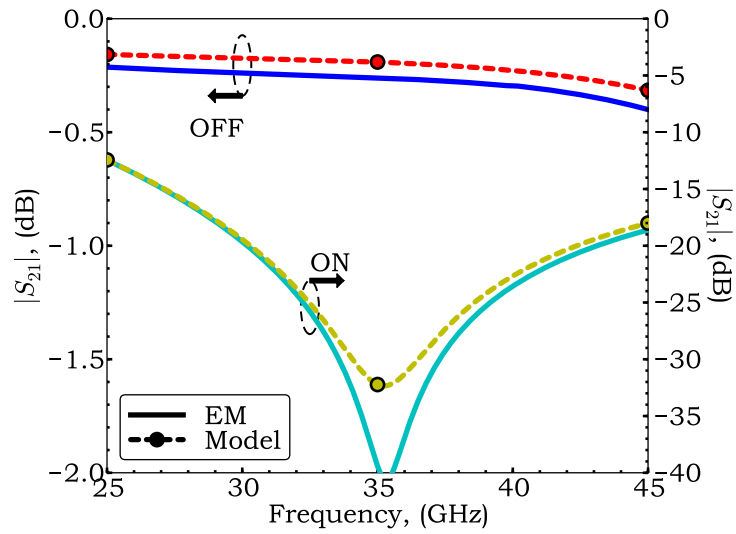
(b) $|S_{21}|$ for both states.

Figure 4.15: *Electromagnetically simulated and modeled magnitude S-parameters for Design #2 after integration of CPW transitions ($H_{\mathrm{brd}} = 1.5\ \mu m$).*

Table 4.7: *Switch configurations and corresponding circuit model parameters attained at the end of electromagnetic design cycle following the integration of CPW transitions.*

DESIGN	LAYOUT PARAMETERS[a]	CIRCUIT MODEL PARAMETERS
DESIGN #1	$H_{\mathrm{brd}} = 2.0\ \mu m$ $W = 150\ \mu m$ $G = 120\ \mu m$ $W_{\mathrm{rec}} = 40\ \mu m$ $D_{\mathrm{rec}} = 100\ \mu m$ $G_0 = 17\ \mu m,\ W_0 = 180\ \mu m$ $L_{\mathrm{tran}} = L_{\mathrm{ext}} = 50\ \mu m$	$Z_0 = 89.8\ \Omega,\ \epsilon_{\mathrm{eff}} = 2.37,\ L_{\mathrm{CPW}} = 135\ \mu m$ $\alpha_{\mathrm{CPW}} = 440.3$ dB/m (@ 35 GHz) $C_d = 6.66$ fF, $L_r = 42.25$ pH $C_{\mathrm{b,OFF}} = 41.44$ fF, $C_{\mathrm{b,ON}} = 561.6$ fF $L_b = 37.01$ pH, $R_b = 0.37\ \Omega$ $Z_{0,t} = 76.7\ \Omega,\ \epsilon_{\mathrm{eff}} = 2.37,\ L_t = 100\ \mu m$ $\alpha_{\mathrm{CPW}} = 0$ dB/m (@ 35 GHz)
DESIGN #2	$H_{\mathrm{brd}} = 1.5\ \mu m$ $W = 130\ \mu m$ $G = 90\ \mu m$ $W_{\mathrm{rec}} = 80\ \mu m$ $D_{\mathrm{rec}} = 145\ \mu m$ $G_0 = 17\ \mu m,\ W_0 = 180\ \mu m$ $L_{\mathrm{tran}} = L_{\mathrm{ext}} = 50\ \mu m$	$Z_0 = 85.9\ \Omega,\ \epsilon_{\mathrm{eff}} = 2.38,\ L_{\mathrm{CPW}} = 95\ \mu m$ $\alpha_{\mathrm{CPW}} = 713.4$ dB/m (@ 35 GHz) $C_d = 7.19$ fF, $L_r = 73.24$ pH $C_{\mathrm{b,OFF}} = 52.90$ fF, $C_{\mathrm{b,ON}} = 472.5$ fF $L_b = 43.26$ pH, $R_b = 0.78\ \Omega$ $Z_{0,t} = 68.0\ \Omega,\ \epsilon_{\mathrm{eff}} = 2.38,\ L_t = 100\ \mu m$ $\alpha_{\mathrm{CPW}} = 0$ dB/m (@ 35 GHz)

[a] For material properties and other common layout parameters, refer to Table 4.2.

An examination of Figures 4.14-4.15 and Table 4.8 reveals that switch configurations continue to meet previously stated millimeter-wave design specifications after integration with CPW transitions. In fact, OFF and ON-state responses are observed to improve compared to transition-free case, the only exception being OFF-state return loss of Design #1 which marginally satisfies the -20 dB criterion. It is moreover noticed that

Table 4.8: *Millimeter-wave performance summary of Design #1 and Design #2 following the integration of CPW transitions. Relevant data are obtained from corresponding EM simulations.*

DESIGN	PERFORMANCE DATA	
	OFF-STATE	ON-STATE
DESIGN #1	INSERTION LOSS ≤ 0.27 dB, $f \leq 40.0$ GHz ≤ 0.30 dB, $f \leq 45.0$ GHz RETURN LOSS ≤ -19.3 dB, 25.0–40.0 GHz ≤ -20.0 dB, 31.7–45.0 GHz	ISOLATION OPTIMUM LEVEL: 42.1 dB ($f_0 = 35.0$ GHz) ≥ 20 dB, 29.4–43.5 GHz ≥ 30 dB, 33.0–37.2 GHz
DESIGN #2	INSERTION LOSS ≤ 0.30 dB, $f \leq 40.0$ GHz ≤ 0.40 dB, $f \leq 45.0$ GHz RETURN LOSS ≤ -21.3 dB, 25.0–40.0 GHz ≤ -20.0 dB, 25.0–44.7 GHz	ISOLATION OPTIMUM LEVEL: 40.6 dB ($f_0 = 35.3$ GHz) ≥ 20 dB, 30.2–43.1 GHz ≥ 30 dB, 33.6–37.3 GHz

the agreement between EM simulation and circuit model results is degraded compared to the transition-free case and loss is somewhat overestimated (compare ON-state resonance dips for instance). Pointed problems associated with circuit modeling will be addressed later on.

4.3 Mechanical Characteristics of the Switch Configurations

In the previous section, two switch configurations satisfying a given set of millimeter-wave specifications are set forth as a result of the electromagnetic design procedure. Having thus finished the first part of the design stage, this section now investigates mechanical characteristics of these configurations. Following analyses, which are applications of the formulations established in Chapter 3, compare mechanical aspects of the two design candidates and ultimately help to elect one of them for implementation.

4.3.1 A Mechanical Constraint for the Switch Devices

A favorable mechanical property for the electrostatically actuated Ka-band shunt, capacitive contact switch would be a low actuation voltage since a too high value for the relevant voltage not only endangers the lifetime of the device (due to dielectric charging mechanism [131]), but also elevates the specifications for the control electronics biasing it. In particular, during the course of this study, a 30 V limit is imposed on the actuation voltage to achieve a proper ON-state isolation around 35 GHz.

4.3.2 Pull-in Voltage Analysis

A first implication of the mechanical constraint stated in §4.3.1 is that pull-in of the switches should occur prior to 30 V. Feasibility of this first requirement can be readily investigated using the pull-in formulation derived in §3.5.2.2 owing to the fact that switch configurations at hand are of fixed-fixed beam type[3]. For this purpose, physical properties of switch configurations found in Tables 4.2 and 4.7 are substituted into Equation (3.162)

---

[3] Although Figures 4.5 and 4.11 might imply the presence of step-ups near the mechanical anchors which violate the fixed-fixed beam assumption, those anchors are reinforced in the fabrication process; a step which improves applicability of this assumption.

to calculate the corresponding pull-in voltages. Since a complete mechanical character-ization of the bridge metallization is not available, Young's modulus and Poisson's ratio are assumed typical values of $E = 78$ GPa and $v = 0.44$ [132], while the biaxial resid-ual stress is swept in $0 - 100$ MPa range. Figure 4.16 compares obtained pull-in voltage curves of Design #1 and Design #2 as a function of the biaxial residual stress σ_0.

It is observed from Figure 4.16 that Design #2 exhibits lower pull-in voltages compared to Design #1 in the considered σ_0 range and this is primarily due to the lower bridge height value employed for Design #2. Design #1, featuring a higher bridge length/thickness ratio, is moreover more susceptible to residual stress (see for instance Equation (3.81b) describing the normalized stress variable) as evidenced from increased separation be-tween pull-in voltages with increasing σ_0. Furthermore, pull-in voltage curve for Design #2 stays below the intended 30 V limit unlike Design #1. These observations render Design #2 more favorable than Design #1 in terms of its actuation characteristics.
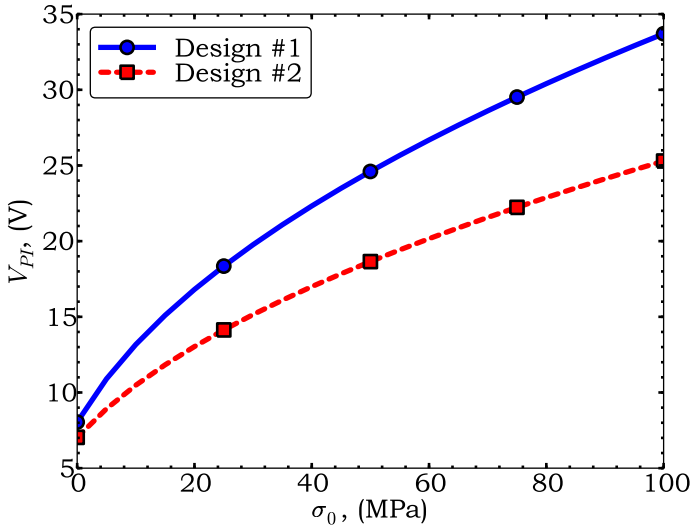
Figure 4.16: *Simulated pull-in voltages of Design #1 and Design #2 as a function of the biaxial residual stress σ_0 ($E = 78$ GPa, $v = 0.44$).*

4.3.3 ON-State Contact Analysis

Recall from §3.6 that capacitance between the electrodes of fixed-fixed beams varies as a function of the applied voltage in the contact state. An interpretation of this fact for

the switch devices is that ON-state capacitance, hence resonance frequency, would change with the applied actuation voltage level. In order to ensure that designed switches exhibit ON-state resonances around 35 GHz for voltages not larger than 30 V, a Finite Difference contact simulation is run for each switch configuration using 251 points along the guidelines of §3.6.3. The physical parameters are the same as the ones employed in the pull-in analysis except for the biaxial residual stress parameter which is discretized to five points in $0 - 100$ MPa range. Figure 4.17 presents obtained fractional capacitance results as a function of applied voltage for both Design #1 and Design #2.

It is observed from Figure 4.17 that the ON-state capacitance at 30 V lies in 97.5-98.3% and 97.1-97.9% of the maximum capacitances for Design #1 and Design #2 respectively for σ_0 in $0 - 100$ MPa range. Obtained fractional capacitances are actually similar to each other and slightly better contact characteristics of Design #1 stem from lower normalized dielectric thickness values which in turn increases the normalized electrostatic force (due to higher H_{brd}, see Equations (3.78c) and (3.77)). One can moreover translate these fractional capacitance values to ON-state resonance frequencies using Equation (4.3): Using f_0 values tabulated in Table 4.8, one can deduce that ON-state resonance frequencies lie in $35.3 - 35.5$ GHz and $35.7 - 35.8$ GHz at 30 V actuation for Design #1 and Design #2 respectively. Although the latter observation might seem as a disadvantage for Design #2, notice that 3.7 GHz 30 dB isolation bandwidth for the relevant design assures a high isolation level at 35 GHz. Therefore, it can be deduced that Design #1 does not pose a

(a) Design #1   (b) Design #2
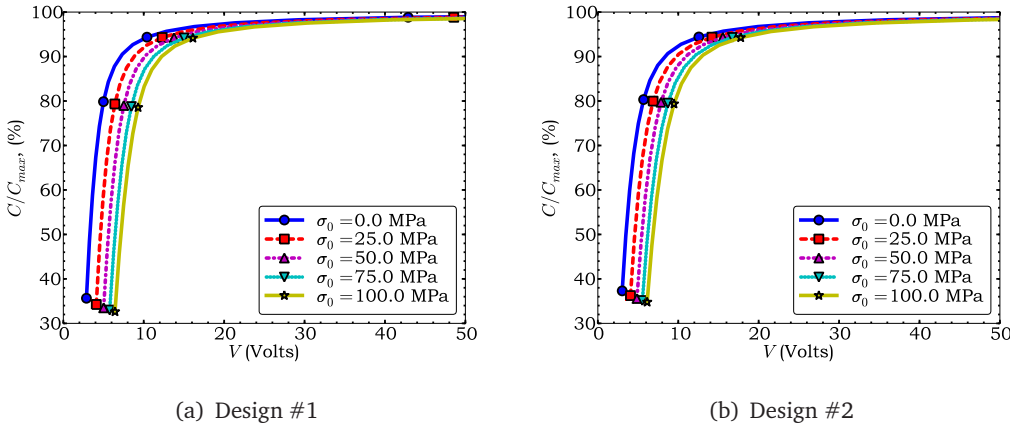
Figure 4.17: *Simulated fractional capacitance versus applied voltage characteristics for switch configurations ($E = 78$ GPa, $v = 0.44$, $N = 251$).*

significant advantage over Design #2 in terms of ON-state contact characteristics.

4.3.4 The Verdict for Design Selection

It is decided to elect Design #2 for implementation rather than Design #1 due to the following reasons:

- Millimeter-wave characteristics obtained after the integration of CPW transitions are slightly better for Design #2, especially in terms of OFF-state return loss, as evidenced by Table 4.8.

- Pull-in properties of Design #2 are superior compared to Design #1 as demonstrated in Figure 4.16.

- ON-state contact properties of Design #2 are similar to that of Design #1 as shown in Figure 4.17.

In the remainder of this chapter, it is solely concentrated on Design #2 according to the design election performed in this section.

4.4 Fabrication and Measurements of the Switch Device

This section concentrates on fabrication details and millimeter-wave measurement results of Ka-band shunt, capacitive-contact RF MEMS switch devices.

4.4.1 Fabrication Details

Ka-band shunt, capacitive-contact RF MEMS switch devices were fabricated in METU MEMS Center Facilities using the in-house process developed by METU RF MEMS Group. The process sequence consists of several surface-micromachining steps which are illustrated in Figure 4.18 and detailed below[4]:

---

[4] Relevant steps are formed by Dr. Mehmet Ünlü.

1. Top surfaces of quartz wafers are coated with sputtered gold metallization. Relevant layer is subsequently patterned to form CPW lines and CPW ground plane recesses (with measured $t_{\text{CPW}} = 0.9\ \mu m$, $\sigma = 30$ MS/m).

2. Silicon nitride is deposited over the wafer surface using PECVD and it is then patterned to form the dielectric layer on top of CPW signal trace (with $t_{\text{di}} = 0.3\ \mu m$, $\epsilon_{\text{di}} = 7.0$).

3. Wafer is next spin-coated with the polyimide sacrificial layer of thickness 1.2 μm. Following a photolithographic step, mechanical anchor zones, at which the MEMS bridge would be supported, are defined.

4. In order to form the MEMS bridge (or structural) layer, gold metallization is sputtered on the underlying topology with a measured thickness of $t_{\text{brd}} = 1.1\ \mu m$.

5. A selective gold electroplating step is applied at the mechanical anchor zones in order to reinforce relevant supports (with a thickness ranging between $5-10\ \mu m$).

6. Structural layer is then patterned to form the MEMS bridges.

7. Finally, sacrificial layer is etched away to release the MEMS bridges for operational switch devices.

Figure 4.19 shows a micrograph of a successfully fabricated switch device.
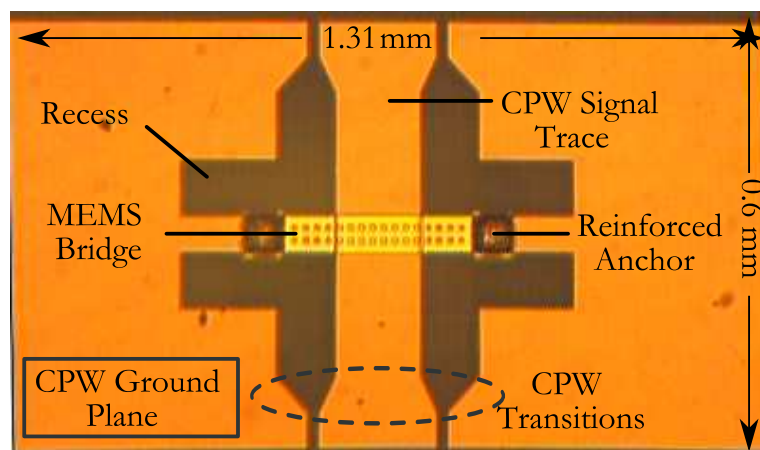
Figure 4.19: *Micrograph of a successfully fabricated Ka-band shunt, capacitive-contact RF MEMS switch. Device features are indicated.*
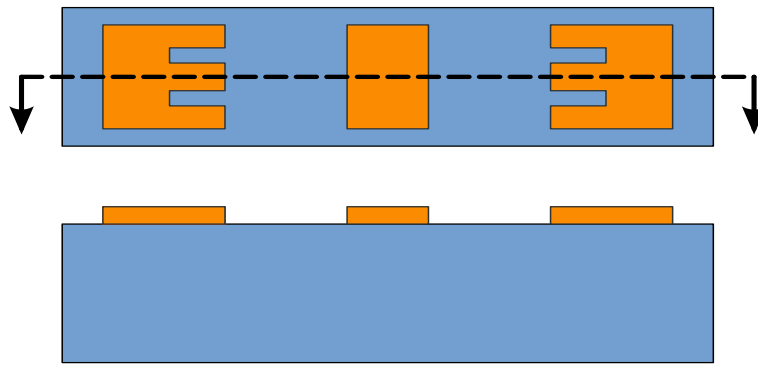
(a) Step#1: Gold metallization deposition and patterning for CPW lines.
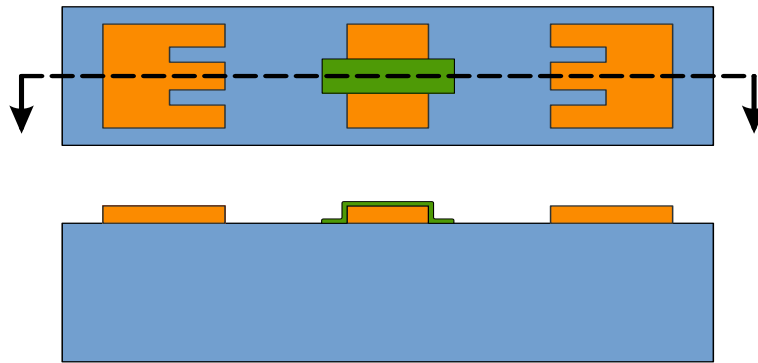
(b) Step#2: Silicon nitride deposition and patterning for isolation dielectric.
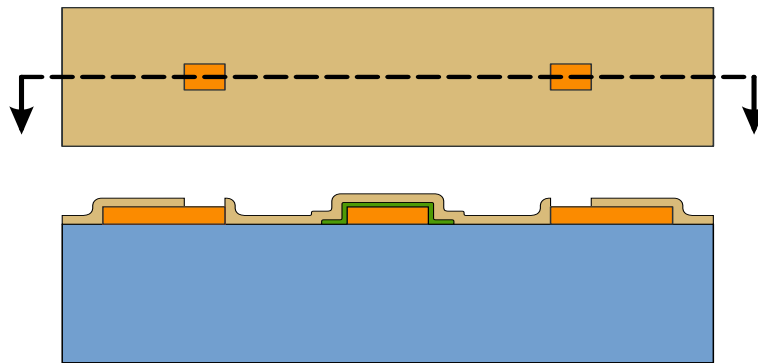
(c) Step#3: Sacrificial layer coating and patterning for mechanical anchor zones.
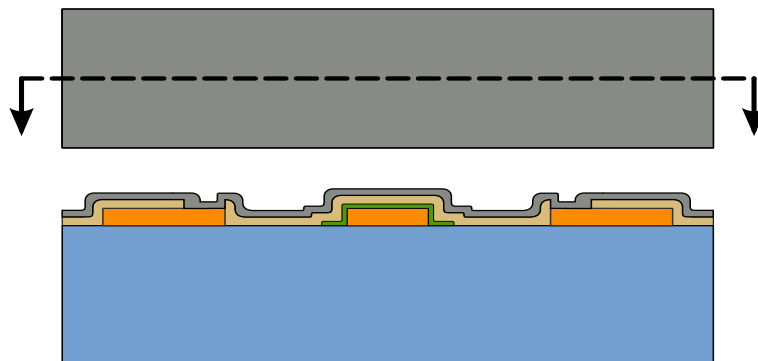
(d) Step#4: Structural layer (gold bridge metallization) deposition.
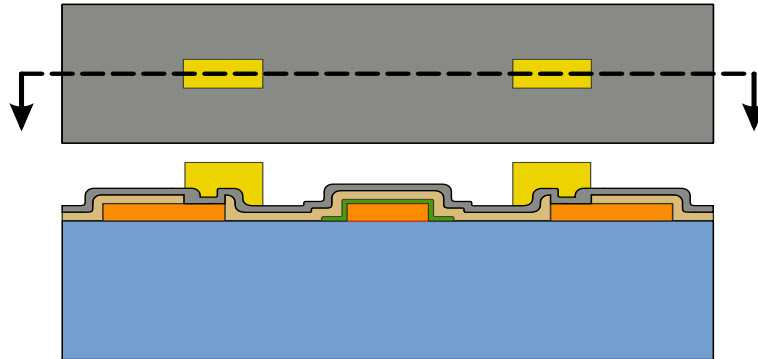
(e) Step#5: Selective gold electroplating for mechanical anchor reinforcements.
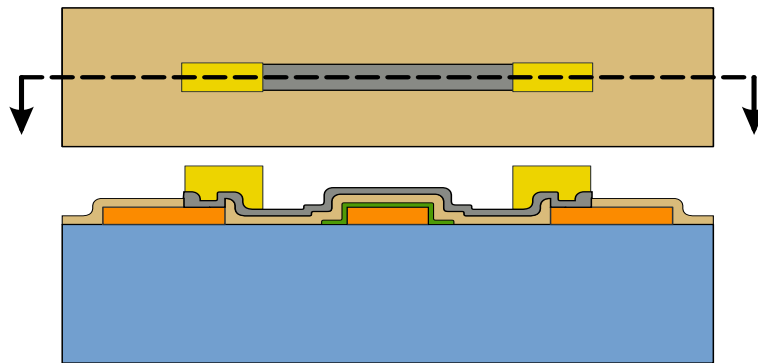
(f) Step#6: Patterning of structural layer for bridge formation.
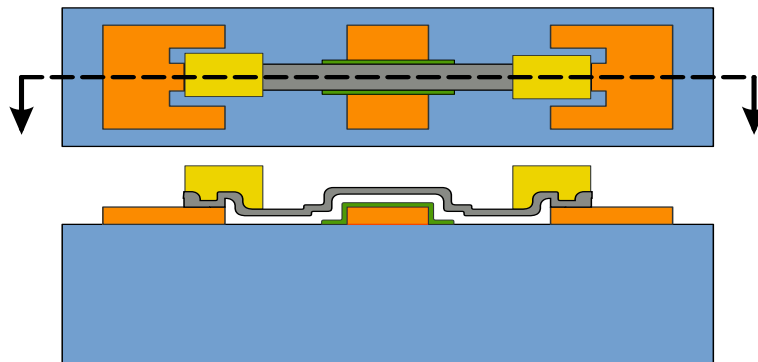
(g) Step#7: Removal of the sacrificial layer for suspended bridges.

Figure 4.18: *Fabrication process sequence of Ka-band shunt, capacitive-contact RF MEMS switches (drawings are not to scale).*

4.4.2 Millimeter-wave Measurements of the Switch Device

Millimeter-wave measurements of the Ka-band shunt, capacitive-contact RF MEMS switch devices were conducted in METU Department of Electrical and Electronics Engineering Millimeter-wave Laboratory using Cascade Microtech Summit 9000 Analytical Probe Station in conjunction with Agilent E8361A Vector Network Analyzer (VNA). For ON-state measurements, switches were actuated by applying a 200 Hz, unilevel, bipolar square waveform[5] to one of the bias-tees connected to the measurement setup. Prior to the measurements; VNA was calibrated through an SOLT (Short-Open-Load-Thru) calibration scheme performed in 10-40 GHz frequency band using Cascade 101-190 Impedance Standard Substrate (ISS) and reference planes were brought to Cascade ACP40-GSG-150 probe tips having a pitch spacing (2G+W) of approximately 220 μm. Measured OFF-state performance of a number of switch samples are plotted in Figure 4.20. A typical ON-state measurement result is shown in Figure 4.21.

It is observed from Figure 4.20(a) that measured OFF-state return losses of the switch samples correlate well, but are not in accordance with the one anticipated from the EM simulation. In particular, return loss increases gradually and may reach up to -10 dB at 40 GHz, a behavior which clearly violates the relevant design specification. Similar comments apply to the OFF-state insertion loss performance depicted in Figure 4.20(b): Due to increased reflection towards the end of the frequency band, insertion losses increase significantly, exceeding the design specification of 0.5 dB. Another noteworthy observation made from the latter figure is that, loss of the switch samples are estimated correctly by the EM simulation: Simulated and measured insertion losses agree up to 30 GHz, where the additional loss due to reflection remains negligible.

Like the OFF-state responses, measured ON-state performance of the switch samples is also inferior than the intended specifications as shown in Figure 4.21. In particular, ON-state resonance frequency is noted to decrease with increased voltage, an observation consistent with the zipping phenomenon described in §3.6.3.3. At the maximum volt-

---

[5] Relevant waveform was obtained from the Bias Generator Card which had been developed by Halil İbrahim Atasoy [98].

age specification of 30 V, relevant resonance appears at 38.3 GHz, a frequency which is considerably higher than maximum expected value of 35.8 GHz. It is moreover noticed that ON-state resonance frequency saturates at around 37 GHz as the applied voltage increases up to $60V$, a behavior which apparently does not agree with previous anticipations. In particular, measured switch sample cannot attain an isolation of 30 dB even at that extreme voltage and isolation at 30 V stays around 25 dB.

Having evidently not met the design specifications with the fabricated switch samples, the reasons for relevant discrepancies are investigated next.

4.5 Post-Fabrication Studies for Switch Devices

As indicated in §4.4.2, measured millimeter-wave performance of the fabricated switch samples is not sufficient to satisfy the design requirements. This section analyzes the reasons for the observed discrepancies in ON and OFF-states of the switches. The findings established in this section will later prove useful for the subsequent fabrication attempt.

4.5.1 Identification of Discrepancies for ON-State

It was pointed in §4.4.2 that measured ON-state resonance frequencies of the fabricated switch samples cannot be brought below 37 GHz even at voltages as high as 60 V. This observation suggests the presence of a systematic error involved in EM simulations of ON-state switch configurations, a topic which is discussed in this subsection.

During the electromagnetic design of the switch configurations, a single mode, namely the CPW mode, was utilized to excite and characterize the relevant structure. A consequence of such procedure is that evanescent modes, which are converted from the CPW mode at the discontinuities of the structure (such as ground plane recesses and CPW transitions), are not properly accounted for when S-parameters are calculated at the input and output ports. This in turn results in incorrectly simulated S-parameters for the switch configurations. In order to properly simulate relevant configurations, hence, effect

175
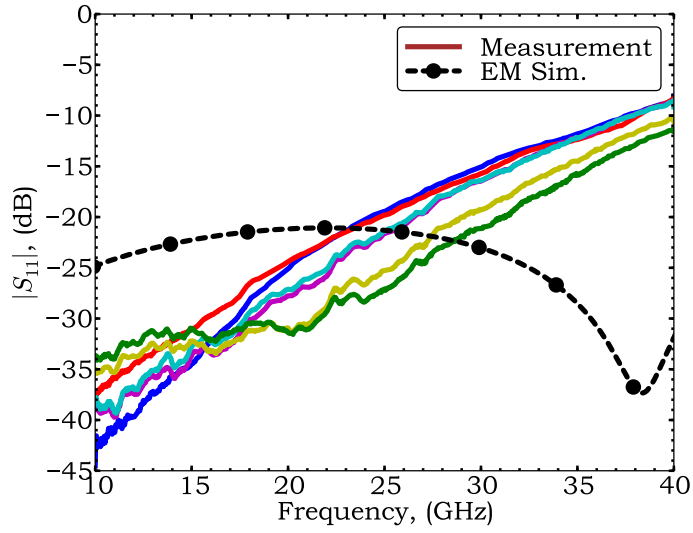
(a) Return loss performance.
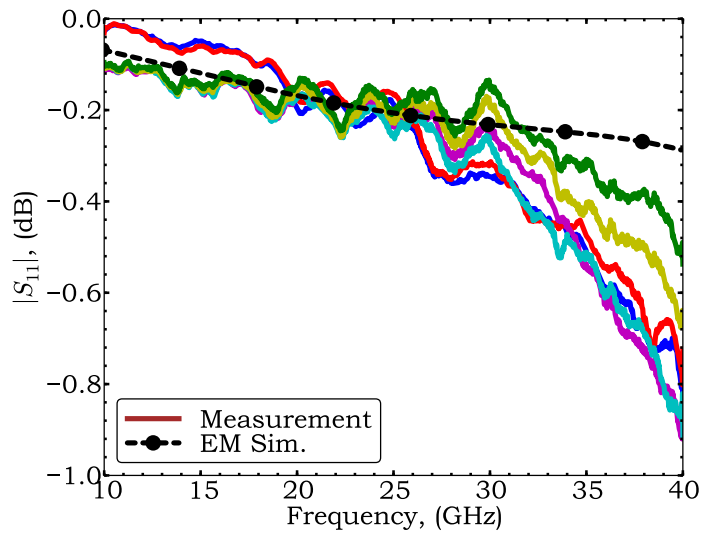
(b) Insertion loss performance.

Figure 4.20: *Measured OFF-state return loss and insertion loss of a number of switch samples. For comparison purposes, corresponding EM simulation results are overlaid on the same plots.*

of mentioned evanescent modes must be incorporated into the calculations. One way of achieving the latter is to employ *lumped ports* referenced to 50 Ω impedance [133].

In order to justify the claim described above, EM simulation of switch configuration #2 is repeated in ON-state using lumped ports and obtained isolation response is compared with those of the fabricated samples measured at 50 − 60 V actuation voltages. Figure 4.22 provides the relevant comparison. It is observed from Figure 4.22 that simulated ON-state resonance is found at 36.7 GHz with lumped ports, which is noted to agree well with measured frequencies. Apparent discrepancy of the previously simulated isolation response can be also spotted from the provided curves.

In the light of the observations made above, it can be concluded that failure of the fabricated switch devices to meet the design specifications in their ON-state is entirely due to improperly configured EM simulations conducted during the design stage. This information will be exploited later to establish a predictable design in the subsequent section.
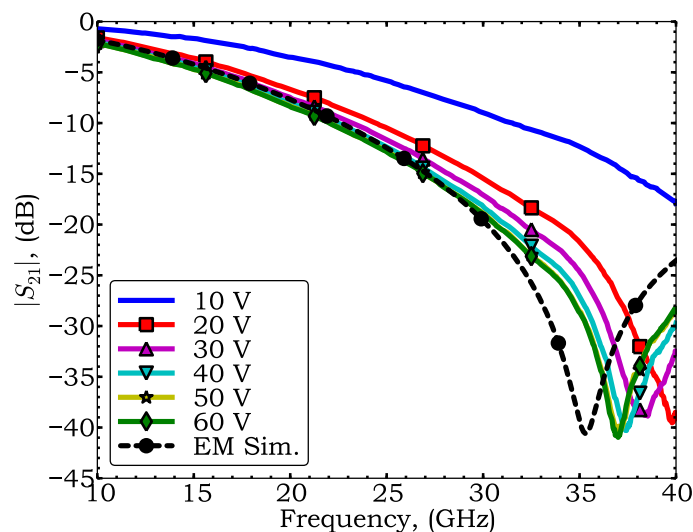
Figure 4.21: *Measured ON-state isolation of a typical switch sample. For comparison purposes, relevant EM simulation result is overlaid on the same plot.*

4.5.2 Identification of Discrepancies for OFF-State

The source of the discrepancies between designed and measured OFF-state millimeter-wave responses of the fabricated switches are tracked down to fabrication issues, unlike the ON-state. Figure 4.23 shows the cause of the problem by providing optical profilometer measurement results of a sample MEMS bridge which belongs to a similar RF MEMS structure fabricated in the same process run. It is realized from the supplied Y-profile plot that bridge height of the measured sample is 1.1 μm ($= 2.2\ \mu m - t_{\text{brd}}$) as opposed to the intended 1.5 μm value. In other words, MEMS bridges collapsed from 1.5 μm to 1.1 μm after the release process as evident from the X-profile.

An interpretation of the experimentally confirmed bridge height reduction issue from the perspective of electrical performance can be facilitated as follows: A MEMS bridge located at a lower height than the intended one implies an increased capacitive loading. This in turn causes a degraded OFF-state return loss (hence insertion loss) performance since loaded-line impedance decreases below the aimed 50 Ω as a consequence of that loading. EM simulations are found to validate this reasoning: Figure 4.24 shows a comparison between measured and simulated OFF-state S-parameters. It is clear from the good agree-
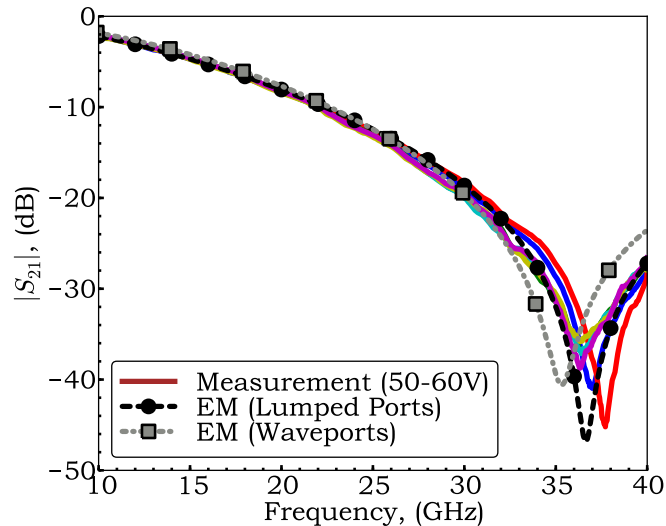
Figure 4.22: *A comparison for ON-state isolation responses of the switch device between measurements and EM simulations. Measured responses are obtained at* $50 - 60$ *V actuation voltages.*
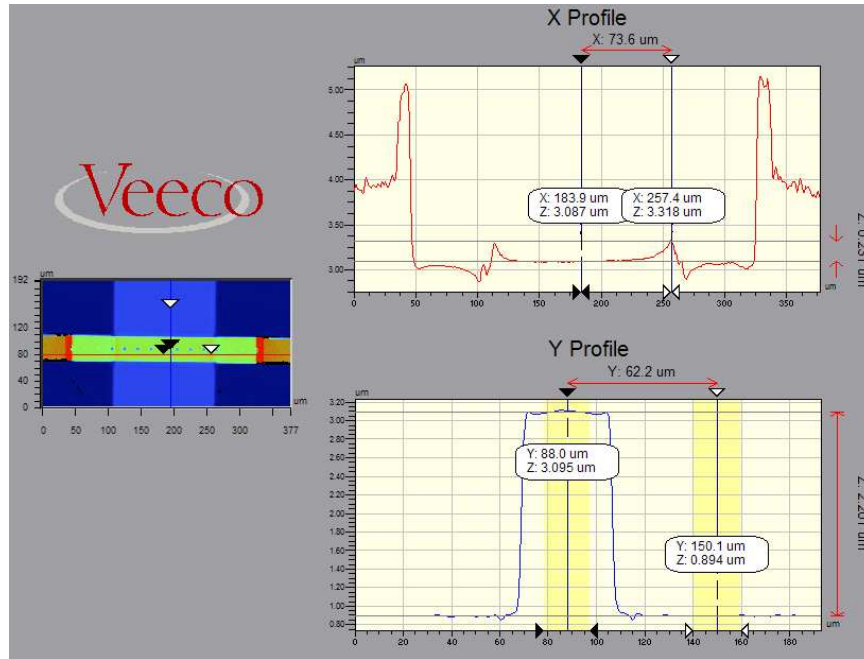
Figure 4.23: *Optical profilometer measurement results of a sample MEMS bridge fabricated in the same process run along with the Ka-band shunt, capacitive-contact RF MEMS switches.*

ment of provided curves that degradation associated with OFF-state performance of the fabricated switches can be mainly attributed to reduced bridge height. The bridge height is determined as 1.0 μm from EM simulations following a trial-error procedure and this value is found to agree well with the optical profilometer results. The latter observation further enhances the confidence in the EM simulations utilizing lumped-ports.

4.6 Design Modification for the Switch Device

Previous section identified the reasons for the discrepancies between measured and designed millimeter-wave responses of the fabricated switch devices. That established knowledge is now put into use in this section to improve the performance of the Ka-band shunt, capacitive-contact RF MEMS switch through slight modifications on the existing configuration.

4.6.1 Partial Contact Approach

The first modification on the Ka-band shunt, capacitive-contact RF MEMS switch is the utilization of a partial contact rather than a full one. Such an adjustment bears two
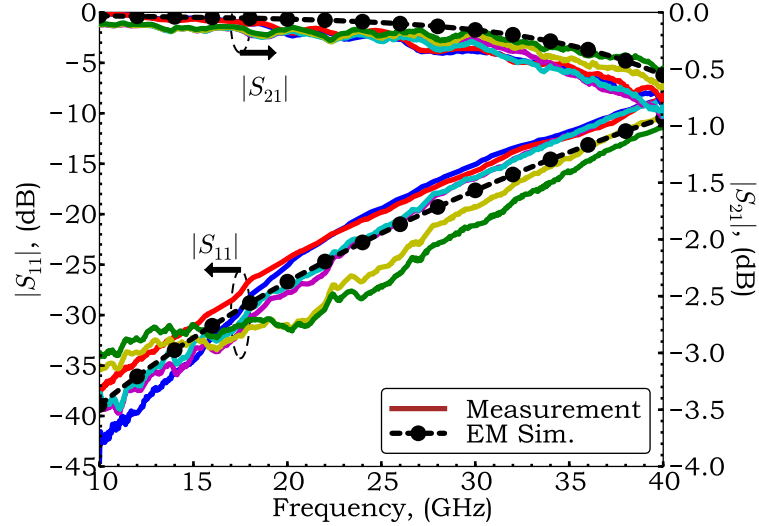
Figure 4.24: *A comparison between measured and simulated OFF-state S-parameters of the switch devices. EM simulations utilize lumped-ports for excitation. Bridge height value is determined to be $H_{\mathrm{brd}} = 1.0\ \mu m$.*

advantages:

- Actuation voltages can be lowered for a desired ON-state resonance frequency.

- ON-state resonance can be precisely tuned to a specific frequency by altering the actuation voltage.

For the switch to possess these favorable properties, a measurement-based contact characterization study is conducted. Within the scope of this study, initially, a design goal is set which states to achieve an optimum isolation at 35 GHz with an actuation voltage of 20 V. Next, the connection between EM simulations and measurements is tried to be established through a geometric model of the partial ON-state contact. For that purpose, the simple linear geometric model depicted in Figure 4.25 is adopted for EM simulations. In particular, partial contact is described by the variable η and the characterization procedure aims to find the value of η for a given actuation voltage (in this case 20 V) based on the measurement results.

In order to determine the value of η from the measurement results at 20 V, first, fabricated switch configuration is simulated in its ON-state for several η values (with lumped-
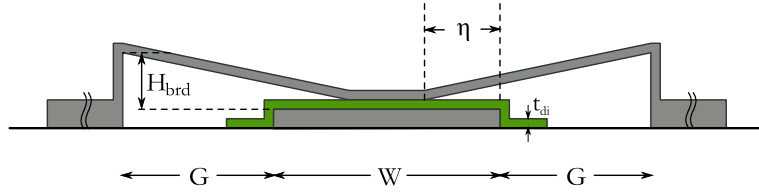
Figure 4.25: *Illustration of the linear partial contact geometric model adopted for EM simulations.*
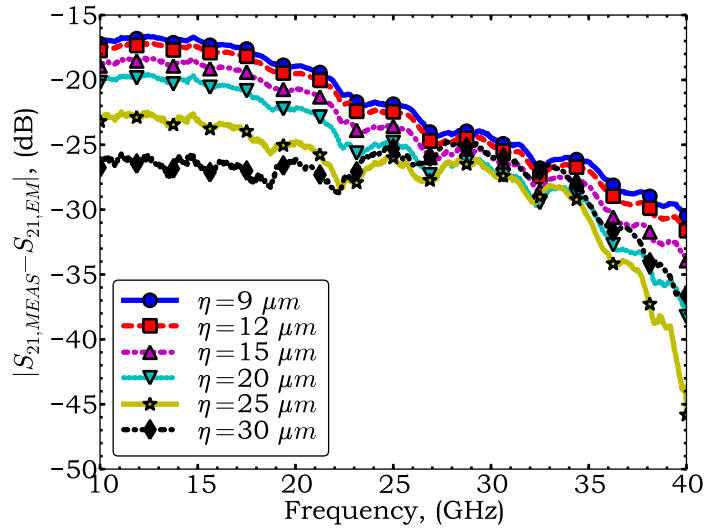
Figure 4.26: *Results of the error analysis for determination of the partial contact variable η at 20 V actuation voltage.*

ports and $H_{\mathrm{b}} = 1.0 \; \mu m$) and a simulated isolation response database is generated. Then, complex S_{21} responses obtained from measurement results at 20 V and simulations are compared. The latter is accomplished by evaluating the complex error between averaged measurement results and simulated isolation responses at each frequency point and for every η. Figure 4.26 provides the results of that error analysis.

It is observed from Figure 4.26 that $\eta = 25 \; \mu m$ accomplishes the smallest error between simulated and measured isolation responses for 20 V over the Ka frequency band. According to this result, η is fixed to 25 μm in the remainder of the design modification stage.

Table 4.9: *Layout and circuit model parameters for the modified design.*

DESIGN	LAYOUT PARAMETERS[a]	CIRCUIT MODEL PARAMETERS
MODIFIED DESIGN	$H_{\text{brd}} = 1.5\ \mu m$, $\eta = 25\ \mu m$ $W = 130\ \mu m$ $G = 90\ \mu m$ $W_{\text{rec}} = 80\ \mu m$ $D_{\text{rec}} = 210\ \mu m$ $G_0 = 17\ \mu m$, $W_0 = 180\ \mu m$ $L_{\text{tran}} = L_{\text{ext}} = 50\ \mu m$	$Z_0 = 85.9\ \Omega$, $\epsilon_{\text{eff}} = 2.38$, $L_{\text{CPW}} = 95\ \mu m$ $\alpha_{\text{CPW}} = 163.6$ dB/m (@ 35 GHz) $C_{\text{d}} = 1.43$ fF, $L_{\text{r}} = 104.57$ pH $C_{\text{b,OFF}} = 63.06$ fF, $C_{\text{b,ON}} = 433.42$ fF $L_{\text{b}} = 48.13$ pH, $R_{\text{b}} = 0.17\ \Omega$ $Z_{0,\text{t}} = 40.4\ \Omega$, $\epsilon_{\text{eff}} = 2.38$, $L_{\text{t}} = 100\ \mu m$ $\alpha_{\text{CPW}} = 299.8$ dB/m (@ 35 GHz)

[a] For material properties and other common layout parameters, refer to Table 4.2. In particular, t_{CPW} and t_{brd} are adopted as 0.9 μm and 1.1 μm respectively according optical profilometer results.

4.6.2 Inductive Tuning for Partial Contact

Having determined the value of the partial contact variable η, hence the ON-state capacitance, ON-state isolation can now be tuned precisely to 35 GHz through inductive tuning. Utilizing the approach outlined in §4.2.4.2 for $H_{\text{brd}} = 1.5\ \mu m$ (intended bridge height) and $\eta = 25\ \mu m$, it is found that increasing the recess depth D_{rec} from 145 μm to 210 μm merely accomplishes the desired tuning. Furthermore, OFF-state performance is noted to be virtually unaffected as a result of this modification, a behavior sparing the designer from a rather involved design cycle. Table 4.9 summarizes the obtained configuration for the modified switch design along with the corresponding circuit model parameters. Figure 4.27 presents simulated and modeled S-parameters of the modified design. Finally, Table 4.10 provides a millimeter-wave performance summary obtained from relevant EM simulation data.

It is noted from Figure 4.27 and Table 4.10 that modified design exhibits a superior performance compared to the previous Design #2. This is in part caused by utilization of lumped-ports instead of a single-mode excitation[6]. Notice moreover from the provided S-parameter plots that the agreement between EM simulations and circuit model is excellent unlike previous case wherein a true modeling could not be achieved. This latter observation once again emphasizes the importance of utilizing correct stimulus settings in EM simulations.

---

[6] It is furthermore expected that loss of the structure is underestimated due to change of absorbing boundary conditions surrounding the switch volume.
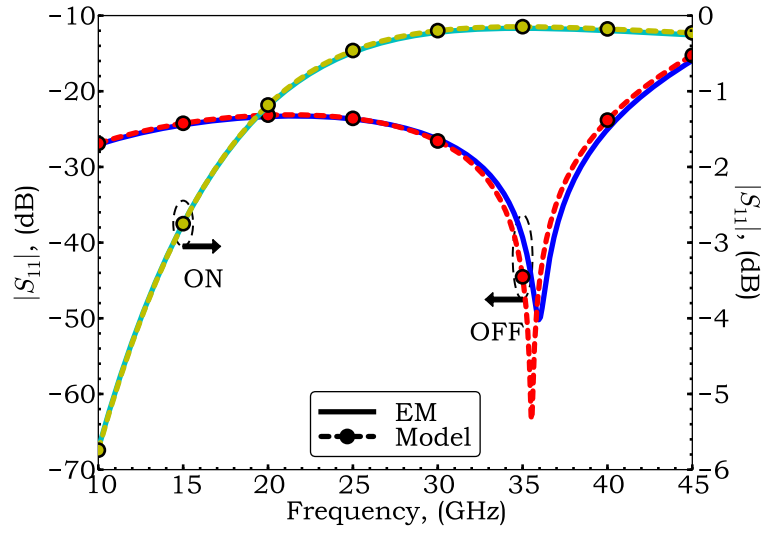
(a) $|S_{11}|$ for both states.
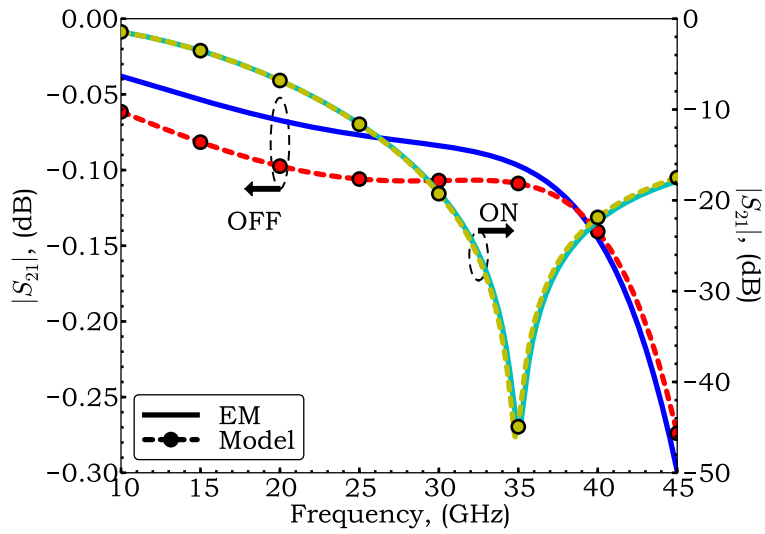
(b) $|S_{21}|$ for both states.

Figure 4.27: *Electromagnetically simulated and modeled magnitude S-parameters for the modified design (CPW transitions included, $H_{\mathrm{brd}} = 1.5$ μm).*

Table 4.10: *Millimeter-wave performance summary of the modified design. Relevant data are obtained from corresponding EM simulations. CPW transitions are included.*

DESIGN	PERFORMANCE DATA	
	OFF-STATE	ON-STATE
MODIFIED DESIGN	INSERTION LOSS ≤ 0.15 dB, $f \leq 40.0$ GHz ≤ 0.30 dB, $f \leq 45.0$ GHz	ISOLATION OPTIMUM LEVEL: 45.6 dB ($f_0 = 35.0$ GHz)
	RETURN LOSS ≤ -25.0 dB, 25.0–40.0 GHz ≤ -20.0 dB, 25.0–42.4 GHz	≥ 20 dB, 30.4–42.0 GHz ≥ 30 dB, 33.4–36.8 GHz

4.6.3 Anchor Extensions for Bridge Height Stability

It was demonstrated in §4.5.2 that failure to attain a given bridge height value could drastically alter the OFF-state performance of fabricated switches. Consequently, some stabilization means is necessary for the fabricated MEMS bridges in order to ensure a properly working switch design. A possible stabilization method, which does not require any modification to the current process sequence, is to utilize base-metal *anchor extensions*. The idea[7] is illustrated in Figure 4.28 and explained below:

- In the regular process sequence, MEMS bridges feature step-ups due to conformal coating properties of the sacrificial layer and the structural layer deposited over it. In particular, the step-ups near the CPW signal trace edges form weak mechanical joints (shown in small dots in Figure 4.28(a)), which might not prevent buckling of the bridge after the removal of the sacrificial layer. In other words, relevant step-ups promote bridge height variation issue due to their stress-relieving properties.

- If conformal coating property of the sacrificial layer could be prevented especially around the CPW signal trace edges, step-ups in the MEMS bridges could be eliminated. Base-metal anchor extensions accomplish that prevention task: It is observed in a few coating experiments that sacrificial layer fails to cover too narrow features in a conformal fashion. By extending base-metal extensions from CPW grounds to the CPW signal trace with a small clearance, such a narrow feature can be generated and consequently step-ups in the MEMS bridge can be mitigated as shown in Figure 4.28(b).

---

[7] This concept is developed together with Dr. Kağan Topallı and Dr. Mehmet Ünlü.

(a) Without anchor extensions. (b) With anchor extensions.
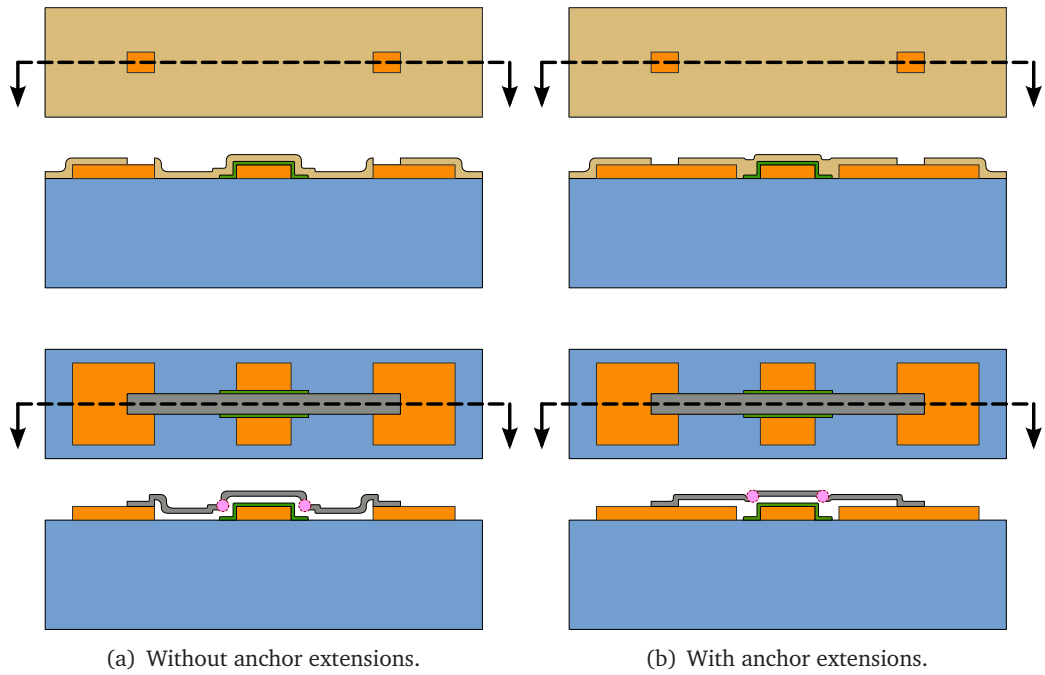
Figure 4.28: *Process flow diagrams describing the operation of the anchor extension concept.*

The anchor extension concept, although seems plausible from a mechanical viewpoint, must be tested for its millimeter-wave aspects in order to become a completely viable solution. In particular, bringing these CPW ground plane extensions toward the CPW signal trace in a close proximity might affect the millimeter-wave performance of the switch devices by forming additional shunt capacitances and/or altering the bridge inductance values. In order to see whether such a disturbance would occur or not, a few EM simulations are conducted for several values of the ground-to-signal proximity. Figure 4.29 compares obtained S-parameter results. It is observed from Figure 4.29 that anchor extensions have no appreciable effect on the millimeter-wave performance of the switch device even at a proximity of 10 μm. This result can be interpreted as follows: Since bridge height is much smaller than the minimum employed proximity of 10 μm, transmission properties of the effective inverted microstrip line (formed by the MEMS bridge and the CPW signal trace) are not affected due to the presence anchor extensions.

In the light of the discussions provided in this subsection, anchor extension concept is justified to be a viable bridge height stabilization means.
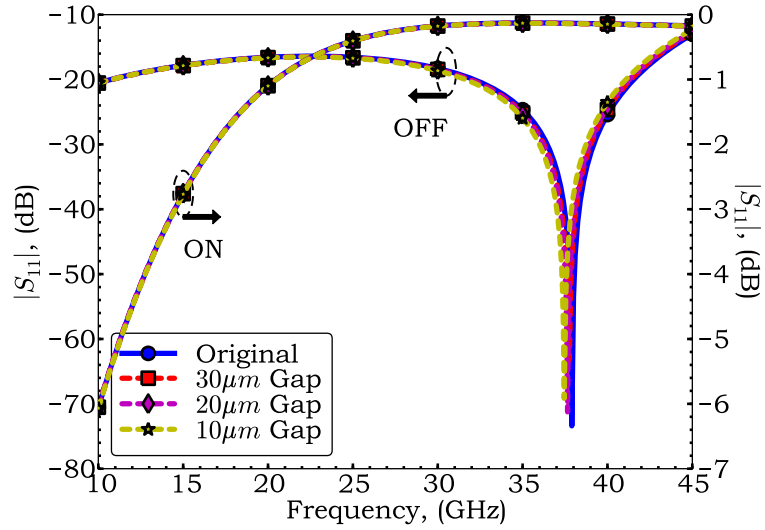
(a) $|S_{11}|$ for both states.
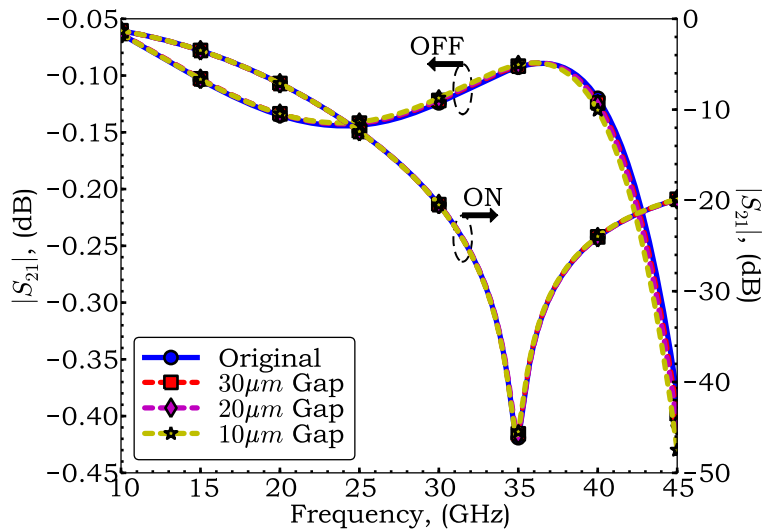
(b) $|S_{21}|$ for both states.

Figure 4.29: *A comparison between electromagnetically simulated S-parameters of the switch device for different ground-to-signal proximity values of base-metal anchor extensions (CPW transitions are omitted, $H_{\mathrm{brd}} = 1.5~\mu m$).*

4.6.4 Modification of the Bridge Height

Due to change of fabrication plans for the next process run, bridge height value of the switch devices required a modification. In particular, relevant plans dictated a new bridge height of 1.8 μm instead of the previously adopted 1.5 μm value. In order to eliminate the need for a complete re-design, it is decided first to observe the millimeter-wave performance of the switch configuration depicted in Table 4.9 with the updated bridge height specification. Figure 4.30 show simulated S-parameters of this new configuration, while Table 4.11 summarizes obtained millimeter-wave performance.

It is noted from Figure 4.30 and Table 4.11 that OFF-state return loss performance of the switch device degrades noticeably when bridge height is elevated from 1.5 μm to 1.8 μm. OFF-state insertion loss and ON-state isolation, on the other hand, are observed to change negligibly. Due to time limitations for a complete re-design and acceptable nature of the worst case OFF-state return loss, it is decided to terminate the design modification at this point and to implement the resulting switch device in a second fabrication run. Table 4.12 lists the layout and circuit model parameters for the finalized switch configuration.

Table 4.11: *Millimeter-wave performance summary of the modified design with $H_{\mathrm{brd}} = 1.8\ \mu m$. Relevant data are obtained from corresponding EM simulations. CPW transitions are included.*

DESIGN	PERFORMANCE DATA	
	OFF-STATE	ON-STATE
MODIFIED DESIGN	INSERTION LOSS ≤ 0.15 dB, $f \leq 40.0$ GHz ≤ 0.16 dB, $f \leq 45.0$ GHz RETURN LOSS ≤ -17.8 dB, 25.0–45.0 GHz	ISOLATION OPTIMUM LEVEL: 45.6 dB ($f_0 = 35.4$ GHz) ≥ 20 dB, 30.8–42.5 GHz ≥ 30 dB, 33.8–37.2 GHz

4.7 Second Fabrication Iteration and Measurement Results

This final section encompasses fabrication of the switch structures modified for increased robustness and provides their successful measurement results.
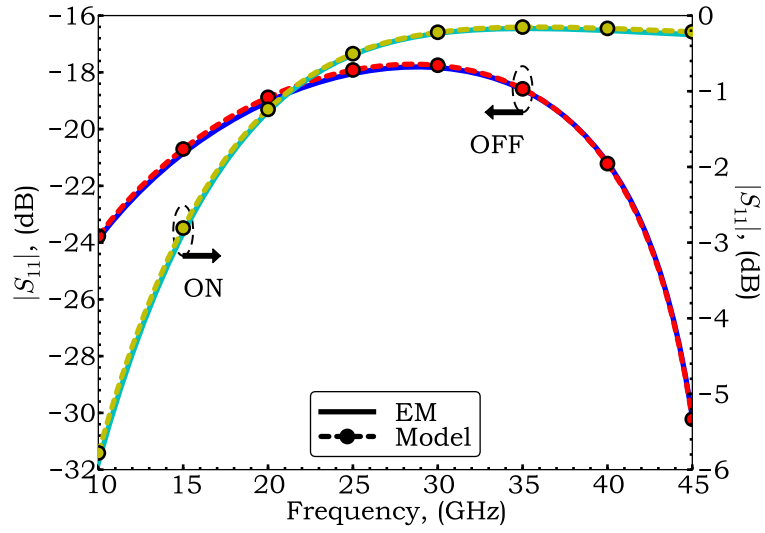
(a) $|S_{11}|$ for both states.
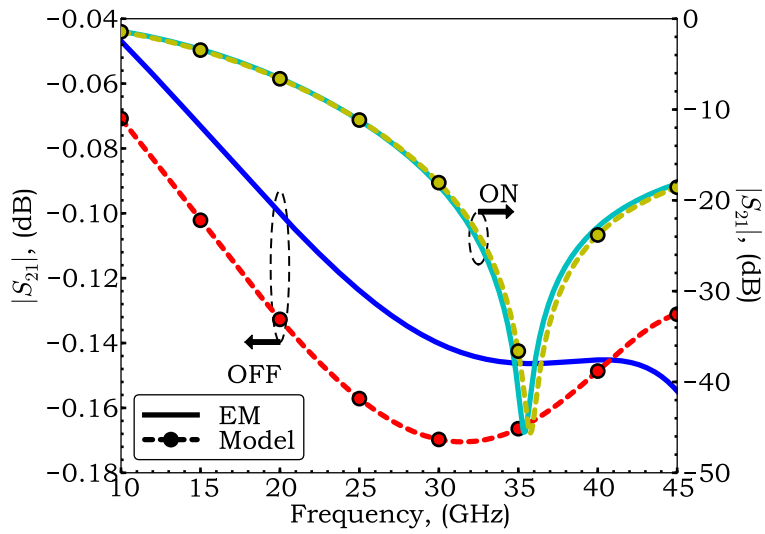
(b) $|S_{21}|$ for both states.

Figure 4.30: *Electromagnetically simulated and modeled magnitude S-parameters for the modified design (CPW transitions included, $H_{\mathrm{brd}} = 1.8\ \mu m$).*

Table 4.12: *Layout and circuit model parameters for the modified design with updated bridge height specification.*

DESIGN	LAYOUT PARAMETERS[a]	CIRCUIT MODEL PARAMETERS
MODIFIED DESIGN	$H_{\text{brd}} = 1.8\ \mu m,\ \eta = 25\ \mu m$ $W = 130\ \mu m$ $G = 90\ \mu m$ $W_{\text{rec}} = 80\ \mu m$ $D_{\text{rec}} = 210\ \mu m$ $G_0 = 17\ \mu m,\ W_0 = 180\ \mu m$ $L_{\text{tran}} = L_{\text{ext}} = 50\ \mu m$	$Z_0 = 85.9\ \Omega,\ \epsilon_{\text{eff}} = 2.38,\ L_{\text{CPW}} = 95\ \mu m$ $\alpha_{\text{CPW}} = 163.6\ \text{dB/m}$ (@ 35 GHz) $C_d = 1.43\ \text{fF},\ L_r = 104.57\ \text{pH}$ $C_{\text{b,OFF}} = 51.06\ \text{fF},\ C_{\text{b,ON}} = 433.42\ \text{fF}$ $L_b = 45.70\ \text{pH},\ R_b = 0.17\ \Omega$ $Z_{0,\text{t}} = 40.4\ \Omega,\ \epsilon_{\text{eff}} = 2.38,\ L_t = 100\ \mu m$ $\alpha_{\text{CPW}} = 299.8\ \text{dB/m}$ (@ 35 GHz)

[a] For material properties and other common layout parameters, refer to Table 4.2. In particular, t_{CPW} and t_{brd} are adopted as 0.9 μm and 1.1 μm respectively according optical profilometer results.

4.7.1 Fabrication Details

Fabrication of the modified switch devices was performed once again in METU MEMS Center Facilities using the fabrication steps detailed in §4.4.1[8]. The only exception was that sacrificial layer thickness was increased to 1.5 μm in order to establish a bridge height of 1.8 μm. Figure 4.31 shows a micrograph of a successfully fabricated switch device.
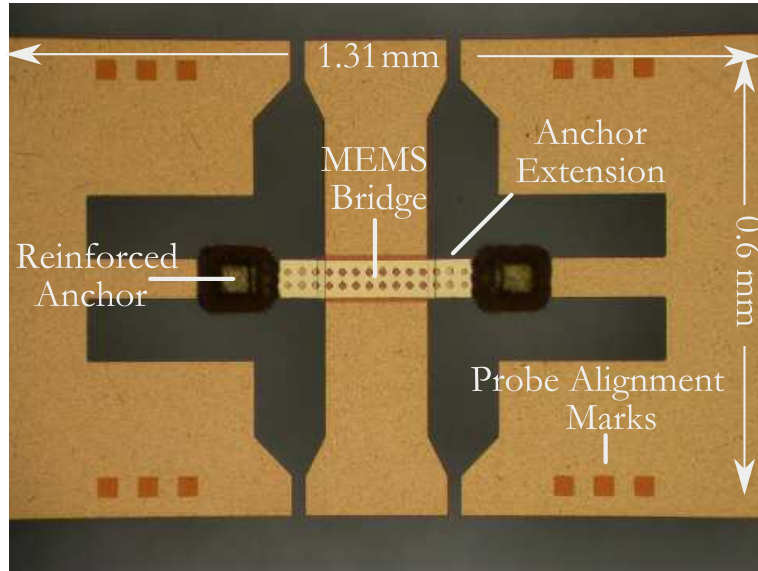
Figure 4.31: *Micrograph of a successfully fabricated Ka-band shunt, capacitive-contact RF MEMS switch (second iteration). Device features are indicated.*

---

[8] Process steps were completed by Dr. Kağan Topallı , Evrim Özçakır and Ozan Doğan Gürbüz.
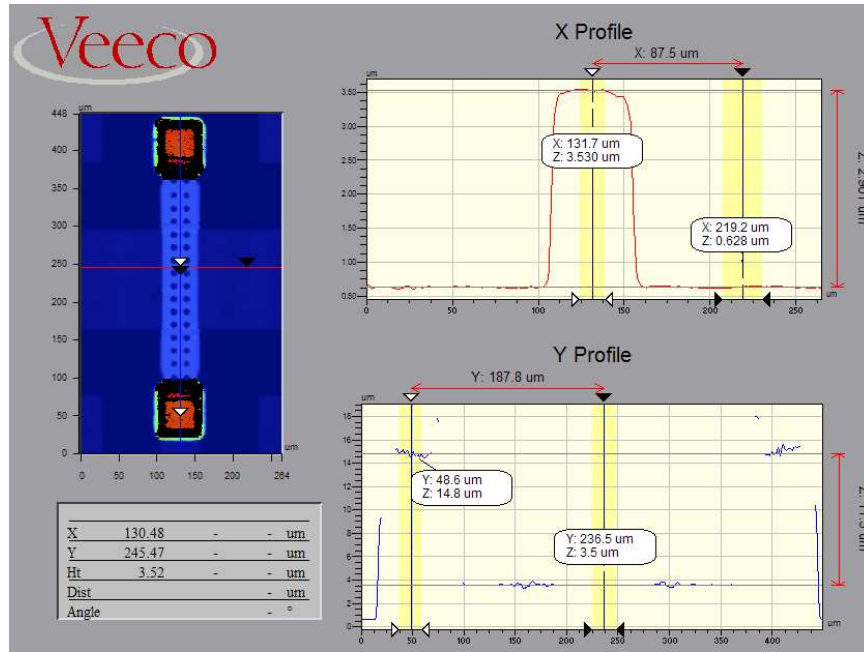
Figure 4.32: *Optical profilometer measurement results of a sample switch device. Measured bridge height is precisely* 1.8 *μm.*

4.7.2 Optical Profilometer Measurement Results

Before advancing to millimeter-wave measurements, bridge height value of the fabricated switch devices was measured with an optical profilometer in order to check whether the anchor extension concept indeed worked. Figure 4.32 shows relevant measurement result for a typical switch sample. As it can be readily noticed from the X-profile plot, a precise bridge height of 1.8 μm (= 2.9 $\mu m - t_{\mathrm{brd}}$) is attained successfully, an observation validating the anchor extension solution for bridge height stabilization problem.

4.7.3 Millimeter-wave Measurement Results

Millimeter-wave measurements of fabricated switch samples were conducted using the measurement setup and calibration method described in §4.4.2. Figures 4.33 and 4.34 provide measured S-parameters for two switch samples. Table 4.13 summarizes millimeter wave performance attained by those switch samples.

190
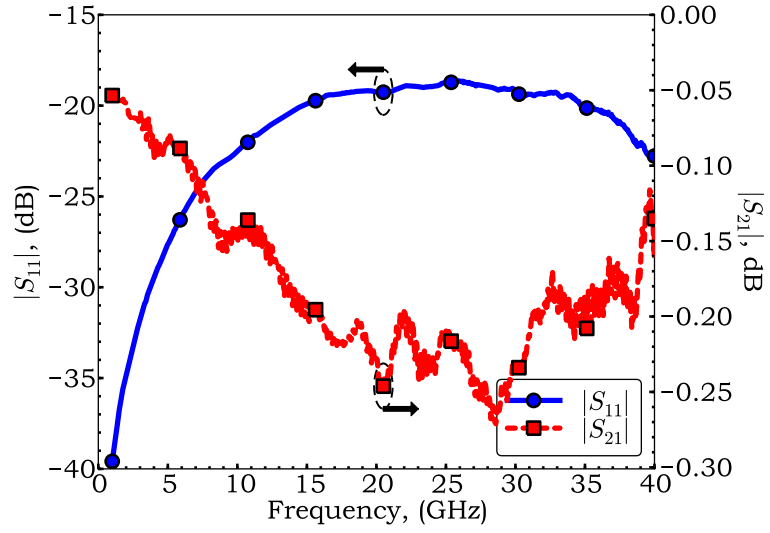
(a) OFF-state return loss and insertion loss.
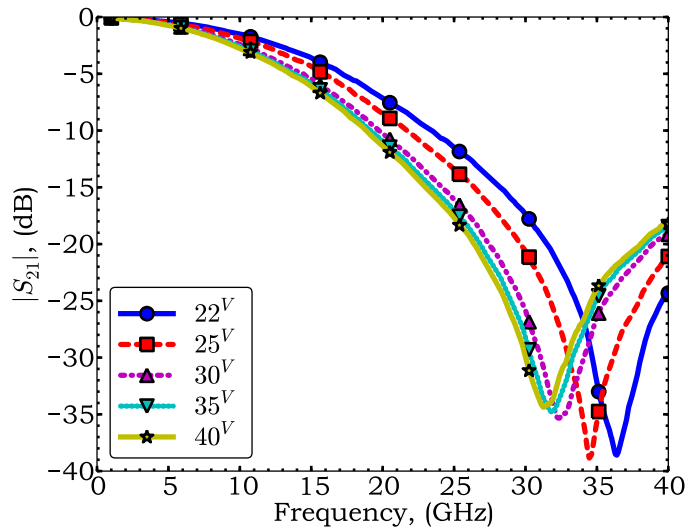
(b) ON-state isolation.

Figure 4.33: *Measured S-parameters of a Ka-band shunt, capacitive-contact RF MEMS switch sample (Sample #1).*
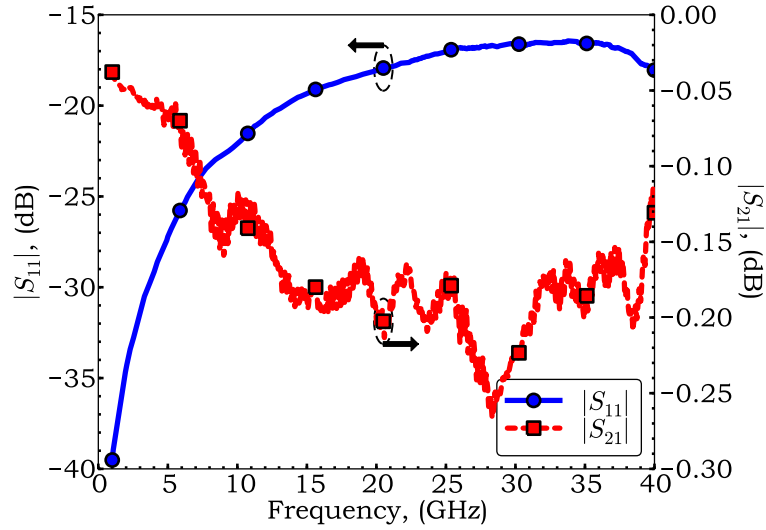
(a) OFF-state return loss and insertion loss.
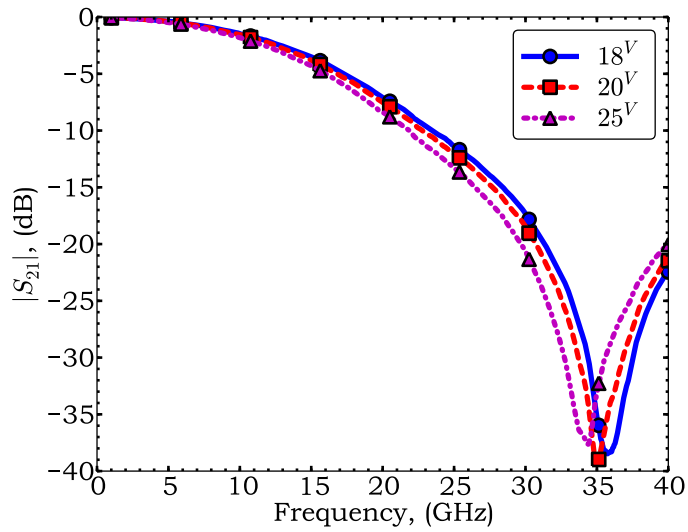
(b) ON-state isolation.

Figure 4.34: *Measured S-parameters of another Ka-band shunt, capacitive-contact RF MEMS switch sample (Sample #2).*

Table 4.13: *Millimeter-wave performance summary of fabricated two switch samples.*

SAMPLE	PERFORMANCE DATA	
	OFF-STATE	ON-STATE
SAMPLE #1	INSERTION LOSS ≤ 0.27 dB, 1–40 GHz RETURN LOSS ≤ -18.6 dB, 1–40 GHz	ISOLATION OPTIMUM LEVEL: 38.9 dB ($f_0 = 34.5$ GHz @ 25 V) ≥ 20 dB, 29.7–40.0 GHz ≥ 30 dB, 33.0–36.2 GHz
SAMPLE #2	INSERTION LOSS ≤ 0.27 dB, 1–40 GHz RETURN LOSS ≤ -16.4 dB, 1–40 GHz	ISOLATION OPTIMUM LEVEL: 39.2 dB ($f_0 = 35.0$ GHz @ 20 V) ≥ 20 dB, 30.7–40.0 GHz ≥ 30 dB, 33.7–36.8 GHz

An examination of Figures 4.33-4.34 and Table 4.13 shows that fabricated switch samples exhibit expected OFF and ON-state millimeter-wave responses: Thanks to anchor extensions, MEMS bridges are formed precisely at a bridge height of $H_b = 1.8$ μm and consequently OFF-state return loss and insertion loss are obtained as intended. Moreover, ON-state resonance frequency can be successfully tuned to 35 GHz with 25 V and 20 V actuation voltages for Sample #1 and Sample #2 respectively. Furthermore, measured performance parameters satisfy the design requirements stated at the beginning of this chapter, except for the return losses which are nevertheless acceptable for a non-optimized design.

In the light of these results, it can be stated that a Ka-band shunt, capacitive-contact RF MEMS switch is successfully realized.

4.8   Conclusion

This chapter presented electromagnetic and mechanical design, fabrication and millimeter wave measurements of a Ka-band shunt, capacitive-contact RF MEMS switch. Relevant switch devices with desired specifications could not be fabricated in a single run and the sources for relevant discrepancies were investigated, identified and remedies were proposed. Building upon the developed knowledge, successfully operating switches were realized at the end of the second fabrication iteration.

CHAPTER 5

CONCLUSION AND FUTURE WORK

This thesis presents distinct works aimed for the development of microwave and millimeter-wave components suited to RF MEMS technology-based applications. Conducted research is three-fold in its scope. First of the established studies encompasses analysis, design and implementation of single-layer microwave lumped elements that feature advantages of easy and low-cost fabrication enabling potential mass production. Within the framework of this first work, a monolithically integrated filter device is successfully realized using those components. A self-contained, accurate mechanical characterization of a frequently encountered beam structure forms the second research subject. The latter theoretical work, constituting the first part of RF MEMS component oriented studies but whose scope also includes other MEMS-based devices as well, concentrates mainly on electrostatically actuated fixed-fixed type beams and establishes numerical analysis methods enabling investigation of a variety of phenomena such as pull-in, release and zipping. Development of a RF MEMS switch component tailored for millimeter-wave applications composes the last research topic of this thesis. In particular, the Ka-band shunt, capacitive RF MEMS switch designed, fabricated and measured within the scope of this final work helps extend capabilities of the METU RF MEMS Group to millimeter-wave applications.

In the light of the research conducted in this thesis, following specific conclusions can be drawn:

1. Microstrip lumped elements for a particular surface micromachining-based technology are developed for microwave applications. Relevant technology bears the advantage of utilizing a single metallization layer. Associated fabrication is there-

fore easy, low-cost and has the potential for mass production.

2. As an example application of the developed lumped elements, an S-band bandpass filter is successfully designed, fabricated monolithically and characterized with microwave measurements. Fabricated filter structures are found to attain an in-band return loss better than -20 dB, an in-band insertion loss of 1.2 dB, a pass-band slightly narrower than 2-4 GHz band and a stop-band extending up to 20 GHz.

3. Grounding related issues encountered during the microwave measurements of the filter structures are successfully identified and the importance of good grounding practices are highlighted for systems incorporating both CPW and microstrip topologies.

4. Analytical deflection profile expressions are derived for fixed-fixed type beams subject to uniform distributed transverse loads. During the derivations, axial effects of built-in residual stress and bending induced non-linear stretching are rigorously taken into account. Using those results, effective spring constant of the beam is evaluated. Moreover, small and large-argument forms of the effective spring constant are established by using series approximations. Those latter expressions are rendered closed-form and their validity range is justified to be broader than that of widely used formulations existing in the literature.

5. An analysis of the electrostatic actuation problem is carried out for fixed-fixed type beams. Attention is directed particularly to wide beams for which fringing effects can be neglected. Progressing with increased difficulty, Finite Difference numerical solution schemes are formulated and subsequently implemented for zero-tension and nonzero-tension problems. Pull-in phenomenon is observed and tried to be quantified using the simulation results.

6. Semi-empirical pull-in formulations are developed for electrostatically actuated fixed-fixed type beams by using the previously derived spring constant expression and numerical simulation results for the zero-tension electrostatic actuation problem. This study is initially intended to compensate for the lack of accurate determination of pull-in voltages with the nonzero-tension numerical scheme. Upon evaluating the proposed formulations for sample case studies, resulting accuracies

are found comparable to, if not better than, those exhibited by other expressions in the literature.

7. In order to complete the characterization of fixed-fixed type beams under electrostatic actuation, Finite Difference solution schemes are proposed and implemented for the electromechanical contact problem. Zipping phenomenon is observed and its trend is qualitatively investigated with respect to the problem parameters. Moreover, release phenomenon is identified and numerical schemes are developed to evaluate associated hold voltages. With those accomplishments, hysteresis properties of electrostatically actuated fixed-fixed type beams are characterized completely.

8. A Ka-band shunt, capacitive-contact RF MEMS switch is designed in electromagnetic and mechanical domains, fabricated and measured. Having not met the design specifications at the end of the fabrication run, post-fabrication studies are conducted on the switch samples. Reasons for the observed discrepancies are successfully identified.

9. Having determined the sources of discrepancies between measured and designed characteristics of the switch samples, a design modification is attempted. A partial contact design approach is proposed and utilized for a flexible and more robust switch configuration. Moreover, the anchor extension concept is introduced and employed for bridge height stabilization purposes.

10. Modified switch devices fabricated in a second iteration are observed to work successfully. In particular, anchor extension solution is justified as a viable means for stabilizing MEMS bridge heights. Partial contact approach is also noted to work with success: ON-state resonance frequencies of the switches are precisely tuned to 35 GHz at actuation voltages in 20-25 V range with an associated optimum isolation level of 39 dB and isolation bandwidths of 3.2 GHz/10.0 GHz (according to 30 dB/20 dB criteria). Measured OFF-state return loss and insertion losses are found better than -16.4 dB and 0.27 dB respectively over 1-40 GHz.

Presented accomplishments can be improved or extended further with the following future works:

- Developed microwave lumped elements can be designed and utilized at different frequency bands, possibly for other lumped element based applications such as phase shifters and impedance matching networks. Moreover, tunable or reconfigurable monolithic designs can be realized by integrating RF MEMS switches to the fabrication process.

- Fringing field correction can be incorporated into the established Finite Difference formulations of pre-pull-in and post-pull-in electrostatic actuation problems for accurate electromechanical simulation of narrow beams. Moreover, solution of non-linear Finite Difference equation set may be improved with better algorithms in order to circumvent the stability issue pertaining to pull-in simulations.

- Zipping phenomenon can be characterized quantitatively for electrostatically actuated fixed-fixed type beams through semi-empirical expressions. A similar quantification can be also applied to hold voltages.

- Millimeter-wave performance of the Ka-band shunt, capacitive-contact switches can be improved further with a fully optimized design for a specific bridge height. In addition, thickness of the base metallization may be selectively increased in order to reduce conductor losses since currently utilized 0.9 μm value does not permit proper application of skin-effect formulations especially at lower frequencies.

- Fabricated Ka-band shunt, capacitive-contact RF MEMS switches may be utilized to realize switchable or reconfigurable circuits. In fact such a study has already been undertaken: A 5-bit DMTL phase shifter, a tunable capacitor and a phased-array have been designed recently by METU RF MEMS Group members (including the author) at millimeter-wave frequencies.

- RF MEMS switches having a different contact-type (namely, ohmic), circuit configuration (i.e. series) and microwave topology (like microstrip) can be implemented in various frequency bands. Mechanical bridge structures requiring lower actuation voltages or switching times may be analyzed and fabricated for specific applications. Switches with improved lifetimes may be realized by using different dielectric materials and by enclosing the switches within hermetic packages.

REFERENCES

[1] G. Chien and K.L. Loh, "Past, Present and Future of RF Design in Wireless Communication", in *Proc. Int. Symp. on VLSI Design, Automation and Test*, 2009, pp. 36–38.

[2] P.W. Hooijmans, "RF Front End Application and Technology Trends", in *Proc. Design Automation Conf.*, 2003, pp. 73–78.

[3] M.L. McMahan, A. Khatzibadeh, and P. Shah, "Wireless Systems and Technology Overview", *Texas Instruments, Dallas*, 1994.

[4] L.E. Larson, "Microwave MEMS Technology for Next-Generation Wireless Communications", in *Proc. IEEE MTT-S Int. Microwave Symp.*, 1999, Vol. 3, pp. 1073–1076.

[5] H.J. Santos, G. Fischer, H.A.C. Tilmans, and J.T.M. Beek, "RF MEMS for Ubiquitous Wireless Connectivity: Part 1–Fabrication", *IEEE Microwave Mag.*, Vol. 5, No. 4, pp. 36–49, 2004.

[6] H.J. Santos, G. Fischer, H.A.C. Tilmans, and J.T.M. Beek, "RF MEMS for Ubiquitous Wireless Connectivity: Part 2–Application", *IEEE Microwave Mag.*, Vol. 5, No. 4, pp. 50–65, 2004.

[7] H.A.C. Tilmans, W. De Raedt, and E. Beyne, "MEMS for Wireless Communications: 'From RF-MEMS Components to RF-MEMS-SiP'", *J. Micromech. Microeng*, Vol. 13, No. 4, pp. 139, 2003.

[8] G.M. Rebeiz, *RF MEMS: Theory, Design, and Technology*, John Wiley and Sons, 2003.

[9] H.J Santos, *Introduction to Microelectromechanical Microwave Systems*, Artech House, 2004.

[10] J. Bouchaud, B. Knoblich, and H. Wicht, "Will RF MEMS Live up Their Promise?", in *36th European Microwave Conf. Dig.*, 2006, pp. 1076–1079.

[11] J.J. Yao, "RF MEMS From a Device Perspective", *J. Micromech. Microeng.*, Vol. 10, No. 4, pp. R9, 2000.

[12] S. Lucyszyn, "Review of Radio Frequency Microelectromechanical Systems Technology", *IEE Proc on Science, Measurement and Technology*, Vol. 151, No. 2, pp. 93–103, 2004.

[13] R.J. Richards and H.J. Santos, "MEMS for RF/Microwave Wireless Applications: The Next Wave", *Microwave Journal*, Vol. 44, No. 3, pp. 20, 2001.

[14] R.J. Richards and H.J. Santos, "MEMS for RF/Microwave Wireless Applications: The Next Wave – Part II", *Microwave Journal*, Vol. 44, No. 7, pp. 142–144, 2001.

[15] Y. Sun, H. Van Zejl, J.L. Tauritz, and R.G.F Baets, "Suspended Membrane Inductors and Capacitors for Application in Silicon MMIC's", in *IEEE Microwave and Millimeter-Wave Monolithic Circuits Symp., Dig. of Papers*, 1996, pp. 99–102.

[16] J.B. Yoon, B.K. Kim, C.H. Han, E. Yoon, and C.K. Kim, "Surface Micromachined Solenoid on-Si and on-Glass Inductors for RF Applications", *Electron Device Lett., IEEE*, Vol. 20, No. 9, pp. 487–489, 1999.

[17] G.W. Dahlmann, E.M. Yeatman, P. Young, I.D. Robertson, and S. Lucyszyn, "Fabrication, RF Characteristics and Mechanical Stability of Self-Assembled 3D Microwave Inductors", *Sensors and Actuators A: Physical*, Vol. 97–98, pp. 215–220, 2002.

[18] J. Papapolymerou, J.C. Cheng, J. East, and L.P.B. Katehi, "A Micromachined High-Q X-Band Resonator", *Microwave and Guided Wave Lett., IEEE*, Vol. 7, No. 6, pp. 168–170, 1997.

[19] C. Kim, I. Song, C. Song, C. Cheon, Y. Kwon, and S. Lee, "A Micromachined Cavity Resonator for Millimeter-Wave Oscillator Applications", *10th Int. Conf. on Solid-State Sensors and Actuators, Tech. Dig.*, Vol. 83, No. 1–3, pp. 1–5, 2000.

[20] T.M. Weller, L.P.B. Katehi, M.I. Herman, P.D. Wamhof, K. Lee, E.A. Kolawa, and B.H. Tai, "New Results using Membrane-Supported Circuits: A Ka-band Power Amplifier and Survivability Testing", *IEEE Trans. on Microwave Theory and Tech.*, Vol. 44, No. 9, pp. 1603–1606, 1996.

[21] M. Ozgur, V. Milanov, C. Zincke, M. Gaitan, and M.E. Zaghloul, "Quasi-TEM Characteristic Impedance of Micromachined CMOS Coplanar Waveguides", *IEEE Trans. on Microwave Theory and Tech.*, Vol. 48, No. 5, pp. 852–854, 2000.

[22] G.M. Rebeiz, L.P.B. Katehi, T.M. Weller, C.Y. Chi, and S.V. Robertson, "Micromachined Membrane Filters for Microwave and Millimeter-Wave Applications", *Int. Journal of Microwave and Millimeter-Wave Computer-Aided Engineering*, Vol. 7, No. 2, pp. 149–166, 1997.

[23] I. Papapolymerou, R.F. Drayton, and L.P.B. Katehi, "Micromachined Patch Antennas", *IEEE Trans. on Antennas and Propagation*, Vol. 46, No. 2, pp. 275–283, 1998.

[24] B. Pillans, G.M. Rebeiz, and J.B. Lee, "Advances in RF MEMS Technology", in *IEEE 25th Annual GaAs IC Symp., Technical Dig. 2003*, 2003, pp. 17–20.

[25] S.V. Krishnaswamy, J. Rosenbaum, S. Horwitz, C. Yale, and R.A. Moore, "Compact FBAR Filters Offer Low-Loss Performance", *Microwaves & RF*, pp. 127–136, 1991.

[26] R.C. Ruby, A. Barfknecht, C. Han, Y. Desai, F. Geefay, G. Gan, M. Gat, and T. Verhoeven, "High-Q FBAR Filters in a Wafer-Level Chip-Scale Package", in *IEEE Int. Solid-State Circuits Conf., Dig. of Technical Papers*, 2002, Vol. 1, pp. 184–458.

[27] C.T.C. Nguyen, "Transceiver Front-End Architectures using Vibrating Micromechanical Signal Processors", in *Topical Meeting on Silicon Monolithic Integrated Circuits in RF Systems, Dig. of Papers*, 2001, pp. 23–32.

[28] A.N. Cleland and M.L. Roukes, "Fabrication of High Frequency Nanometer Scale Mechanical Resonators from Bulk Si Crystals", *Applied Physics Lett.*, Vol. 69, No. 18, pp. 2653 –2655, 1996.

[29] S. Majumder, J. Lampen, R. Morrison, and J. Maciel, "A Packaged, High-Lifetime Ohmic MEMS RF Switch", in *IEEE MTT-S Int. Microwave Symp. Dig.*, 2003, Vol. 3, pp. 1935–1940.

[30] R.E. Mihailovich, M. Kim, J.B. Hacker, E.A. Sovero, J. Studer, J.A. Higgins, J.F. DeNatale, R.S. Center, and T. Oaks, "MEM Relay for Reconfigurable RF Circuits", *IEEE Microwave and Wireless Components Letters*, Vol. 11, No. 2, pp. 53–55, 2001.

[31] D. Hyman, J. Lam, B. Warneke, A. Schmitz, T.Y. Hsu, J. Brown, J. Schaffner, A. Walston, R.Y. Loo, and M. Mehregany, "Surface-micromachined RF MEMS Switches on GaAs Substrates", *International Journal of Microwave and Millimeter-Wave Computer-Aided Engineering*, Vol. 9, No. 4, pp. 348–361, 1999.

[32] Z.J. Yao, S. Chen, S. Eshelman, D. Denniston, and C. Goldsmith, "Micromachined Low-Loss Microwave Switches", *IEEE JMEMS*, Vol. 8, No. 2, pp. 129–134, 1999.

[33] S. Duffy, C. Bozler, S. Rabe, J. Knecht, L. Travis, P. Wyatt, C. Keast, and M. Gouker, "MEMS Microswitches for Reconfigurable Microwave Circuitry", *IEEE Microwave and Wireless Components Letters*, Vol. 11, No. 3, pp. 106–108, 2001.

[34] M. Sakata, Y. Komura, T. Seki, K. Kobayashi, K. Sano, and S. Horiike, "Micromachined Relay which Utilizes Single Crystal Silicon Electrostatic Actuator", in 12th *IEEE Int. Conf. on MEMS*, 1999, pp. 21–24.

[35] D. Peroulis, S. Pacheco, K. Sarabandi, and L.P.B. Katehi, "MEMS Devices for High Isolation Switching and Tunable Filtering", in *IEEE MTT-S Int. Microwave Symp. Dig.*, 2000, Vol. 2, pp. 1217–1220.

[36] J.B. Muldavin and G.M. Rebeiz, "High-Isolation CPW MEMS Shunt Switches–Part 1: Modeling", *IEEE Trans. on Microwave Theory and Tech.*, Vol. 48, No. 6, pp. 1045–1052, 2000.

[37] J.B. Muldavin and G.M. Rebeiz, "High-Isolation CPW MEMS Shunt Switches- Part 2: Design", *IEEE Trans. on Microwave Theory and Tech.*, Vol. 48, No. 6, pp. 1053–1056, 2000.

[38] M. Ruan, G. Tam, R. Vaitkus, C. Wheeler, and J. Shen, "Micro-magnetic Latching RF Switches", in *Proc. Wireless Design Conf., London*, 2002, pp. 59–66.

[39] H.C. Lee, J.Y. Park, and J.U. Bu, "Piezoelectrically Actuated RF MEMS DC Contact Switches with Low Voltage Operation", *IEEE Microwave and Wireless Components Letters*, Vol. 15, No. 4, pp. 202–204, 2005.

[40] P. Blondy, D. Mercier, D. Cros, P. Guillon, P. Rey, P. Charvet, B. Diem, C. Zanchi, L. Lapierre, and J. Sombrin, "Packaged Millimeter Wave Thermal MEMS Switches", in *31st European Microwave Conf.*, 2001, pp. 1–4.

[41] D.J. Young and B.E. Boser, "A Micromachined Variable Capacitor for Monolithic Low–Noise VCOs", in *Solid-State Sensor and Actuator Workshop, Hilton Head Island, South Carolina, June 3-6, Technical Dig.*, 1996, pp. 86–89.

[42] E.S. Hung and S.D. Senturia, "Tunable Capacitors with Programmable Capacitance-Voltage Characteristic", in *Solid-State Sensors and Actuators Workshop Dig.*, 1998, pp. 292–295.

[43] L. Dussopt and G.M. Rebeiz, "High-Q Millimeter-Wave MEMS Varactors: Extended Tuning Range and Discrete-Position Designs", in *IEEE MTT-S Int. Microwave Symp. Dig.*, 2002, Vol. 2, pp. 1205–1208.

[44] J.J. Yao, S. Park, and J. DeNatale, "High Tuning–Ratio MEMS–based Tunable Capacitors for RF Communications Applications", in *Solid-State Sensors and Actuators Workshop Tech. Dig.*, 1998, pp. 124–127.

[45] C.L. Goldsmith, A. Malczewski, Z.J. Yao, S. Chen, J. Ehmke, and D.H. Hinzel, "RF MEMS Variable Capacitors for Tunable Filters", *Int. Journal of RF and Microwave Computer-Aided Engineering*, Vol. 9, No. 4, pp. 362–374, 1999.

[46] G.M. Rebeiz, "RF MEMS Switches: Status of the Technology", in *Proc. 12th Int. Conf. on Transducers, Solid-State Sensors, Actuators and Microsystems*, 2003, Vol. 2, pp. 1726–1729.

[47] G.M. Rebeiz, K. Entesari, I. Reines, S. Park, M. El-tanani, A. Grichener, and A. Brown, "Tuning in to RF MEMS", *IEEE Microwave Mag.*, Vol. 10, No. 6, pp. 55 –72, 2009.

[48] J. Ebel, R. Corez, K. Leedy, and R. Strawser, "Hermetic Thin-Film Encapsulation for RF MEMS Switches", in *Proc. GOMAC Tech. Conf., Las Vegas, NV,*, 2005, pp. 327–330.

[49] D.I. Forehand and C.L. Goldsmith, "Wafer Level Micropackaging for RF MEMS Switches", in *ASME InterPACK '05 Tech Conf*, 2005.

[50] J.H. Park, H.T. Kim, W. Choi, Y. Kwon, and Y.K. Kim, "V-band Reflection-type Phase Shifters using Micromachined CPW Coupler and RF Switches", *IEEE JMEMS*, Vol. 11, No. 6, pp. 808–814, 2002.

[51] M. Scardelletti, G. Ponchak, and N. Varaljay, "MEMS, Ka-band Single-Pole Double-Throw (SPDT) Switch for Switched Line Phase Shifters", in *IEEE Antennas and Propagation Society Int. Symp. Dig.*, 2002, Vol. 2, pp. 2–5.

[52] J.S. Hayden and G.M. Rebeiz, "Very Low-Loss Distributed X-Band and Ka-Band MEMS Phase Shifters using Metal-Air-Metal Capacitors", *IEEE Trans. on Microwave Theory and Tech.*, Vol. 51, No. 1, pp. 309–314, 2003.

[53] H.T. Kim, S. Jung, K. Kang, J.H. Park, Y.K. Kim, and Y. Kwon, "Low-Loss Analog and Digital Micromachined Impedance Tuners at the Ka-Band", *IEEE Trans. on Microwave Theory and Tech.*, Vol. 49, No. 12, pp. 2394–2400, 2001.

[54] J. Papapolymerou, K.L. Lange, C.L. Goldsmith, A. Malczewski, and J. Kleber, "Reconfigurable Double-Stub Tuners using MEMS Switches for Intelligent RF Front-Ends", *IEEE Trans. on Microwave Theory and Tech.*, Vol. 51, No. 1, pp. 271–278, 2003.

[55] M. Ünlü, K. Topallı, H.İ. Atasoy, E.U. Temoçin, İ. İstanbulluoğlu, Ö. Bayraktar, Ş. Demir, Ö.A. Çivi, S. Koç, and T. Akın, "A Reconfigurable RF MEMS Triple Stub Impedance Matching Network", in *Proc. 36th European Microwave Conf.*, 2006, pp. 1370–1373.

[56] J. Brank, Z.J. Yao, M. Eberly, A. Malczewski, K. Varian, and C.L. Goldsmith, "RF MEMS-Based Tunable Filters", *Int. Journal of RF and Microwave Computer-Aided Engineering*, Vol. 11, No. 5, pp. 276–284, 2001.

[57] J.H. Park, H.T. Kim, Y. Kwon, and Y.K. Kim, "Tunable Millimeter-Wave Filters using a Coplanar Waveguide and Micromachined Variable Capacitors", *J. Micromech. Microeng*, Vol. 11, No. 6, pp. 706–712, 2001.

[58] R.N. Simons, D. Chun, and L.P.B. Katehi, "Microelectromechanical Systems (MEMS) Actuators for Antenna Reconfigurability", in *IEEE MTT-S Int. Microwave Symp. Dig.*, 2001, Vol. 1, pp. 215–218.

[59] D.E. Anagnostou, G. Zheng, M.T. Chryssomallis, J.C. Lyke, G.E. Ponchak, J. Papapolymerou, and C.G. Christodoulou, "Design, Fabrication, and Measurements of an RF-MEMS-based Self-Similar Reconfigurable Antenna", *IEEE Trans. on Antennas and Propagation*, Vol. 54, No. 2, pp. 422–432, 2006.

[60] E. Erdil, K. Topallı, M. Ünlü, Ö.A. Çivi, and T. Akın, "Frequency Tunable Microstrip Patch Antenna using RF MEMS Technology", *IEEE Trans. on Antennas and Propagation*, Vol. 55, No. 4, pp. 1193, 2007.

[61] B. Lakshminarayanan and G.M. Rebeiz, "High-Power High-Reliability Sub-Microsecond RF MEMS Switched Capacitors", in *IEEE-MTT-S Int. Microwave Symp. Dig.*, 2007, pp. 1801–1804.

[62] C. Goldsmith, J. Maciel, and J. McKillop, "Demonstrating Reliability", *IEEE Microwave Mag.*, Vol. 8, No. 6, pp. 56–60, 2007.

[63] D.A. Daly, S.P. Knight, M. Caulton, and R. Ekholdt, "Lumped Elements in Microwave Integrated Circuits", *IEEE Trans. on Microwave Theory and Tech.*, Vol. 15, No. 12, pp. 713 – 721, 1967.

[64] M. Caulton, B. Hershenov, S.P. Knight, and R.E. DeBrecht, "Status of Lumped Elements in Microwave Integrated Circuits – Present and Future", *IEEE Trans. on Microwave Theory and Tech.*, Vol. 19, No. 7, pp. 588–599, 1971.

[65] R.E. Chaddock, "The Application of Lumped-Element Techniques to High Frequency Hybrid Integrated Circuits", *Radio and Electronic Engineer*, Vol. 44, No. 8, pp. 414–420, 1974.

[66] R.A. Pucel, "Design Considerations for Monolithic Microwave Circuits", *IEEE Trans. on Microwave Theory and Tech.*, Vol. 29, No. 6, pp. 513–534, 1981.

[67] I.J. Bahl, *Lumped Elements for RF and Microwave Circuits*, Artech House, 2003.

[68] E. Pettenpaul, H. Kapusta, A. Weisgerber, H. Mampe, J. Luginsland, and I. Wolff, "CAD Models of Lumped Elements on GaAs up to 18 GHz", *IEEE Trans. on Microwave Theory and Tech.*, Vol. 36, No. 2, pp. 294–304, 1988.

[69] E.U. Temoçin, "Design and Implementation of Microwave Lumped Components and System Integration using MEMS Technology", MSc Thesis, Middle East Technical University, Dept. of Electrical and Electronics Engineering, September 2006.

[70] Y. Ahn, H. Guckel, and J.D. Zook, "Capacitive Microbeam Resonator Design", *J. Micromech. Microeng*, Vol. 11, No. 1, pp. 70–80, 2001.

[71] S. Pourkamali, A. Hashimura, R. Abdolvand, G.K. Ho, A. Erbil, and F. Ayazi, "High-Q single Crystal Silicon HARPSS Capacitive Beam Resonators with Self-Aligned Sub-100-nm Transduction Gaps", *IEEE JMEMS*, Vol. 12, No. 4, pp. 487–496, 2003.

[72] C.T.C. Nguyen, L.P.B. Katehi, and G.M. Rebeiz, "Micromachined Devices for Wireless Communications", *Proc. of IEEE*, Vol. 86, No. 8, pp. 1756–1768, 1998.

[73] R.T. Howe and R.S. Muller, "Resonant-Microbridge Vapor Sensor", *IEEE Trans. on Electron Devices*, Vol. 33, No. 4, pp. 499–506, 1986.

[74] D.W. Burns, R.D. Horning, W.R. Herb, J.D. Zook, and H. Guckel, "Sealed-Cavity Resonant Microbeam Accelerometer", *Sensors and Actuators A: Physical*, Vol. 53, No. 1–3, pp. 249–255, 1996.

[75] Q. Zou, Z. Li, and L. Liu, "New Methods for Measuring Mechanical Properties of Thin Films in Micromachining: Beam Pull-in Voltage (VPI) Method and Long Beam Deflection (LBD) Method", *Sensors and Actuators A: Physical*, Vol. 48, No. 2, pp. 137–143, 1995.

[76] P.M. Osterberg and S.D. Senturia, "M-TEST: A Test Chip for MEMS Material Property Measurement using Electrostatically Actuated Test Structures", *IEEE JMEMS*, Vol. 6, No. 2, pp. 107–118, 1997.

[77] R.K. Gupta, "Electrostatic Pull-In Test Structure Design for In-Situ Mechanical Property Measurements of Microelectromechanical Systems (MEMS)", PhD Thesis, Massachusetts Institute of Technology, Dept. of Electrical Engineering and Computer Science, June 1997.

[78] P.M. Osterberg, H. Yie, X. Cai, J. White, and S.D. Senturia, "Self-consistent Simulation and Modelling of Electrostatically Deformed Diaphragms", in *Proc. of IEEE Workshop on MEMS*, 1994, pp. 28–32.

[79] B. Choi and E.G. Lovell, "Improved Analysis of Microbeams under Mechanical and Electrostatic Loads", *J. Micromech. Microeng*, Vol. 7, No. 1, pp. 24–29, 1997.

[80] S. Pamidighantam, R. Puers, K. Baert, and H.A.C. Tilmans, "Pull-in Voltage Analysis of Electrostatically Actuated Beam Structures with Fixed–Fixed and Fixed–Free End Conditions", *J. Micromech. Microeng.*, Vol. 12, No. 4, pp. 458–464, 2002.

[81] S. Gorthi, A. Mohanty, and A. Chatterjee, "Cantilever Beam Electrostatic MEMS Actuators Beyond Pull-in", *J. Micromech. Microeng.*, Vol. 16, pp. 1800–1810, 2006.

[82] E.M. Abdel-Rahman, M.I. Younis, and A.H. Nayfeh, "Characterization of the Mechanical Behavior of an Electrically Actuated Microbeam", *J. Micromech. Microeng.*, Vol. 12, No. 6, pp. 759–766, 2002.

[83] H.C. Nathanson, W.E. Newell, R.A. Wickstrom, and J.R. Davis Jr, "The Resonant Gate Transistor", *IEEE Trans. on Electron Devices*, Vol. 14, No. 3, pp. 117–133, 1967.

[84] R. Puers and D. Lapadatu, "Electrostatic Forces and Their Effects on Capacitive Mechanical Sensors", *Sensors and Actuators A: Physical*, Vol. 56, No. 3, pp. 203–210, 1996.

[85] S.D. Senturia, *Microsystem Design*, Kluwer Academic Publishers, 2001.

[86] P.M. Osterberg, "Electrostatically Actuated Microelectromechanical Test Structures for Material Property Measurement", PhD Thesis, Massachusetts Institute of Technology, Dept. of Electrical Engineering and Computer Science, September 1995.

[87] D.J. Ijntema and H.A.C. Tilmans, "Static and Dynamic Aspects of an Air-Gap Capacitor", *Sensors and Actuators A: Physical*, Vol. 35, No. 2, pp. 121–128, 1992.

[88] H.A.C. Tilmans and R. Legtenberg, "Electrostatically Driven Vacuum-Encapsulated Polysilicon Resonators Part II – Theory And Performance", *Sensors and Actuators A: Physical*, Vol. 45, No. 1, pp. 67–84, 1994.

[89] C. O'Mahony, M. Hill, R. Duane, and A. Mathewson, "Analysis of Electromechanical Boundary Effects on the Pull-In of Micromachined Fixed–Fixed Beams", *J. Micromech. Microeng.*, Vol. 13, No. 4, pp. 75–80, 2003.

[90] J.R. Gilbert and S.D. Senturia, "Two-Phase Actuators: Stable Zipping Devices without Fabrication of Curved Structures", in *Solid-State Sensor and Actuator Workshop, Hilton Head Island, South Carolina, June 3-6*, 1996, p. 98.

[91] J.R. Gilbert, G.K. Ananthasuresh, and S.D. Senturia, "3D Modeling of Contact Problems and Hysteresis In Coupled Electro-Mechanics", in *Proc. MEMS*, 1996, Vol. 96, pp. 11–15.

[92] L.A. Rocha, E. Cretu, and R.F. Wolffenbuttel, "Analysis and Analytical Modeling of Static Pull-in with Application to MEMS-Based Voltage Reference and Process Monitoring", *IEEE JMEMS*, Vol. 13, No. 2, pp. 342–354, 2004.

[93] L.E. Larson, R.H. Hackett, M.A. Melendes, and R.F. Lohr, "Micromachined Microwave Actuator (MIMAC) Technology – A New Tuning Approach for Microwave Integrated Circuits", in *IEEE Microwave and Millimeter-Wave Monolithic Circuits Symp. Dig.*, 1991, pp. 27–30.

[94] "RadantMEMS", `www.radantmems.com/radantmems/switchperformance.html`, last visited on February 2010.

[95] J. Muldavin, C.O. Bozler, S. Rabe, P.W. Wyatt, and C.L. Keast, "Wafer-Scale Packaged RF Microelectromechanical Switches", *IEEE Trans. on Microwave Theory and Tech.*, Vol. 56, No. 2, pp. 522–529, 2008.

[96] B. Pillans, J. Kleber, C. Goldsmith, and M. Eberly, "RF Power Handling of Capacitive RF MEMS Devices", in *IEEE MTT-S Int. Microwave Symp. Dig.*, 2002, Vol. 1, pp. 329–332.

[97] K. Topallı, "A Monolithic Phased Array using RF MEMS Technology", PhD Thesis, Middle East Technical University, Dept. of Electrical and Electronics Engineering, June 2007.

[98] H.İ Atasoy, "Design and Fabrication of RF MEMS Switches and Instrumentation for Performance Evaluation", MSc Thesis, Middle East Technical University, Dept. of Electrical and Electronics Engineering, September 2007.

[99] Ö. Bayraktar, "Beam Switching Reflectarray with RF MEMS Technology", MSc Thesis, Middle East Technical University, Dept. of Electrical and Electronics Engineering, September 2007.

[100] M. Ünlü, "An Adjustable Impedance Matching Network using RF MEMS Technology", MSc Thesis, Middle East Technical University, Dept. of Electrical and Electronics Engineering, September 2003.

[101] D. Swanson, A. Inc, and C.A. Milpitas, "Thin-Film Lumped-Element Microwave Filters", in *IEEE MTT-S Int. Microwave Symp. Dig.*, 1989, pp. 671–674.

[102] J.S. Hong and M.J. Lancaster, *Microstrip Filters for RF/Microwave Applications*, Wiley-Interscience, 2001.

[103] F.R. Gleason, "Thin-Film Microelectronic Inductors", in *Proc. Nat. Electronics Conf.*, 1964, pp. 197–198.

[104] G.D. Alley, "Interdigital Capacitors and Their Application to Lumped-Element Microwave Integrated Circuits", *IEEE Trans. on Microwave Theory and Tech.*, Vol. 18, No. 12, pp. 1028–1033, 1970.

[105] R.S. Pengelly and D.C. Rickard, "Design, Measurement and Application of Lumped Elements up to J-Band", in *7th European Microwave Conf.*, 1977, pp. 460–464.

[106] W.T. Lo, C.K.C. Tzuang, S.T. Peng, C.C. Tien, C.C. Chang, and J.W. Huang, "Resonant Phenomena in Conductor-Backed Coplanar Waveguides (CBCPW's)", *IEEE Trans. on Microwave Theory and Tech.*, Vol. 41, No. 12, pp. 2099–2108, 1993.

[107] C.C. Tien, C.K.C. Tzuang, S.T. Peng, and C.H.I. Chang, "Transmission Characteristics of Finite-Width Conductor-Backed Coplanar Waveguide", *IEEE Trans. on Microwave Theory and Tech.*, Vol. 41, No. 9, pp. 1616–1624, 1993.

[108] S.P. Timoshenko and J.M. Gere, *Theory of Elastic Stability*, McGraw Hill Inc., Second Edition, 1963.

[109] S.P. Timoshenko, *Strength of Materials, Part II : Advanced Theory and Problems*, D. Van Nostrand Company, Second Edition, 1940.

[110] S.P. Timoshenko and S.W. Krieger, *Theory of Plates and Shells*, McGraw-Hill Inc., Second Edition, 1959.

[111] S.P. Timoshenko, *Strength of Materials, Part I : Elementary Theory and Problems*, D. Van Nostrand Company, Second Edition, 1940.

[112] R.C. Hibbeler, *Engineering Mechanics: Statics*, Prentice Hall, 12th Edition, 2009.

[113] E.S. Hung and S.D. Senturia, "Extending the Travel Range of Analog-Tuned Electrostatic Actuators", *IEEE JMEMS*, Vol. 8, No. 4, pp. 497–505, 1999.

[114] N.S. Barker and G.M. Rebeiz, "Distributed MEMS True-Time Delay Phase Shifters and Wide-Band Switches", *IEEE Trans. on Microwave Theory and Tech.*, Vol. 46, No. 11, pp. 1881–1890, 1998.

[115] R. Plonsey and R.E. Collin, *Principles and Applications of Electromagnetic Fields*, pp. 107–109, McGraw Hill Inc., First Edition, 1961.

[116] R. LeVeque, *Finite Difference Methods for Ordinary and Partial Differential Equations: Steady-State and Time-Dependent Problems*, Society for Industrial and Applied Mathematics, 2007.

[117] W.H. Press, S.A. Teukolsky, W.T. Vetterling, and B.P. Flannery, *Numerical Recipes in C: The Art of Scientific Computing*, Cambridge University Press, 2nd Edition, 1992.

[118] "Numpy", `http://numpy.scipy.org/`, Last visited on February 2010.

[119] "SciPy: Open source scientific tools for Python", `http://www.scipy.org/`, Last visited on February 2010.

[120] B.S. Garbow, K.E. Hillstrom, J.J. More, and D.C. Sorenson, "Minpack Project, Argonne National Laboratory", `http://www.netlib.org/minpack`, 1980, Last visited on February 2010.

[121] H.A.C. Tilmans, M. Elwenspoek, and J.H.J. Fluitman, "Micro Resonant Force Gauges", *Sensors and Actuators A: Physical*, Vol. 30, No. 1-2, pp. 35–53, 1992.

[122] M. Abramowitz and I.A. Stegun, *Handbook of Mathematical Functions with Formulas, Graphs, and Mathematical Tables*, Dover Publications, 1972.

[123] E.K.L. Chan, "Characterization and Modeling of Electrostatically Actuated Polysilicon Micromechanical Devices", PhD Thesis, Stanford University, Dept. of Electrical Engineering, 1999.

[124] G.M. Rebeiz and J.B. Muldavin, "RF MEMS Switches and Switch Circuits", *IEEE Microwave Mag.*, Vol. 2, No. 4, pp. 59–71, 2001.

[125] J.B. Muldavin and G.M. Rebeiz, "High-Isolation Inductively-Tuned X-Band MEMS Shunt Switches", in *IEEE MTT-S Int. Microwave Symp. Dig.*, 2000, Vol. 1, pp. 169–172.

[126] K. Topallı, M. Ünlü, H.İ. Atasoy, Ş. Demir, Ö.A. Çivi, and T. Akın, "Empirical Formulation of Bridge Inductance in Inductively Tuned RF MEMS Shunt Switches", *Progress In Electromagnetics Research,* PIER97, pp. 343–356, 2009.

[127] G. Ghione and C.U. Naldi, "Coplanar Waveguides for MMIC Applications: Effect of Upper Shielding, Conductor Backing, Finite-Extent Ground Planes, and Line-to-Line Coupling", *IEEE Trans. on Microwave Theory and Tech.*, Vol. 35, No. 3, pp. 260–267, 1987.

[128] R.E. Collin, *Foundations for Microwave Engineering*, pp. 177–178, IEEE Press, 2001.

[129] I. Wolff, *Coplanar Microwave Integrated Circuits*, pp. 175–176, John Wiley and Sons, 2006.

[130] N.S. Barker and G.M. Rebeiz, "Optimization of Distributed MEMS Phase Shifters", in *IEEE MTT-S Int. Microwave Symp. Dig.*, 1999, Vol. 1, pp. 299–302.

[131] C. Goldsmith, J. Ehmke, A. Malczewski, B. Pillans, S. Eshelman, Z. Yao, J. Brank, and M. Eberly, "Lifetime Characterization of Capacitive RF MEMS Switches", in *IEEE MTT-S Int. Microwave Symp. Dig.*, 2001, Vol. 3, pp. 227–230.

[132] "Webelements", `http://www.webelements.com/gold/physics.html`, last visited on February 2010.

[133] Ansoft HFSS v9.2 Online Help.

[134] A.D. Polyanin and V.F. Zaitsev, *Handbook of Exact Solutions for Ordinary Differential Equations*, CRC Press, Second Edition, 2003.

DERIVATION OF THE BEAM DEFLECTION PROFILE FOR A CONCENTRATED TRANSVERSE LOAD

In this appendix, solution of the beam differential equation for a concentrated transverse load is outlined for the case of tensile axial state. Relevant beam equation was derived in §3.2.1.1 as:

$$\frac{d^4 y(x)}{dx^4} - k^2 \frac{d^2 y(x)}{dx^2} = \frac{Q}{E'I}\,\delta(x - x_0) \tag{A.1}$$

Equation (A.1) can be integrated twice to obtain,

$$\frac{d^2 y(x)}{dx^2} - k^2 y(x) = \frac{Q}{E'I}(x - x_0)\,u(x - x_0) + c_1 x + c_0 \tag{A.2}$$

where c_i are arbitrary constants and $u(x)$ is the unit-step function respectively. For convenience in the following discussion, let us represent the first term of the right-hand-side of Equation (A.2) with,

$$\frac{Q}{E'I}(x - x_0)\,u(x - x_0) = f(x - x_0)\,u(x - x_0) \tag{A.3}$$

A general solution to Equation (A.2) can be stated as [134],

$$y(x) = \frac{1}{k} \int_{x_1}^{x} f(t - x_0)\,u(t - x_0) \sinh\left[k(x - t)\right] dt$$

$$+ d_1 x + d_0 + A\cosh(kx) + B\sinh(kx) \tag{A.4}$$

where x_1 is an arbitrary number. From the discontinuous nature of the forcing function, it is expected for $y(x)$ (or more explicitly for its third derivative) to possess a similar discontinuity at $x = x_0$. It must be noted also that x_1 must be selected carefully in order to

preserve non-impulsive behavior of $\frac{\mathrm{d}^2 y(x)}{\mathrm{d}x^2}$ and to facilitate the relevant integration. Let us now confine our attention to the integration term and try to find a proper x_1 to satisfy the mentioned requirement.

Let $y_{p,1}(x)$ denote the particular solution due to only the first term of RHS of Equation (A.2). From the mini-discussion in the previous paragraph, it is expected that;

$$y_{p,1}(x) = g(x - x_0)\, u(x - x_0) \tag{A.5}$$

where $g(x)$ is a smooth function. Moreover, $y_{p,1}(x)$ must satisfy,

$$\frac{\mathrm{d}^2 y_{p,1}(x)}{\mathrm{d}x^2} - k^2 y_{p,1}(x) = f(x - x_0)\, u(x - x_0)$$

Carrying out the differentiations, one obtains;

$$f(x - x_0)\, u(x - x_0) = \left[g''(x - x_0) - k^2 g(x - x_0) \right]\, u(x - x_0)$$
$$+ g'(0)\, \delta(x - x_0) \tag{A.6}$$
$$+ g(0)\, \delta'(x - x_0)$$

It is observed clearly from Equation (A.6) that

$$g(0) = 0$$
$$g'(0) = 0 \tag{A.7}$$

since relevant forcing function does not contain any impulses nor its derivatives. Using these conditions, Equation (A.6) translates to,

$$g''(x) - k^2 g(x) = f(x)$$

which has the identified solution as,

$$g(x) = \frac{1}{k} \int_{x_1'}^{x} f(t) \sinh\left[k(x - t)\right] \mathrm{d}t$$

Now notice that,

$$g(0) = -\frac{1}{k} \int_{x_1'}^{0} f(t) \sinh(kt)\mathrm{d}t = 0 \tag{A.8}$$

209

Also, through the use of Leibniz Integral Rule, one can show that,

$$g'(0) = \int_{x_1'}^{0} f(t)\cosh(kt)\,dt = 0 \tag{A.9}$$

In the light of Equations (A.8) and (A.9), it can be stated that $x_1' = 0$ is a proper selection that simultaneously satisfies Equation Set (A.7). With the pointed choice of x_1', $g(x)$ can now be evaluated as follows:

$$
\begin{aligned}
g(x) &= \frac{1}{k} \int_{0}^{x} \frac{Q}{E'I} t \sinh\left[k(x-t)\right] dt \\
&= \frac{Q}{E'Ik^2} \int_{0}^{kx} \left(x - \frac{t'}{k}\right) \sinh(t')\,dt' \\
&= \frac{Q}{E'Ik^2} \left[x\cosh(t') - \frac{t'\cosh(t') - \sinh(t')}{k} \right]_{0}^{kx} \\
&= \frac{Q}{E'Ik^3} \left[\sinh(kx) - kx\right]
\end{aligned}
\tag{A.10}
$$

Having determined a closed-form expression for $g(x)$, $y_{p,1}(x)$ can be readily obtained through Equation (A.5).

Now let us return our attention back to the general solution described by Equation (A.4). Replacing the integration term with its evaluated form, relevant equation becomes,

$$y(x) = g(x - x_0)\,u(x - x_0) + d_1 x + d_0 + A\cosh(kx) + B\sinh(kx)$$

In order to determine the constants A, B, d_1 and d_0, boundary conditions at $x = 0$ and $x = L$ will be enforced next. Since the beam under consideration has built-in ends, it is required that

$$y(0) = 0 \tag{A.11a}$$

$$y'(0) = 0 \tag{A.11b}$$

$$y(L) = 0 \tag{A.11c}$$

$$y'(L) = 0 \tag{A.11d}$$

First of these conditions results in,

$$y(0) = d_0 + A = 0$$

$$\therefore d_0 = -A$$

In order to investigate the second condition, let us first evaluate the derivative of $y(x)$:

$$y'(x) = g'(x - x_0)\, u(x - x_0) + d_1 + Ak\sinh(kx) + Bk\cosh(kx)$$

where $g(0) = 0$ is utilized to cancel the impulsive term. Equation (A.11b) then yields,

$$y'(0) = d_1 + Bk = 0$$

$$\therefore d_1 = -Bk$$

Remaining boundary conditions at $x = L$ leads to

$$A[\cosh(kL) - 1] + B[\sinh(kL) - kL] = -\frac{Q}{E'Ik^3}\left\{\sinh\left[k(L - x_0)\right] - k(L - x_0)\right\}$$
$$A\sinh(kL) + B[\cosh(kL) - 1] = -\frac{Q}{E'Ik^3}\left\{\cosh\left[k(L - x_0)\right] - 1\right\} \tag{A.12}$$

After solving Equation Set (A.12) for A and B, one obtains,

$$A = \frac{Q}{E'Ik^3}\frac{\sinh\left[k(L-x_0)\right] - kL\cosh\left[k(L-x_0)\right] + k(L-x_0)\cosh(kL) + \sinh(kx_0) + kx_0 - \sinh(kL)}{kL\sinh(kL) - 2\cosh(kL) + 2}$$
$$B = \frac{Q}{E'Ik^3}\frac{\cosh\left[k(L-x_0)\right] - k(L-x_0)\sinh(kL) - \cosh(kx_0) + \cosh(kL) - 1}{kL\sinh(kL) - 2\cosh(kL) + 2} \tag{A.13}$$

Deflection profile for the beam can be therefore determined as,

$$y(x) = g(x - x_0)\, u(x - x_0) + A[\cosh(kx) - 1] + B[\sinh(kx) - kx] \tag{A.14}$$

with $g(x)$ and the coefficients A, B expressed by Equations (A.10) and (A.13) respectively.